WADD TECHNICAL REPORT 60-182

FEASIBILITY STUDY OF AN INFLATABLE TYPE STABILIZATION AND DECELERATION SYSTEM FOR HIGH-ALTITUDE AND HIGH-SPEED RECOVERY

F. R. NEBIKER

GOODYEAR AIRCRAFT CORPORATION
AKRON, OHIO

DECEMBER 1961

AERONAUTICAL SYSTEMS DIVISION
AIR FORCE SYSTEMS COMMAND
UNITED STATES AIR FORCE
WRIGHT-PATTERSON AIR FORCE BASE, OHIO

FOREWORD

The work presented in this report was performed by Goodyear Aircraft Corporation, Akron, Ohio, under the authority of Project 8 (7-6065), Task 61526, entitled "Feasibility Study for a Balloon Type Stabilization and Deceleration System for High-Altitude and High-Speed Recovery," and Air Force Contract No. AF33(616)-6010.

This is the final report.

Mr. T. J. Cox, Flight Accessories Laboratory, Wright Air Development Division, served as contract monitor.

The authors and contributing personnel of Goodyear Aircraft Corporation who cooperated in the research and the preparation of this report were: F. R. Nebiker, Project Engineer; N. T. Karaffa, Report Coordinator; L. M. Cerreta, Thermal and Flow Analysis; J. J. Graham, Design; N. E. Houtz, Structural Analysis.

WADD TR 60-182

ABSTRACT

On the basis of the theoretical and experimental wind tunnel test data obtained, it has been concluded that an inflatable sphere is a practicable stabilization and deceleration system for initial recovery from high-altitude, high-speed flight regimes (up to Mach 4.0 at 200,000 feet). Inflatable spheres tested were fabricated utilizing standard manufacturing methods and readily available materials. The recovery system tested exhibited considerable potential as an initial stabilization and deceleration recovery system for a disoriented or tumbling high-altitude, high-speed payload. Included in this report are theoretical and wind tunnel test data on the effects of various shaped primary bodies on a secondary spherical body at various trailing distances. Also included is a limited amount of experimental data on flight testing of a full-scale operational unit.

PUBLICATION REVIEW

This report has been reviewed and is approved.

FOR THE COMMANDER:

GEORGE A. SOLT, JR.
CHIEF, RETARDATION AND RECOVERY
BRANCH
FLIGHT ACCESSORIES LABORATORY

TABLE OF CONTENTS

TABLE OF CONTENTS (Continued)

LIST OF ILLUSTRATIONS

LIST OF TABLES

SECTION I

INTRODUCTION

Under contract AF33(616)-6010, Goodyear Aircraft Corporation has conducted a detailed study and test program to establish a feasible high-altitude, high-speed recovery system utilizing expandable structures.

With the advent of high-speed, high-altitude flight, new methods of stabilization and deceleration must be developed for successful recovery of such payloads as manned escape capsules, rocket boosters, nose cones, and instrument data packages. Initial stabilization is required so that protective re-entry devices (heat shields, ablation shields, drag producing devices) of a payload tumbling or disoriented in space can be aligned with the flight path. Initial deceleration is required to reduce aerodynamic heating and loading, and to gradually reduce the velocity of the payload through a varying dynamic loading regime.

If conventional methods of recovery are to be utilized in the final stage, it is particularly important that the velocity of the payload be gradually reduced as the payload re-enters the atmosphere from high-speed, high-altitude flight. Recent investigations indicate that conventional parachutes are not satisfactory for this first-stage deceleration, because of aerodynamic heating and erratic loading at supersonic flow conditions.

An initial deceleration system which will reduce the velocity of the payload by substantially decreasing its ballistic coefficient will lessen the initial shock on the payload and on final recovery devices such as rotor blades, flexible wings, inflatable wings, and parachutes.

The three-fold objectives of this study and test program are as follows:

(1) To conduct an analysis of the feasibility and practicality of an inflatable system for initial stabilization and deceleration at velocities up to Mach 4.0 at an altitude of 200,000 feet over a range of six ballistic coefficients $(W/C_D A)$ - 0.1, 1.0, 10, 25, 50, and 100. This system is to perform down to an altitude of 60,000 feet.

(2) To select a ballistic coefficient $(W/C_D A)$ and to design, fabricate, and test a scale-model inflatable drag producing system. Existing materials and methods were to be used in the design and fabrication of the partial and full scale model. Subsystem functionals and wind tunnel tests were to be included in the testing.

(3) To design and fabricate a full-scale mock-up, perform functional tests to verify design, and design, fabricate, and test a full-scale operational system. The system would be capable of operation at a velocity of Mach 4.0 at an altitude of 200,000 feet; gross weight of recoverable payload, 500 pounds; gross weight-to-drag ratio $(W/C_D A)$ selected from the results of the analytical study, considering material and design installation requirements.

This report presents the results of the preliminary theoretical analysis, the supporting wind tunnel, design, and functional test data. The final detail design criteria of the full-scale system selected by mutual agreement between WADD personnel and Goodyear Aircraft Corporation is also included.

SECTION II

DISCUSSION

Flight vehicle performance has reached a point at which previous concepts of recovery systems for manned or unmanned vehicles are no longer satisfactory. At supersonic velocities utilization of a conventional parachute for initial stabilization and deceleration is presently not adequate with regard to reliability and performance. Conventional fabric parachutes do not fully inflate under these conditions and do not have satisfactory stability characteristics and capability of withstanding aerodynamic heating and loading which are necessary for successful recovery.

During the preliminary study phase to develop a system for providing initial stabilization and deceleration, trajectories, aerodynamic characteristics, thermodynamic effects, load distributions, and stress factors were investigated for various inflatable shapes.

The aerodynamic study revealed that an isolated sphere in subsonic flow is stable only in the supercritical regime (R_n 3.85 x 10^5). Below this critical Reynolds number, the flow is laminar and the Von Karman vortex streets are released at spasmodic intervals from the after-portion of the sphere, creating unbalanced forces and resultant instability. In the supercritical regime at subsonic and transonic speeds, the flow separates evenly aft of the sphere, resulting in balanced forces and stability. However, positive flow separation occurs at supersonic and hypersonic conditions without Reynolds number considerations. The non-lifting aerodynamic property of a sphere was also considered desirable for a stable drag device.

The stress analysis study further confirmed the feasibility of utilizing a spherical shape during these preliminary stages to develop a practical recovery system because of structural simplicity. The spherical shape is advantageous in that its shape is maintained without complicated tailoring and internal bracing, distribution of stresses resulting from aerodynamic loads and internal pressures are more uniform, and the inflation method does not require complex manifolding or control. The drag load applied at a single point should be equally distributed to the inflated structure to avoid undesirable stress concentrations. The drag load can be equally distributed to a spherical shape by a network of meridian cables encircling a sphere.

Various methods were investigated to determine a light-weight system for inflating the drag device at high altitudes, and to maintain sufficient pressure during the descending portion of trajectory, thereby providing the necessary initial deceleration and stability for recovery.

Because of the near vacuum at the initial flight condition (200,000-foot altitude at zero velocity), the air pressure required to inflate a sphere is approximately 1/3000 of that required at sea level.

In addition to the foregoing, consideration had to be given to determining the effect of the distance between the primary shape and secondary (trailing) shape. Only a nominal amount of data was available on effects of the primary shape on the secondary shape; therefore, various-shaped primary shapes were also considered.

Considerable effort was expended on the determination of the optimum method of suspension and deployment for stabilization of a towed inflatable drag device at subsonic, transonic, and super-sonic speeds.

Therefore, for the foregoing reasons, a spherical shape with a network of meridian cables and a lightweight pressure system was determined to be the most optimum experimental design for an inflatable decelerating and stabilizing device.

SECTION III

PRELIMINARY STUDY PROGRAM

A. TRAJECTORY ANALYSIS

A complete trajectory analysis of the high-speed recovery and the free-fall flight conditions for each of the given ballistic coefficient or W/A conditions was obtained using digital computer equipment. The trajectory program used was one that had been in the process of refinement and improvement over several months.

For the trajectory analysis, two basic assumptions were made:

(1) The inflatable drag producing device is considered to be a perfect sphere.

(2) Shielding effects of any payload leading the device are neglected in drag estimates. Mutual interference of flow fields is neglected. This probably leads to somewhat optimistic (high) drag values for the drag device payload system. Drag of the payload is neglected.

The equations of motion and symbol definitions used in the trajectory analysis are given in Appendix II. Orbit equations for a body in motion under the influence of the inverse square attraction only are shown in Eq (1) through (14).

$$V^2 = V_x^2 + V_z^2 . \tag{1}$$

$$r = Z + 20,908,800 = Z + R_E. \tag{2}$$

$$e = \frac{1}{\mu} \sqrt{(rV_x^2 - \mu)^2 + (rV_xV_z)^2} \quad \text{where } \mu = 1.4065107 \times 10^{16}. \tag{3}$$

$$\tan \theta = \frac{rV_xV_z}{rV_x^2 - \mu} . \tag{4}$$

$$\tan E = \frac{V_z \sqrt{r(2\mu - rV^2)}}{rV^2 - \mu} . \tag{5}$$

$$a = \frac{r\mu}{2\mu - rV^2} . \tag{6}$$

$$\Delta t = a \sqrt{a/\mu} \left[E + 2e \cos (E + \Delta E/2) \sin (\Delta E/2) \right]. \tag{7}$$

$$\Delta Z = -e\, a \sin (E + \Delta E/2) \sin (\Delta E/2) . \tag{8}$$

$$\Delta V_x = \frac{(V_x r) - V_{x_0}}{r + \Delta Z} . \tag{9}$$

$$\Delta V_z = \frac{-e \sqrt{a \mu} \, \sin (E + \Delta E)}{r + \Delta Z} - V_{z_0} \quad . \tag{10}$$

$$\Delta \theta = \arctan \frac{\sqrt{1 - e^2} \, \sin (E + \Delta E)}{e + \cos (E + \Delta E)} - \theta_0 \quad . \tag{11}$$

Eq (1) through (11) are derivable from differential equations

$$\ddot{r} - r (\dot{\theta})^2 = \frac{\mu}{r^2} \tag{12}$$

and

$$2 \dot{r} \dot{\theta} + r \ddot{\theta} = 0 \tag{13}$$

and their solution

$$r = \frac{a (1 - e^2)}{1 - e \cos (\theta - \theta_0)}, \tag{14}$$

with the definitions

$$V_x = r \dot{\theta} \text{ and } V_z = \dot{r}.$$

The independent variable in the solution is ΔE rather than Δt. This is necessary for exact solutions because of the nature of the equations. If it were necessary to solve in terms of Δt, a solution for E in Eq (7) would be required. Unfortunately, this is a transcendental equation for which no exact solution can be written. The computer solution is therefore written as shown in Eq (1) through (11).

The solutions of Eq 1 through 11 do not include any forces other than inertial and gravitational. The aerodynamic forces are given by Eq (15).

$$A_{aero} = A_{drag} + A_{lift} \tag{15}$$

where

$$A_{drag} = \frac{\pi}{4} \frac{d^2}{w} \, q C_d \quad \text{(Acceleration due to drag)}$$

and

$$A_{lift} = \frac{L}{D} \, A_{drag} \quad \text{(Acceleration due to lift)}.$$

The change of velocity due to aerodynamic drag during a time increment is given by Eq (16)

$$\int_0^{\Delta t} A_{aero} \, dt = \int_0^{\Delta t} \frac{\pi}{4} \frac{d^2}{w} q \, C_D \, dt \qquad (16)$$

where q and C_D are functions of time. The dynamic pressure ($q = 1/2\rho V^2$) is affected by the rapidly changing atmospheric density (ρ) with respect to time for the high vertical velocities (since it is approximately exponential with altitude). This being the case, the integral is approximated in the computer by assuming the following: (1) A constant vertical velocity over each increment and (2) a constant rate of change of log density with altitude that is equal to the rate of change of log density at the initial altitude. With the assumptions included in Eq (15), the equation becomes:

$$\Delta V_{aero} = \frac{\pi}{4} \left(\frac{d^2}{w}\right) q \, C_D \left(\frac{1}{\rho}\right) \int_0^{\Delta t} \rho \, dt = A_d \left(\frac{1}{\rho}\right) \int_0^{\Delta t} \rho \, dt. \qquad (17)$$

Since C_D is also a variable, the curve of the drag coefficient of a smooth sphere versus Mach number, for both the subcritical and supercritical Reynolds number, was obtained from recent data. Equations were developed for this curve for programming in the computer. Stabilization accessories were not considered.

The change of vertical position due to aerodynamics was approximated as shown in Eq (18).

$$\Delta Z_{aero} = \Delta V_{z_{aero}} \frac{\Delta t}{2} \cong \int_0^{\Delta t} \Delta V_{z_{aero}} \, dt \qquad (18)$$

Similar assumptions were made for horizontal velocity and position. The accelerations were resolved into vertical and horizontal components.

From the preceding development, it may be seen that the choice of the computer increment affects the accuracy of the aerodynamic section only. The inertial - gravitational portion is exact under the assumptions of a perfectly spherical non-rotating earth with a radius of 3960 status miles and a mass of $1.4065107 \times 10^{16}/G$ slugs where G is the universal gravity constant. The gravitational influence of all other bodies is ignored.

The computer program was chosen so that the ratio of the non-exact portion of the solution to the exact portion would be small. This was accomplished by selecting an interval and testing it to find this ratio. If the ratio exceeded the arbitrary limit, the increment was reduced and tested again. This was repeated until the ratio was sufficiently small. (For this analysis the arbitrary ratio selected was five percent.) Since it is possible for no change to occur in the gravitational inertial term in the case of the high-speed recovery, a zero interval would take place in such a case. This is avoided by setting an arbitrary lower limit on the gravitational-inertial term used in defining the ratio.

In actual practice three ratios are used. They are the ratio of the change due to outside forces to the gravity-inertia change of (1) altitude, (2) horizontal velocity, and (3) vertical velocity.

The use of the chosen ΔE increment for the lowest weight to drag ratios produced extremely lengthy computer runs because of an extremely small increment in these cases.

Other formulae involved in the solution of the general problem include those for finding atmospheric properties as a function of altitude (see Figure 1). These formulae, listed in Reference 1 as modified by the Smithsonian Astrophysical Observatory on the basis of Sputnik I observations as of March 1958, are as follows:

$$H = Z (1 + Z/R_E). \tag{19}$$

$$T_M = T_{M_B} + L_M (H - H_B). \tag{20}$$

$$P = P_b \exp \left[\frac{-Q (H - H_B)}{T_{M_B}} \right] \quad \text{where Q is a constant and } L_M = 0. \tag{21}$$

$$P = P_b \exp \left[\frac{-Q}{L_M} \ln \frac{T_M}{T_{M_B}} \right] \quad \text{where Q is a constant and } L_M \neq 0. \tag{22}$$

$$\rho = (M/R_e) \frac{(P)}{T_M} \quad \text{where } M/R_e = \text{constant}, \ \rho = \text{density}. \tag{23}$$

$$V_S = \sqrt{\gamma \frac{(R_e) T_M}{M_0}} \quad \begin{array}{l} \text{where } \gamma = \text{constant} \\ \text{and } V_S = \text{velocity of sound}. \end{array} \tag{24}$$

The results of the computer work for both the high-speed recovery (Mach 4.0 from 200,000 to 60,000-foot altitude level flight) and the free-fall flight (zero velocity from 100,000 to 60,000-foot altitude vertical flight) conditions are shown in Figures 1 through 13. These data, although based on theoretical curves, were analyzed and were utilized in the determination of the recovery system requirements. Curves of altitude, velocity, Mach number, and acceleration versus time are given for each $W/C_D A$ and each W/A.

The free-fall flight conditions covered a low velocity range increasing from zero velocity at initiation of the fall. Because of this fact, the inflatable drag device passes through the region of critical Reynolds number, causing a decrease in its drag coefficient at some point in its trajectory, dependent on its diameter. Based on this observation, it was felt that computer runs using both the subcritical and supercritical portions of the drag coefficient curve shown in Figures 14 and 15 would be of value.

As may be noted from the resultant curves for the free-fall condition, this change in drag based on Reynolds number has a significant effect at the lower W/A values, but the magnitude of this effect decreases considerably with increase in the weight to drag area ratio.

B. AERODYNAMIC ANALYSIS

Since a spherical shape was selected as a basis for the analytical study, it was necessary to investigate the aerodynamic properties of such a body with special regard to drag producing ability, pressures existing on the body, and stability.

The spherical drag body offers an efficient drag producing device at supersonic speeds as shown by the drag coefficient curve in Figure 15. The stagnation pressures and the pressure coefficient distribution encountered by the sphere over the Mach number range given are shown in Figures 16 and 17. Based on both theoretical and experimental results, the pressure distribution over the spherical surface is given for the various Mach numbers in Figure 18.

As the inherent stability of the sphere was held to be an extremely important factor, a detailed study of this property was made, based on existing aerodynamic knowledge. The stability of a
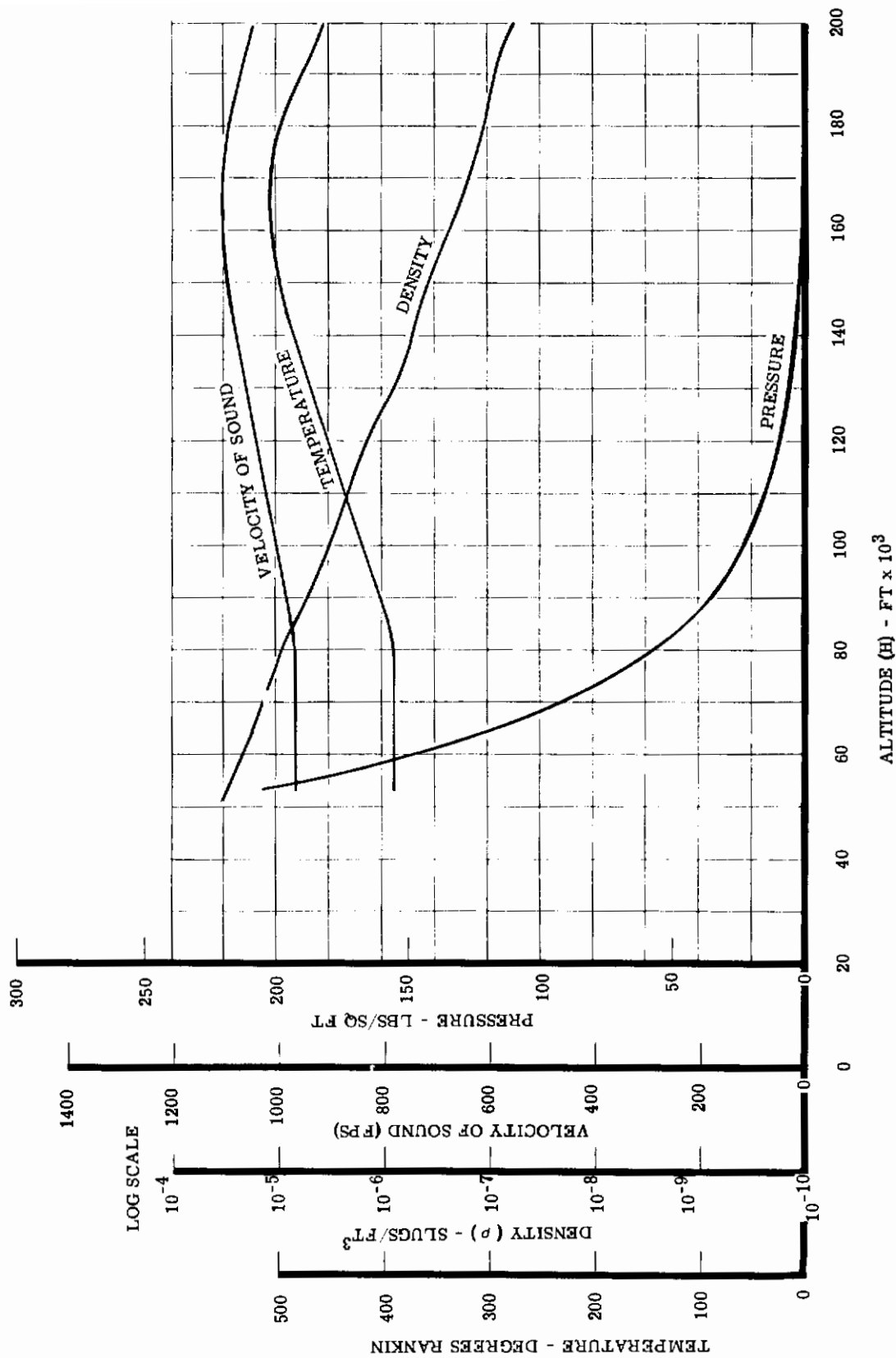
Figure 1. Properties of Atmospheric Air versus Altitude
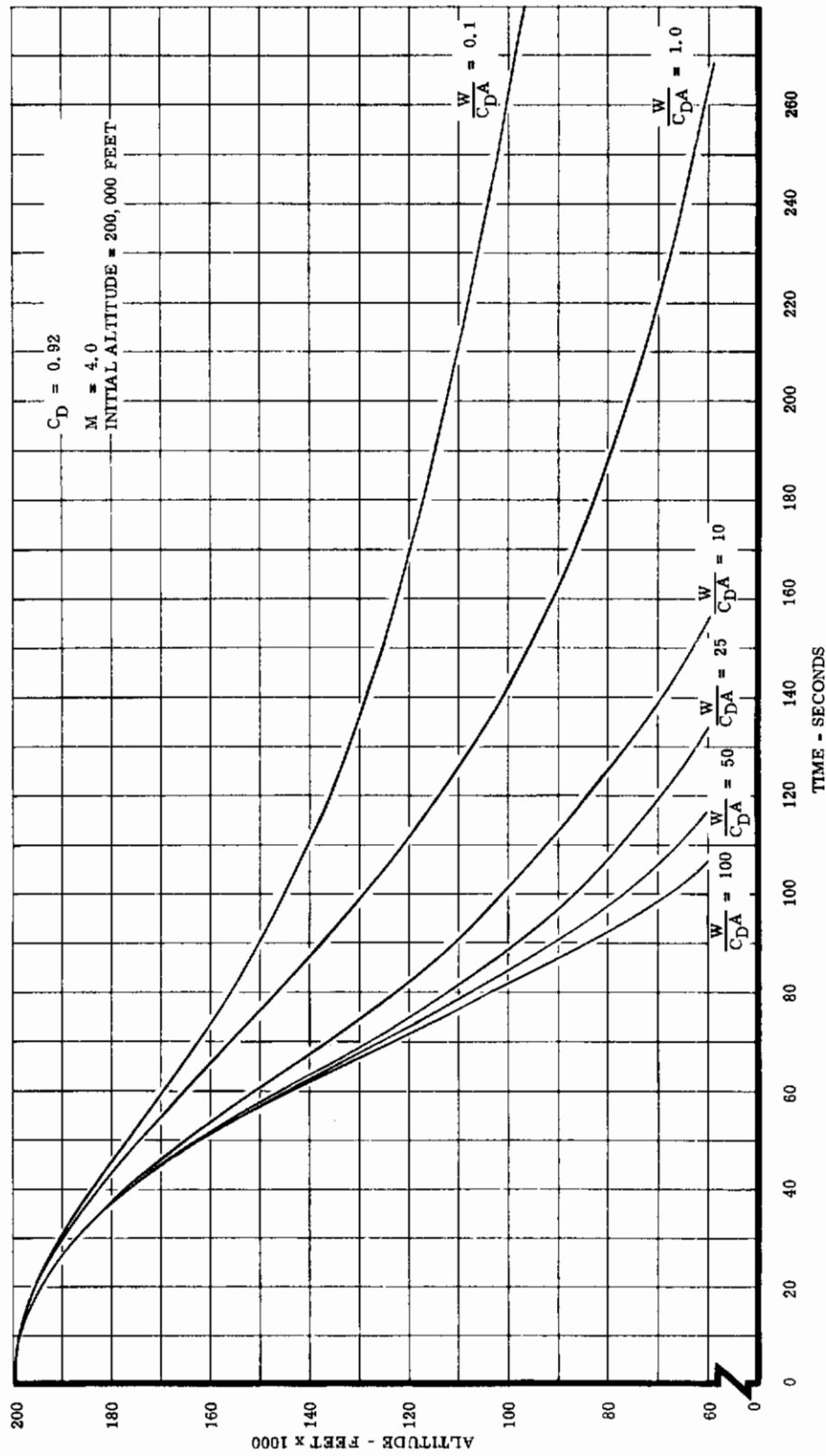
Figure 2.   Altitude versus Time for a High-Speed Recovery Using a Spherical Drag Device

M = 0
INITIAL ALTITUDE = 100,000 FEET
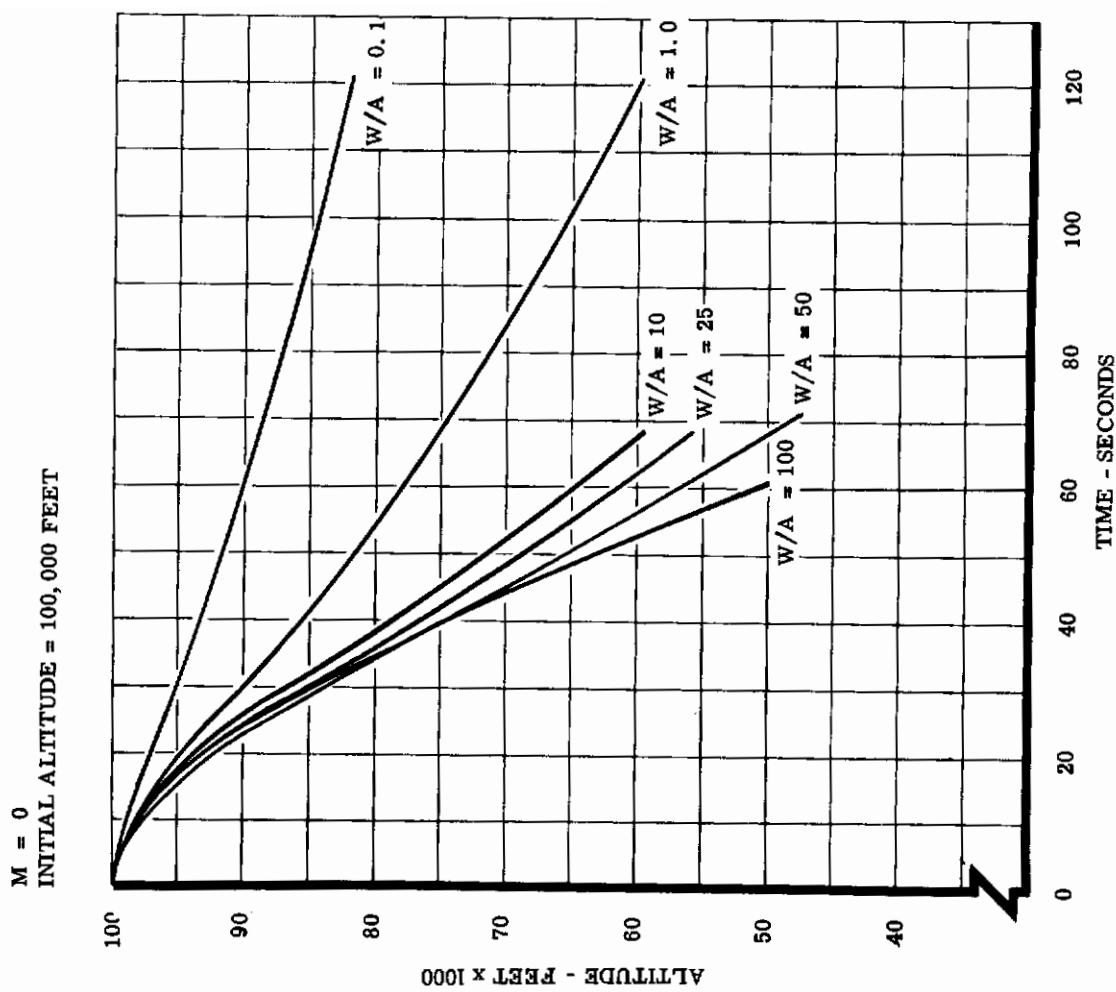
Figure 4. Altitude versus Time for a Vertical Drop Test of a Spherical
Drag Device at Supercritical Reynolds Numbers

M = 0
INITIAL ALTITUDE = 100,000 FEET
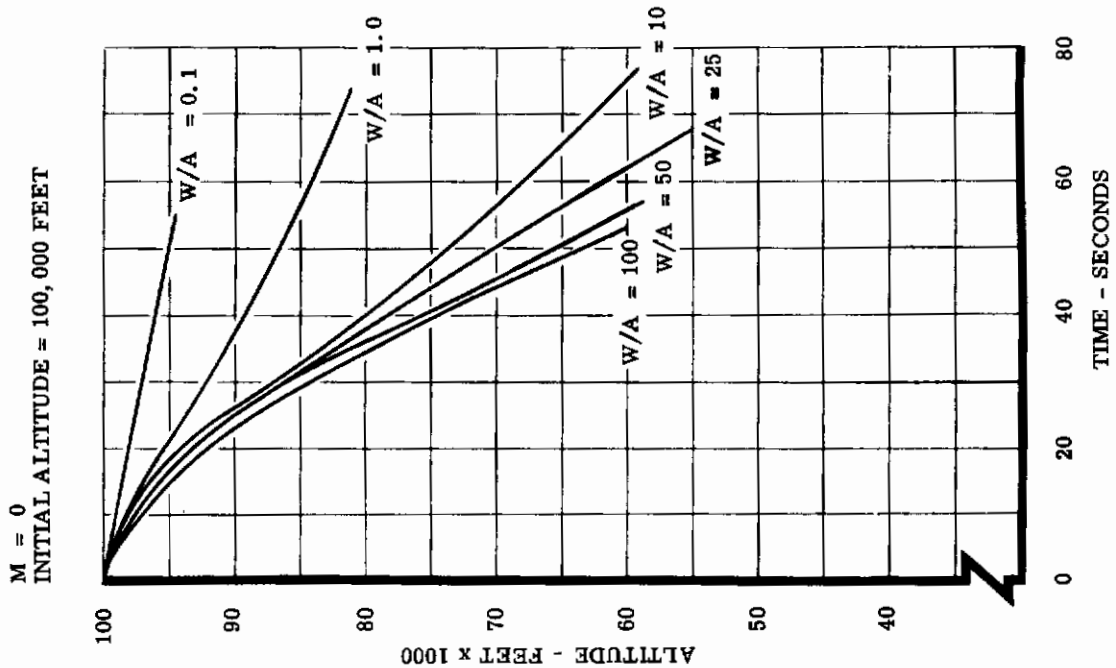
Figure 3. Altitude versus Time for a Vertical Drop
Test of a Spherical Drag Device at
Subcritical Reynolds Numbers
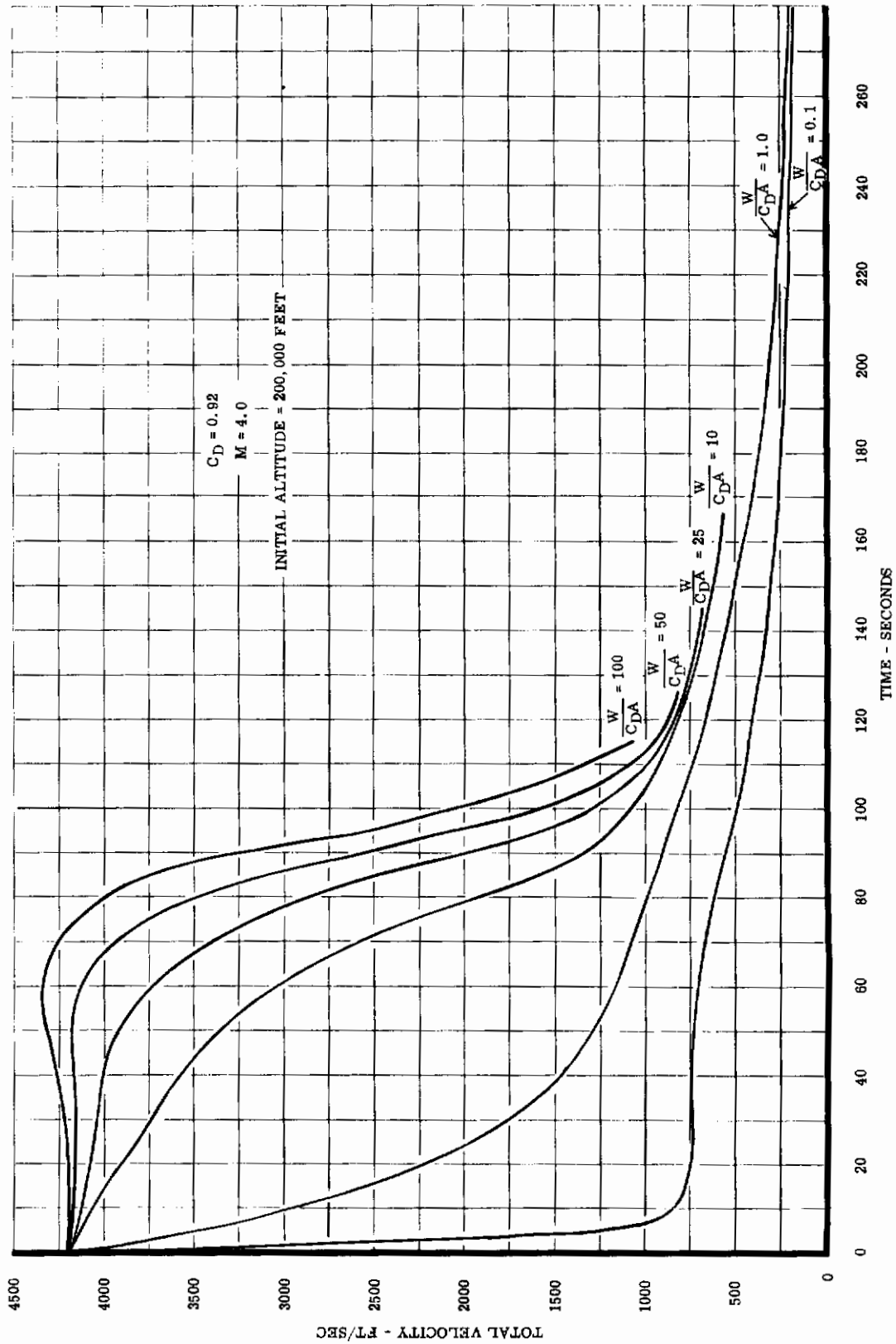
Figure 5. Velocity versus Time for a High-Speed Recovery of a Spherical Drag Device

$C_D = 0.92$

$M = 4.0$

INITIAL ALTITUDE = 200,000 FEET

TIME - SECONDS

TOTAL VELOCITY - FT/SEC

$\dfrac{W}{C_D A} = 100$

$\dfrac{W}{C_D A} = 50$

$\dfrac{W}{C_D A} = 25$

$\dfrac{W}{C_D A} = 10$

$\dfrac{W}{C_D A} = 1.0$

$\dfrac{W}{C_D A} = 0.1$

Figure 7. Velocity versus Time for a Vertical Drop Test of a Spherical Drag Device at Supercritical Reynolds Numbers
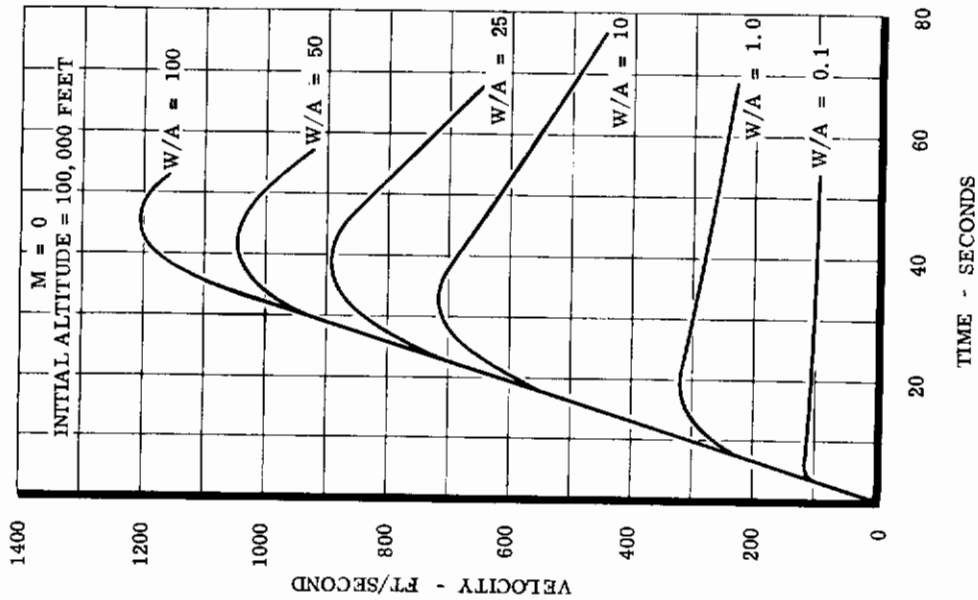
Figure 6. Velocity versus Time for a Vertical Drop Test of a Spherical Drag Device at Subcritical Reynolds Numbers
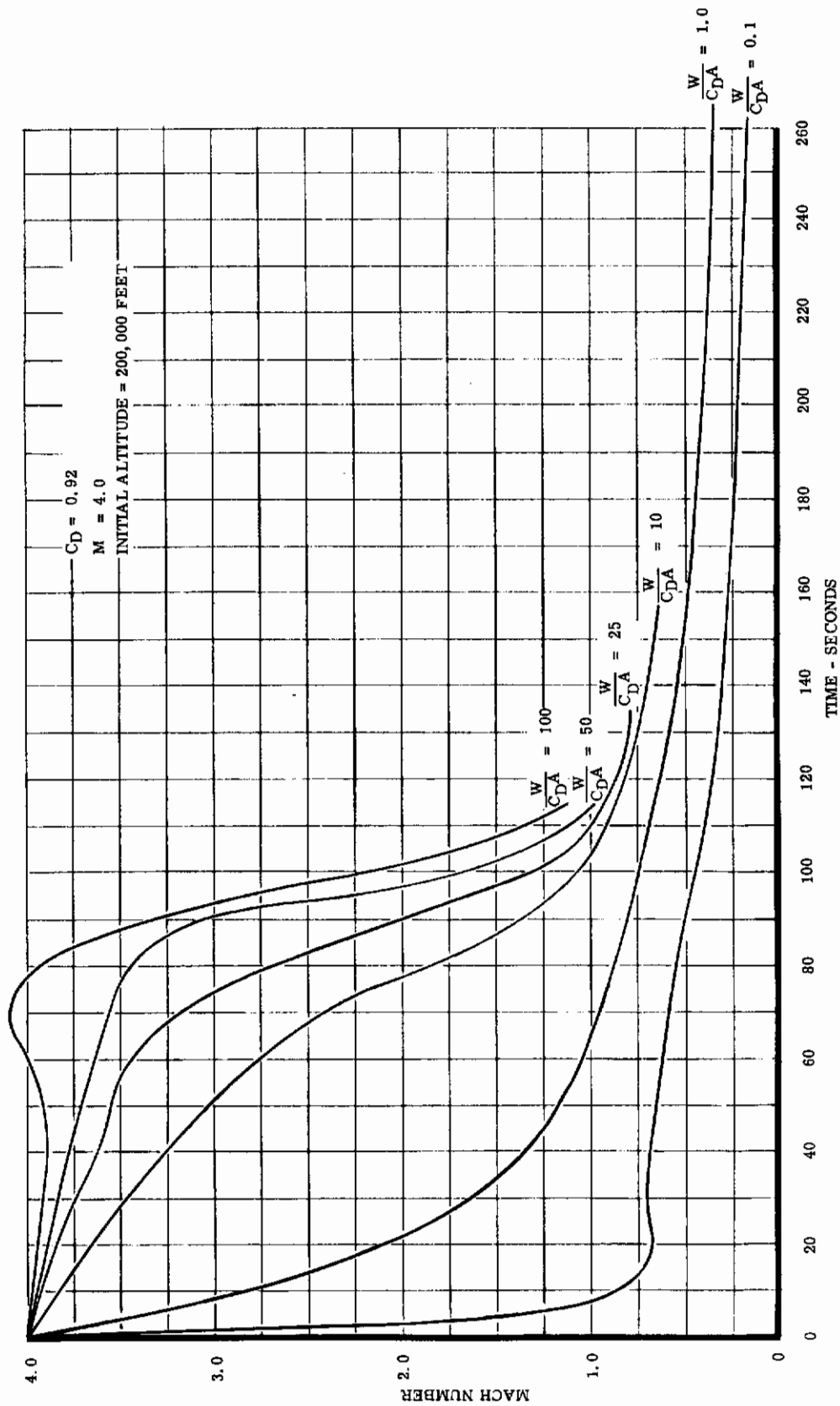
Figure 8. Mach Number versus Time for a High-Speed Recovery Using a Spherical Drag Device
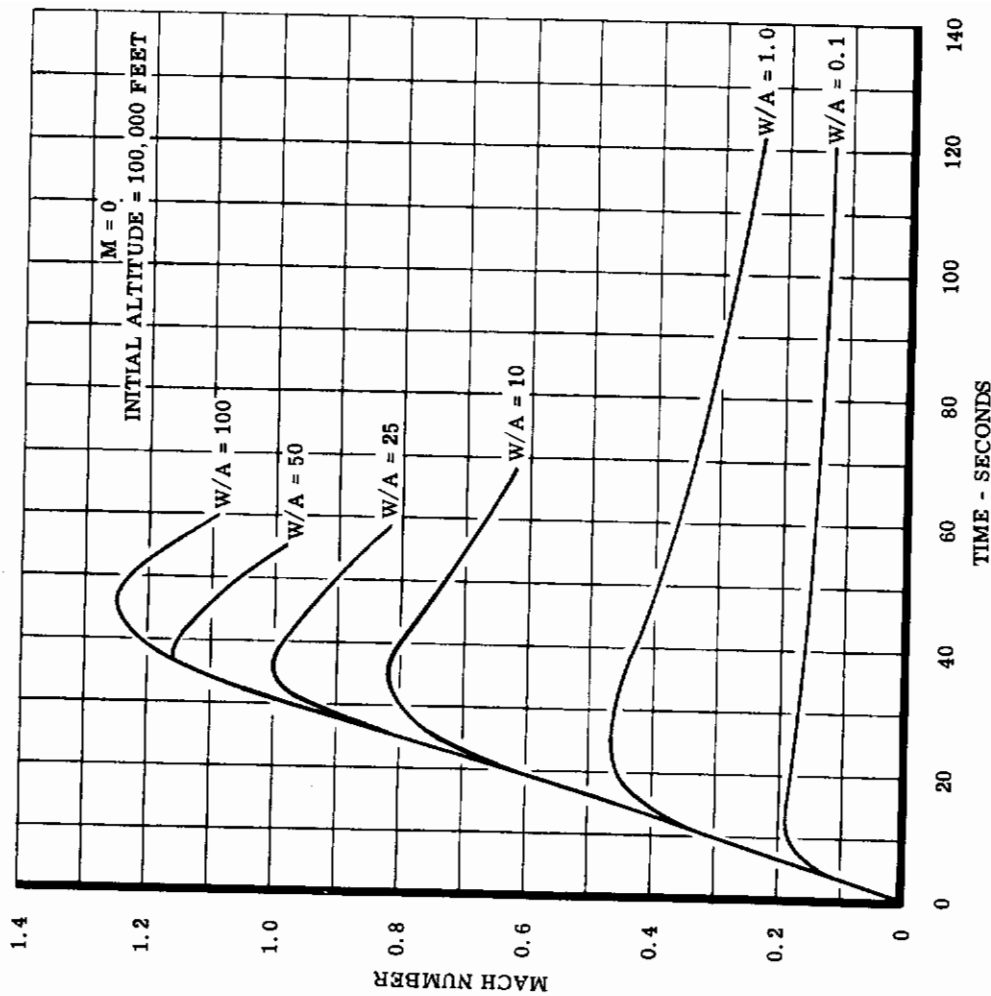
Figure 10. Mach Number versus Time for a Vertical Drop Test of a Spherical Drag Device at Supercritical Reynolds Numbers
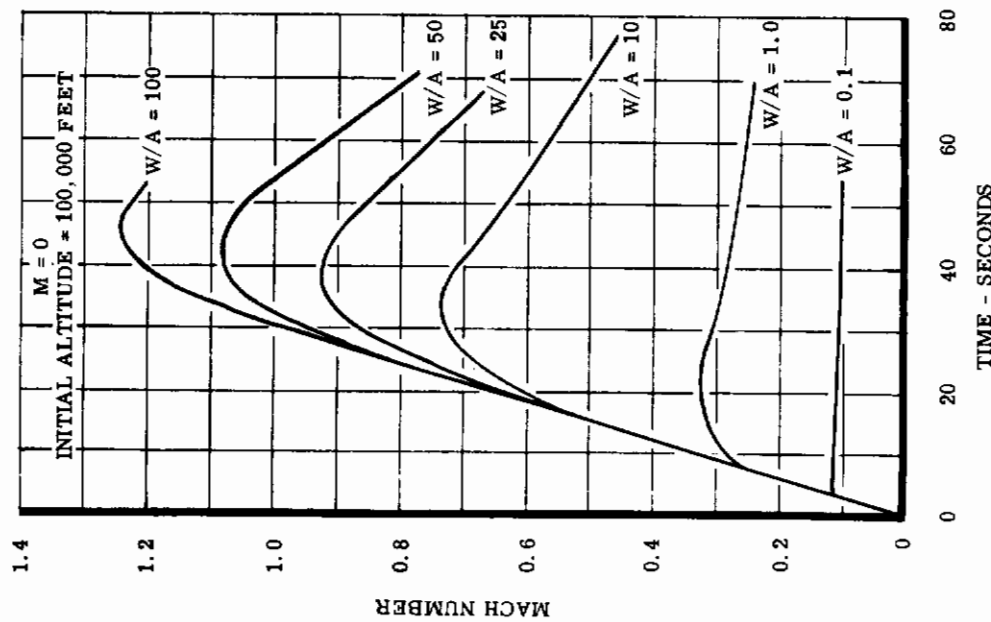
Figure 9. Mach Number versus Time for a Vertical Drop Test of a Spherical Drag Device at Subcritical Reynolds Numbers
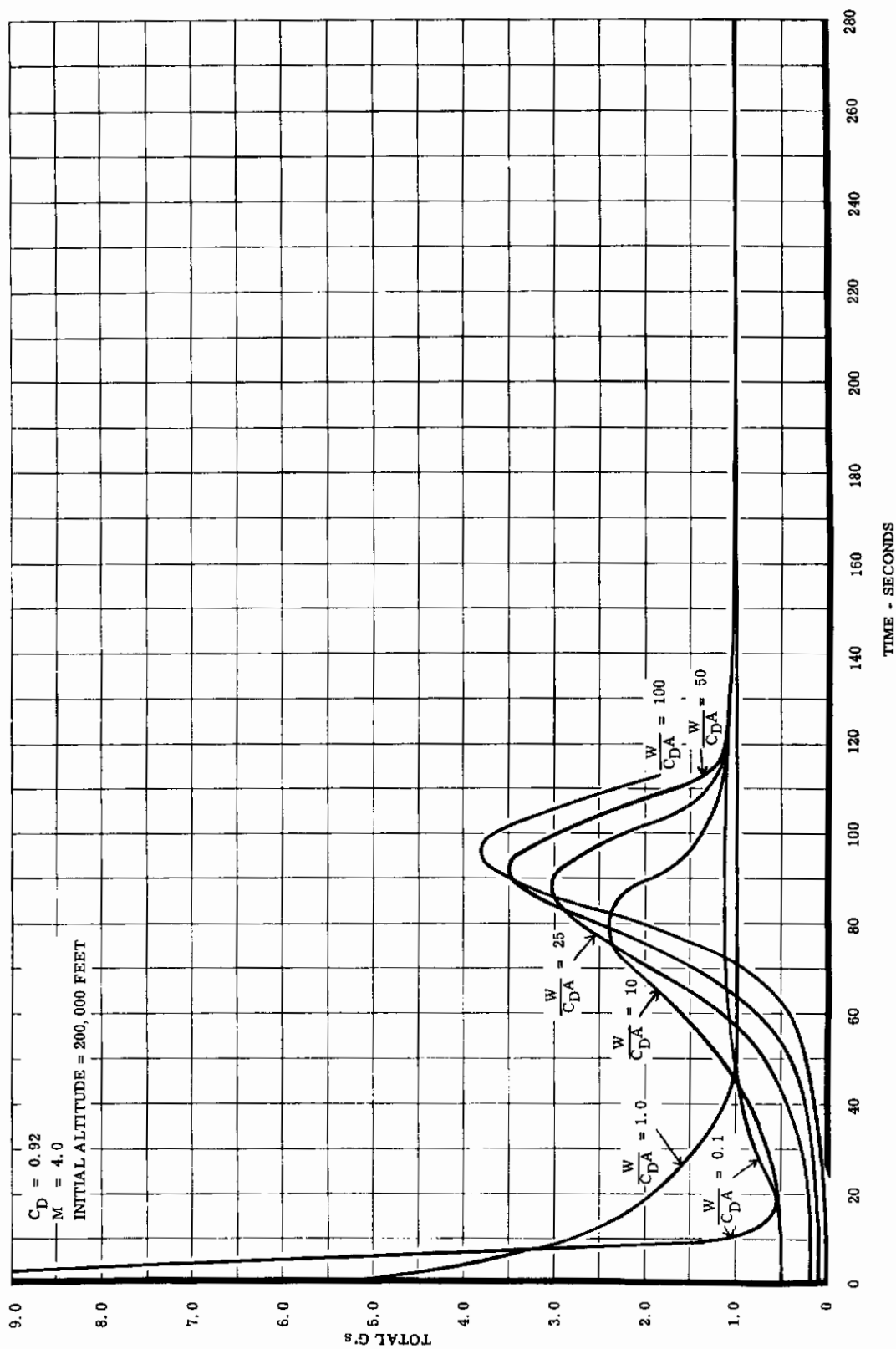
Figure 11. Acceleration versus Time for a High-Speed Recovery of a Spherical Drag Device

Figure 13. Acceleration versus Time for a Vertical Drop Test of a Spherical Drag Device at Supercritical Reynolds Numbers
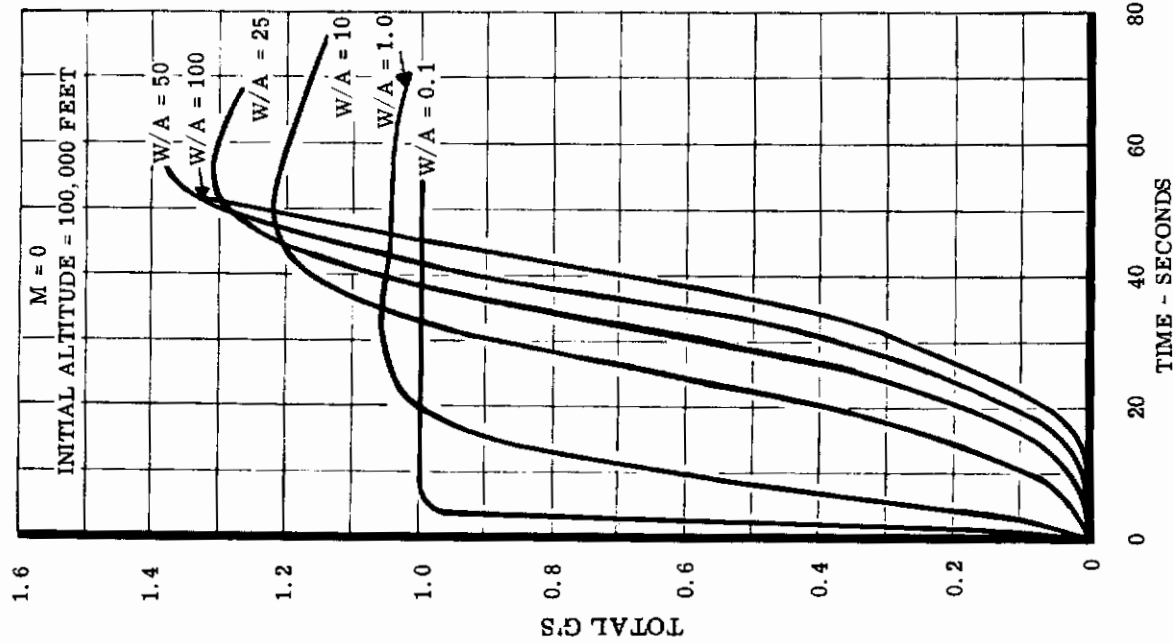
Figure 12. Acceleration versus Time for a Vertical Drop Test of a Spherical Drag Device at Subcritical Reynolds Numbers

$$C_D = \frac{DRAG}{q A}$$

A = FRONTAL AREA
OF SPHERE (πR^2)

AIR TURBULENCE $\cong$ 0
MACH NUMBER $\cong$ 0

AT $R_n \times 10^8 \sim C_D = 0.10$
(HOERNER)
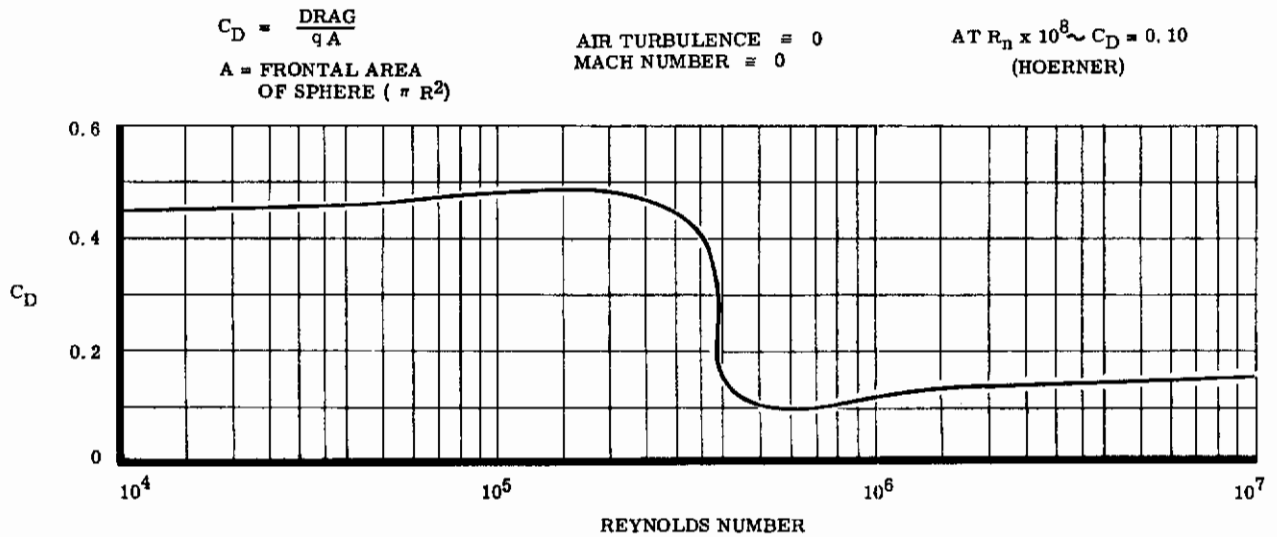
Figure 14. C_D versus Reynolds Number for a Sphere (Average Curve)

SUBCRITICAL $R_n < 3.85 \times 10^5$

SUPERCRITICAL $R_n > 3.85 \times 10^5$

$$C_D = \frac{DRAG}{q A}$$
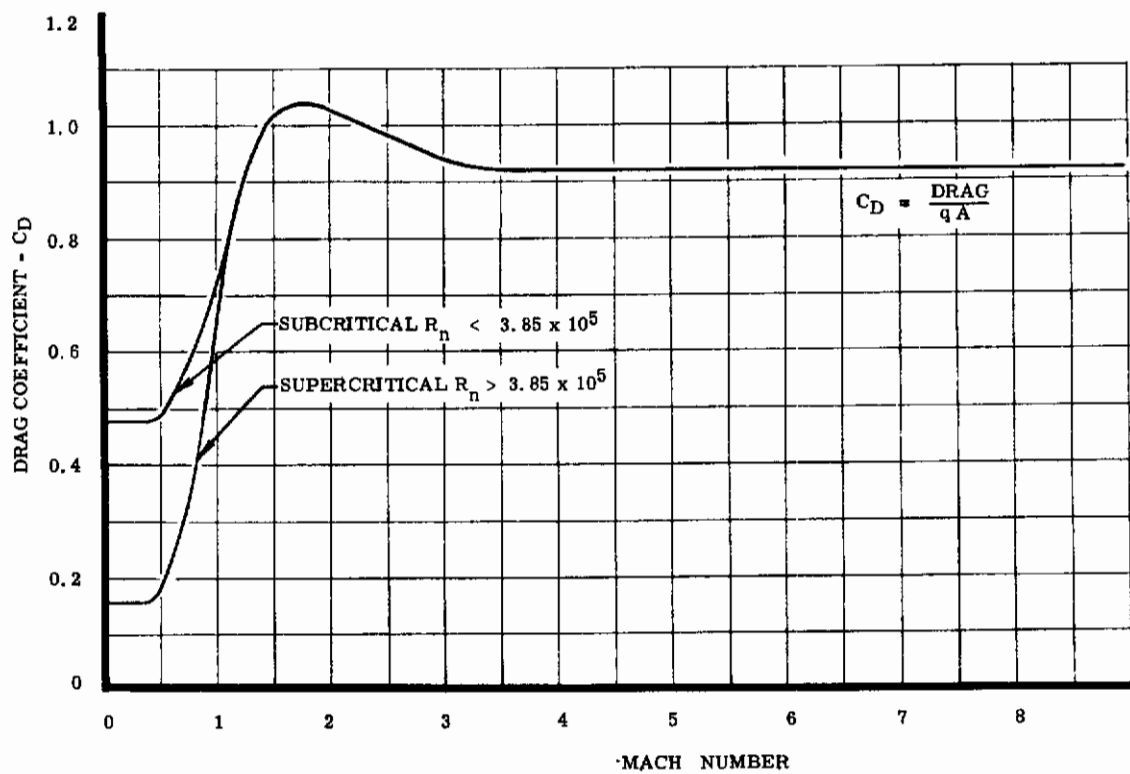
Figure 15. Drag Coefficient of a Sphere versus Mach Number

SEE REF 30, FIG-
URES 21 AND 22.

M_1

θ – DEGREES

$M_1 = 4.0$

$M_1 = 3.0$

$M_1 = 2.0$

$M_1 = 1.0$

$M_1 = 0.57$

$C_p = \dfrac{\Delta P}{q}$
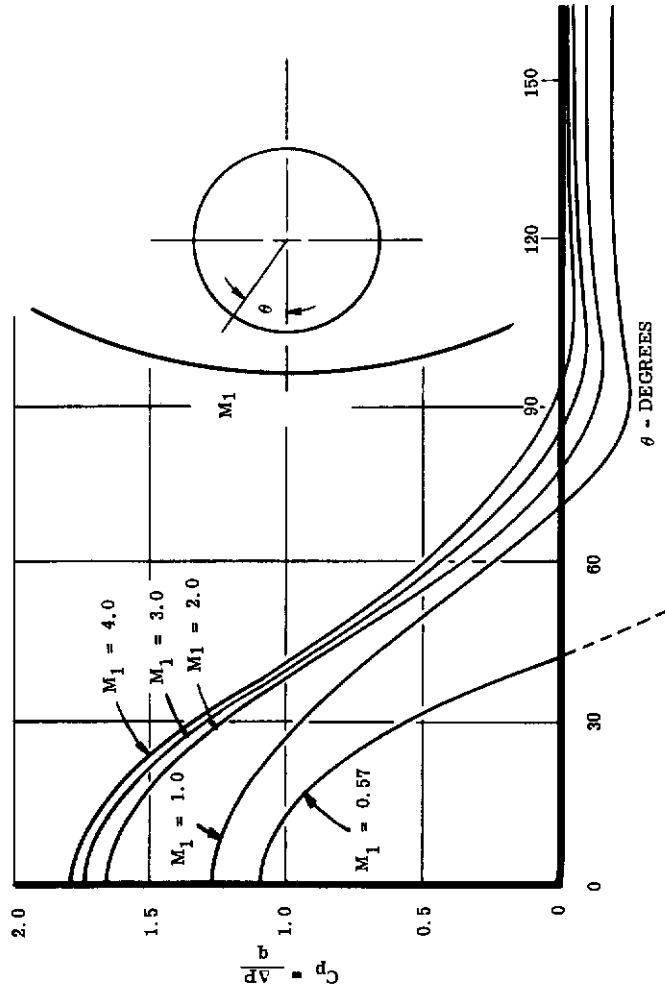
Figure 17. Pressure Coefficient Distribution on the Sphere

P_T = IMPACT PRESSURE ABSOLUTE

P_∞ = REMOTE PRESSURE

γ = 1.4

$\dfrac{P_T}{P_\infty} = \left[1 + \dfrac{\gamma-1}{2} M_1^2 \right]^{\frac{\gamma}{\gamma-1}}$ FOR $M < 1$

$*\dfrac{P_T}{P_\infty} = \dfrac{1}{2} \left[\dfrac{(\gamma+1)}{(4\gamma M_1^2 - 2\gamma + 2)} \dfrac{\gamma+1}{\gamma-1} \dfrac{2\gamma}{\gamma-1} -1 \right] \dfrac{1}{\gamma-1}$ FOR $M \geq 1$

M_1

P_∞

V_∞

P_T

$\dfrac{P_T}{P_\infty}$

MACH NUMBER

* REF RALEIGH PITOT EQUATION

Figure 16. Impact Pressure Ratio
versus Mach Number
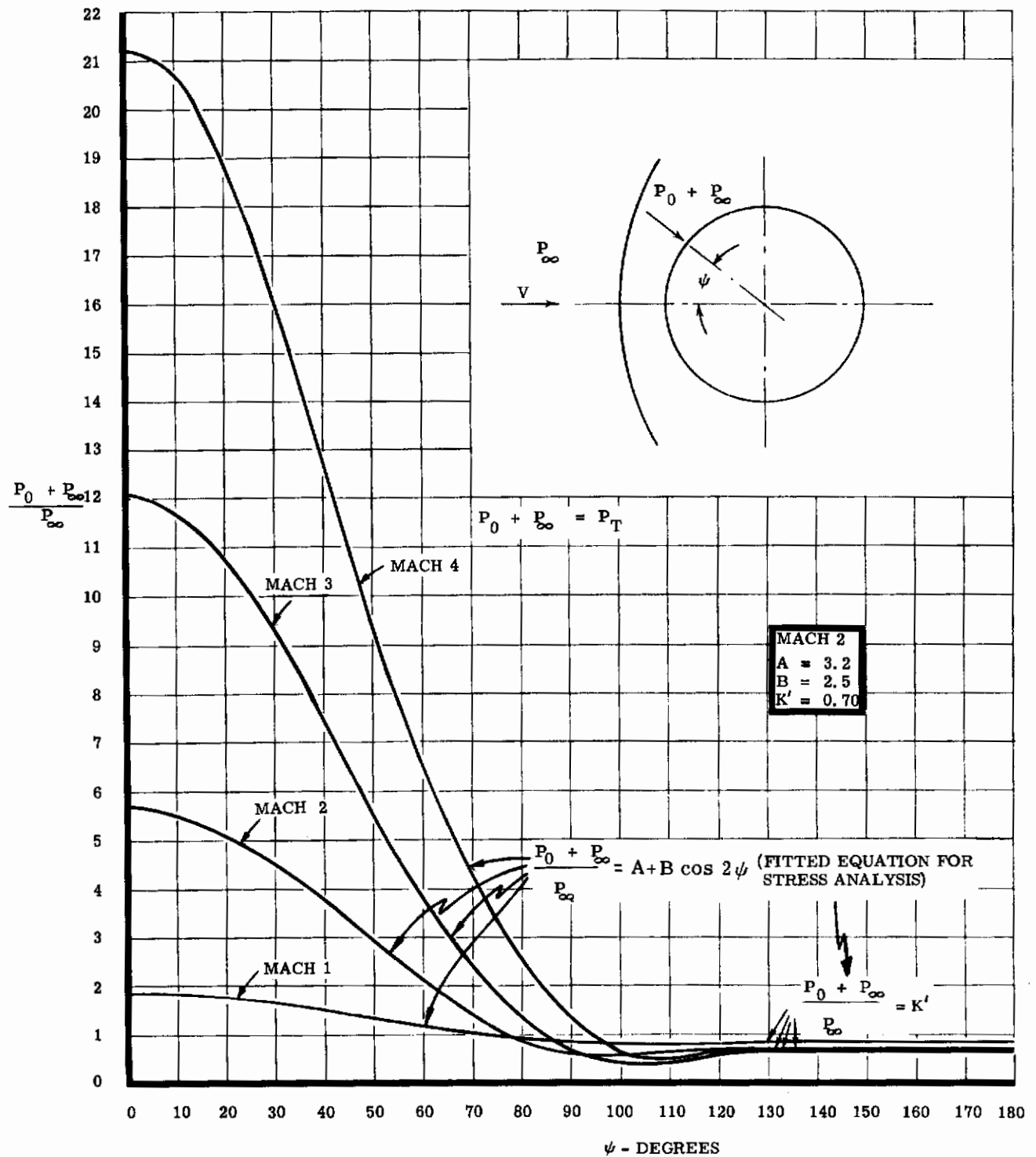
Figure 18. Pressure Distribution Over a Sphere

solid sphere is directly related to the flow field around the sphere. The evaluation of the flow field around a solid sphere is divided into subsonic, transonic, and supersonic flow.

1. Subsonic Flow

The only force acting on a solid sphere under constant velocity is drag, resulting from the pressure distribution on the body. A change in the pressure distribution will change the center of pressure, causing the body to oscillate because of unbalanced moments about the center of gravity.

An unstable pressure distribution moves the center of pressure, causing the sphere to rotate about the center of gravity until summation of moments about the center of gravity equals zero. (ΣM_{cg} = 0.) A changing flow field (i.e., a changing pressure distribution) causes the body to oscillate.

The flow around the upstream part of the sphere is stable. If the flow around the downstream part of the sphere is stable, the sphere may be assumed to be stable. Flow over a cylinder lends itself to theoretical treatment, but little is known of the three-dimensional flow in the wake of a sphere. However, a correlation of the following experimental data on two-dimensional flow about a cylinder seems logical to three-dimensional flow about a sphere:

(1) When the cylinder is in the Reynolds number range of 200 to 1×10^3, a regular succession of vortices, known as the Von Karman vortex sheet, are shed at regular intervals. By Helmoltz vortex laws, the cylinder oscillates with the same frequency as that at which the vortices are shed (see Reference 2, pp 292 and 293).

(2) The Reynolds number regime, 1×10^5 to 6×10^5, is a transition range. The flow field changes from vortex shedding to all turbulent flow. As higher speeds are reached, the wake flow is turbulent, effectively a steady state condition is reached, and the sphere is stable.

In three-dimensional flow for a sphere, there is evidence that a spiral vortex train develops in the Reynolds number range 200 to 1×10^5. No systematic investigation of the periodicity of the discharge under different conditions appears to have been made.

At higher Reynolds numbers, the vortex-shed and the vortex-loops diffuse very rapidly. At still greater Reynolds numbers, the flow becomes completely turbulent (see Reference 3, p 577).

The experimental results prove that in a certain Reynolds number range the flow field in the wake of a sphere is not stable. It is concluded that a solid sphere in a subsonic flow field is stable in the Reynolds number range of 0 to 200 and for a Reynolds number greater than 1×10^6.

2. Transonic and Supersonic Flow

In this flow range the drag coefficient (C_D) is a function of Mach (M) and Reynolds numbers (R_n) with M being the controlling independent variable. No evidence of unstable spheres in transonic or supersonic flow has been found. However, there is evidence of stable spheres in transonic and supersonic flow:

(1) Ballistic data shows that spheres fired from guns are stable.

(2) Schlieren system photographs have been taken of spheres at supersonic flight speeds which show definite turbulent wakes (see Reference 4, p 350). A turbulent wake, with no vortex shedding, results in a stable sphere.

(3) The trajectory of a sphere at supersonic and hypersonic speeds can be predicted. (Schlieren photographs can be made of free-flight spheres.)

As the results of the analysis indicate that the Reynolds number for most of the $W/C_D A$ conditions falls into the stable range for the high-speed recovery to 60,000 feet (see Figure 19), stability of an isolated spherical drag device may be assumed. For the free-fall flight conditions,
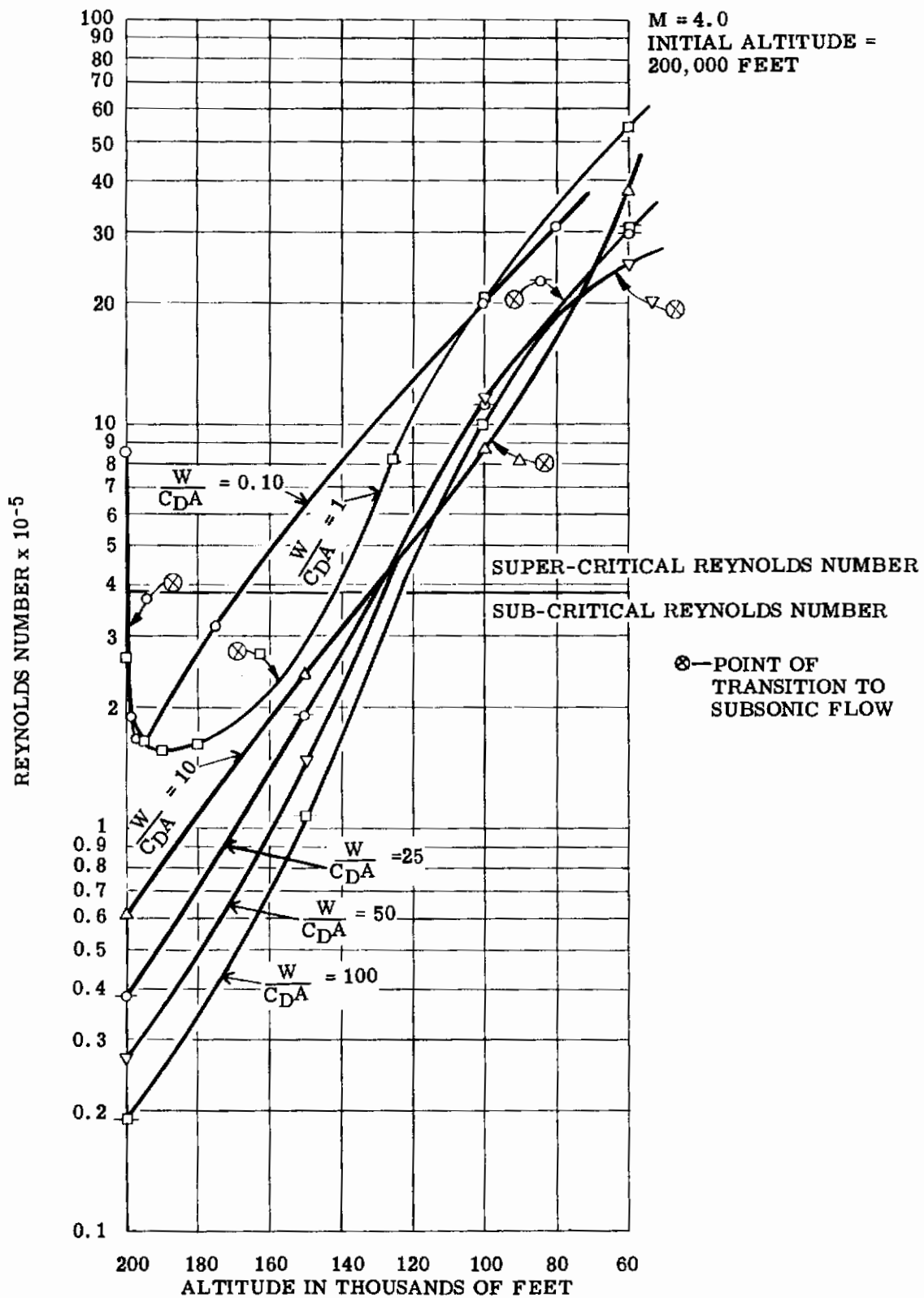
Figure 19. Reynolds Number versus Altitude for a High-Speed Recovery Using a
Spherical Drag Device

however, the spherical drag device will pass through the unstable range 200 R_n to 1×10^6. Although the free-flight conditions were not considered a critical design parameter, wind tunnel tests were made to indicate the effects of this increasing velocity on the stability of the spherical drag device during the drop (tests described in Section V).

Despite the fact that the sphere itself may be assumed stable during the high-speed recovery, very little information exists with regard to the stability of an inflatable sphere system. When the sphere is attached to a payload, it may no longer exhibit the properties of an isolated body. However, additional wind tunnel tests were made to indicate the characteristics of such a system and are described in Section V. Results of these tests indicated a relatively stable body when rigged with a nose cone and burble fence (see Figure 20).

C. THERMODYNAMIC ANALYSIS

A thermodynamic investigation was made based on the information obtained from the previous flight analysis to determine the heating effects encountered by inflatable spheres for the various W/C_DA's during the high-speed recovery and the vertical drop test.

The radiation equilibrium stagnation point temperatures shown in Figure 21, 22, and 23 were computed using the available trajectory information for the various W/C_DA ratios. Sphere radii for the given W/C_DA values were calculated using the total weight of the recovery system and a fabric weight of 0.056 lb/ft2.

Supersonic flow correlations from Van Driest were used in calculating the aerodynamic heating rates in the vicinity of the stagnation point. The heating rates were then equated to the radiation equilibrium correlation for obtaining the temperatures by steady state solutions. An emissivity of 0.8 was assumed in these calculations.

These temperatures are, in general, the maximum to be expected during the descent of inflatable spheres during high-speed recovery. An investigation of the Reynolds numbers shows that transition from laminar to turbulent flow may occur somewhere along the surface of the spheres with W/C_DA of 50 to 100. This transition may result in an increase in the heat transfer rate and somewhat higher temperature (approximately 20%) than these indicated at the stagnation points. However for W/C_DA, of less than 50, where the flow is laminar, this temperature rise will not occur.

The basic equation used in calculation, the heat transfer rate/steady state conditions for the high-speed recovery systems, is as follows:

$$q_{stag} = C_H \rho_\infty V_\infty \, C_{p_a} \, (T_r - T_s) \quad \text{(see Reference 5)}. \tag{25}$$

Since the time of deceleration for an inflated drag device is on the order of several minutes, it was decided that a transient solution for a closer approximation of the actual temperatures to be experienced could be obtained using IBM 650 computation of Eq (26), (27), and (28) rather than the steady state condition under which the temperatures in Figures 21 and 22 were calculated.

$$\left[\rho_m C_{p_m} \frac{\Delta X}{Z} \right] \frac{dT_s}{d\theta} = h \, (\theta) \left[T_{aw} \, (\theta) - T_s \right] - \epsilon \sigma T_s^4 - \left(\frac{K}{\Delta X} \right) (T_s - T_1). \tag{26}$$

$$\left[\rho_m C_{p_m} \Delta X \right] \frac{dT_n}{d\theta} = \left(\frac{K}{\Delta X} \right) \, (T_{n-1} - 2T_n + T_{n+1})^*. \tag{27}$$

*The convective heat transfer term in Eq (27) was calculated using the Van Driest correlation and the trajectory data.

M = 4.0
INITIAL ALTITUDE = 200,000 FEET
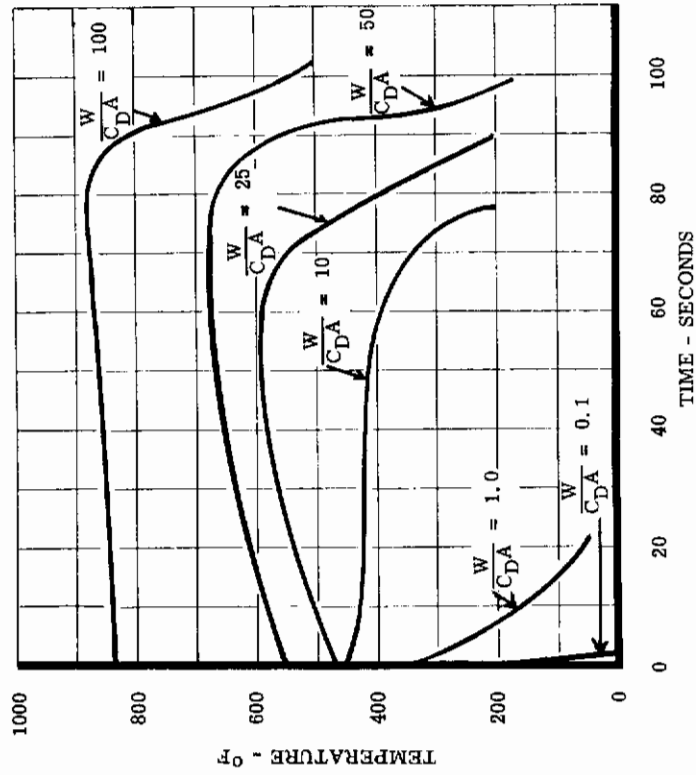
Figure 21. Equilibrium Stagnation Point Temperatures versus Time for High-Speed Recovery

$\frac{W}{C_D A} = 100$

$\frac{W}{C_D A} = 50$

$\frac{W}{C_D A} = 25$

$\frac{W}{C_D A} = 10$

$\frac{W}{C_D A} = 1.0$

$\frac{W}{C_D A} = 0.1$

TIME - SECONDS

TEMPERATURE - °F

LARGE NOSE CONE (CONE TANGENT TO SPHERE SIDES)

2.2' DIA 16 GORE SPHERE

FABRIC CONE SUSPENDED ON RISER LINES

SMALL NOSE CONE (CONE SIZE APPROXIMATELY THAT OF PROPOSED INFLATION SYSTEM)

2.2' DIA 16 GORE SPHERE

FABRIC CONE SUSPENDED ON RISER LINES

TUBING ATTACHED AROUND MODEL AT APPROXIMATELY 75°

ATTACHMENT LINE

Figure 20. Various Sphere Configurations
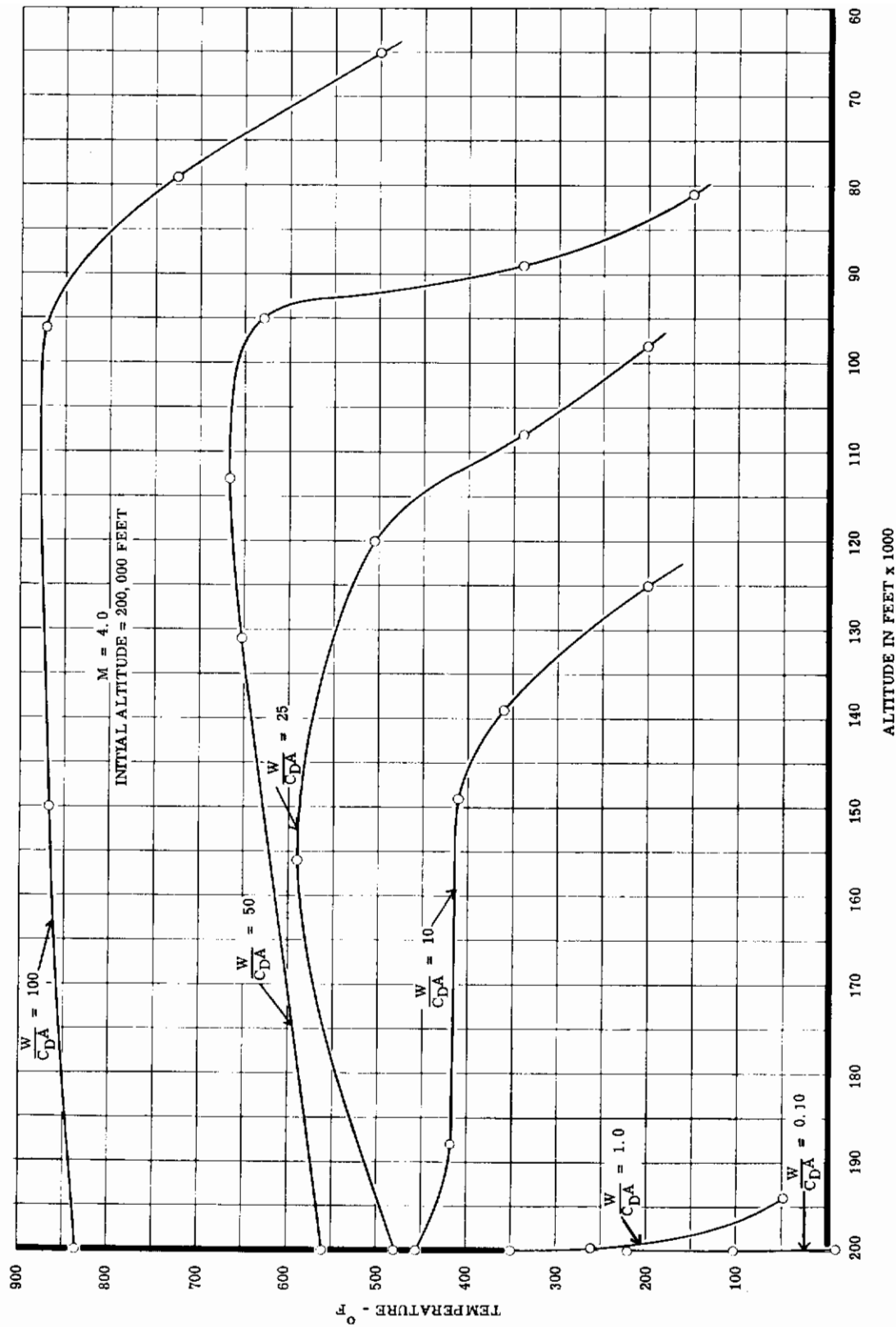
Figure 22. Equilibrium Stagnation Point Temperatures versus Altitude for High-Speed Recovery

M = 4
INITIAL ALTITUDE = 200,000 FEET
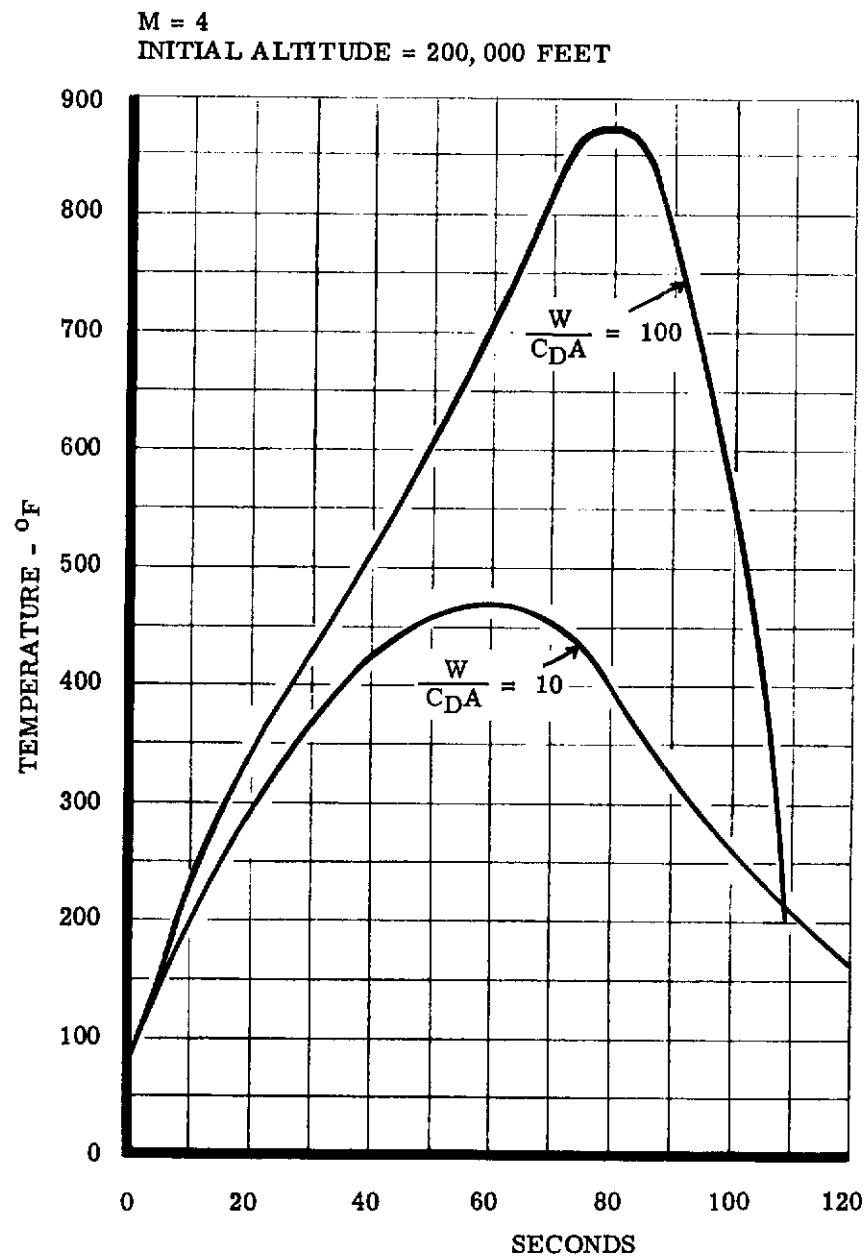
Figure 23. Equilibrium Stagnation Point Temperatures-Transient Solution

$$\left[\rho_m \ C_{p_m} \ \frac{\Delta X}{2} \right] \quad \frac{dT_8}{d\theta} \quad = \quad \frac{K}{\Delta X} \quad (T_7 - T_8) \tag{28}$$

A comparison of these transient solutions with curves based on the radiation equilibrium information obtained previously indicates that the heating effects are less severe than anticipated.

An investigation was made to determine what temperatures could be encountered during the free-fall flight conditions. The heating effects, however, were found to be so slight that no critical conditions were encountered.

The total temperatures for this free-fall condition were calculated from

$$T_s = T_\infty \left[1 + 0.2 \ (M_\infty^{\ 2}) \right]^* \tag{29}$$

*using a recovery factor of 1.

The maximum temperature encountered by any of the inflatable sphere systems was found to be less than 100°F for the free-fall condition.

D. STRESS ANALYSIS

An investigation was conducted of spherical drag body stresses and deformations under various conditions of loading. Several systems of suspension were considered along with early design concepts of the balloon.

The single-line suspension system, using one cable attached directly to the apex of the spherical drag body gores, would produce very high stresses around the attachment point and would require the spherical drag body to deform considerably from its spherical shape under load. The single-line system could be combined with some sort of internal suspension as an aid in supporting the load; however, such internal structure is undesirable from the standpoint of construction, and it was not chosen for consideration in the early stages.

A modification of the multiline system, which is treated in this analysis, was used in an attempt to distribute the applied load over a large area and thereby reduce fabric stresses. The preliminary design concept considered for development of the deformation theory was a spherical drag device with a suspension system as shown in Figure 24. In this design the suspension cables are attached to a cable hoop bearing against the fabric in the forward section of the sphere.

The evaluation of the drag load was made using the pressure distributions over a sphere as shown in Figures 18 and 25.

The stress analysis of the spherical drag device is shown schematically in Figures 25 and 26.

It was found that the pressure distribution over the front half of the sphere can be closely approximated by the function $(P_0 + P_\infty)/P_\infty = A + B \cos 2\psi$ for any given Mach number (see Figure 18). The pressure over the back half is assumed to be a constant for each Mach number $(P_0 + P_\infty)/P_\infty = K'$.

If a differential strip enclosed by angle $d\psi$ is considered, as in Figure 26, taking the component of P_0 in the vertical direction:

$$dD = 2\pi a^2 \ \sin\psi \ \cos\psi \ P_0 d\psi \ .$$

4. 30'R

HOOP - FLEXIBLE CABLE 36" DIA

BRIDLE LINES (12)

NOSE CONE AND
SUPPORT FLANGE

EXTERNAL HOOP
SUSPENSION
SYSTEM
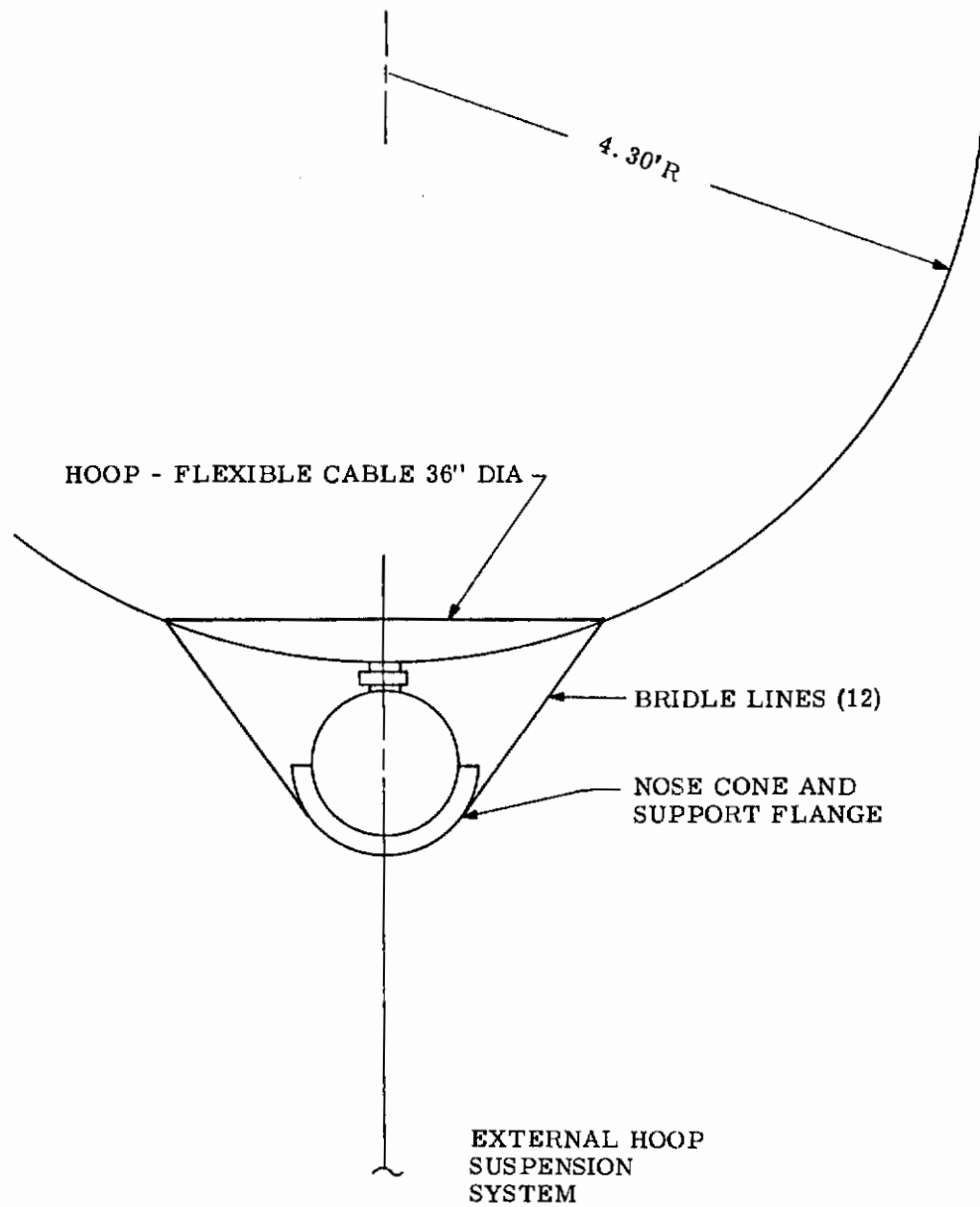
Figure 24. External Hoop Suspension System

PARALLEL CIRCLES

$$\frac{P_0 + P_\infty}{P_\infty} = K'$$

MERIDIAN CIRCLES

N_ψ N_θ

N_θ

N_ψ a

$d\psi$

ψ_0 ψ $ad\psi$

r_0

VIEW A-A

β WIRE HOOP

n ATTACHING CABLES

$$\frac{P_0 + P_\infty}{P_\infty} = A + B\ \cos 2\psi$$

WIND VELOCITY

MAIN CABLE

R

PATCH BONDED
TO FABRIC

HOOP CABLE

VIEW A-A
ATTACHMENT
DETAIL
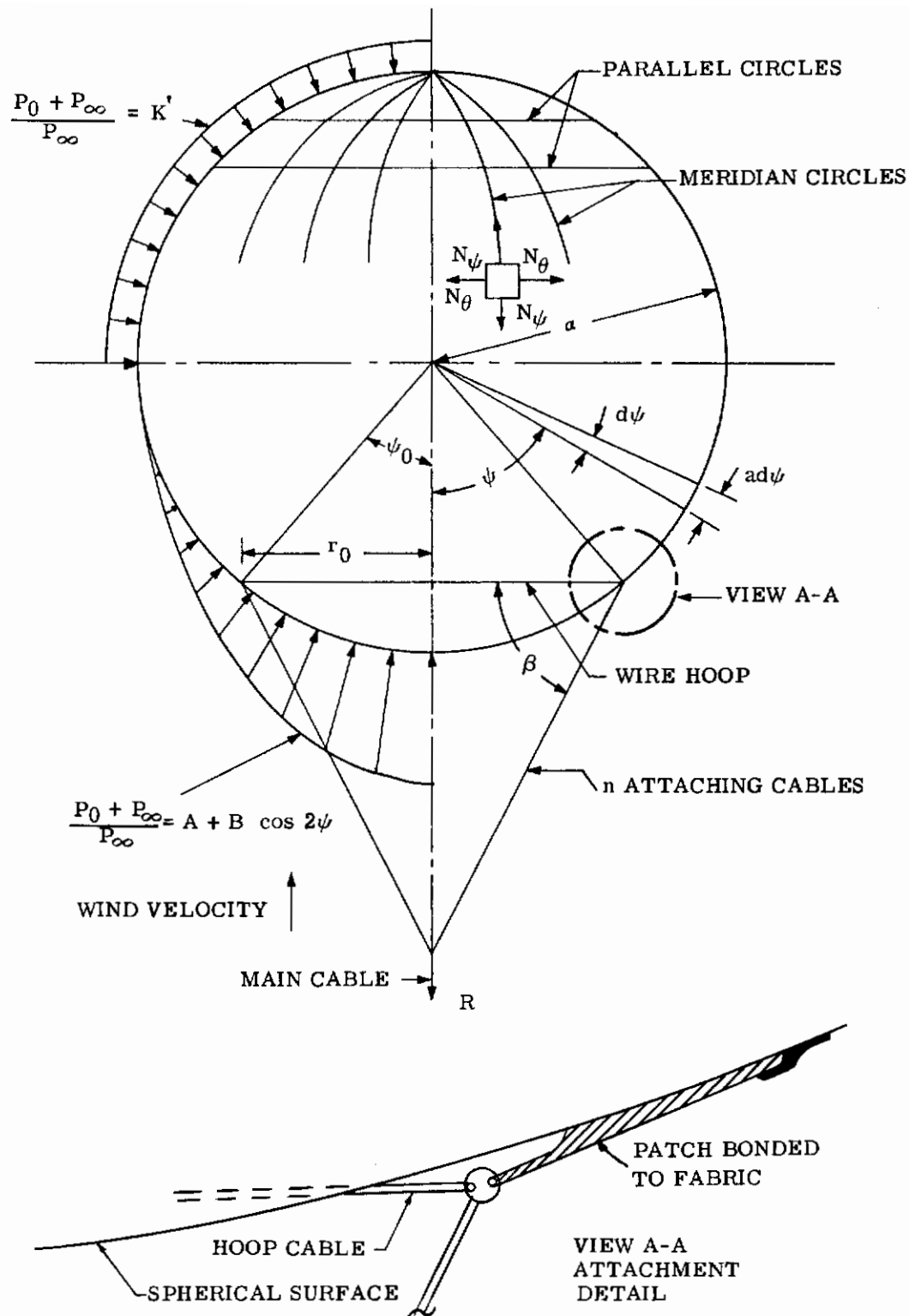
SPHERICAL SURFACE

Figure 25. Stress Schematic of Spherical Drag Body
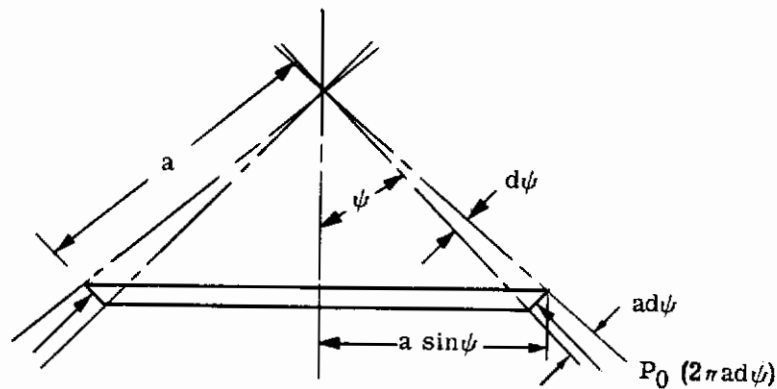
Figure 26. Differential Increment of Spherical Surface Formed by Adjacent Parallel Circles

Substituting for P_0,

$$dD = 2\pi a^2 P_\infty \left[(A-1) \sin\psi \cos\psi + B \cos 2\psi \cos\psi \sin\psi\right] d\psi$$

or, for the front half of the sphere,

$$D_\psi = 2\pi a^2 P_\infty \int_0^\psi \left[(A-1) \sin\psi \cos\psi + B \cos 2\psi \cos\psi \sin\psi\right] d\psi$$

Integrating:

$$D\psi = \pi a^2 P_\infty \sin^2\psi \left[(A-1) + B \cos^2\psi\right]. \tag{30}$$

For the front half:

$$D_F = \pi a^2 P_\infty (A-1). \tag{31}$$

For the leeward half:

$$D_B = -\pi a^2 P_\infty (K' - 1). \tag{32}$$

The total drag

$$D = D_F + D_B = \pi a^2 P_\infty (A - K'). \tag{33}$$

The vertical load factor for the system is equal to D/W,

which gives

$$R = \frac{DW_p}{W} \ .$$ (34)

The suspension system consists of a main cable, which carries load R, and n attaching cables, which are attached to the sphere at equally spaced intervals around circle r_0, describing a conical surface (see Figure 25). As the attachment to the sphere is not necessarily tangent to the surface, a hoop cable in the plane of the parallel circle at ψ_0 will be used to minimize distortion of the inflated drag device from its spherical shape. A possible means of attaching the cables to the sphere is shown in Figure 25.

In order to balance the load R,

$$T = \frac{R}{n \sin\beta} \ .$$ (35)

The free body force diagram of attaching cable is shown in Figure 27.
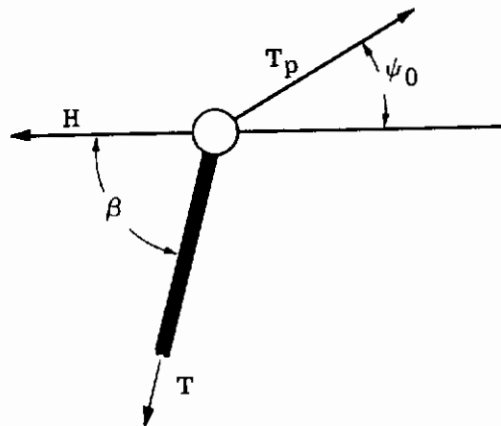
Figure 27. Free Body Force Diagram of Attaching Cables

Summing forces

$$T_p = \frac{T \sin\beta}{\sin\psi_0} = \frac{R}{n \sin\psi_0}$$ (36)

$$H = T_p \cos\psi_0 - T \cos\beta = \frac{R}{n} (\cot\psi_0 - \cot\beta)$$ (37)

Forces H cause the hoop cable to take the shape of a regular polygon of n sides, as shown in Figure 28.
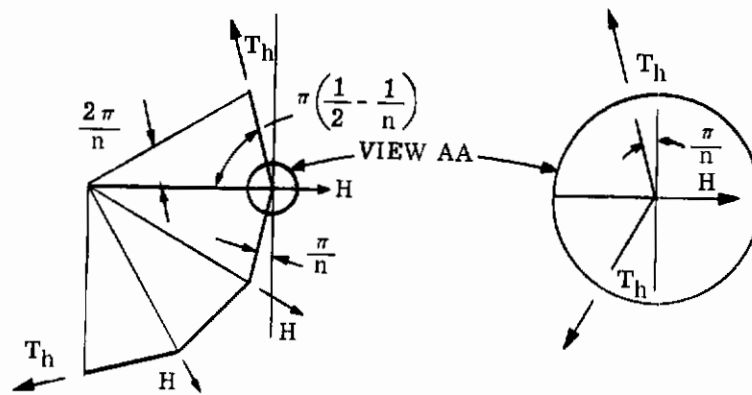
Figure 28. Force Diagram of Hoop Cable

Summing forces in horizontal direction and solving for T_h,

$$T_h = \frac{R(\cot\psi_0 - \cot\beta)}{2n \sin\frac{\pi}{n}} \tag{38}$$

Stresses in the fabric will be analyzed using the membrane theory given in Reference 6, p 358. The coordinates on the surface of the sphere are formed by the intersection of meridian circles and parallel circles, with the meridians and parallels being defined in the same manner as those on the surface of the earth (see Figure 25). A differential element is formed by two adjacent meridians and two adjacent parallels, with the stresses N_ψ and N_θ acting perpendicular to the sides of the element, as shown in Figure 25.

Because of the symmetrical loading of the sphere, there will be no shear stresses (see Reference 6, p 357). Equations of equilibrium of the element are developed in Reference 6, p 358, and will not be repeated here. Integration of these equations allows the determination of N_ψ and N_θ.

The stress N_ψ can also be found by taking a section through a parallel circle and summing forces in the vertical direction (see Reference 6, p 358, Eq 209). Stresses caused by acceleration of the fabric weight will be neglected, as the weight is small compared to that of the payload.
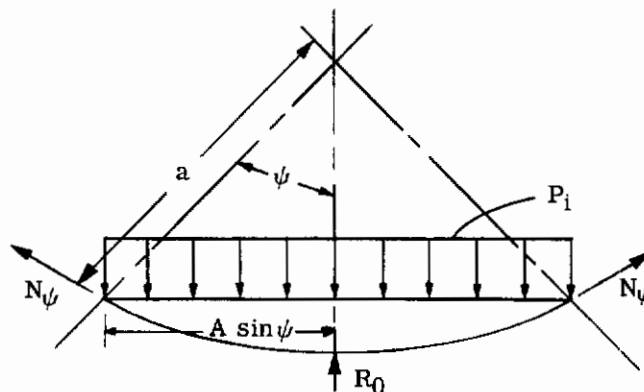
Figure 29. Segment of Sphere Cut by Plane through Parallel Circle

$$N_\psi \ (2\pi \ a \sin\psi) \sin\psi \ = \ P_i \pi \ a^2 \sin^2\psi - R_0 \quad \text{(Figure 29)}.$$

Solving for N_ψ,

$$N_\psi \ = \ \frac{P_i a}{2} \ - \ \frac{R_0}{2\pi a \sin^2\psi}$$

Inside hoop cable $R_0 = D_\psi$, which gives, using Eq (30)

$$N_{\psi_1} \ = \ \frac{P_i a}{2} \ - \ \frac{P_\infty \ a \ (A - 1 + B \cos^2\psi)}{2} \tag{39}$$

Outside hoop cable $R_0 = D_\psi - R$, which gives, using Eq (30) and (34)

$$N_{\psi_2} \ = \ \frac{P_i a}{2} \ - \ \frac{P_\infty \ a \ (A - 1 + B \cos^2\psi)}{2} \ + \ \frac{P_\infty \ a \ (A - K')}{2 \sin^2\psi} \ \frac{W_p}{W} \tag{40}$$

From Eq (210), p 359, Reference 6,

$$\frac{N_{\psi 1}}{a} \ + \ \frac{N_{\theta 1}}{a} \ = \ P_i - P_0 \ = \ P_i - P_\infty \ (A - 1 + B \cos 2\psi)$$

or, substituting for $N_{\psi 1}$,

$$N_{\theta 1} \ = \ \frac{P_i a}{2} \ - \ \frac{P_\infty \ a \ (A - 1 + 3B \cos^2\psi - 2B)}{2} \ . \tag{41}$$

Similarly,

$$N_{\theta 2} \ = \ \frac{P_i a}{2} \ - \ \frac{P_\infty \ a \ (A - 1 + 3B \cos^2\psi - 2B)}{2} \ - \ \frac{P_\infty \ a \ (A - K')}{2 \sin^2\psi} \ \frac{W_p}{W} \ . \tag{42}$$

Over the leeward half of the balloon,

$$N_\psi \ = \ N_\theta \ = \ \frac{\left[P_i - (K' - 1) \ P_\infty \right] a}{2} \ . \tag{43}$$

The deflection of any point under load will be defined by a component v tangent to the meridian circle and a component w in the radial direction at the point. The positive values are taken in the directions of increasing ψ and decreasing radius, respectively. From Eq (b), p 371, Reference 6,

$$v = \sin\psi \left[\int \frac{a(1+\mu)(N_\psi - N_\theta)\, d\psi}{E \sin\psi} + C_1 \right]$$

(44)

Inside hoop cable, from Eq (39) and (41),

$$N_{\psi_1} - N_{\theta_1} = -P_\infty\, a\, B \sin^2\psi .$$

Substituting in Eq (44),

$$v_1 = \frac{P_\infty\, a^2 B\, (1+\mu)\, \sin\psi \cos\psi}{E} + C_1 \sin\psi .$$

If the hoop cable is taken as a reference plane, $v = 0$ when $\psi = \psi_0$, which gives:

$$C_1 = -K(1+\mu)\cos\psi_0$$

where

$$K = \frac{P_\infty\, a^2 B}{E} .$$

The expression for v_1 then becomes

$$v_1 = K(1+\mu)\sin\psi\,(\cos\psi - \cos\psi_0).$$

(45)

$$w = v \cot\psi - \epsilon_\theta\, a \qquad \text{(see Eq (b), p 371, Reference 6)}$$

(46)

where

$$\epsilon_\theta = \frac{N_\theta - \mu N_\psi}{E} .$$

Substituting for v_1, N_{θ_1}, and $N_{\psi 1}$ from Eq (45), (41), and (39) and simplifying,

$$w_1 = K \left[\cos^2 \psi \left(\frac{5}{2} + \frac{\mu}{2} \right) - \cos \psi \cos \psi_0 (1 + \mu) - 1 \right] + \frac{a^2 (1 - \mu)}{2E} \left[P_\infty (A - 1) - P_i \right] \quad (47)$$

Outside hoop cable, substituting for $N_{\psi 2}$ and $N_{\theta 2}$ in Eq (44),

$$v_2 = \sin \psi \left(\frac{P_\infty a^2 (A - K')(1 + \mu) W_p}{2EW} \left[\ln \tan \frac{\psi}{2} - \frac{\cos \psi}{\sin^2 \psi} \right] + K (1 + \mu) \cos \psi + C_2 \right) \quad (48)$$

When $\psi = \psi_0$, $v = 0$, which gives:

$$C_2 = \frac{-(1 - \mu) P_\infty a^2 (A - K')}{2E} \left[\ln \tan \frac{\psi_0}{2} - \frac{\cos \psi_0}{\sin^2 \psi_0} \right] \frac{W_p}{W} - K (1 + \mu) \cos \psi_0. \quad (49)$$

Substituting for v_2, $N_{\theta 2}$, and $N_{\psi 2}$ from (48), (47), and (40), Eq (46) becomes

$$w_2 = \cos \psi \left(\frac{P_\infty a^2 (A - K')(1 + \mu) W_p}{2EW} \left[\ln \tan \frac{\psi}{2} - \frac{\cos \psi}{\sin^2 \psi} \right] + K (1 + \mu) \cos \psi + C2 \right)$$

$$+ \frac{a}{E} \left[\frac{P_\infty a B}{2} \left(3 \cos^2 \psi - \mu \cos^2 \psi - 2 \right) + \frac{P_\infty a (A - K')(1 + \mu) W_p}{2 \sin^2 \psi} \frac{W_p}{W} \right. \quad (50)$$

$$\left. + \frac{\left[P_\infty (A - 1) - P_i \right] a (1 - \mu)}{2} \right]$$

Based on Eq (45), (47), (48), and (50), the deflection of the inflated sphere for the W/CDA = 10 condition was calculated for the various Mach numbers and altitudes experienced during its trajectory. The absolute stagnation pressure on the inflated sphere during its flight varies as shown in Figure 30. The pressures are quite small and reach a maximum at 60,000 feet, which is the final condition for the analysis. A constant inflation pressure of 1.5 psia was assumed for the initiation of flight, equal to the absolute stagnation pressure at a 60,000-foot altitude.

Figure 31 shows an example of the deformation of the spherical drag body under the Mach 1.8 condition, occurring at an altitude of 123,000 feet. The drag loads reach a maximum around Mach 2 (see Figures 11 and 18), and the stresses are rather high. However, the deformations are quite small because the inflation pressure is large enough to withstand the pressures on the surfaces of the sphere.

The preceding analysis was developed with the assumption that the principal radii of curvature for every point on the sphere remain equal. The plot of the deflected shape shows that this is not true in the area where the cables are attached. The theoretical curve gives a large discontinuity at the attaching circle, which of course is not possible with the actual inflated sphere. By inspecting the equations for N_ψ and N_θ, the true shape was estimated and drawn in as a dashed line. The assumption of a constant radius appears to be fairly good over the remainder of the sphere.
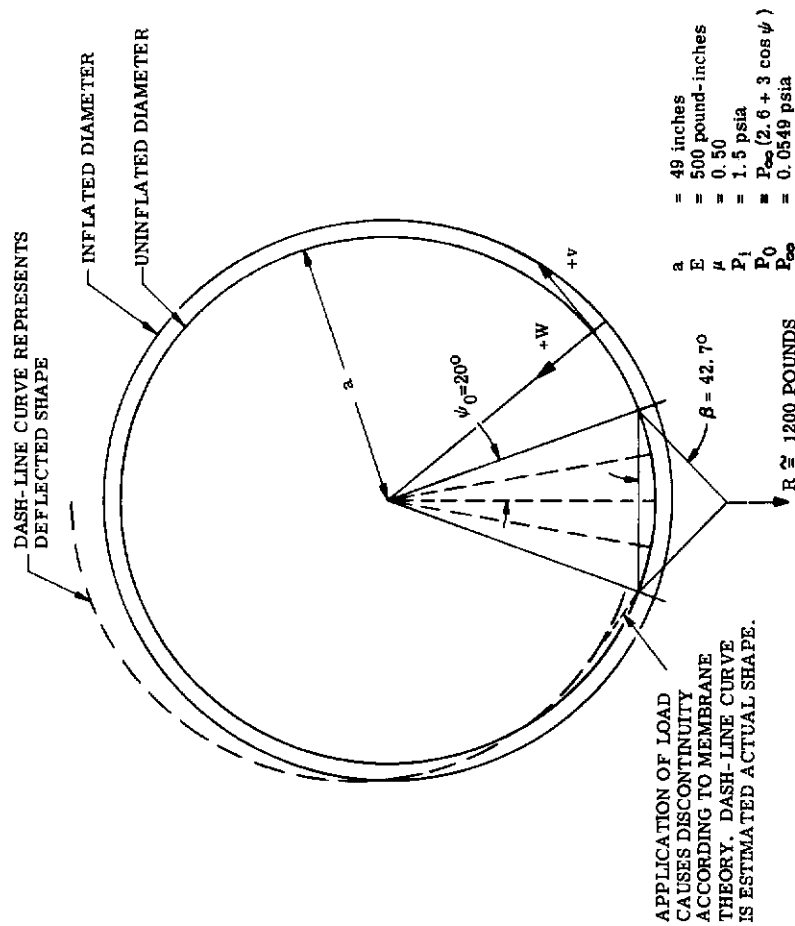
Figure 31. Deformation of Inflatable Sphere at Mach 2 Condition

a = 49 inches
E = 500 pound-inches
μ = 0.50
P_i = 1.5 psia
P_0 = $P_\infty(2.6 + 3 \cos \psi)$
P_∞ = 0.0549 psia

DASH-LINE CURVE REPRESENTS DEFLECTED SHAPE

INFLATED DIAMETER

UNINFLATED DIAMETER

$\psi_0 = 20°$

+w

+v

$\beta = 42.7°$

$R \cong 1200$ POUNDS

APPLICATION OF LOAD CAUSES DISCONTINUITY ACCORDING TO MEMBRANE THEORY. DASH-LINE CURVE IS ESTIMATED ACTUAL SHAPE.
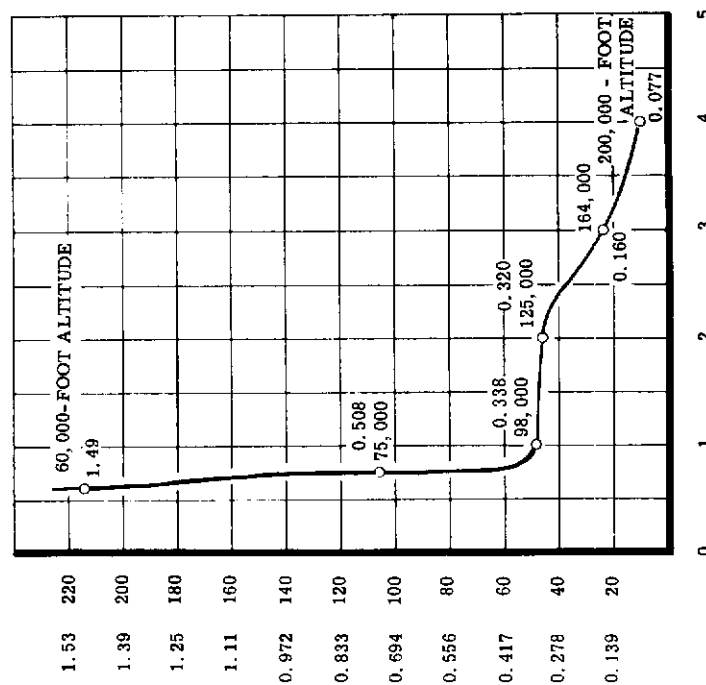
Figure 30. Total Stagnation Pressure versus Mach Number for Spherical Drag Body

Under the external pressure loading of Figure 25, the inflated drag device will maintain a very nearly spherical shape as long as the internal pressure is equal to or greater than the maximum external pressure, which occurs at the stagnation point. In this case the fabric is in tension throughout the sphere. If P_i goes below the maximum value of P_0, the nose of the sphere must "dimple" to maintain static equilibrium, and the assumption of a spherical shape used in the previous development is no longer valid in the dimpled region. A different approach to the method of deformations is therefore required.

As P_i is decreased, the inflated sphere will begin to lose its shape and possibly could become ineffective as a drag device. As it is possible, for one reason or another, for the internal pressure to be less than the design value, it is important to know the deflected shape of the inflated sphere under conditions of partial inflation.

For the purposes of this analysis, the external pressure distribution which was derived for a sphere will be assumed to remain unchanged as the inflated drag device deforms. This is not true, of course, but for the preliminary investigation it is felt to be satisfactory. Also, the elasticity of the fabric will be neglected, and the inflated drag device will be assumed to remain spherical over the portion in which the internal pressure is sufficient to maintain tension in the fabric.

Suppose P_i is reduced to the point where the nose of the sphere "dimples" slightly. In the center region of the dimple where $P_0 > P_i$, the fabric merely turns inside out and again assumes a spherical shape. At first glance it would seem logical to extend the concave arc until it intersects the convex shape of the main part of the sphere, as in Figure 32(a). However, this would cause a discontinuity in the slope of the curve, which requires that $N_{\psi 1} \rightarrow 0$ in the region of the discontinuity. From Eq (209) in Reference 6, if $N_{\psi 1}$ is zero, R_{ψ} must also be 0, and $P_0 - P_i$ takes the form shown in Figure 32(b). Considering the region where $P_0 - P_i$ is negative, r_1 and r_2 are both negative and N_{ψ} is positive.

Rewriting Eq (210) in Reference 6,

$$\frac{N_\psi}{r_1} + \frac{N_\theta}{r_2} = P_i - P_0 . \tag{51}$$

To satisfy Eq (51), $N_{\theta 1}$ must be negative; this is not possible with thin fabric. It must be assumed, therefore, that there is a smooth radius connecting the dimpled area with the main portion of the inflated sphere, as in Figure 33(a). Because the surface formed by this small radius is not compatible with the tailored shape of the sphere, wrinkling must occur and N_θ will therefore disappear. Let angle ψ_1 be drawn to the point of inflection on the dimpled curve, and let ψ_2 be drawn to the place where the tangent is perpendicular to the $\psi = 0$ axis of the sphere. In Figure 33(b), a free body of the area inside ψ_1 is drawn. As ψ_1 is adjacent to the wrinkled zone, $N_{\theta 1} = 0$. Because ψ_1 is drawn to the point of inflection, $r_1 = \infty$. From Eq (51), $P_i - P_0 = 0$ at ψ_1. Figure 33(c) shows a free body of the area inside ψ_2. As $N_{\psi 1}$ can have no component parallel to the $\psi = 0$ axis, R_ψ must equal 0 at ψ_2. Also, r_1 is +, $N_{\theta 1} = 0$, and $P_i - P_0$ is +. Eq (51) then shows N_ψ is positive.

As P_i continues to decrease, the dimpled area will enlarge until it reaches ψ_0, then the area outside ψ_0 will also dimple in as shown in Figure 33. Dimpling in outside ψ_0 causes wrinkles to form in the meridian direction, and $N_{\theta 2}$ in this region is zero. $N_{\psi 2}$ must be positive if the sphere is to remain inflated. Eq (51) shows that where $P_i - P_0$ is positive, r_1 is positive and where $P_i - P_0$ is negative, r_1 is negative. The inflated sphere, then, takes a concave shape which is connected to the spherical portion by a convex curve. At the point of inflection between these two curves, r_1 is ∞ and $P_i - P_0$ is therefore 0.

A free body of a strip of fabric of unit width in the region of the attaching circle is shown in Figure 34. As the inflated sphere dimples in, the angles of the fabric on either side of the attaching circle change. $N_{\psi 2}$ must always have sufficient component perpendicular to the attaching cables to balance $N_{\psi 1}$. If the deflection reaches the point where this is impossible with the given angle β and attaching radius r_0, the attaching circle will collapse radially until equilibrium is reached. Figure 35(c) is an example of this condition. When this happens, the shape has deviated from a sphere to
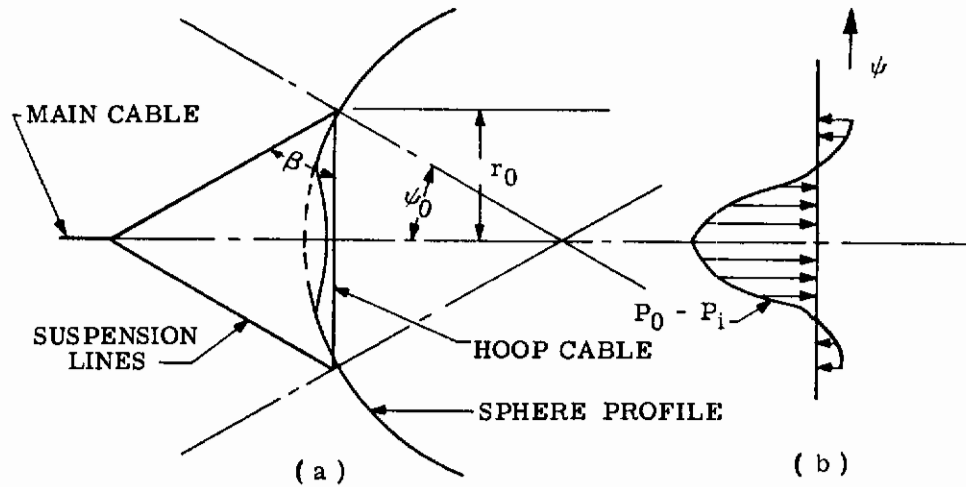
Figure 32. Nose Deformation Showing Pressure Distribution (First Assumption)

SMOOTH CURVE CONNECTING CONCAVE
AND CONVEX PORTIONS OF SPHERE
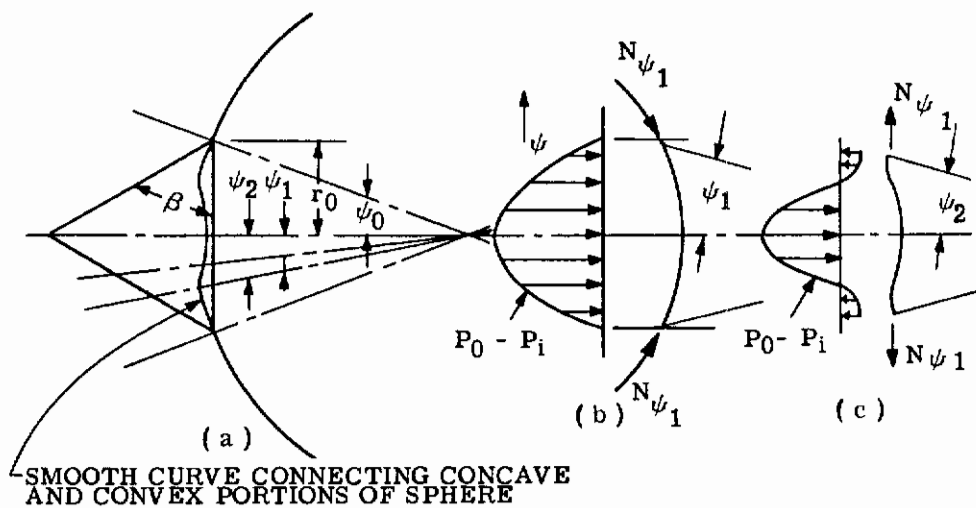
Figure 33. Nose Deformation (Actual Shape)

DETAIL A-A

r_0

β

ψ_0

r_0

FULLY INFLATED
PROFILE

PROFILE UNDER
PARTIAL INFLATION

$N\psi_2$

β

$N\psi_1$

$\dfrac{nT}{2\pi r_0}$

DETAIL A-A
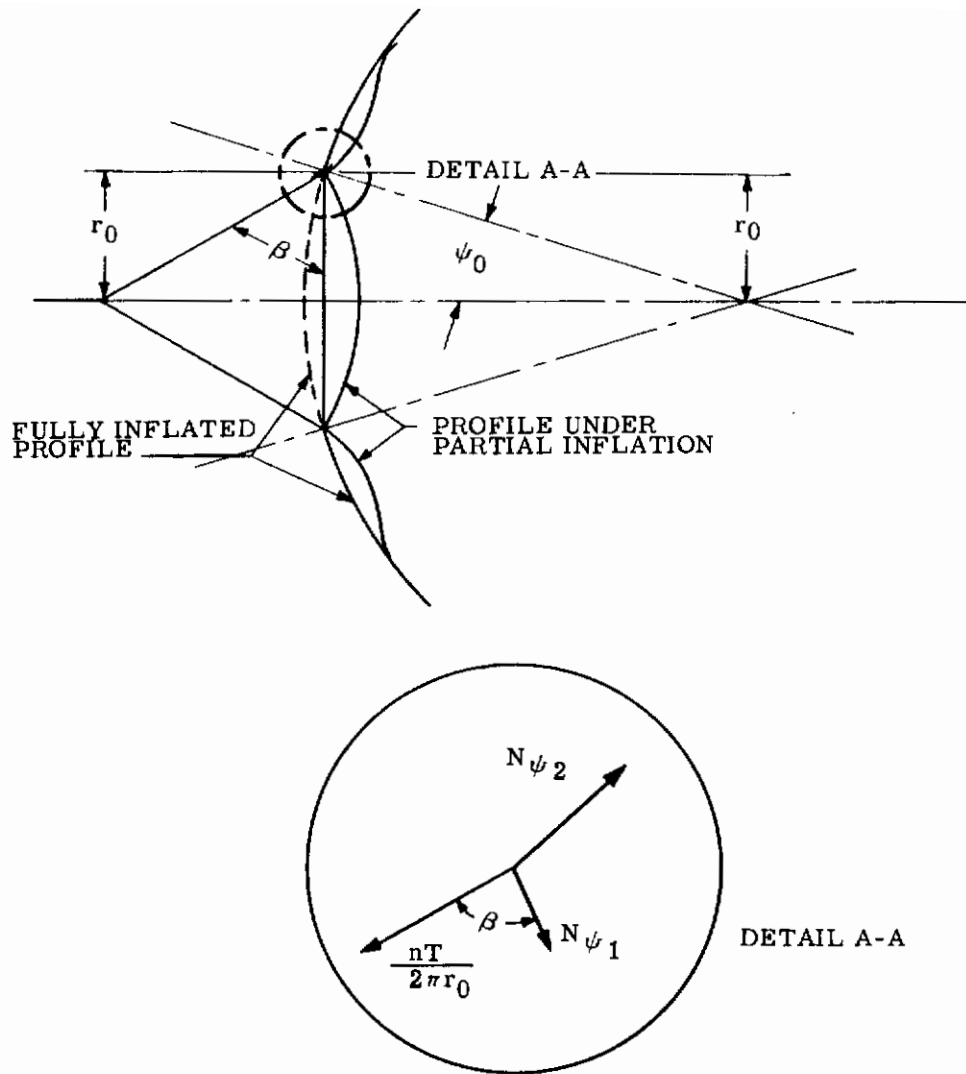
Figure 34. Nose Deformation after Further Reduction in Internal Pressure

$$\frac{W}{W_0} = 0.90$$

M = 2
P_∞ = 79 psfa
P_i = 39.2 psfg
$P_{0\ max}$ = 52.2 psfa
ψ_0 = 20°

ψ_0

POINT OF INFLECTION
ON SPHERE PROFILE $(P_i = P_0)$

(a)

$$\frac{W}{W_0} = 0.60$$

M = 2
P_∞ = 79 psfa
P_i = 25.1 psfg
$P_{0\ max}$ = 52.2 psfa
ψ_0 = 20°

ψ_0

POINT OF INFLECTION
ON SPHERE PROFILE

(b)

$$\frac{W}{W_0} = 0.20$$

M = 2
P_∞ = 79 psfa
P_i = 4.7 psfg
$P_{0\ max}$ = 52.2 psfa
ψ_0 = 20°

ψ_0

POINT OF INFLECTION
ON SPHERE PROFILE

(c)
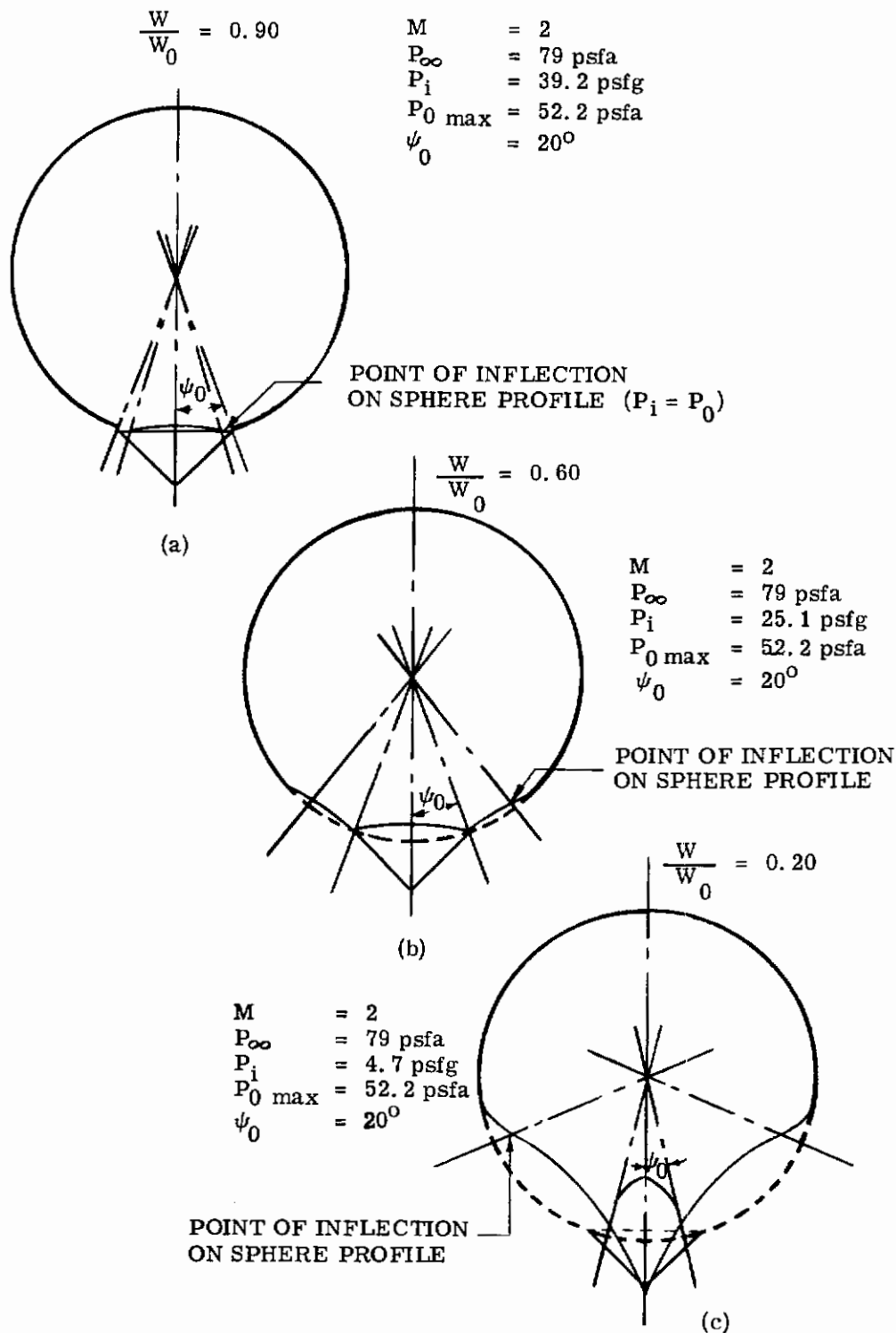
Figure 35. Spherical Inflated Shape under Various W/W_0 Ratios

the extent that the pressure distribution computed for a sphere is probably greatly in error; there-fore, no attempt will be made here to carry the problem further.

Example: The preceding analysis will now be applied to the balloon with the dimensions and loading of Figure 31. W_0 will be defined as the minimum weight of air required to maintain the spherical shape for a given temperature. If the weight (W) is reduced below W_0, dimpling will occur and both the absolute pressure (P) and the volume (V) will decrease until the equation of a perfect gas is satisfied. Figure 35 illustrates this phenomenon for various ratios of W'/W'_0. In Figure 35(c) with $W'/W'_0 = 0.20$, the external pressure around the leeward side is equal to the internal pressure P_i. Further reduction in the weight of air will be compensated for by a proportionate change in volume, with the pressure remaining at a constant value. Wrinkles will then form over the entire length of the sphere, which will assume a somewhat elliptical shape.

SECTION IV

PRELIMINARY DESIGN

A. GENERAL

An analysis of the free-fall and high-speed recovery flight conditions given on page 8 for the inflated sphere system requirements indicated that the high-speed recovery condition presented a far more severe criteria for fabrication than the planned free-fall drop test. Because of this fact and also because it was felt that the free-fall drop conditions were established only as a test parameter and would not be encountered in actual use of such an inflated sphere system, it was decided that the final design of the balloon to be fabricated during the experimental program would be based on the high-speed recovery conditions.

B. FABRICS AND COATINGS

One of the primary design parameters in the selection of a sphere size and design was the choice of a fabric which was readily available and would meet the temperatures encountered in the high-speed recovery. Based on the temperature range indicated in the thermodynamic analysis, a number of yarns, coatings, and films were considered. Table I contains the resulting data.

Table I. Yarn Comparison (to 400°F)

YARN	ELONGATION	STRENGTH RETENTION % OF ROOM TEMP STRENGTH	TENACITY* (Grams/Denier)	MELTING TEMP (°F)
Nylon 66	29.0	49.5	3.20	480
Nylon 6	22.0	42.9	2.76	430
Dacron	18.0	50.9	2.65	480
Fortisan 36	8.0	58.8	2.51	500
HT-1	18.0	67.9	2.30	700
Viscose Rayon (Hi-ten)	10.0	62.9	1.69	500
Viscose Rayon	10.0	60.6	1.51	500
Teflon	25.0	31.1	1.31	590
Cotton	7.0	47.6	1.00	500

*Tenacity is a term used in the fabric industry to indicate strength-to-weight ratio. Its units are grams tensile per denier. It is used in this text to offer a comparison between the various yarns.

The specimens were taken to 400°F, held for two minutes, and tensile tested. According to Table I, nylon offers the best strength-to-weight ratio (tenacity) of all materials tested. Its elongation, however, is quite high. Fortisan tests fairly high, but experience has shown elastomer-coated Fortisan to be unreliable. Extreme care must be taken in manufacturing Fortisan to avoid damaging the material. Rayon, Teflon, and cotton possess relatively low strength-to-weight properties. HT-1, a relatively new product, was not readily available. Dacron combines a fairly high strength-to-weight ratio with an average elongation, is readily available, and is easy to handle. Table II shows a comparison of the essential properties. Additional materials were considered for temperatures up to 900°F.

Fiberglass, a readily available, nonmetallic yarn, was also considered. Tensile tests of elastomer-coated fiberglass have been performed up to 1250°F. All of the materials listed in Table I will melt or charr at temperatures below 900°F. In screening tests at 900°F in air, elastomer-coated fiberglass specimens held up to 35 lb/in., or 35 percent of their room-temperature tensile strength.

Table II. Cloth Comparison (400 - 900°F)

YARN	PERCENT ELONGATION	PERCENT STRENGTH RETENTION (at 600°F)	TENACITY (Strength-to-Weight Ratio)	MAXIMUM USEFUL TEMP (°F)
Fiberglass	3.0	50 - 75	3.77	900
304 Stainless Steel	1.9	80	2.57	900 - 1100
Inconel X	8.2	65	1.15	1400

Tensile tests of fiberglass yarns at 600°F range from 1.3 - 5.93 tenacity, depending on the finish applied to the fiberglass. This compares to a 1.39 tenacity at 600°F for HT-1, the only material in Table I capable of reaching this temperature.

Tests made on asbestos cloth indicated only a slight deterioration at 1560°F. Asbestos, however, is undesirable because of its very low strength-to-weight ratio. Because they possess a wide range of tenacities, metal yarns are able to withstand the highest temperatures encountered in this study. Hardened 304 stainless steel has a tenacity of 2.07 at 600°F, and other metal yarns tested were up to 40 percent stronger. These included molybdenum, tungsten, and René-41.

Neoprene is the most impermeable to gas leakage of the coatings tested, has a low specific gravity, is compatible with all of the yarns mentioned in the preceding paragraphs, is readily available, relatively inexpensive, and the easiest to handle. However, little is known of its low-temperature properties.

In comparison to neoprene, Viton A is also easily handled, almost as impermeable, and is capable of slightly higher temperatures. However, it has a much high specific gravity, is more expensive, is completely incompatible with fiberglass (its temperature properties are lowered and the fiberglass is rendered more brittle), and is rather brittle below 0°F.

Silicones are capable of a wide range of temperatures. Some silicones will reach 1800°F and remain gas-tight, while others may be flexible to several degrees below 0°F. Silicones have been tested satisfactorily on fiberglass at 700°F for two hours under internal pressure. Results of these tests reveal only slight discoloration. For shorter periods this combination has reached 850 - 900°F and remained flexible and gas-tight. Silicones are recommended as the best coating for temperatures over 600°F.

Silicones have a low specific gravity and are generally compatible with most yarns. However, they are more expensive and more difficult to handle than neoprene, and coating and curing are difficult. Before curing, the coating has the consistency of fly-paper glue, and seaming before or after curing involves other problems. Because of the necessity for a partial cure between spreads of the coating material, silicone-coated, multi-ply fabrics tend to delaminate under heat and load. Because of these difficulties, the use of silicones was avoided.

Other configurations, such as reinforced films were also considered. Mylar film on Dacron cloth has been tested, but the results are inconclusive over 400°F.

For the lower temperature conditions encountered in the high-speed recovery, the use of Mylar, polyethylene, or Videne with no reinforcing fabric was considered. Refer to Table III for characteristics. The tensile strengths in Table III are given at room temperature and a considerable decrease in this value at the higher service temperatures is expected. Mylar undergoes a considerable decrease in tensile strength at 212°F, but the film retains useful properties at 302 to 347°F.

Considering the preceding fabric investigation and the thermodynamic analysis (Section III), two possible choices appeared evident:

(1) The selection of a W/C_DA of 0.1 to 10, hence range of maximum temperature from 0 to 450°F, and the possible use of Dacron cloth coated with neoprene (or some lighter weight material in the case of W/C_DA of 0.1) for the fabric.

Table III. Film Comparison

FILMS	TENSILE STRENGTH AT ROOM TEMP	WEIGHT (Oz/Yd^2)	SERVICE TEMP	MELTING TEMP
Mylar (1 Mil)	20 lb/in.	1.04	-75°F to 347°F	482 - 491°F
Polyethylene (1 Mil)	3 - 5 lb/in.	0.70	-40°F to 220°F	350°F
Videne (1 Mil)	9 lb/in.	1.0	-40°F to 220°F	350°F

(2) The selection of a W/C_DA of 25 to 100, hence a range of maximum temperatures from 590 to 900°F and the use of fiberglass cloth coated with a silicone for the fabric.

As these possibilities were being considered for fabrication, there was a strong inclination toward selecting a readily available, presently familiar fabric. Because of the recommendation to avoid the use of silicones, the first condition was selected.

The three W/C_DA's included in this selection were then considered:

(1) $W/C_DA = 0.1$. The sphere required for a W/C_DA of 0.1 must be fabricated from a very light-weight fabric to meet such a low weight-to-drag value. Using even the light-weight films, Mylar and polyethylene, the total inflated sphere system weight (calculated as described in paragraph E) is quite high, approximately 85 percent of the 500 pound payload weight for polyethylene, and 120 percent for Mylar. Although these films could conceivably withstand the temperatures encountered over the trajectory for this sphere size, the initial deceleration force, as indicated by the data from the flight analysis, is extremely high at deployment (53 g's), and the distribution of such a load over a sphere fabricated from these films would be extremely complex and impractical. Packaged volume for such a large sphere (approximately 112 to 122 feet in diameter) would be impractical for use in recovery of a manned vehicle.

(2) $W/C_DA = 1.0$. For this W/C_DA the weight penalty is quite high. Assuming that the fabric weight is 0.5 pound/square yard (which would probably be required to overcome the heating effects encountered in this trajectory), the weight penalty of the system is 72 percent of the payload.

(3) $W/C_DA = 10$. From an analysis of this W/C_DA condition it appears that the weight of an inflated sphere system (to recover a 500-pound payload) would be approximately 45 to 60 pounds, depending upon the fabric weight chosen. This weight penalty is more compatible with present recovery systems. In view of this fact and because of the disadvantages offered by the two preceding W/C_DA's, this condition was selected as the weight-to-drag ratio to be utilized in the preliminary design and future fabrication.

Because of its ability to meet the necessary qualifications, Dacron-neoprene was the fabric selected for further investigation during the preliminary study and for probable use in the experimental phase of the program. The actual fabric chosen was a two-ply (cross-ply) Dacron-neoprene (N313A25) weighing 10.2 oz/yd^2.

C. INFLATION AND DEPLOYMENT TECHNIQUES

Following the selection of a W/C_DA of 10 based on an investigation of available fabrics capable of withstanding the temperatures encountered in the high-speed recovery, a study was made involving various systems of inflation.

Several assumptions were made prior to this study:

(1) A spherical body approximately 8.7 feet diameter with an inflated volume of 343 cubic feet would be used in the high-speed recovery (based on $W/C_DA = 10$).

(2) The maximum allowable inflation pressure governed by the seam strength of the fabric (55 pounds/inch) would be 2.08 psig.

(3) "One Shot" inflation immediately following deployment is assumed.

(4) No heating of the inflation gases will occur over the trajectory. This assumption is based on the fact that if a gas such as helium is used, it will receive no heat by radiation, and only convective heating currents set up inside the sphere will effect its temperature. As the flight at the high temperatures is of such short duration, the heating will be negligible and is therefore neglected. Therefore, the maximum pressure differential across the walls of the sphere is assumed to exist at 200,000 feet altitude immediately following inflation.

Inflation systems were investigated on the basis of reliability, rate of flow weight, and "off-the-shelf" availability. Table IV presents the various systems which were investigated. The selection of a commercial and readily available device was necessary for fabrication during the experimental program. However, several other concepts under development appeared to have merit, and were included in the study.

Table IV. Inflation System Comparison Chart

TYPE OF SYSTEM	MAJOR PARTS REQUIRED	APPROX TOTAL WEIGHT (Pounds)	INFLATION TIME (Seconds)	COMMENTS
COMMERCIALLY AVAILABLE EQUIPMENT				
Compressed gas contained in fiberglass sphere	Flood valve, pressure sphere, coupling	12.5	3 - 5	Readily available system; easily packaged, reliable.
Compressed gas contained in metal cylinder	Flood valve, pressure sphere, coupling	22	3 - 5	Readily available system; easily packaged, (weight penalty), reliable.
Cool gas generator	Valving, generator, coupling	30	30 - 60	Relatively new device; may present packaging problems, reliability unknown.
SYSTEMS REQUIRING DEVELOPMENT OR FURTHER RESEARCH				
Liquified gas under pressure (ammonia) freon, ethyl (alcohol), etc.	Pressure container, valving and couplings, heat source (ballistic)	15	30 - 60	Development required for heat generating system; reliability unknown.
Gas generation by chemical reaction (nitrogen)	Mixing chamber, valving, coupling	13	30 - 60	Efficiency approximately 30 percent on a weight-to-weight basis; reliability unknown.
Pre-inflation and storage under pressure	Pressure vessel, quick-release mechanism (squib-operated)	15	Instant	Packaging and fabrication of container research required; reliability appears good.

Pressurized gas containers offer a relatively simple yet effective means of inflation. Standard metal cylinders are available in a complete range of sizes with standard valves and fittings. A new development, fiberglass spheres, offers an advantage over the metal bottles because of its high strength-to-weight ratio. Standard valving is also available for the fiberglass spheres.

Of the inflation methods considered, the fiberglass container plus necessary valving provided the most desirable characteristics for the high-speed recovery system. This system was incorporated in the final preliminary design. In addition to its light weight and high reliability, the fiberglass container and valving offer rapid inflation essential to stabilizing a manned capsule immediately following ejection from an aircraft or space vehicle.

The cool gas generator, a recent commercial development, mixes hot gases evolving from the ignition of a propellant with a coolant such as freon. This action produces relatively cool volumes of gas for inflation purposes. The device could be utilized with few or no modifications. However, it involves a weight and inflation time penalty relative to the other systems.

The use of liquified gases such as liquid ammonia, ethyl alcohol, and acetone offered a possible means of inflation while affording such advantages as ease of storage and small volume requirements. The high temperatures encountered in the high-speed recovery could possibly be utilized as the heat source necessary for vaporization of the liquid. Such a system would require considerable development and the use of non-standard parts.

A quick-release air chamber for testing liquified gas inflation systems was designed and fabricated (see Figure 36). The following test method utilizing the quick-release chamber was employed to expose the test system to conditions in the environmental chamber.

(1) The unfilled sphere is injected with approximately 2 cc of ethyl alcohol or acetone and placed in the quick-release chamber.

Figure 36. Exposed Sphere and Quick Release in Environmental Chamber

(2) The quick-release chamber is closed and placed in the environmental chamber.

(3) An environment is established in the environmental chamber, simulating altitudes ranging from 60,000 to 80,000 feet at temperatures of -20 to +80°F.

(4) Upon reaching the desired environmental conditions, the quick-release chamber is opened, exposing the test system to the low-pressure environment. The liquid gas flashes to a vapor which inflates the sphere.

The possibility of pre-inflation of the sphere, prior to sealing it into a pressurized container from which it might be deployed at high altitudes has been considered. A sketch of such a system is shown in Figure 37. A spherical container (aluminum) may be opened by explosive bolts to initiate deployment. This system would require no inflation apparatus and offers the advantage of immediate inflation upon release from its restrictive pressurized environment. The method would, however, require considerable development to prevent fabric rupture, and use of non-standard parts.
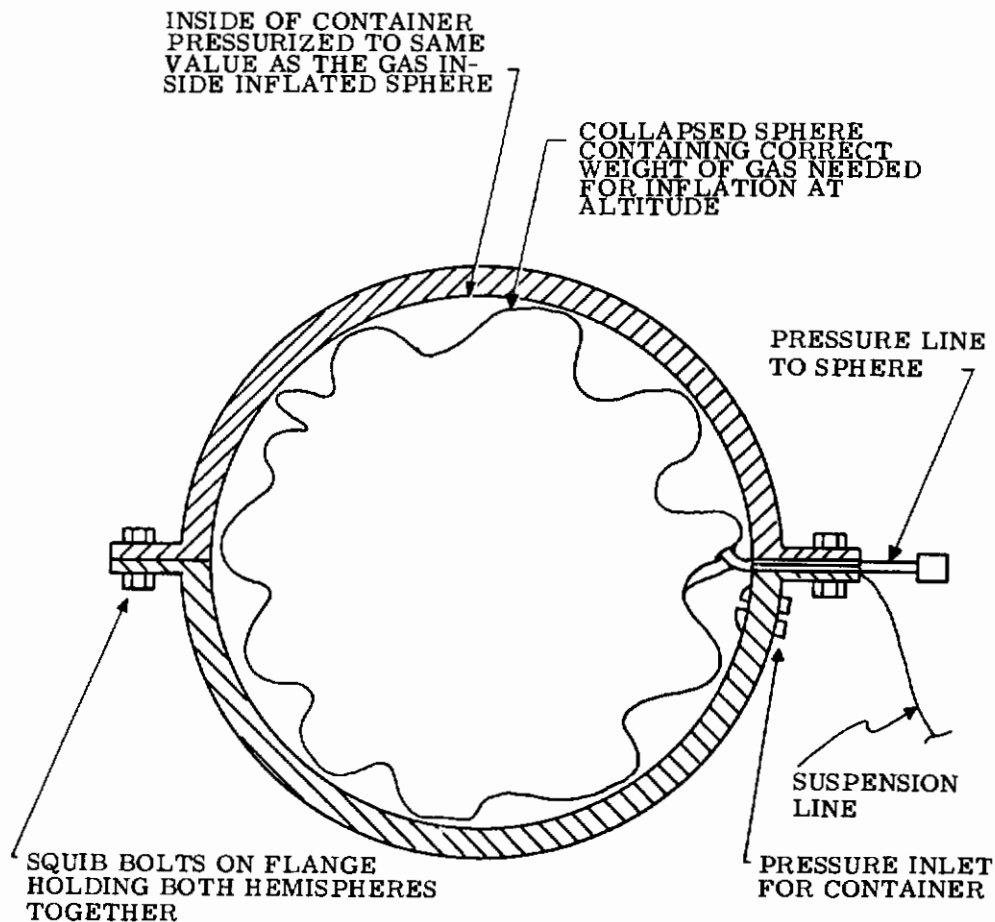
Figure 37. Pre-Inflation of Sphere

Frankford Arsenal has conducted experimental tests for Goodyear Aircraft Corporation on the pyrotechnic inflation of fabric "bumper bags" for escape capsules. Results indicate that this method of inflation would be feasible for small diameter spheres such as those required for the W/C_DA = 100 or 50 for the high-speed recovery. Transient temperatures up to 400^0F would be experienced, but spheres fabricated for these recovery conditions could adequately withstand even higher values. A method of shielding the charge would have to be developed; however, standard parts with slight modifications would constitute the bulk of the system.

Because of the large volume presented for the W/C_DA = 10 condition, pyrotechnic inflation was not recommended by Frankford Arsenal for this sphere size. A high weight penalty relative to other devices and excessive temperatures would be encountered in the use of such a system for so large a sphere.

Functional testing of the full-scale mockup inflatable sphere and canister (see Figure 38) was accomplished at the WADC, 20-foot diameter systems altitude chamber. The mockup consisted of a wooden platform and a three-sectioned truncated cone canister which packaged the entire fabric sphere and simulated deployment hardware. The inflation system consisted of an 836-cubic-inch pressurized bottle and a squib-actuated valve.
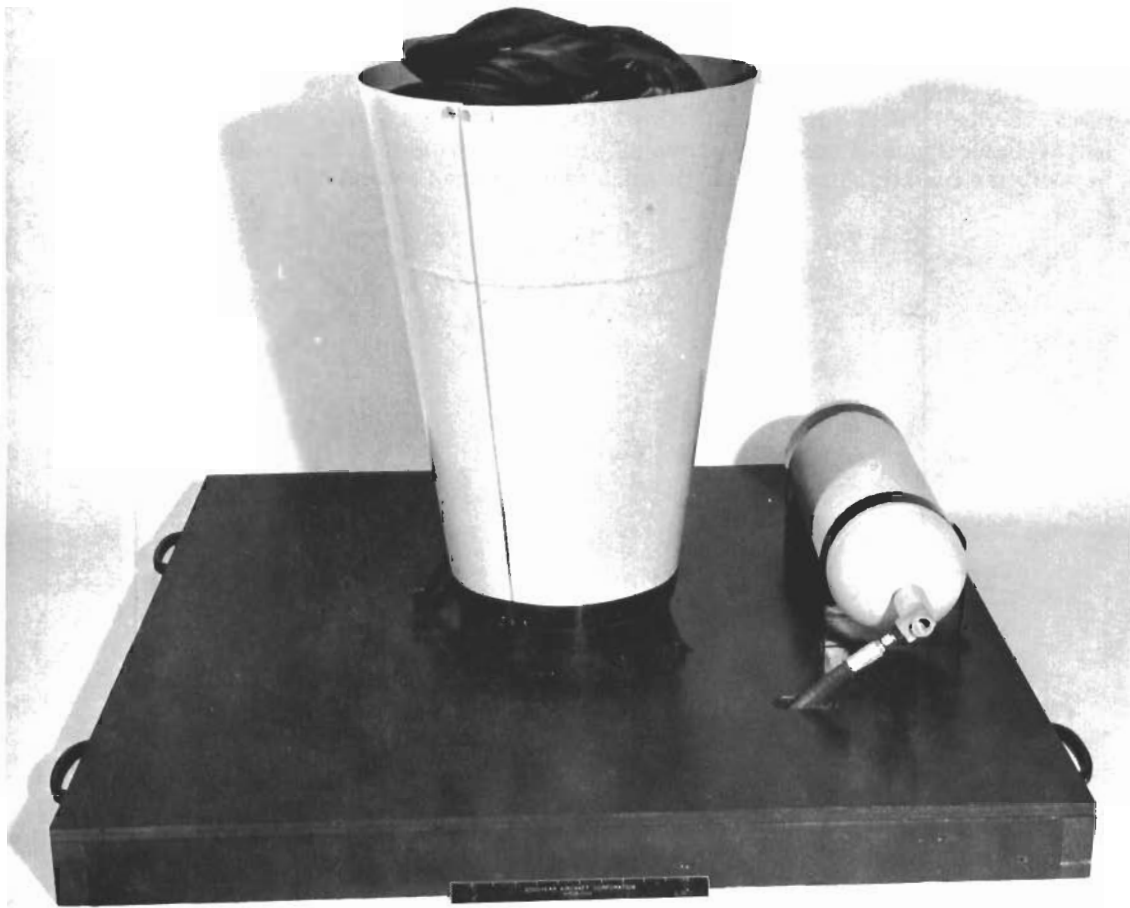
Figure 38. Full-Scale Inflation and Deployment Model

Two tests were conducted. The first test was conducted utilizing an 800-psia bottle at a simulated altitude of 100,000 feet at -10^0F. The deployment time from packaged state to full size (inflation pressure equals ambient) was 0.24 second. The second test was conducted using 1500 psia in the 800-cubic-inch bottle at a simulated altitude of 120,000 feet at -20^0F. The deployment time for the second test was 0.035 second.

The results of these tests indicated that a very rapid inflation is possible and is within the strength capability of the Dacron-neoprene fabric. The tests also showed that the sphere can be packaged within the canister and that it can be freely deployed and separated from the canister with no binding or pinching of the fabric.

Two sets of booster and canister separation flanges were tested for reliability and back blast effects by Thiokol Chemical Corporation.

The first series of separation tests was conducted on a 9-inch-diameter forward separation section. This section was cut into five pie-shaped pieces. Four of the five pieces were used to determine proper cutting action and back blast effects of two different sizes of mild detonating fuse (MDF). The MDF sizes used were 10 grains per foot and 15 grains per foot. In the four tests conducted, separation was complete and all back blast effects were contained. Approximately 80 percent of the 0.125-inch-thick section was cut by the shaped charge and the remaining 20 percent of the casting was blasted through. The remaining section was used to check initiation, propagation, and to ensure separation at the epoxy-filled slot. The test was successful in that all back blast effects from the detonators and end primers were contained by the detonator cap, and separation was complete.

The second series of separation tests was successfully conducted as a reliability check on the remaining three sets of rings, using MDF of 10 grains per foot.

D. SUSPENSION SYSTEMS

Two basic types of suspension systems were investigated. These were single line and multiline systems for attachment of the payload (see Figures 39 and 40).
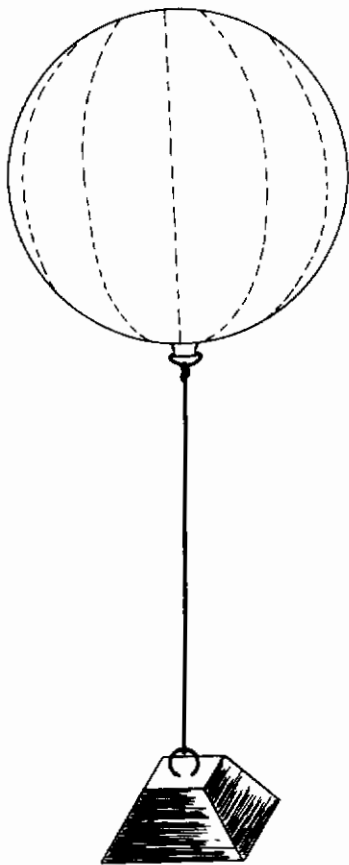
Figure 39. 15-Inch-Diameter Test Model Using Single-Line Suspension
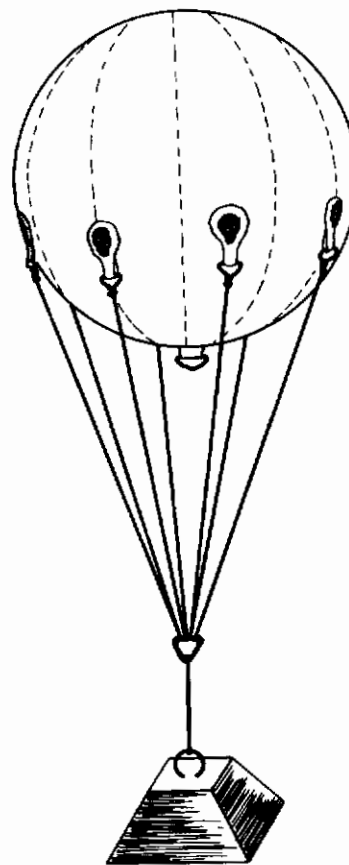
Figure 40. 15-Inch-Diameter Test Model Using Multiline Suspension

The advantages of the single over the multiline system are as follows:

(1) Simplicity of packing is achieved; lower package volume requirements.

(2) Recovery system is not as susceptible to fouling, tangling, and wrap-up with the payload.

(3) Load relieving tendencies are obtained.

Since the inflated sphere is flexible it will deform to some extent to adapt to applied loads within the structural limits of the fabric. This property will permit a fully inflated sphere to assume an elongated shape during high drag loads. The achievement of an elongated shape with the accompanying reduction in frontal area will reduce the drag of the sphere and consequently will reduce the deceleration forces. This intrinsic property of the inflated sphere is exploited by the use of the single point attachment feature, the line to the payload being attached to the sphere in a region very near its apex, or stagnation point.

The multiline system also offers certain advantages as follows:

(1) No internal distribution of load required.

(2) At low speed and low Reynolds numbers the multiline system appears more stable than the single line (based on information from Section V-B).

Some consideration was given to a geodetic type suspension as utilized in aerial bomb stabilization (see Figure 41). This method of attaching the payload and sphere offers several advantages with regard to stability and load distribution, although the system would appear to be quite susceptible to fouling.
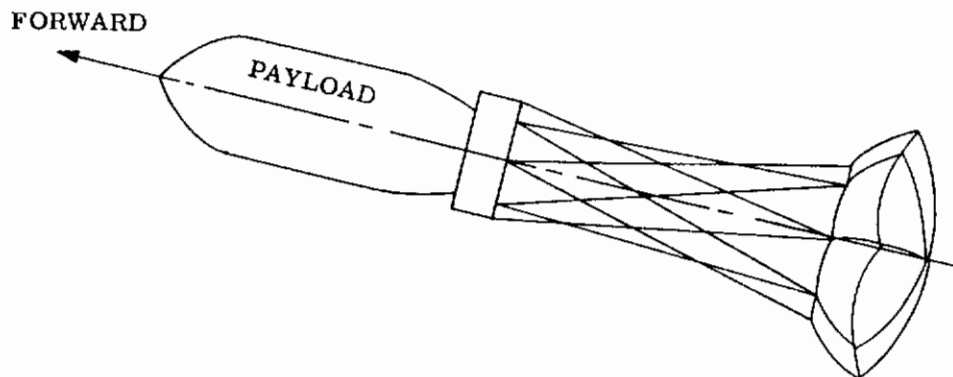
Figure 41. Geodetic Type Suspension

An effort was made to design a system incorporating the advantages of single line and multi-line suspension. A system was envisioned whereby a single line or braided lines might be utilized which could transmit and distribute the loads efficiently over the inflated sphere.

Several designs were investigated. One design (see Figure 15) was an early concept used in the stress analysis of the inflated sphere system. The hoop size required to distribute this load safely to the fabric becomes so large that many of the advantages of the single line system are lost.

In another system the lines extend over the top of the sphere, meet at a small cable hoop at the nose of the body, and intersect with the riser line less than one diameter from the surface. Extending the lines over the sphere in this manner aids in distribution of the stresses while the

intersection of these lines in a small hoop simulates single point suspension to some degree. This type of suspension was incorporated in the final preliminary design (see Figure 42).
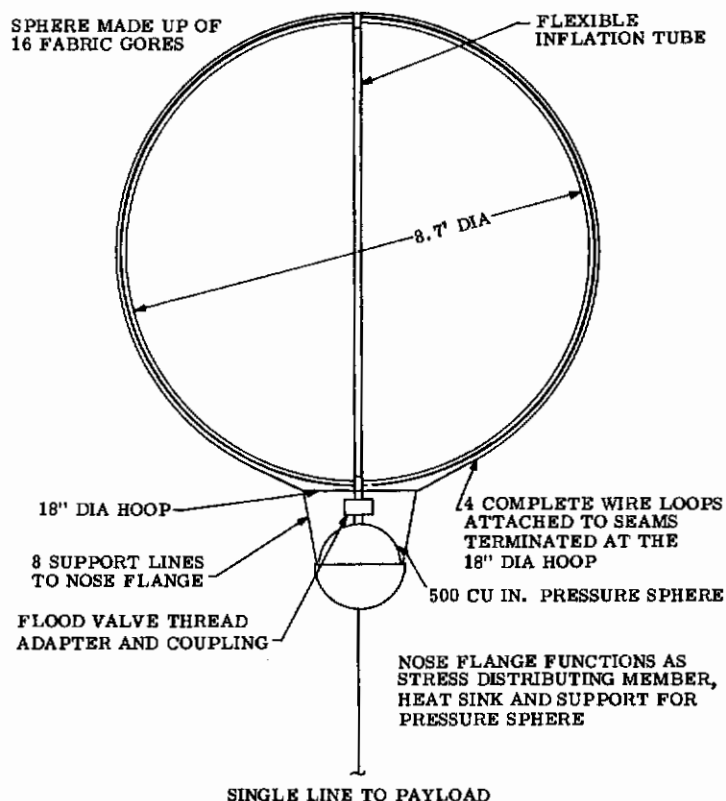
Figure 42. Meridian Cable Suspension System

The length of riser line from payload to inflated sphere was determined to optimize both stabilization and drag effects, and to minimize heating and loads on both the line and sphere. Riser lengths (from five to six sphere diameters) were tentatively selected pending conclusive information on interference effects from wind tunnel tests at NACA. Factors such as final payload weight and shape are included in this testing.

The system finally selected for simplicity was a single-line suspension system. The concept for deployment for initial stabilization before maximum drag utilizes the inflated drag body mounted immediately aft of the primary body. After alignment to a nominal zero flight path angle, the inflated body is deployed to its full riser line length for maximum drag. However, in order to prevent large deployment and snatch loads, a deployment reel was designed and tested.

The deployment reel (see Figure 43) must operate smoothly and evenly under various loading conditions. Primarily, this reel consisted of a drum rotating on a piston which was restricted by oil passing through an orifice. The back pressure provided by the oil was transmitted to a disk brake on the drum which governed the deployment speed. The speed of deployment was adjusted for 4 - 5 ft/sec.

E. INFLATED SPHERE ASSEMBLY

Consideration was given to the variation in the system weight for the assigned values of W/C_DA for the high-speed recovery. Using two representative fabric weights, 0.5 and 1.0 pounds/ square yard, the system weights were determined. Based on the preceding information on inflation systems and detail design work on preliminary inflated sphere concepts, the following assumptions were made:
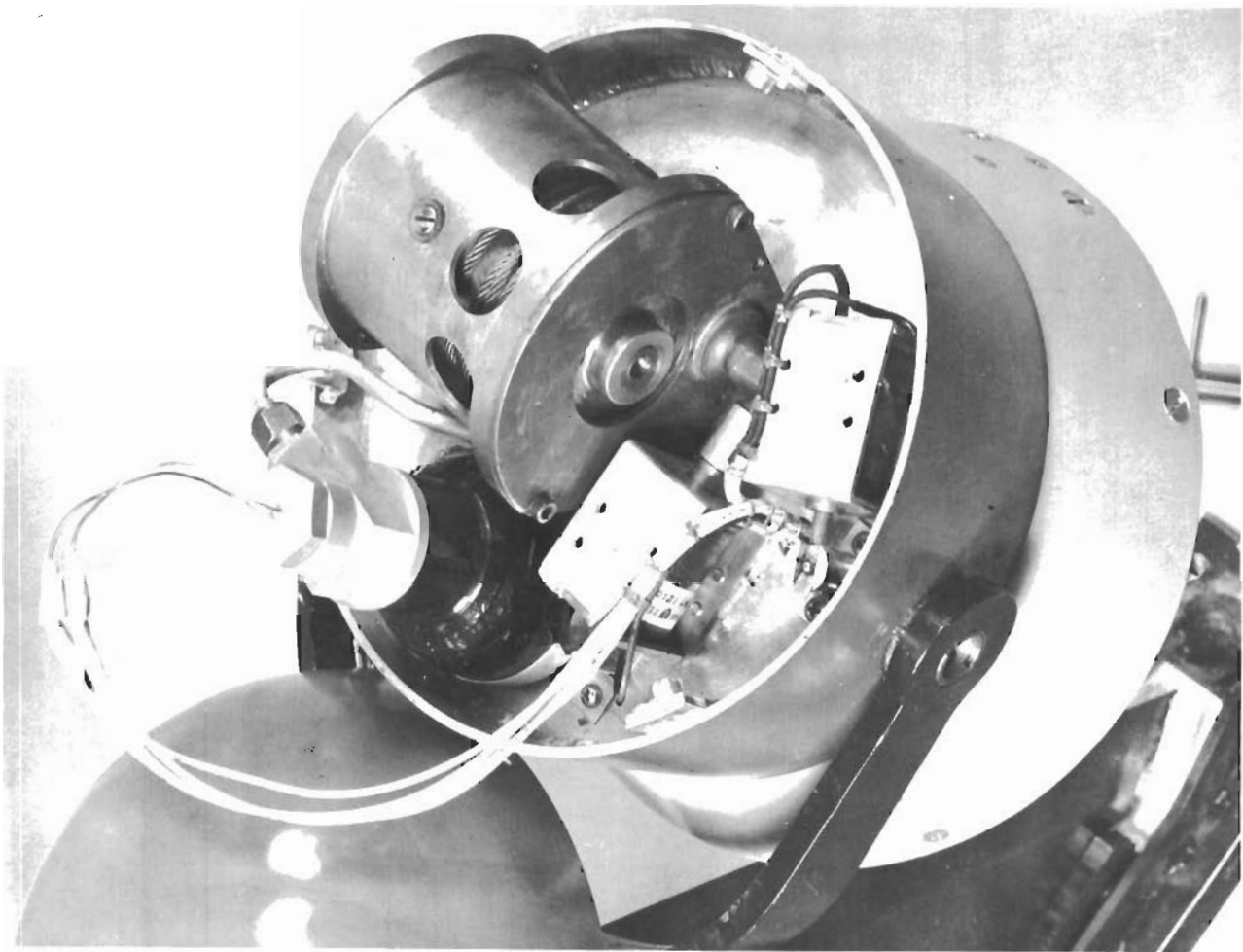
Figure 43. Constant Rate Deployment Reel

(1) Fiberglass pressure containers were used for inflation with compatible valving and hardware.

(2) The required sphere diameter was calculated from the following derivation where:

$$\frac{W}{C_D A} = 10 \qquad D = \text{Diameter of sphere (ft)}$$

$$A = \pi \frac{D^2}{4} \qquad C_D = 0.92 \qquad A_S = \pi D^2$$

$W = 500$ pounds + estimated weight of hardware $+ \pi D^2$ (fabric weight/square feet).

Figure 44 shows the calculation results and the accessory weights based on inflated sphere diameters. It may be noted that the high values of $W/C_D A$ are such a small fraction of the payload weight that they are negligible in determining inflated sphere diameters.
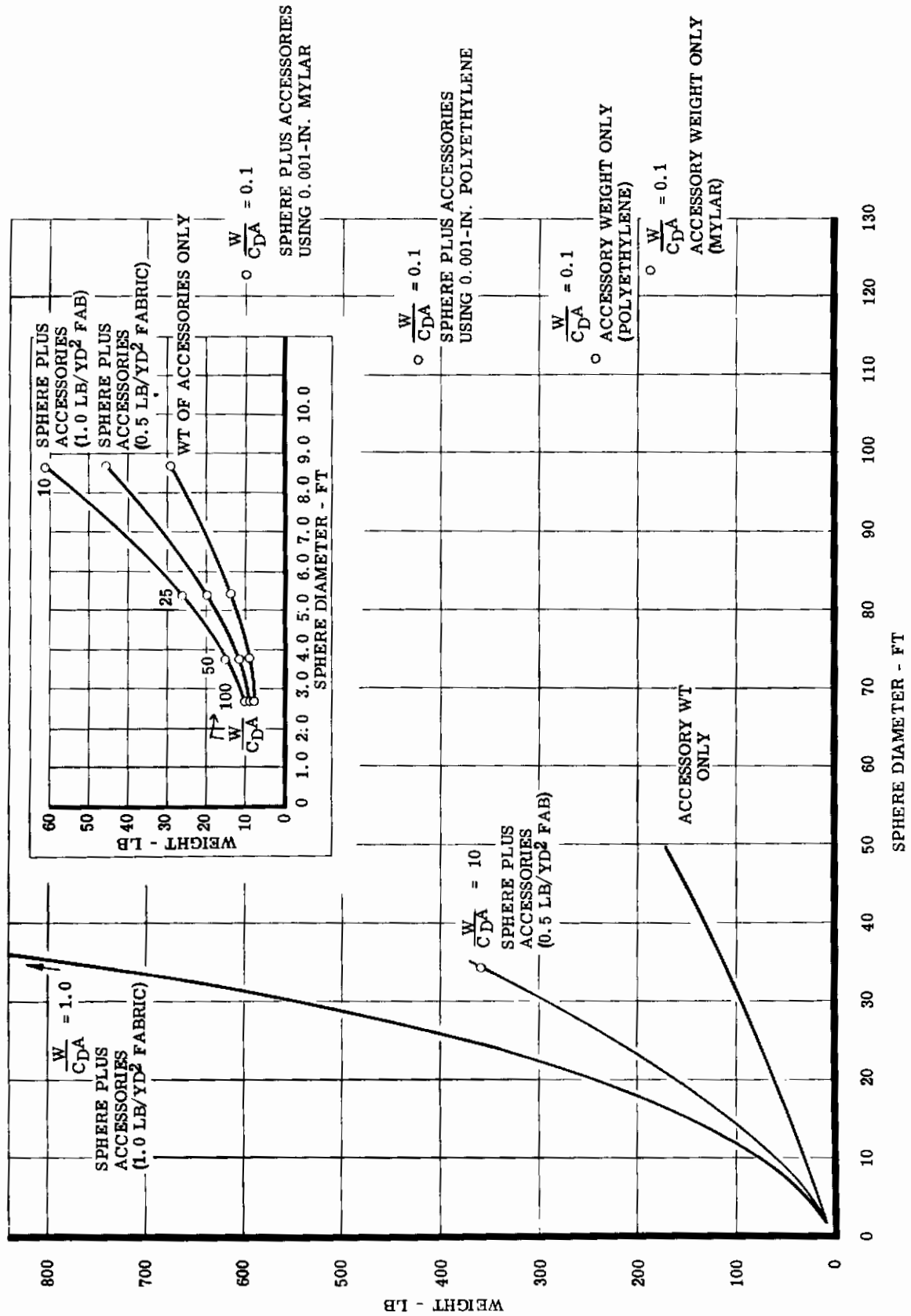
Figure 44. Assembly Weight versus Inflated Sphere Diameter

As it is impractical to fabricate a sphere from either the 0.5 pound or 1.0 pound/square yard fabrics and still meet the $W/C_DA = 0.1$ condition, calculations were made using 1-mil thick nylon and polyethylene materials. The accessory weights for these two spheres were assumed equal. Polyethylene, the lighter of the two materials (although it requires a smaller diameter for the sphere with a given W/C_DA ratio), requires additional accessory weight for load distribution due to its low tensile strength. These strengths are 3 to 5 pounds/inch for polyethylene and 20 pounds/inch for mylar. Since a specific W/C_DA ratio or diameter was selected, singular plots are displayed in Figure 44.

The weight of the final preliminary design (sphere plus accessories using 10.2 ounces/square yard Dacron-neoprene) was 47.5 pounds. The final assembly is illustrated in Figure 42.

The final assembly consists of a sphere of 16 gores. The weight of the payload is distributed over the inflated sphere by eight fine steel, equally spaced cables extending over the top of the sphere and taped over as shown in Figure 45.
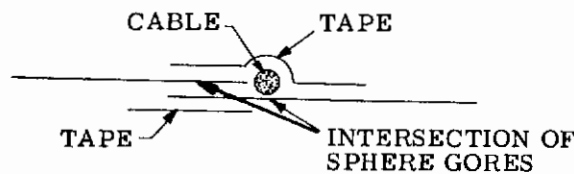
Figure 45. Typical Seam Assembly

These meridian cables are gathered into a hoop at the bottom of the sphere and are fastened to a metal flange attached to a single riser from the payload. Such a system provides the advantages of both the single and multiline systems described in paragraph D.

The flange is made of a lightweight metal shell which is sufficient to transmit the weight of the payload to the cables extended over the sphere. This shell is lined with an insulating material to provide a cushion and support for the inflation sphere as well as protection from the high temperatures encountered.

Installing the flange at the bottom of the sphere provides an additional advantage in that it protects the fabric from the stagnation point temperatures which would otherwise be experienced on the sphere's surface. The improvement of the aerodynamic shape was also further investigated. The wind tunnel tests described in Section V indicate that a nose cone sphere combination with a burble fence is an essentially stable system in the low speed ranges. A partially inflated sphere was another consideration for a stable body due to its pear shape during descent.

Further investigation of the optimum configuration was programmed by drop-testing the 1/4-scale model from the Goodyear Aircraft Corporation airship dock. Test procedure and results are in Section V-B.

The inflation system consists of a 10-inch fiberglass sphere pressurized to 3000 psi with helium gas as the inflation medium. Valving is accomplished through a coupling and thread adapter to a flood valve. This flood valve has a flow capacity to pass the entire 500-cubic inch volume of the pressure sphere in three to five seconds. The valve functions when a small valve is tripped, allowing the pressurized gas to move a cylinder uncovering a large port.

The gas passes from the flood valve through another adapter to a check inlet port incorporated in the sphere. This system is mounted on the nose of the sphere and is shielded from thermodynamic and aerodynamic effects by the support flange and nose piece. The spring-loaded valve is released by a solenoid actuator. An alternate valving assembly can be designed by utilizing squib-operated valves (commercially available) which are actuated by an electrical impulse.

F. FOLDING AND PACKAGING

A full-size 10-foot diameter sphere was made to study various methods of folding and packaging. The sphere was fabricated from 4.75 ounces per square yard foristan-neoprene fabric which is relatively inexpensive and readily available. Based on previous experience in escape capsule recovery and associated problems, a rectangular or cylindrical shape was selected as the most desirable for the sphere package. A rectangular package using a typical folding method is shown in Figure 46. A comparison with the unfolded size may be made from Figure 47.

With several methods of folding, approximate volume for a hard manual pack was established for this particular sphere size. A packaged volume of 908 cubic inches was obtained with the 10 foot diameter sphere using a method of packaging similar to that used with parachutes. This procedure consists of aligning the gores and folding down from the apexes. These figures were readily convertible to other sphere diameters. For example, the occupied volume for an 8.7-foot diameter sphere, as required in the high-speed recovery for a W/C_DA of 10, is equal to approximately 770 cubic inches as determined by this process. This is equal to 0.13 percent of the inflated volume for this sphere. An approximate volume for the inflation system and suspension system was determined to require an additional 600 cubic inches, bringing the total volume to 1370 cubic inches for a hard manual pack (10-inch diameter x 18-inch long).

The sphere will be folded and packaged under standard atmospheric pressure. All air should be evacuated from the sphere prior to packaging.

The following figures were obtained for comparison with various parachute packing densities:

	DENSITY LB/CU IN.
Hard Manual Pack	0.015
Low Pressure Pack	0.018
Medium Pressure Pack	0.022
High Pressure Pack	0.026

Using these figures the volume obtained for the hard manual pack of the sphere was converted to a medium pressure pack. This gives a reduction in packaged volume to 619 cubic inches or 0.09 percent of inflated volume. The volume of the accessories remains constant as they were assumed to be unaffected by a change in methods of packaging. Therefore the total volume occupied by the pressure packaged system would be approximately 1219 cubic inches.

G. DEPLOYMENT

The altitude and speed requirements imposed on the 500-pound escape capsule and an inflatable drag device indicate the need for a forced deployment system.

The two methods considered for forced deployment were the ejector gun and the blast bag system. Both of these systems are accepted procedures in Goodyear Aircraft Corporation's escape capsule system.

In the ejector gun concept, pull action of the projectile forces the sphere from its container. This method was considered for use in deploying the first and second stage chutes of the escape capsule.

The blast bag system consists of a rubber bag inflated by an explosive type cartridge, forcibly ejecting the deceleration sphere into the air stream.

Upon ejection, the collapsed sphere will travel aft the length of the attached riser lines, stretching the lines (100 percent deployment) and releasing an actuating device. This permits the valve in the inflation bottle to open, allowing the pressurized gas to fill the deployed sphere.

Figure 46. Ten-Foot-Diameter Mockup in Packaged State

Figure 47. Ten-Foot-Diameter Mockup Unfolded

Upon descent to 60,000 feet pressure altitude, the sphere will collapse due to the increased ambient pressure. The payload speed is now over 600 ft/sec. A barometric altitude sensor, preset to a 60,000 foot pressure altitude will initiate the deployment of a small ribbon parachute by means of an ejector gun. This chute is used to slow the capsule to a terminal velocity of less than 500 feet/second.

PRELIMINARY TESTING

A. FABRIC TESTS

1. Heating Tests

Preliminary heating tests were run with Dacron-neoprene samples following the tentative selection of this fabric for use in actual fabrication of a model. Strip samples were placed in an altitude chamber simulating 80,000 feet. Heat was applied to the exposed portion of the test specimen by electrical quartz lamps which were located 3/8 inch from the surface of the fabric. Thermocouples were placed through the fabric to record the temperature. See Figure 21 for temperature versus time curve.

The desired temperature versus time curve based on the expected maximum steady state equilibrium stagnation temperatures was determined. By manual regulation of a variac, the actual temperature was controlled to follow the desired curve. The altitude chamber and control apparatus are shown in Figures 48 and 49.

Two of the specimens which were tested are shown in Figure 50. The maximum temperatures encountered in the $W/C_DA = 10$ condition produced no harmful effects on the fabric. Several specimens, however, which were tested at temperatures over the maximum anticipated, deteriorated as shown in Figure 50. The over-temperature fabric specimen melted and charred, losing strength and foldability.

2. Tensile Tests

Following the final decision to use Dacron-neoprene for the high-speed recovery condition of $W/C_DA = 10$, additional tests were made to determine fabric and seam strengths at elevated temperatures. An ambient temperature of 350°F, based on the maximum temperatures expected in transient heating, was selected for the tests. An 800-pound capacity vertical Scott testing machine (Figure 51) was used to test strip-tensile strength 2-inch by 6-1/4-inch specimens. The jaws of the machine separate at the rate of 20 inches per minute following the start of the test, and the break tensile reading is recorded.

Tests were made at room temperature for both warp and fill of the fabric. Additional tests were made at 350°F; the results indicated that the tensile strength of the fabric at this temperature is equal to 60 percent of the room temperature value. For single-ply Dacron-neoprene this tensile strength at 350°F was equal to approximately 86 pounds/inch warp and 65 pounds/inch fill.

It was believed that these results were low considering the actual strength of the fabric when used in the model. This is because cylinder burst tests (strength tests using an actual inflated cylinder of the fabric being evaluated) indicate higher strengths than those from a simple strip-tensile test.

No equipment was available to make cylinder burst tests of the fabric at high temperatures; however, room temperature tests gave strengths of 199 pounds/inch warp and 175 pounds/inch fill. If the same ratio of strengths as was obtained in strip-tensile tests is assumed, cylinder burst values of 119 pounds/inch and 105 pounds/inch may be estimated for the 350°F condition.

Tensile tests of the fabric seam strength were made with an Instron Tensile Testing Instrument, using one- and two-inch lap seams. Two-inch wide specimens seamed over the two-inch width were clamped into the jaws of the machine. During the test these jaws moved at a rate of 1/10 inch per minute. Two readings of tensile strength for each type of seam are given in Table V.

One- and two-inch plain lap seams were tested. The following results were averaged over two series of tests as shown in Table V:

Figure 48. Instrumentation for Altitude Chamber and Control Apparatus
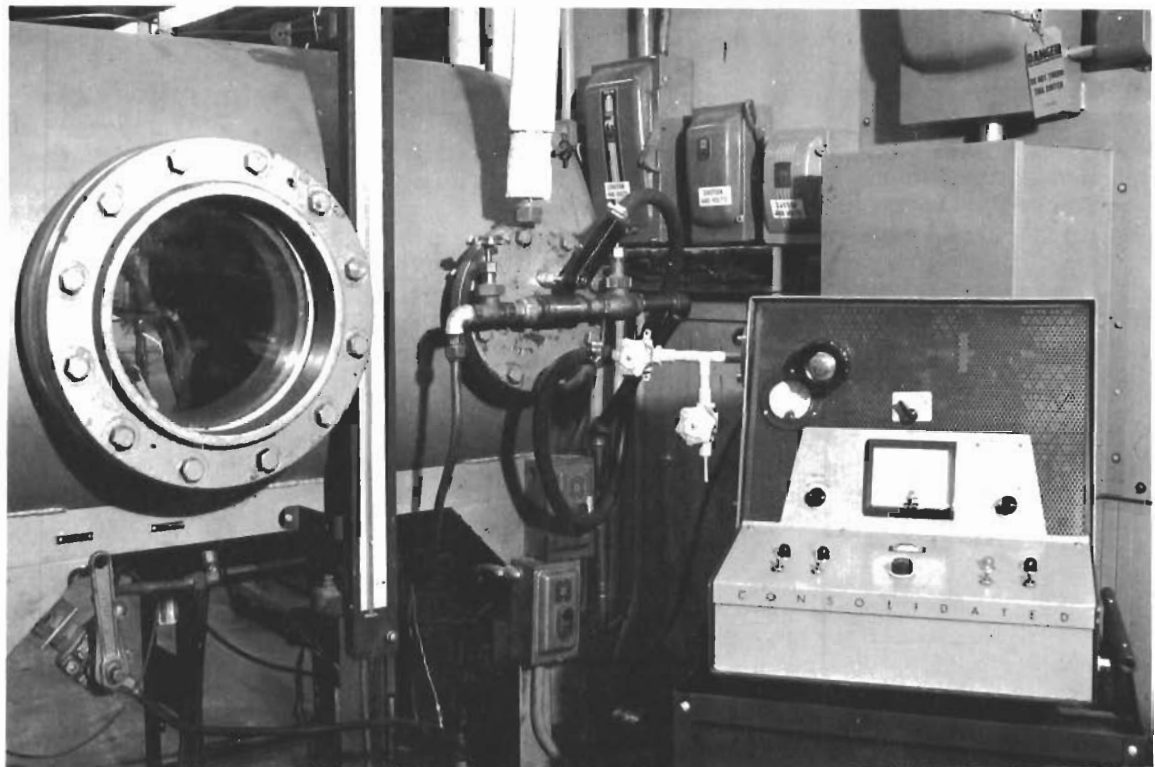
Figure 49. Altitude Chamber and Control Apparatus
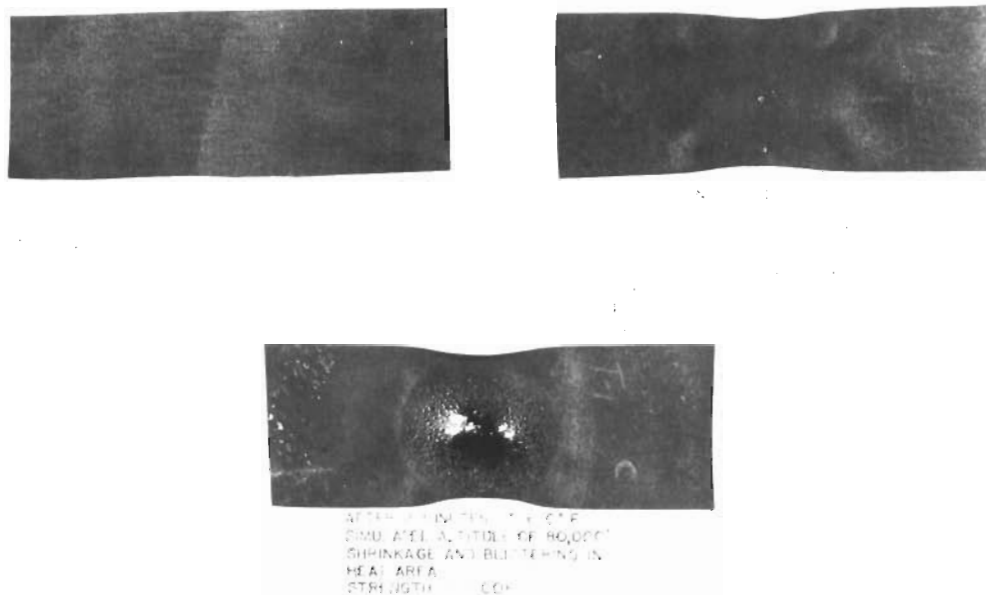
Figure 50. Dacron-Neoprene Temperature Altitude Test
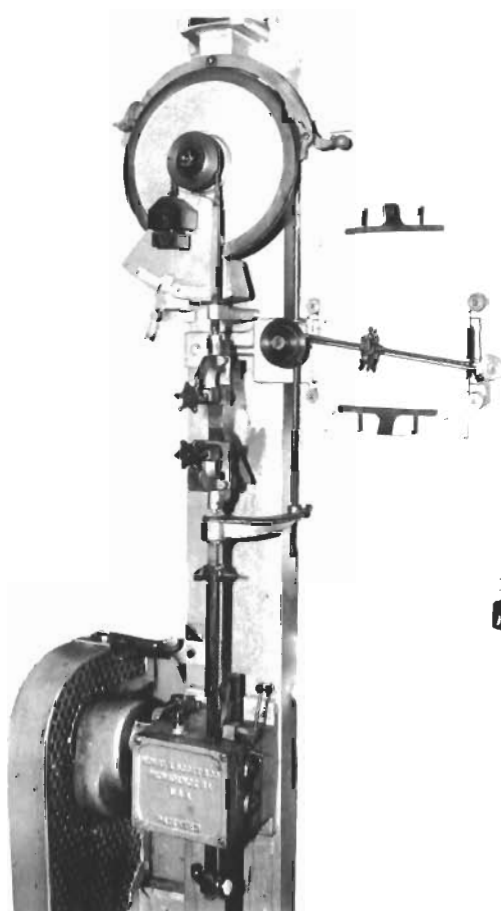
Figure 51. Vertical Scott Testing Machine

Table V. Seam Strength at 350°F

TYPE OF SEAM	TENSILE LOAD TWO MINUTES PRIOR TO BREAK (POUNDS/INCH)	BREAKING TENSILE STRENGTH (POUNDS/INCH)
1-inch lap seam	31	62
1-inch lap seam	40	53
2-inch lap seam	42	69
2-inch lap seam	45	69

The results of the one-inch seam tests appeared erratic; therefore, it was felt that one-inch seams would be undesirable. Based on the results of the two-inch lap seams tests, a design value of 55 pounds/inch was selected.

3. Gas Tightness Test

As helium or a similar gas is to be used in the actual full-scale drag device, it was necessary to determine the gas tightness of the fabric. The altitude chamber shown in Figures 48 and 49 was used for this test. The specimen used was a circular disc of fabric designed for clamping on the pressure vessel located inside the chamber (Figure 52).

During the test the chamber was evacuated to a simulated altitude of 80,000 feet. The quartz lamps heated the fabric to approximately 470°F for several minutes. (Maximum equilibrium stagnation temperature is 450°F.) The pressure vessel over which the sample was clamped was then pressurized with helium to several psig to simulate the actual pressure differential existing across the model at high altitudes.

The concentration of helium in the high-altitude chamber during the pressure-vessel testing was measured with a helium leak detector. The leak detector is actually a mass spectrometer. A gaseous analysis is accomplished by ionization, with an electron beam, of a small sample of gases taken from the high-altitude chamber.

The helium leakage rate was extremely small, amounting to 0.0001 cubic feet/square feet-minute for a temperature of approximately 470°F and a pressure differential of 2 psi. Therefore, the total leakage for the high-speed recovery trajectory will be negligible.

4. Emissivity Test

An emissivity value of 0.8 has been used for preliminary analysis of dacron-neoprene based on information supplied for dacron cloth alone. A test was carried out in the Goodyear Aircraft Fabric Laboratory to verify or disprove this assumed value.

The emissivity[1] was determined by comparing a three-inch diameter sample of the fabric with a standard which possessed a good approximation of black body characteristics. An oxidized iron plate (three inches in diameter) coated with camphor soot was used as this standard. According to data from the Instruction Manual of a Bolometer published by the Servo Corporation of America, a camphor-sooted surface possesses characteristics of radiation versus temperature very nearly equal to a black body source. For the purpose of comparison of emissivity data, it has been assumed that the camphor-sooted standard has an emissivity of 0.985 (versus 1.0 for a true black body) from 100 to 1500°F.

This test apparatus is shown in Figure 53. The procedure was as follows: In each instance, the sample was clamped over the heater element. A thermocouple was embedded with the last turn

---

[1] The ratio of the total radiating power of a non-black surface to that of a black surface at the same temperature.
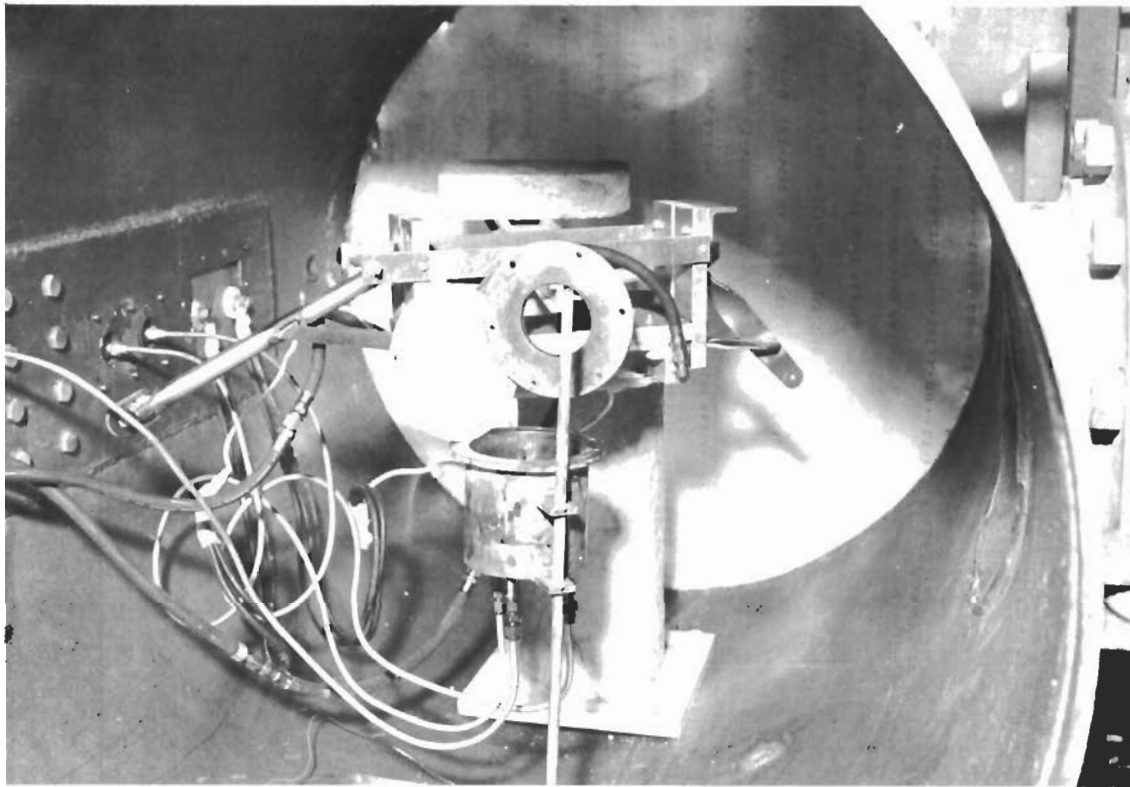
Figure 52. Gas Tightness Test Specimen
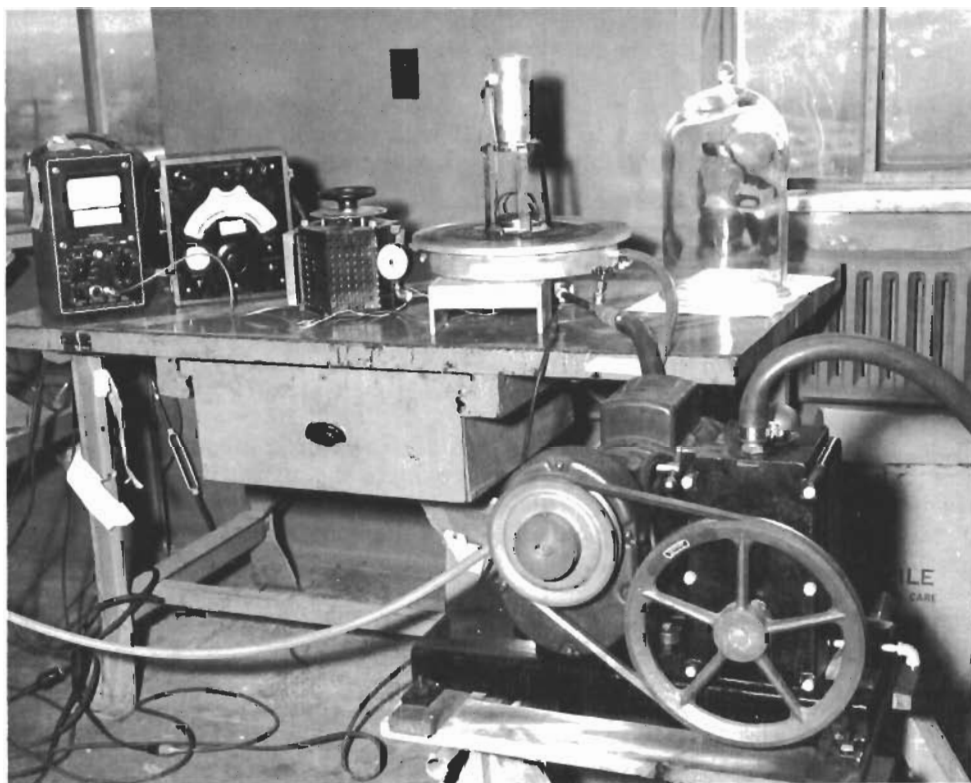
Figure 53. Apparatus for Measuring Total Emissivity of Solid Materials

of the couple at the outer surface of the sample. The thermopile was placed over the sample. The bell jar was placed over the assembly and the space was evacuated by means of high vacuum pump to about 0.75 inch Hg (equivalent to approximately 80,000 feet altitude). The sample was heated by means of electric power controlled by a Variac variable transformer. The temperature (T) of the sample's surface (facing the thermopile) was obtained by reading the output from the imbedded thermocouple on a millivoltmeter calibrated in degrees F. Relative radiation (E) in millivolts (output from the thermopile) was read on another millivoltmeter. For each temperature the corresponding radiation level was read and compared to the radiation level (also in millivolts) read for the standard (Es) at that temperature. Emissivity for a given sample at a given temperature (T) was determined according to Eq (30).

$$\epsilon = \left[\frac{E}{E_s} \quad x \quad \frac{1}{0.985} \right]_{T = K}$$ A curve of ϵ versus ^{O}F is shown in Figure 54.   (30)

From the results of the tests, it appears that the assumed emissivity value of 0.8 is rather high; however, there are several methods of raising the value for the Dacron-neoprene fabric. One such method would be to paint the surface of the model with a flat black paint; another would be to buff the neoprene coating slightly to dull its sheen. Buffing will not weaken the fabric unless the cloth itself is harmed.

B. WIND TUNNEL TESTING AND DROP TESTS AT GOODYEAR AIRCRAFT CORPORATION

The 15-inch spherical drag model was fabricated for tests in the Goodyear Aircraft subsonic horizontal wind tunnel in an attempt to investigate model deformations under varying air loads, a range of model inflation pressures, and two types of suspension systems. Several scale models were fabricated for testing. The first of these was a 15-inch diameter sphere. The 15-inch diameter was selected to achieve supercritical Reynolds numbers at maximum velocity in the Goodyear Aircraft Corporation wind tunnel where testing was planned. The sphere was constructed from two-ounce per square yard one-ply nylon ripstop coated with neoprene No. x A21A381. The sphere was made up of twelve gores bonded together with neoprene cement. Inflation was accomplished through a tire valve located at the apex of the gores on the leeward portion of the sphere.

The model was built so that two types of suspension systems could be used for connection with the payload. The model is shown in Figure 39 with a single line and in Figure 40 with eight lines running tangent from the model and intersecting slightly above the payload.

The model was found to be unstable when mounted in the tunnel, and such tests were impractical. This instability was apparently due largely to blockage in the 3-1/2 x 5-foot tunnel (on the order of 7 percent) and the turbulence characteristics of the tunnel itself (turbulence factor = 1.64). It was thus felt that drop tests should be made to obtain a more realistic picture of spherical drag body performance.

Drop tests were made inside the Goodyear Aircraft airship dock from a height of 190 feet. Six drops were made using three W/A values of 1.0, 2.0, and 10 with each of two suspension systems as shown in Figures 39 and 40. The load was attached approximately 3 feet from the model (5 to 6 diameters of payload). The average velocity of the model during the drop was determined with a stopwatch. The drift was actually measured. The oscillation was estimated by observation. An attempt was made to photograph the model toward the end of each drop to measure deformation with an inflation pressure of 1/2 psig, but this was not found to be feasible without complex instrumentation and lighting.

The results of the test are shown in Table VI.

During each of the tests the model system entered a conical spin, the magnitude of which appeared to lessen with an increase in velocity or Reynolds number. Of the two types of suspension systems tested, the single-line system appeared less stable. The velocities obtained in these tests
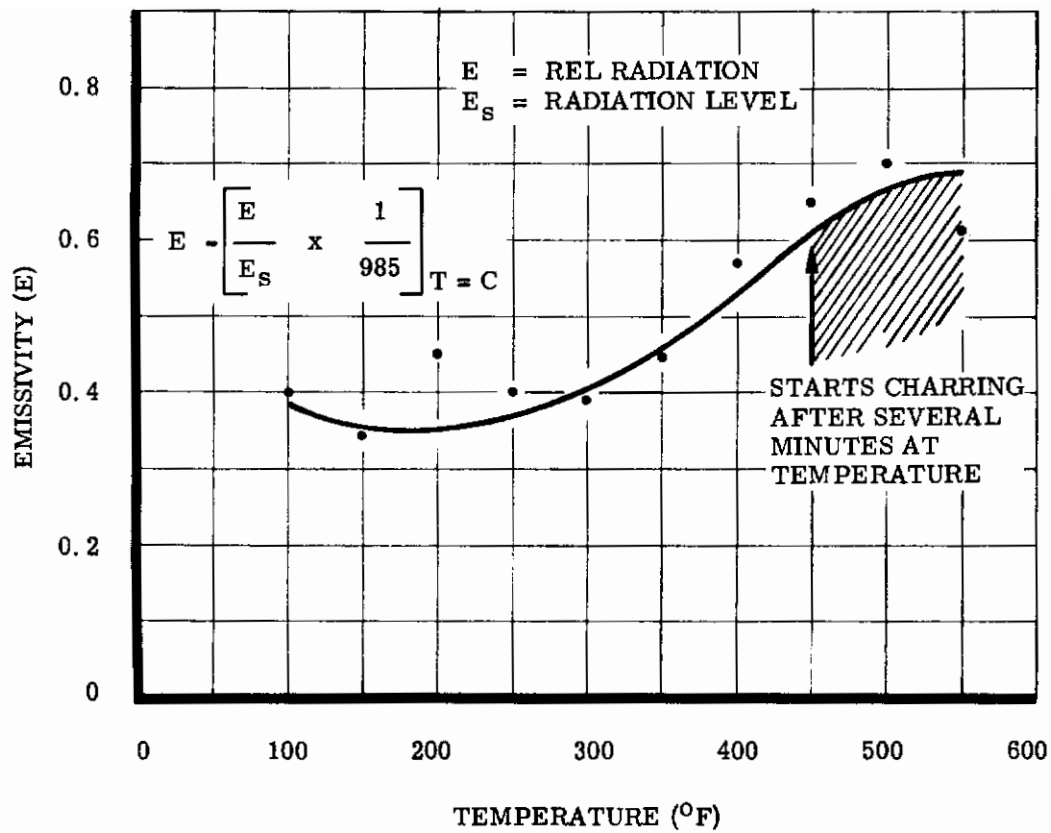
Figure 54. Emissivity versus Temperature (Dacron-Neoprene Fabric)

Table VI. Drop Test Data for 15-Inch Diameter Balloon

TEST NO.	TYPE OF SUSPENSION	PAYLOAD WEIGHT (LB)	W/A	TIME TO DESCENT (SEC)	AVERAGE VELOCITY (FPS)	DRIFT (FT)	PERFORMANCE
1	8 Lines	0.80	1.0	5.1	35.8	6.5	Immediately enters conical spin with load apparently at point. Cone angle = approximately 40 degrees.
2	8 Lines	2.00	2.0	4.2	43.5	4.1	Immediately enters spin as previously, but with higher angular velocity and a lower cone angle.
3	8 Lines	3.08	10	4.05	45.0	1.8	Immediately enters spin. Highest spin velocity and lowest cone angle (approximately 30 degrees) of 3 weights.
4	Single Line	0.80	1	5.1	35.8	1.7	Enters spin approximately 0.2 second after drop begins. Cone angle = approximately 120 degrees. Somewhat lower spin velocity than previously.
5	Single Line	2.00	2	4.2	43.5	3.0	Immediately enters spin. Cone angle = approximately 100 degrees.
6	Single Line	0.80	1	5.1	35.8	1.7	Enters spin approximately 0.2 second after drop begins. Cone angle = approximately 120 degrees. Somewhat lower spin velocity than previously.

were quite low, as were the Reynolds numbers (less than approximately 5×10^5); therefore, more instability was indicated in the system than would be obtained above the critical Reynolds number.

Because of the indications of instability at low velocities, it was felt that additional testing should be carried out to verify theoretical assumptions of stability for a spherical body at supercritical Reynolds numbers.

C. WIND TUNNEL TESTS AT WADC

Two inflatable models were fabricated for wind tunnel testing in the WADC 12-foot vertical wind tunnel. These models were built to 1/4-scale of the 8.69-foot diameter sphere recommended for the $W/C_DA = 10$ condition in the high-speed recovery. This size was selected in an effort to adequately surpass the critical Reynolds number $R_{n\ critical} = 3.85 \times 10^5$ for the body at high tunnel velocities.

The first of these models was a spherical drag shape (see Figure 55) which could be modified by the addition of two nose cones simulating covered inflation assemblies placed on the forward portion of the sphere. A removable tripper strip or fence was attached at a point 75 degrees from the nose. This model was also constructed from nylon-neoprene fabric in an attempt to scale the weight of the full-size model. This model has a diameter of 2.175 feet, weighs one pound, and is made up of 16 gores. It is inflated through a standard tire valve.

The second of these models (see Figure 56) was built in an effort to obtain some information on the stability of a streamlined shape with a 2:1 fineness ratio (diameter 2.2 feet, length 4.4 feet). This model was constructed in the same manner as described in the preceding paragraph. The model was built so that it might be mounted in the tunnel with either end facing the air flow. This was done in order to study the stability of both the teardrop and the inverted teardrop shapes.

Quarter-scale models of various drag bodies shown in Figure 57 were attached to 10- and 25-pound weights, and the system was tested in WADC's 12-foot vertical wind tunnel. The test section velocity was increased until the drag of the model supported the weight of the system. This steady state condition could be maintained effectively for periods of approximately 30 seconds. The resulting motions were recorded on film along with visual observations which are listed in Table VII.

Table VII. Vertical Wind Tunnel Data on 1/4-Scale Test Models

MODEL (see Figure 57)	TUNNEL VELOCITY, FPS	MOTION OF SYSTEM
A	75 to 100	oscillations, ± 10 degrees
B	75 to 100	oscillations, ± 5 degrees
C	75 to 100	oscillations, ± 5 to 10 degrees
D	75 to 100	(fast spin, 45 degrees, body axis
E	75 to 100	of symmetry horizontal
D with no fence	75 to 100	(same as above, fast 45-degree spin

The same general motion was observed when either of the weights was attached. However, the amplitude of the oscillating drag body decreased as the payload weight increased.

Results from the vertical wind tunnel test indicate that a nose cone sphere combination with a vortex generator or burble fence (ring around the body) (see Figure 20) is the most promising configuration model for a stable system in the speed range tested. A partially-filled spherical model may be used to simulate this configuration, since it would assume a similar pear shape upon descent.

The value of a fence for stabilization was demonstrated in the test, and future models should incorporate this technique. The fence positively trips the flow over a body from laminar to turbulent flow, stabilizing the body because of the resulting turbulent wake.

An increase in velocity decreased the amplitude of oscillations, indicating that at very high speeds the amplitude of oscillations should be very small. Because of this result and because the effect of deceleration could not be simulated in the vertical wind tunnel, more stability tests were run so that a final shape could be selected.

Figure 56. Quarter-Scale Test Model (Teardrop)

Figure 55. Quarter-Scale Test Model (Spherical)
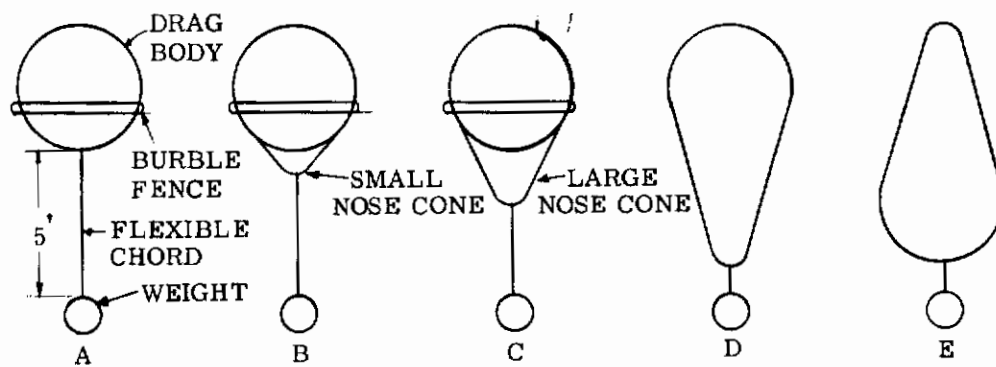
Figure 57. WADC Wind Tunnel Test Models
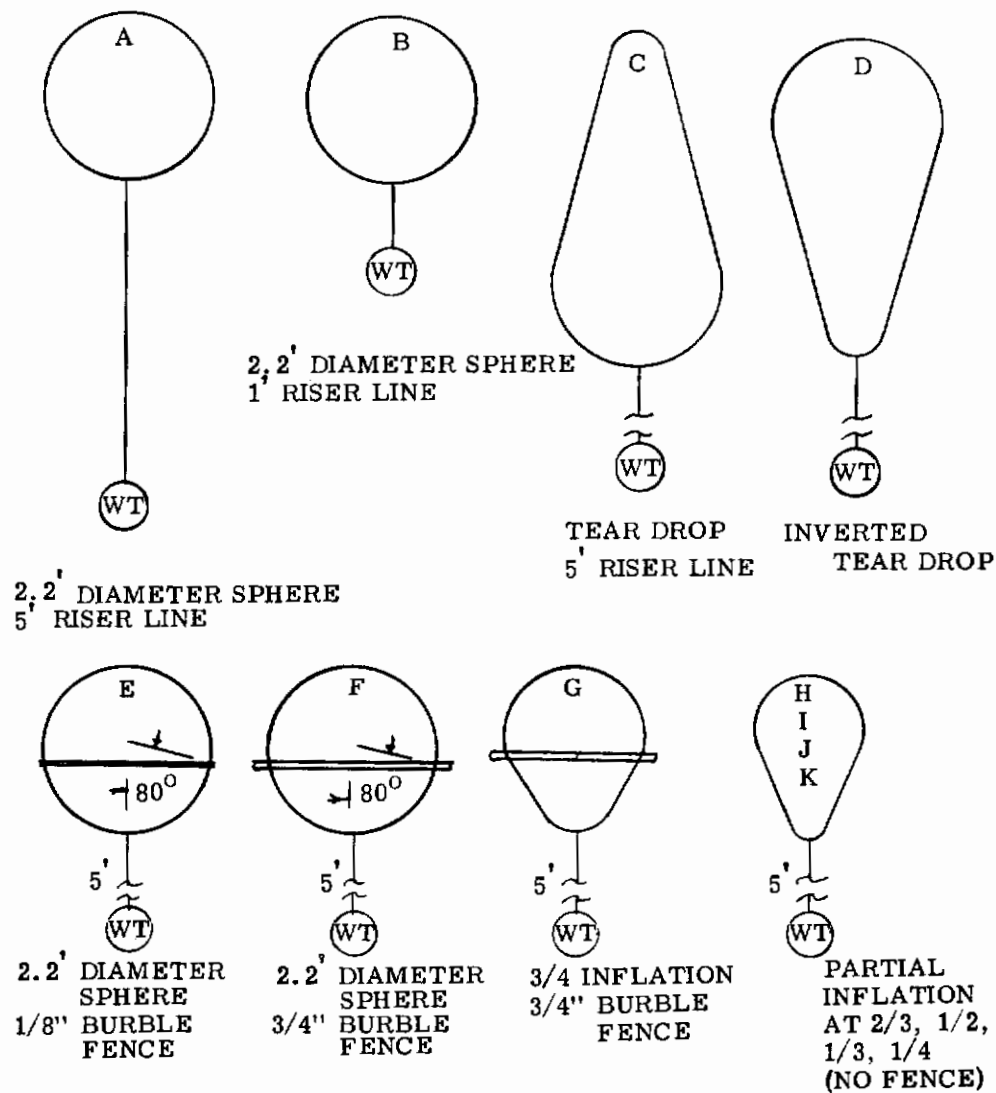
Figure 58. Quarter-Scale Models for Goodyear Aircraft Corporation Drop Tests

D. SCALE MODEL DROP TESTS AT GOODYEAR AIRCRAFT CORPORATION

Additional drop tests of 1/4-scale models were conducted from the 190-foot high Goodyear Aircraft Corporation air dock using 4.57-, 10-, and 25-pound payload weights (see Figure 58 for model configurations). The 4.57-pound payload established a W/C_DA ratio of 10 in the super-critical Reynolds number range. The Reynolds number attained was well into the supercritical range (above 3.85×10^5). The most promising configuration with respect to stability was the sphere equipped with a vortex generator or large burble fence (approximately 3 percent of sphere diameter). During repeated tests using the burble fence configuration, no coning or oscillations were noted, indicating that a vortex generator is required. Accordingly, repeated tests were conducted to determine the optimum location for the vortex generator. The results of these tests established the optimum location of 105° for the vortex generator or burble fence for maximum stability.

SECTION VI

WIND TUNNEL TESTS

A. NASA LANGLEY RESEARCH CENTER TESTS (AERODYNAMIC)

1. General

The primary objective of this phase of the test program was to determine the supersonic aerodynamic characteristics of a sphere located in the wake of various bodies, for in actual payload recovery the sphere would trail by means of a riser line in the payload's wake. The test model configurations consisted of various primary bodies (a payload) and a secondary drag body (a sphere).

Subsonic investigations have been performed by Goodyear Aircraft Corporation on tethered inflatable drag devices of various shapes. Pear-shaped and spherical models attached with different length riser lines to weighted payloads were employed in a vertical free flight tunnel and in drop tests at velocities below 300 feet per second. All of the configurations proved unstable at Reynolds numbers greater than the critical Reynolds number. It was found that the addition of a flow separation fence or vortex generator in the shape of a torus just aft of the maximum diameter of the sphere resulted in excellent pitch and roll stability characteristics. The addition of the separation fence also increased the drag of the sphere. The aerodynamic influence of the separation fence on spheres at supersonic speeds was also an objective of this study program.

2. Wind Tunnel and Auxiliary Equipment

The NASA Langley Research Center 4-foot x 4-foot Unitary Wind Tunnel is a continuous-operation, closed-circuit type in which the pressure, temperature and humidity of the enclosed air can be regulated. The Mach number can be increased from 1.5 to 2.0 without stopping the air flow. In order to increase the Mach number from 2.0 to 2.5 the tunnel air flow must be stopped in order to change compressor modes. See Reference 7 for a general description.

A spark Schlieren system was employed for qualitative flow observations.

The pressure distribution data were obtained with electrical transducers. Force measurements were obtained with a standard six-component strain gage balance. All of the drag coefficients reported herein include the incremental drag value which was obtained from the product of the base pressure and the cross sectional area of the sting support. Brown recorders were used to record the recovery temperature distribution data.

Calibration and operation of the equipment along with collection and reduction of data were performed by NASA personnel.

3. Tunnel Test Conditions

The desired Reynolds number, with the diameter of the 8-inch sphere for the reference length, was obtained with the following tunnel pressures and temperatures.

MACH NUMBER	TOTAL PRESSURE	TOTAL TEMPERATURE
1.5	523 psf	125°F
2.0	506 psf	125°F
2.5	433 psf	150°F

4. Test Model Instrumentation

Pressure orifices were placed on the solid and inflatable sphere of test model configurations 1 through 5 (Figure 59) as follows:

DETAIL OF VARIABLE LENGTH ACTUATOR ROD

Threaded to Receive Primary Body

0.875" Dia   0.750" Dia

Spherical Secondary Body

Retracted
Expanded

10"

0.750" Dia   0.625" Dia   0.490" Dia

Spherical Secondary Body

Threaded to Receive Primary Body

10"   8"   6"

Flow →

1. Solid Fabric-Covered Sphere

θ

8"

Flat Faced 1/4" Dia Knurled Spike

Flow →

105°

8" or 24"   8"

2. Solid Fabric Covered Sphere With Spike Lengths of 8" and 24" With and Without Separation Fence

Separation Fence - 7.719" Inside Dia Torus 0.250" Dia Thick

PRIMARY BODIES

Variable Length Actuator Rod

θ = 105°

3. Solid Fabric Covered Sphere with Separation Fence and Variable Length Actuator Rod Which Supports the Various Primary Bodies

A. Disc

2.81" Dia

10" or 24"   8"

Base of Primary Body

B. Sphere

2.81" Dia

Flow →

8" Dia

0.55"

4. Inflatable Sphere With Separation Fence

12 Meridian Cables 1/32" Dia Placed 30° Apart and Covered With 1/2" Strips of Fabric

C. Symmetrical Man Capsule

1.405" R   15° Flared Skirt

3.37" Dia

0.935"
2.350"
3.750"

NOTE:

Primary Body "C" - Scale NAA Life Support Capsule
Primary Body "D" - Scale GAC Escape Capsule

Symmetrical Man Capsule

0.75" Dia

Flow →

10"   8"

5. Inflatable Sphere With Separation Fence (same as 4 above) and Actuator Rod With Symmetrical Man Capsule

D. Unsymmetrical Man Capsule

77°   1.84"
1.72"
2.96" R   2.91" R   1.66"
3.00" R
3.70"
3.14"
1.83"
0.79"
3.06" R
2.14" Radial Tangent Line

Wall to Wall Support Strut "V" Planform

Unsymmetrical Man Capsule

1/16" Dia Cable 0 to 5' Long

Cable Length Controlled From Outside of Tunnel

8" Dia Inflatable Spherical Balloon

6. Tethered Inflatable Spherical Fabric Balloon With Separation Fence and Unsymmetrical Man Capsule
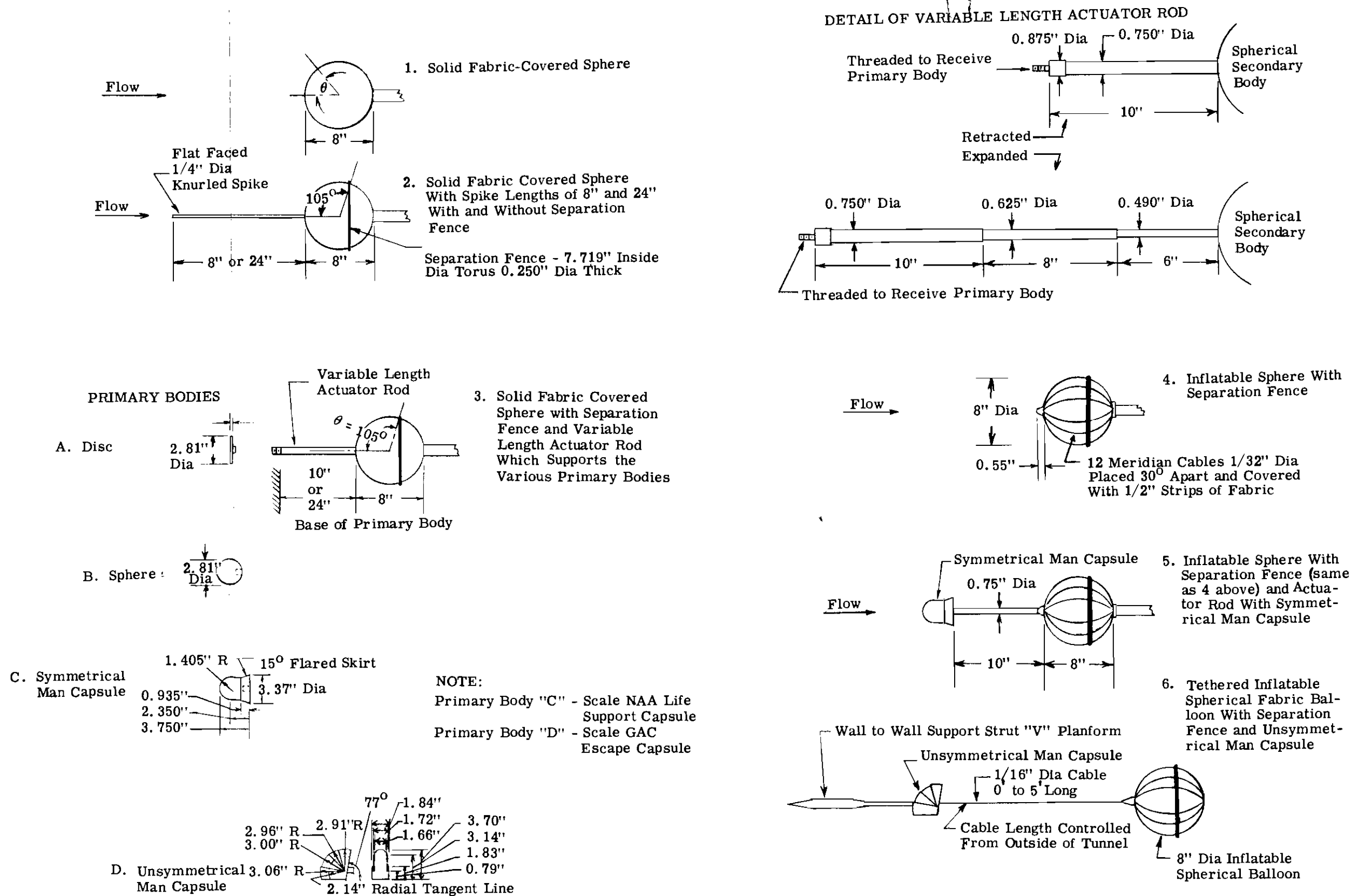
Figure 59. Test Model Configurations

72

WADD TR 60-182

(1) Along the right side in a yaw plane at 10-degree increments from $\theta = 10$ degrees to 160 degrees inclusive.

(2) Along the bottom in a pitch plane at 10-degree increments from $\theta = 10$ degrees to 160 degrees, 65 degrees to 115 degrees, and 120 degrees to 160 degrees inclusive.

Thermocouple heat sinks were placed on the solid sphere of test model configurations 1 through 3 as follows:

(1) Along the left side in a yaw plane at 10-degree increments from $\theta = 10$ degrees to 160 degrees inclusive.

(2) Along the top in a pitch plane at 10-degree increments from $\theta = 10$ degrees to 60 degrees, 65 degrees to 115 degrees, and 120 degrees to 160 degrees inclusive.

A detail drawing of a typical pressure orifice and thermocouple heat sink are shown in Figure 60.

COUNTERSUNK FLATHEAD BOLT
BOLT SLOT POTTED
0.050" DIA HOLE

FABRIC COVERING
ALUMINUM
SPHERE

1/8" x 1/4" 2 MIL PLATINUM HEAT SINK SPOT WELDED TO THE IC THERMOCOUPLE

TEMFLEX 105 No. 17 TUBING

SILASTIC PLUG

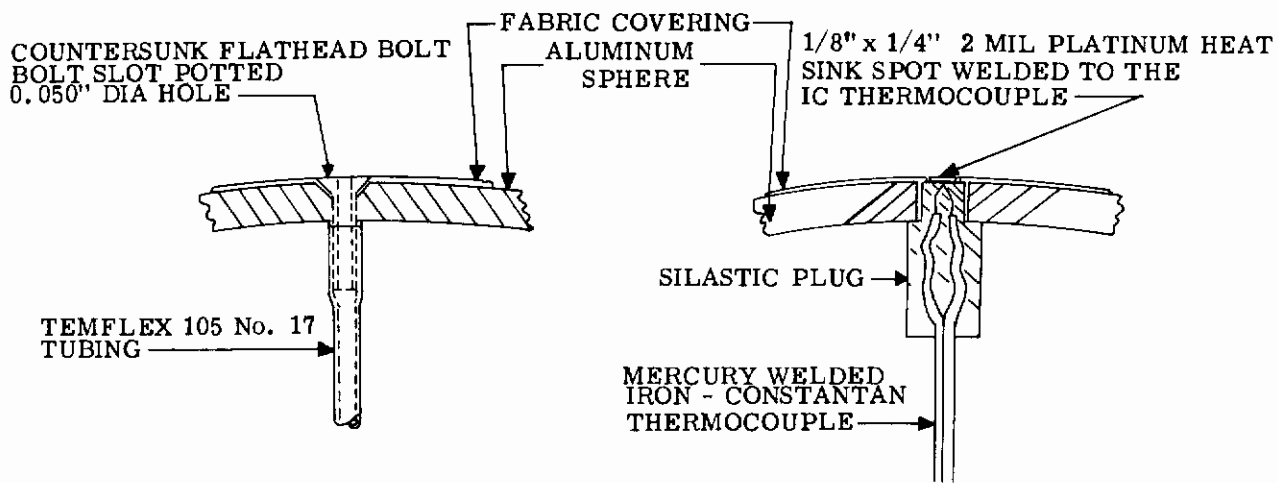MERCURY WELDED IRON - CONSTANTAN THERMOCOUPLE

Figure 60. Pressure Orifice and Thermocouple Detail

5. Test Models

The wind tunnel test models are shown as various configurations in Figure 59.

a. Configuration 1. The solid fabric-covered sphere was constructed of 1/8-inch spun aluminum and covered with sixteen gores of Dacron-neoprene fabric. This model was used to corroborate basic supersonic sphere data. The fabric-covered sphere is shown in the wind tunnel in Figures 61 and 62.

b. Configuration 2. This is the same solid sphere as noted in configuration 1 with additional components of a separation fence and 8-inch and 24-inch spikes. The separation fence was constructed from a 1/4-inch diameter steel rod (3 percent of the sphere diameter) in the form of a torus and was attached to the sphere at $\theta = 105$ degrees. The spikes were constructed from 1/4-inch diameter steel rods which were knurled to simulate a wire strand cable. The front tip of the spikes was flat-faced.

c. Configuration 3. This is the same solid sphere as noted in configuration 1 with the additional components of a separation fence (same as in configuration 2), four primary bodies (payloads), and a variable length actuator rod (to simulate a riser line). The four primary bodies, which were constructed of aluminum, were held in front of the sphere by the variable length actuator rod.

Figure 61. Tunnel Installation of Test Model
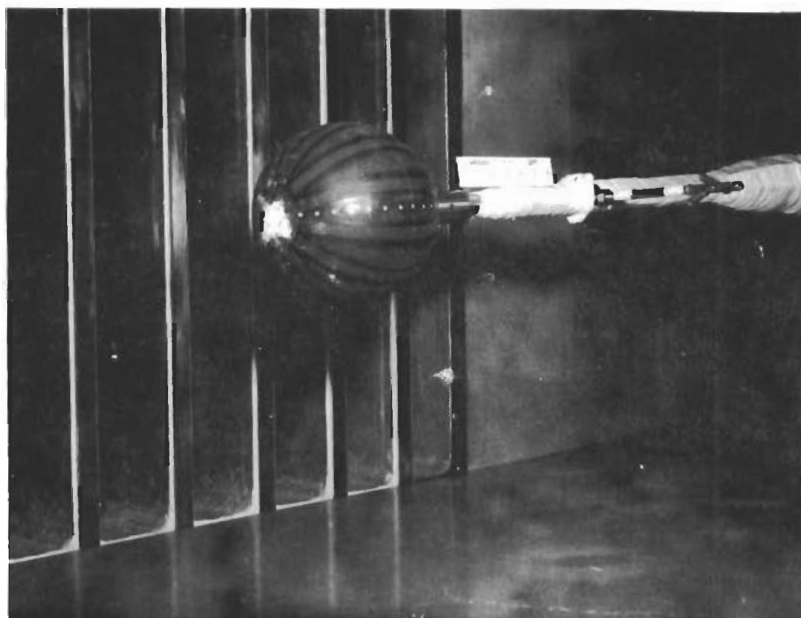Configuration 1 (Upstream View)

Figure 62. Tunnel Installation of Test Model
Configuration 1 (Downstream View)

The length of actuator rod which was used to vary the distance between the primary body and the secondary, spherical body was changed during tunnel shut-down. When the actuator rod was retracted, the distance between the two bodies was 10 inches; when the rod was fully extended, the distance was 24 inches.

Each of the primary bodies was tested at the two actuator rod lengths of 10 and 24 inches. The separation fence was at θ = 105 degrees for all tests. The test model configurations without the separation fence are shown in Figures 63 through 66.

d. Configuration 4. This model consisted of an inflated sphere rigged with a separation fence at θ = 105 degrees. The separation fence was constructed from a 0.25-inch diameter rubber tube. The internal pressure of the sphere was varied during the test in order to determine the minimum differential pressure required to prevent significant deformation and flutter. This inflated sphere had a steel shaft extending from the rear sting mount to the front of the sphere. Twelve meridian cables were attached to rings at both ends of the shaft. The meridian cables were attached to the sphere at 30 degree increments by means of 1/2-inch strips of fabric cemented to the inflated sphere.

e. Configuration 5. This is the same inflated sphere as noted in configuration 4 with the additional components of a variable length actuator rod and a symmetrical man capsule. These components are the same as were discussed under configuration 3. This inflated sphere with the unsymmetrical man capsule is shown in Figure 67.

f. Configuration 6. This consisted of an inflatable fabric sphere which was tethered by a riser line behind the unsymmetrical capsule. The capsule was attached by means of a cylindrical shaft to a "V" planform, wall-to-wall support strut. The inflated sphere was constructed of sixteen gores of Dacron-neoprene fabric. A 0.25-inch diameter rubber tube separation fence was attached at θ = 105 degrees. There were 12 meridian cables of 1/32-inch diameter stranded cable placed 30 degrees apart. These cables were held in place by means of 1/2-inch strips of fabric cemented to the model.

The model was attached to a 15-foot cable that terminated into the unsymmetrical man capsule, through the cylindrical shaft, and through the support strut to the outside of the tunnel. In this manner the riser line length could be varied during the tests to observe the aerodynamic behavior of the model at different distances behind the capsule. The internal pressure of the model was varied by pulling the model up to the capsule where it came in contact with an inflation valve. The capsule and model are shown in Figures 68 and 69. The method in which the capsule was attached to the wall-to-wall strut is shown in Figure 70 with the cable to which the model was attached hanging from the back of the capsule.

The test models of configurations 1 through 5 were mounted on a sting which had a 1-5/8-inch diameter at the base of the instrumentated spherical body. A typical setup from upstream of the test section is shown in Figure 71.

The surface roughness of the test model components were:

Fabric	125 microinches
Spikes	15,000 microinches
Primary Bodies	65 microinches
Actuator Rod	65 microinches

6. Discussion of Results

a. Spheres. The measured drag coefficients for the solid, fabric-covered sphere (test configuration 1) are shown in Figure 72 over a Reynolds number range of 3.6×10^5 to 10^6. Several additional tests were performed to determine the drag coefficient behavior from Mach 1.47 to 2.16.

The reported drag coefficients at Mach 1.5 and 2.5 are not in agreement with other reported values as contained in Reference 8. The indicated pressure coefficient distribution data, which were

Figure 63. Test Model Configuration 3 with Unsymmetrical Man Capsule at $L_R/D = 1.25$ (Separation Fence is not Shown)
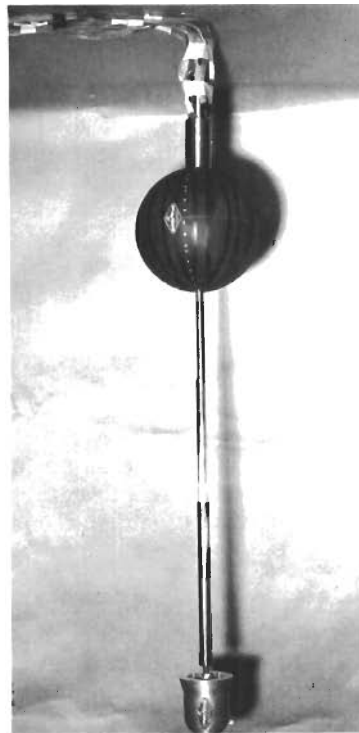

Figure 64. Test Model Configuration 3 with Unsymmetrical Man Capsule at $L_R/D = 3.0$ (Separation Fence is not Shown)
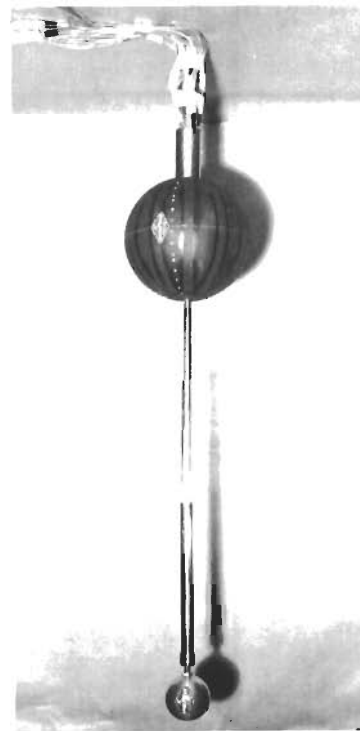

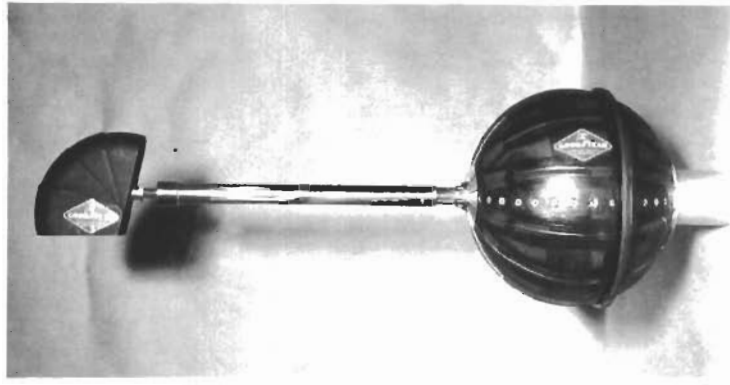Figure 65. Test Model Configuration 3 with Spherical Primary Body at $L_R/D = 3.0$ (Separation Fence is not Shown)

Figure 66. Test Model Configuration 3 with Symmetrical Man Capsule at $L_R/D = 3.0$ (Separation Fence is not Shown)

WADD TR 60-182

76

Figure 67. Test Model Configuration 5 with
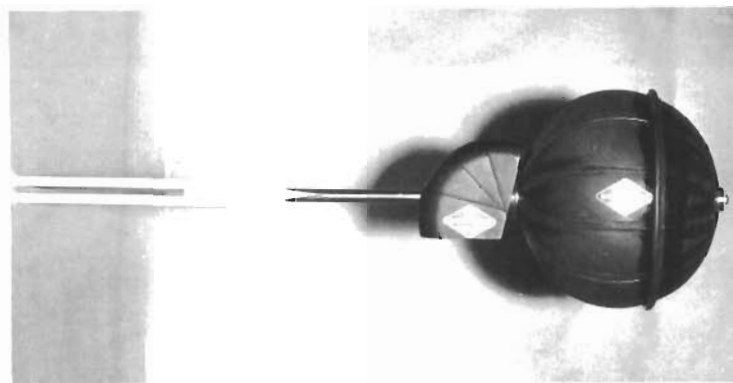Unsymmetrical Man Capsule
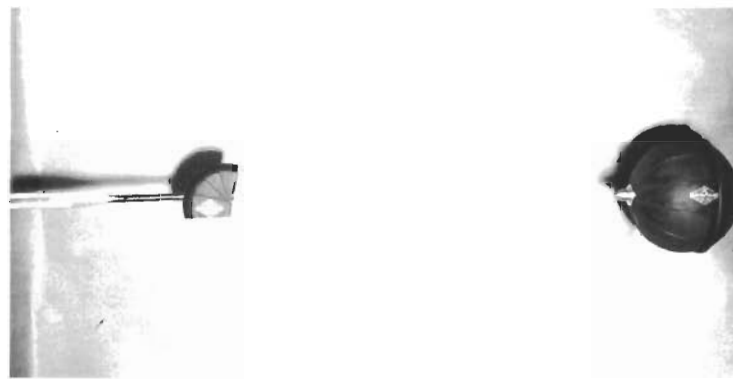

Figure 68. Test Model Configuration 6

Figure 69. Test Model Configuration 6 Showing
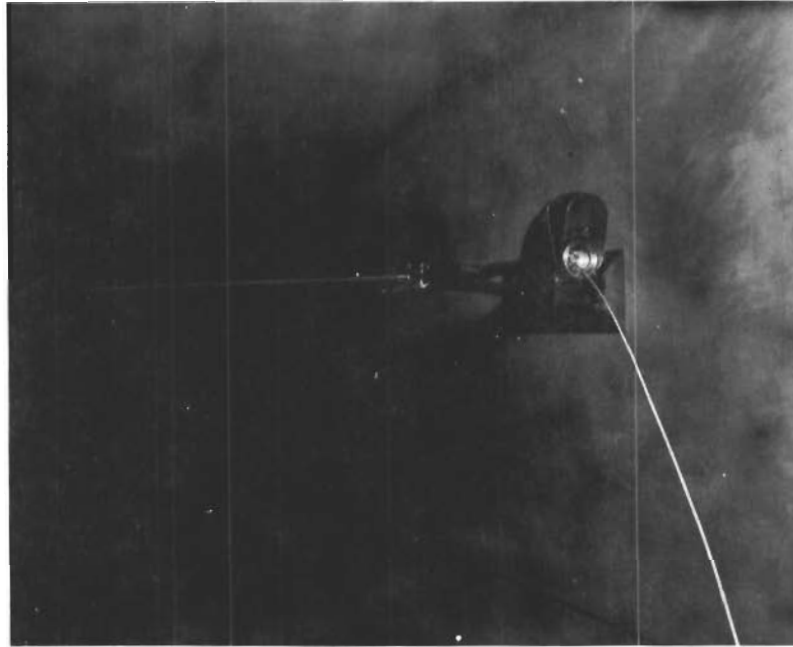Extended Riser Line

Figure 70. Tunnel Wall to Wall Strut Installation of Test Model
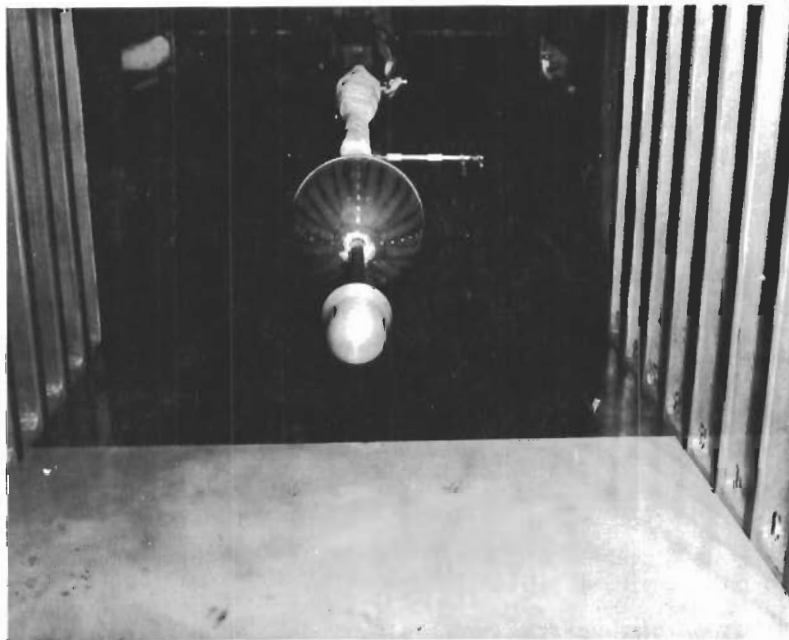Configuration 6 for Tethered Balloon Tests

Figure 71. Tunnel Installation of Test Model Configuration 3
with Symmetrical Man Capsule

obtained during the test program and presented in Figure 73, were used as a further check on the low measured drag coefficients presented in Figure 72. Excluding a frictional drag component, the area enclosed by the plotted curve of $C_p \sin^2 \theta$ versus β represents the pressure drag coefficient of the sphere, for

$$(C_D)_p = \int_0^\pi C_p \sin 2\theta \, d\theta$$

where,

$$(C_D)_p = C_D - (C_D)_f.$$

The pressure drag coefficients are compared with the measured drag coefficients.

M	C_D	$(C_D)_p$
1.5	0.826	0.864
2.0	0.956	0.966
2.5	0.785	0.792

The pressure coefficient data which was in error by ± 0.033 resulted in an error of approximately ± 10 percent for the pressure drag coefficients which were obtained by integrating the pressure coefficient distributions. The difference between the measured and pressure drag coefficients is within the accuracy of the data.

The measured drag coefficients compare favorably with the pressure drag coefficients since the skin friction drag of blunt bodies is small when compared to the total drag (see Reference 9).

It has been concluded with NASA verification that the magnitude of the measured drag coefficients is correct, and further tests are required to determine if the low drag coefficients at Mach 1.5 and 2.5 are caused by the fabric covering on the sphere.

The pressure coefficient distributions shown in Figure 73 for the solid, fabric-covered sphere are not consistent with other investigators' results (References 10 through 17). Of course, this is reflected in the measured drag results; but, it is most alarming to find the difference as large as 30 percent at Mach 2.5 when the distribution is less than that at Mach 1.5 and 2.0.

It has been generally concluded from the results of many tests that the pressure coefficient increases with increasing Mach number. A modified Newtonian theory can be used to predict with reasonable accuracy the pressure coefficient trend on a hemisphere. The Newtonian theory for the pressure coefficient distribution on a hemisphere is $C_p = 2.0 \cos^2 \theta$. The value of 2.0 which is applicable at Mach numbers approaching infinity is modified in the following manner:

$$C_p = C_{p_{max}} \cos^2 \theta$$

where

$$C_{p_{max}}$$

is the stagnation pressure coefficient across a normal shock wave at the free stream Mach number. This theory which has been verified by a multitude of data indicates that the pressure coefficient increases with increasing Mach number. A plot of the modified Newtonian theory for Mach 1.5, 2.0, and 2.5 is presented in Figure 73 for comparison.

The suspected cause of the low pressure coefficients at Mach 2.5 is the fabric cover on the sphere and the low Reynolds number of the tests. The data presented in References 12 and 14 tend to support, but not conclusively, the data presented herein.

In Reference 12 the pressure distribution about a sphere is given for Mach 4.95 and Reynolds numbers of 3.2×10^6, 8.0×10^6, and 13.0×10^6. Although the stagnation pressure coefficient is the same at all three Reynolds numbers, the pressure coefficient distribution about the sphere decreases when the Reynolds number is decreased from 8.0×10^6 to 3.2×10^6. This decrease is within the accuracy of the pressure measurements. In Reference 14 the stagnation pressure coefficient at Mach 2.48 is higher than at Mach 2.67, but the difference between these stagnation pressure coefficients is small and could lie within the error of the data. It is also shown that, at a peripheral distance from the stagnation point, the pressure coefficients at Mach 2.15 are lower than at Mach 1.86.

Further testing will be required to determine conclusively whether the cause of the low drag and pressure coefficients should be attributed to the fabric covering on the sphere or to a low Reynolds number.

b. Spiked Spheres. The drag coefficients of spiked spheres, test model configuration 2, are shown in Figures 74, 75, and 76. The separation fence influences the resultant drag coefficient. As expected, the spike length of $L_R/D = 3.0$ reduces the drag of the sphere by a lesser amount than the spike length of $L_R/D = 1.0$. The effect of various spike diameters on the drag reduction was not investigated, but from Reference 18 it can be concluded that a thicker spike would have resulted in greater drag reductions.

The effect of angle of attack on the drag coefficient of a spiked sphere is shown in Figure 75, and the effect of spike length is shown in Figure 76. The drag coefficient change for $L_R/D = 1.85$ was determined from Reference 19, and is due to flow reattachment on the spike.

Random flow attachment on the spike was observed for the spiked sphere with $L_R/D = 1.0$ at Mach 1.50. The flow separated off the flat face of the 8-inch spike leaving a conical turbulent wake which was slightly greater than the conical shaped wake imposed by the spike tip and sphere. At random, the flow would become attached to the spike approximately 1/2 inch from the tip of the spike. Flow separation then occurred along the spike leaving a conical turbulent wake. This attached flow would last for as long as five seconds and then collapse to the original flow separation off the face of the spike. The measured drag coefficient of 0.765 was observed for the condition of flow separation off the face of the spike. For the flow condition where separation occurred along the spike, it was estimated that the drag coefficient was 0.61. This type of flow oscillation was also observed in References 19 and 20.

The pressure coefficient distributions on the spiked sphere are shown in Figures 77 through 86. It is not known if the random flow attachment influenced the pressure distribution at Mach 1.5 for the spiked sphere where $L_R/D = 1.0$. Without a burble or separation fence, it can be seen that the base pressure coefficient decreases with increasing Mach number. The addition of the separation fence results in a nearly constant base pressure for the Mach numbers of 1.5, 2.0, and 2.5. The high pressure coefficients which occur at angles of attack can be explained by the theory of Ostwatitsch in Reference 21 which is applied to supersonic diffusers where the pressure recovery is greater through a series of oblique shock waves than through a single normal shock wave. This phenomena was also observed for spiked hemispheres in Reference 22.

The pressure coefficient distributions are not presented for various angles of attack at Mach 1.5, for shock waves were reflected off the tunnel walls onto the sphere at this low Mach number. The pressure distribution for angles of attack of 2 degrees and 5 degrees were not obtained.

c. Spheres in the Wake of Various Bodies. The total drag of the various primary and secondary spherical bodies, test configuration 3, was measured. The drag of the secondary, spherical body is of more interest than the total drag, and is presented in coefficient form in Figure 87. The drag coefficients for three of the four primary bodies were known and it was only a matter of subtracting the drag of the primary body from the total measured drag in order to obtain the drag of the secondary, spherical body. The drag coefficients which were used for the primary bodies based on their own reference area were:

M	DISC C_D	SPHERE C_D	UNSYMMETRICAL CAPSULE C_D	SYMMETRICAL CAPSULE C_D
1.5	1.61	1.01	1.065	Unknown
2.0	1.63	0.96	1.085	Unknown
2.5	1.65	0.94	1.050	Unknown

The reference areas of the various primary bodies were:

Disc	6.2 In.^{2}
Sphere	6.2 In.^{2}
Unsymmetrical Capsule	6.05 In.^{2}

The preceding drag coefficients (when based on the reference area of the 8-inch diameter sphere) reduced to:

M	DISC C_D	SPHERE C_D	UNSYMMETRICAL CAPSULE C_D
1.5	0.199	0.129	0.1287
2.0	0.201	0.131	0.1311
2.5	0.204	0.127	0.1267

The total drag coefficient of the primary body and secondary body is shown in Figure 88.

The pressure coefficient distributions on the secondary, spherical body are presented in Figures 89 through 98 for the various body combinations. The influence of the variable length actuator rod, which simulated a riser line, on these distributions is not known. It should be noted that at Mach 2.5 and with L_R/D = 1.25, negative coefficients occur on the forward part of the sphere. Negative pressure coefficients were also observed in Reference 23 on the flat face of a cylinder in the wake of cones. In Figures 89 through 98 there occasionally occurs a large difference between the two plotted data points at a given peripheral location. This was due to tunnel flow inclinations that resulted in small angles of attack. The pressure distribution along the side of the sphere should be the same as along the bottom of the sphere when the symmetrical primary bodies are employed for zero angle of attack.

The pressure coefficient distributions for the fabric-covered sphere in the wake of the unsymmetrical man capsule at L_R/D = 0 and M = 1.5 are not presented, for shock waves were reflected off the tunnel walls onto the sphere at this low Mach number. Also, the validity of the data at Mach 1.5 where the primary body was at L_R/D = 3.0 ahead of the secondary, spherical body is questionable; for, from Schlieren analysis, the bow shock wave from the primary body was reflected off the wind tunnel floor and intersected with the bow shock from the secondary, spherical body.

d. Inflated Sphere. The drag coefficients of the inflated sphere, test model configuration 4, are shown in Figure 99 for different inflation pressures. A drag coefficient curve for the solid, fabric-covered sphere, test model configuration 1, is also presented for comparison. It should be noted that
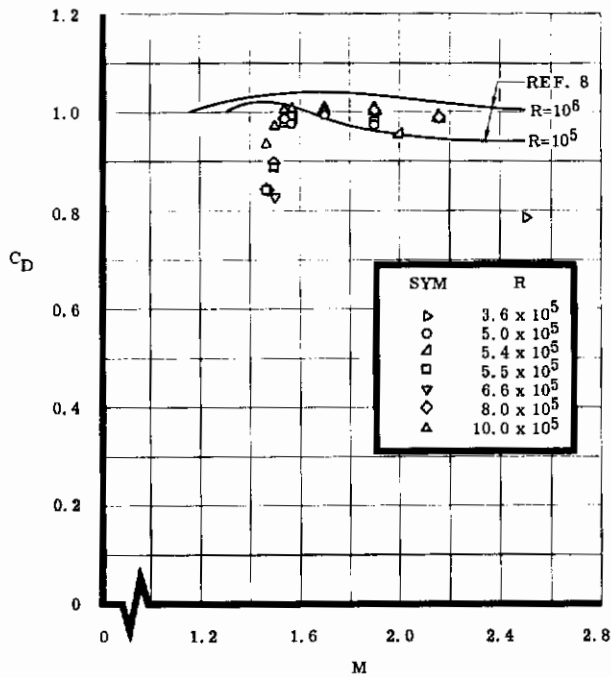
Figure 72. Drag Coefficient versus Mach
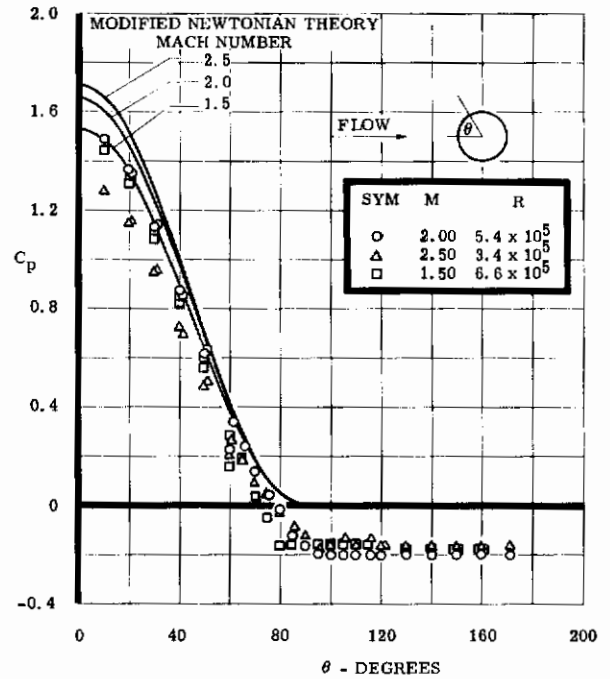Number for a Fabric-Covered Sphere

Figure 73. Pressure Coefficient Distribution on
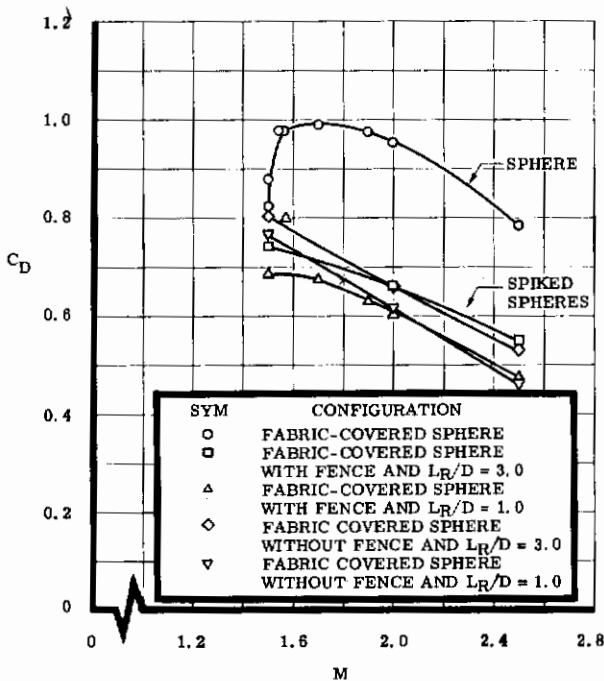the Fabric-Covered Sphere

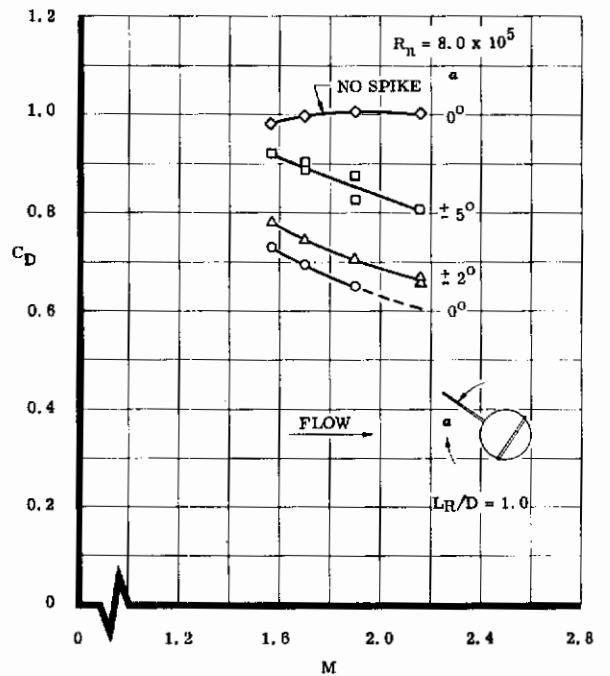Figure 74. Drag Coefficient versus Mach
Number of Spiked Spheres

Figure 75. Drag Coefficient versus Mach
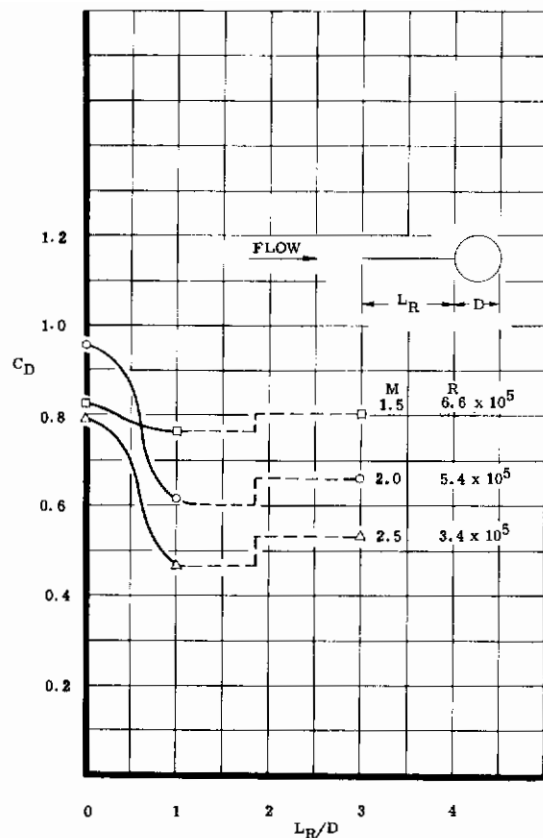Number of a Spiked Sphere
at Angles of Attack

Figure 76. Drag Coefficient versus Spike
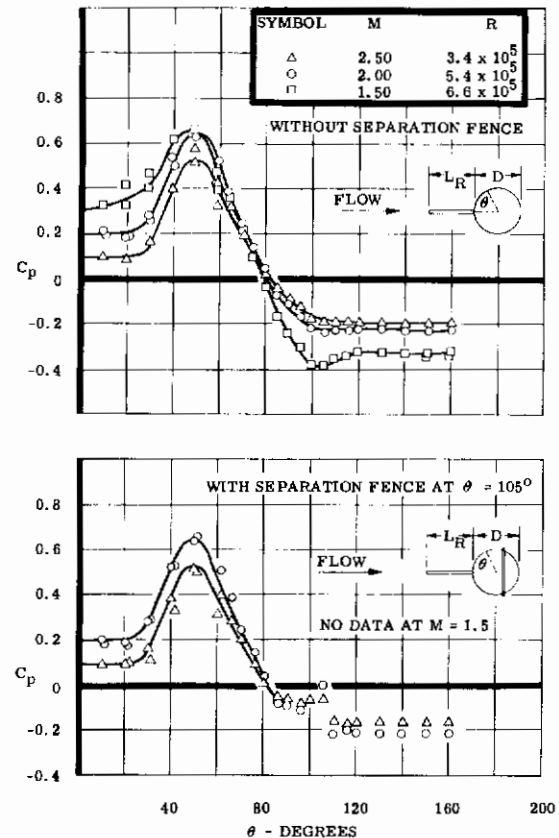Parameter of Spiked Spheres

Figure 77. Pressure Coefficient Distribution
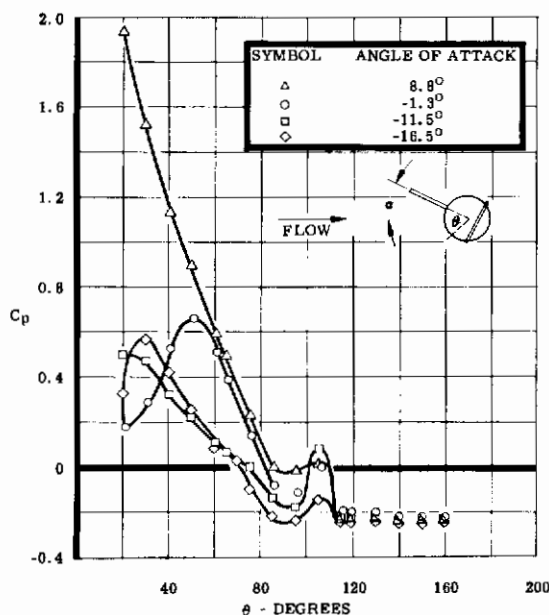on the Spiked Fabric-Covered Spheres,
$L_R/D = 1.0, a = 0^O$

Figure 78. Pressure Coefficient Distribution
in a Pitch Plane on the Spiked Fabric-
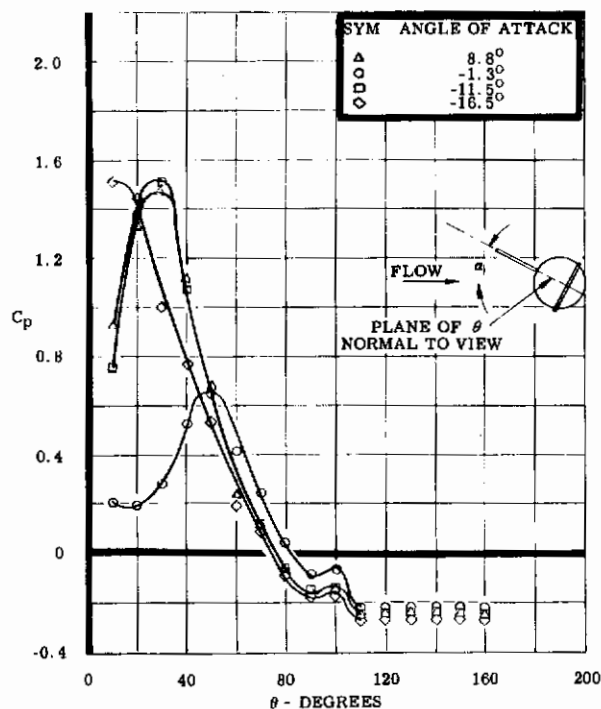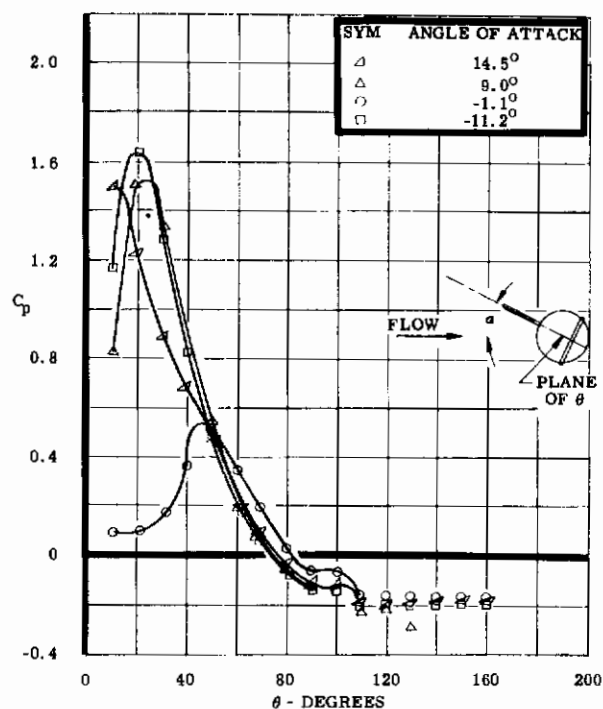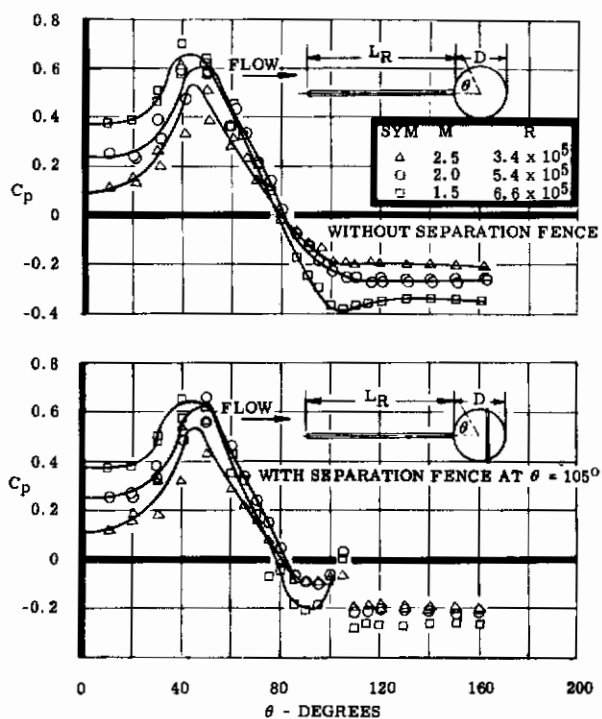Covered Sphere for Various Angles of
Attack, $L_R/D = 1.0, M = 2.00$
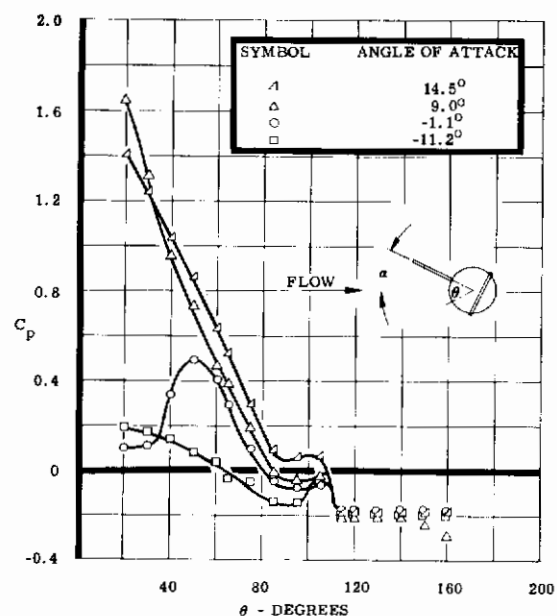
Figure 79. Pressure Coefficient Distribution
in a Pitch Plane on the Spiked Fabric-
Covered Sphere for Various Angles of
Attack, $L_R/D = 1.0, M = 2.50$

Figure 80. Pressure Coefficient Distribution in a Yaw Plane on the Spiked Fabric-Covered Sphere for Various Angles of Attack, $L_R/D = 1.0$, M = 2.00

Figure 81. Pressure Coefficient Distribution in a Yaw Plane on the Spiked Fabric-Covered Sphere for Various Angles of Attack, $L_R/D = 1.0$, M = 2.50

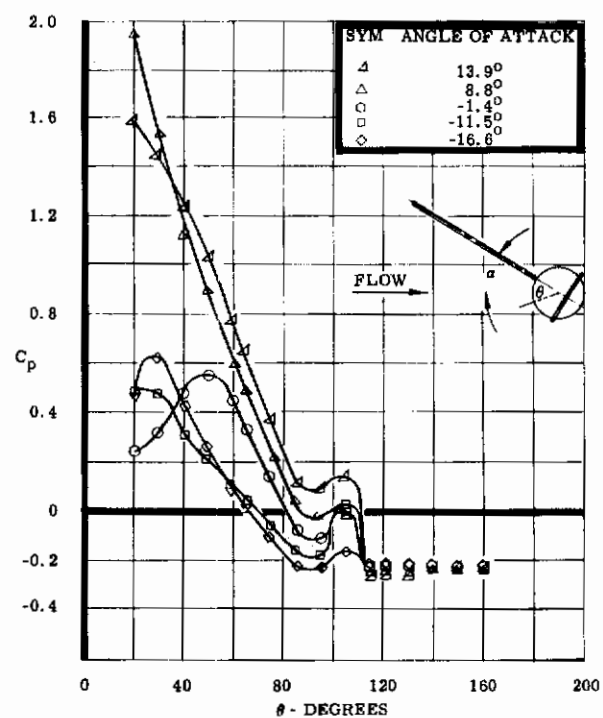Figure 82. Pressure Coefficient Distribution on the Spiked Fabric-Covered Sphere, $L_R/D = 3.0$, $\alpha = 0^O$

Figure 83. Pressure Coefficient Distribution in a Pitch Plane on the Spiked Fabric-Covered Sphere for Various Angles of Attack, $L_R/D = 3.0$, M = 2.00
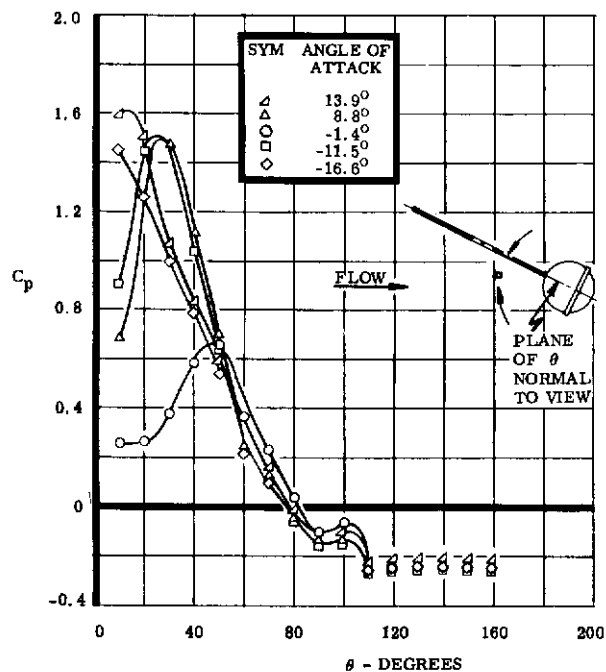
84

Figure 84. Pressure Coefficient Distribution in a Yaw Plane on the Spiked Fabric-Covered Sphere for Various Angles of Attack, $L_R/D = 3.0$, M = 2.00
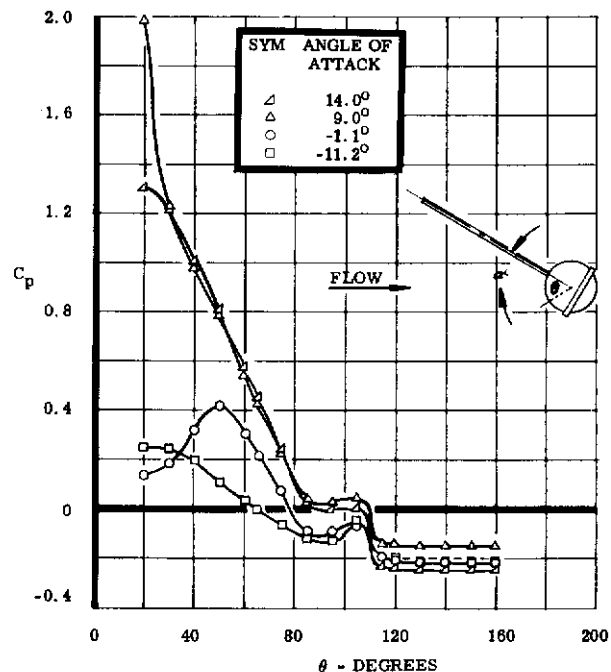

Figure 85. Pressure Coefficient Distribution in a Pitch Plane on the Spiked Fabric-Covered Sphere for Various Angles of Attack, $L_R/D = 3.0$, M = 2.50
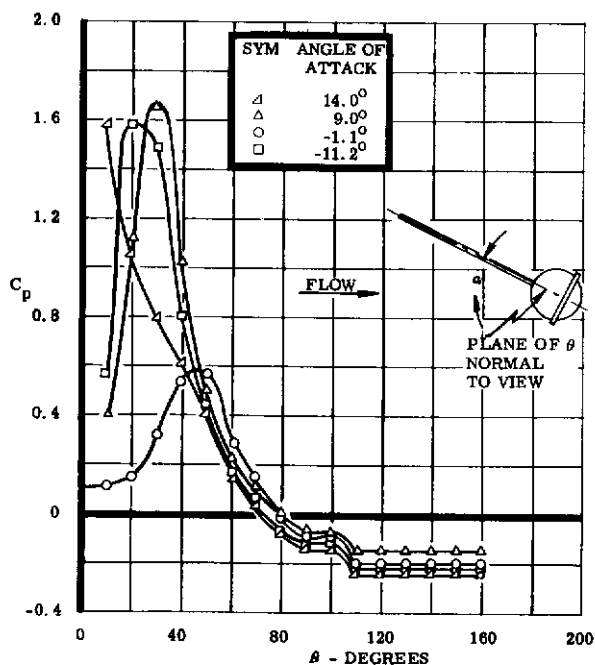

Figure 86. Pressure Coefficient Distribution in a Yaw Plane on the Spiked Fabric-Covered Sphere for Various Angles of Attack, $L_R/D = 3.0$, M = 2.50
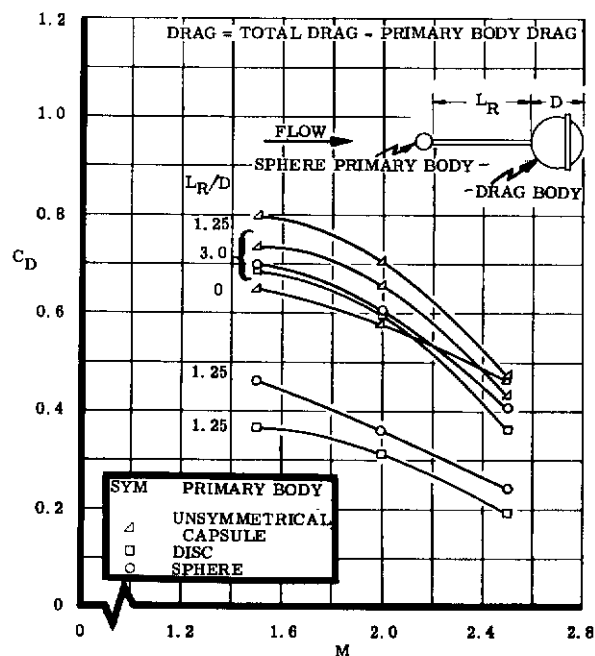

Figure 87. Drag Coefficient versus Mach Number of Spherical Secondary Drag Body
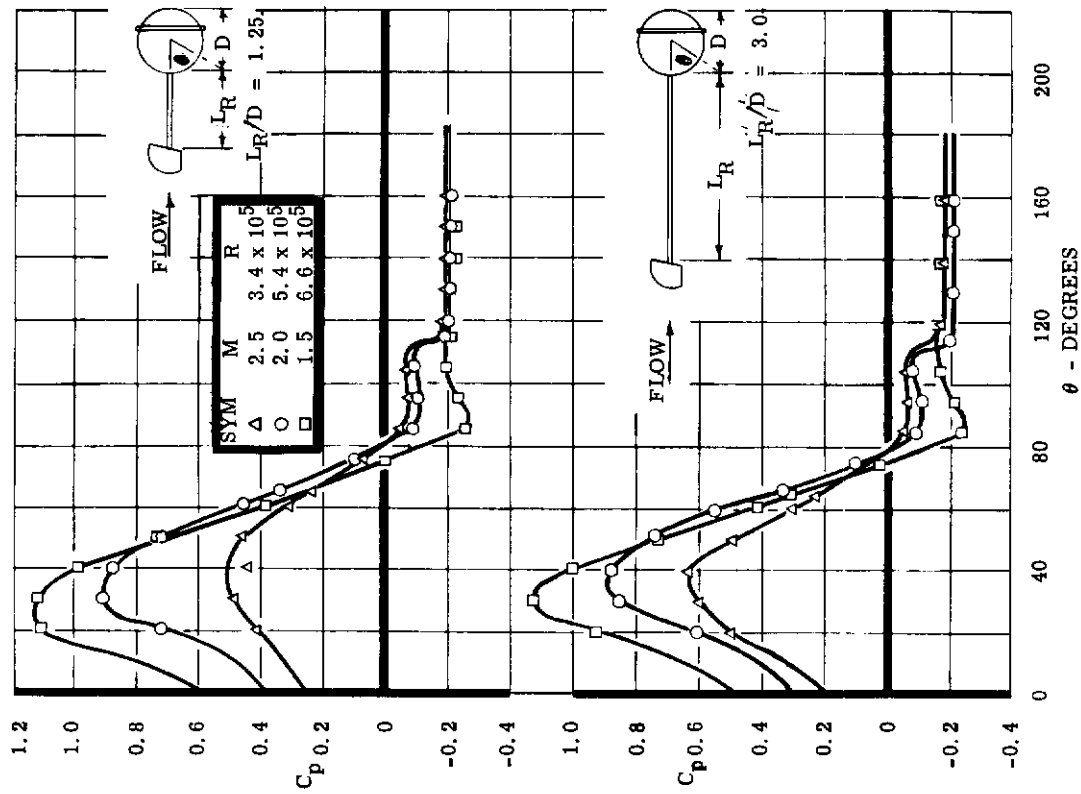
Figure 89. Pressure Coefficient Distribution in a Pitch Plane on the Fabric-Covered Sphere in the Wake of the Unsymmetrical Man Capsule, $L_R/D = 1.25$ and 3.0
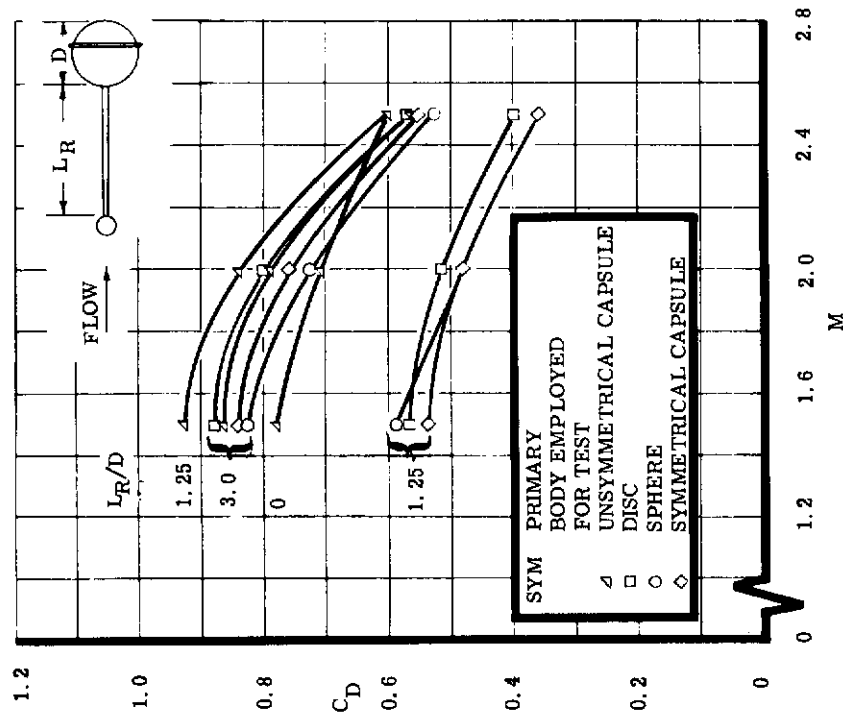

Figure 88. Total Drag Coefficient of the Primary Body and the Spherical Secondary Drag Body versus Mach Number

Figure 91. Pressure Coefficient Distribution in the Pitch and Yaw Planes on the Fabric–Covered Sphere in the Wake of the Unsymmetrical Man Capsule, $L_R/D = 0$, $\alpha = 0°$
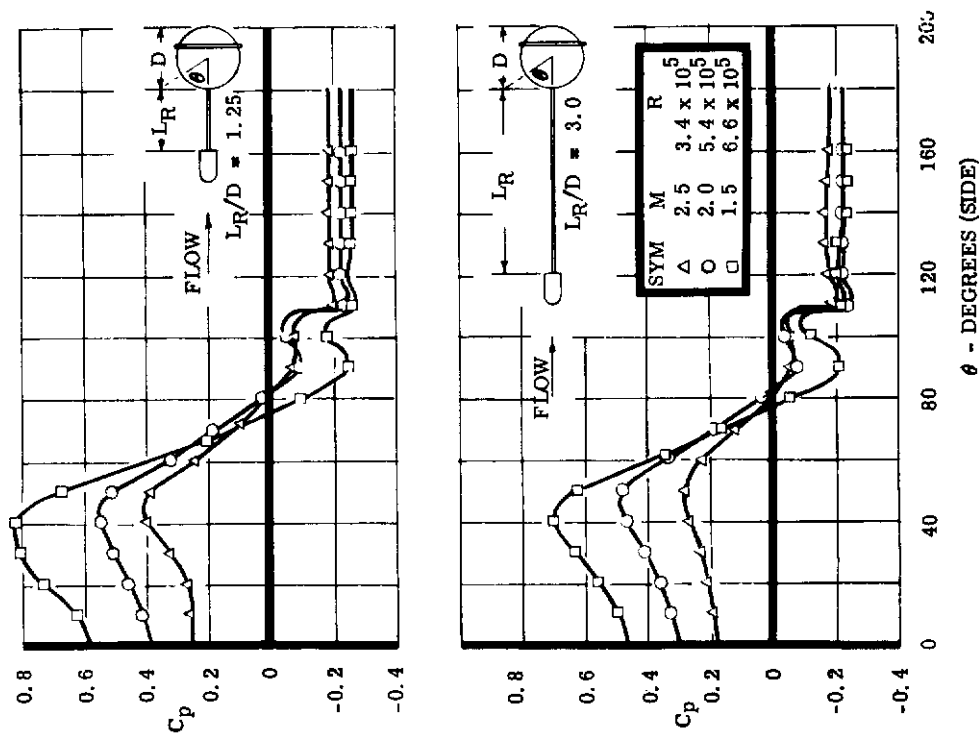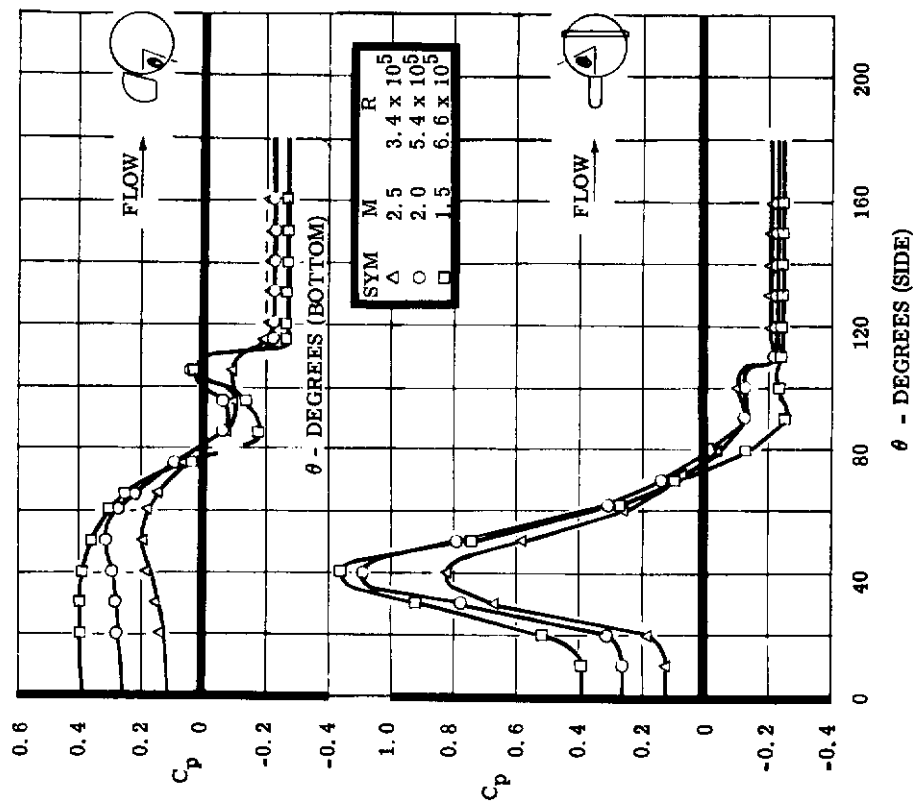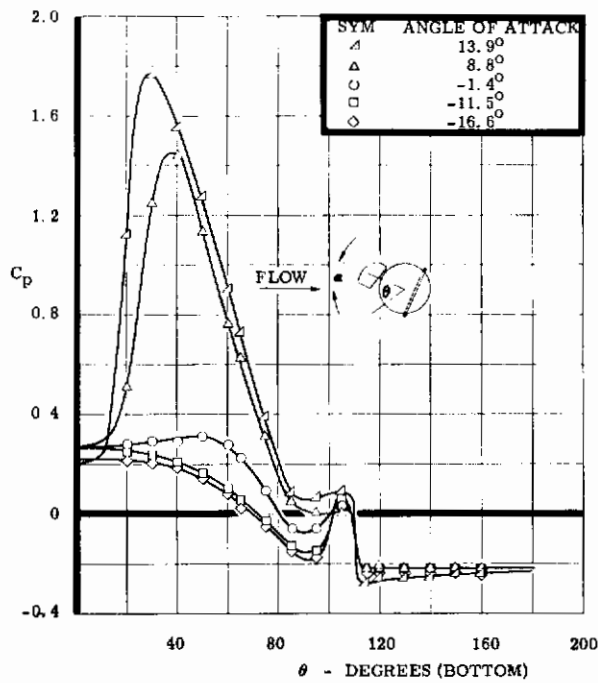

Figure 90. Pressure Coefficient Distribution in a Yaw Plane on the Fabric–Covered Sphere in the Wake of the Unsymmetrical Man Capsule, $L_R/D = 1.0$ and 3.0

Figure 92. Pressure Coefficient Distribution in the Pitch Plane on the Fabric-Covered Sphere in the Wake of the Unsymmetrical Man Capsule at Various Angles of Attack, $L_R/D = 0$, $M = 2.00$

Figure 93. Pressure Coefficient Distribution in the Yaw Plane on the Fabric-Covered Sphere in the Wake of the Unsymmetrical Man Capsule at Various Angles of Attack, $L_R/D = 0$, $M = 2.00$

Figure 94. Pressure Coefficient Distribution in the Pitch Plane on the Fabric-Covered Sphere in the Wake of the Unsymmetrical Man Capsule at Various Angles of Attack, $L_R/D = 0$, $M = 2.50$
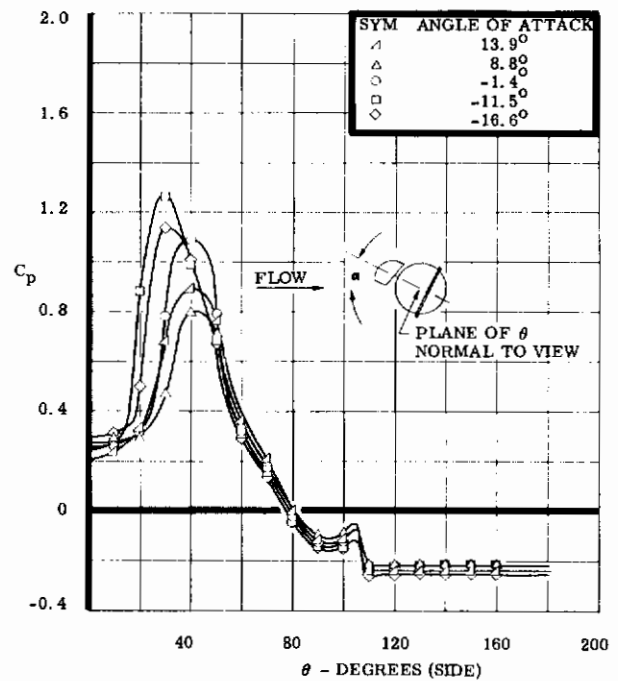

Figure 95. Pressure Coefficient Distribution in the Yaw Plane on the Fabric-Covered Sphere in the Wake of the Unsymmetrical Man Capsule at Various Angles of Attack, $L_R/D = 0$, $M = 2.50$

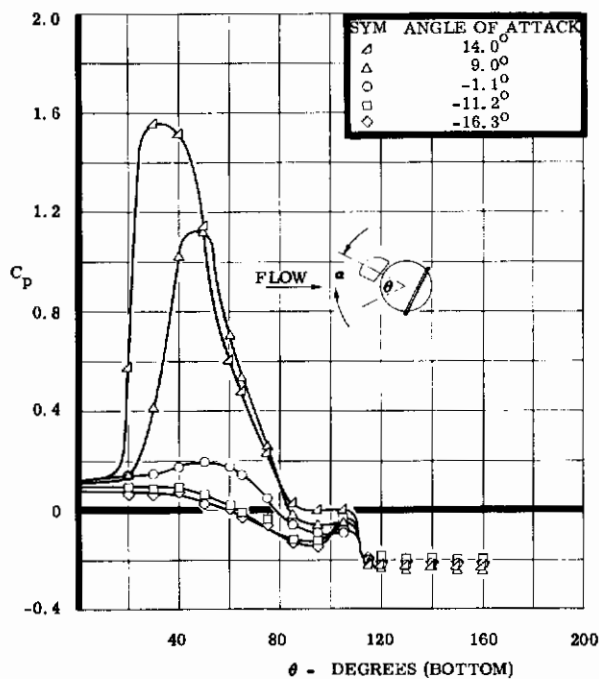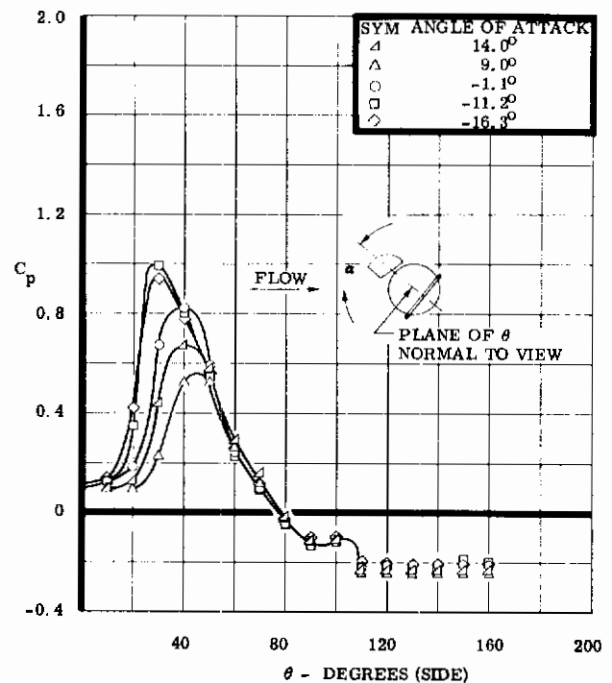Figure 97. Pressure Coefficient Distribution on the Fabric-Covered Sphere with Fence in the Wake of a Sphere $L_R/D = 1.25$ and 3.0
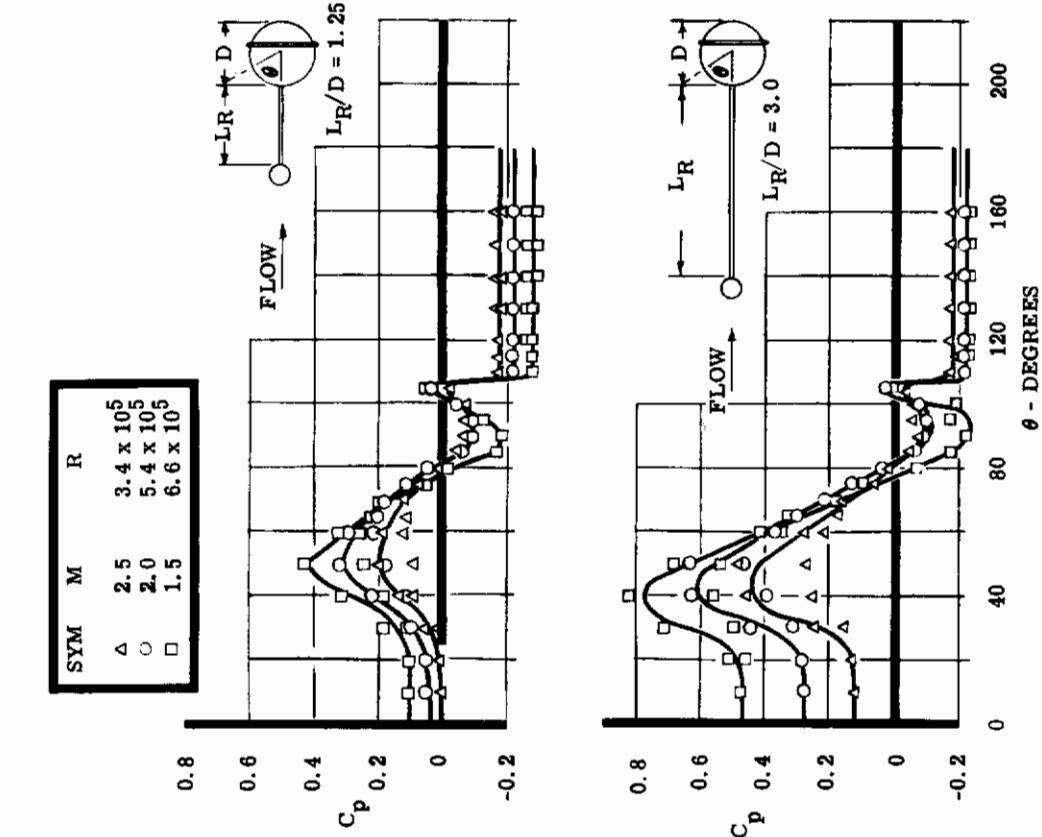
Figure 96. Pressure Coefficient Distribution on the Fabric-Covered Sphere with Fence in the Wake of a Disc, $L_R/D = 1.25$ and 3.0

Figure 99. Drag Coefficient versus Mach Number for the Inflated Sphere with Separation Fence

SYM	INFLATION PRESSURE	TUNNEL TOTAL PRESSURE
○	673.8 psf	523 psf
▽	421.5 psf	523 psf
□	593.8 psf	506 psf
◇	248.7 to 339.1	433 psf

SOLID FABRIC–COVERED SPHERE WITHOUT A SEPARATION FENCE

SYM	M	R
△	2.5	3.4×10^5
○	2.0	5.4×10^5
□	1.5	6.6×10^5

$L_R/D = 1.25$

$L_R/D = 3.0$

Figure 98. Pressure Coefficient Distribution on the Fabric–Covered Sphere with Fence in the Wake of the Symmetrical Man Capsule, L_R/D = 1.25 and 3.0
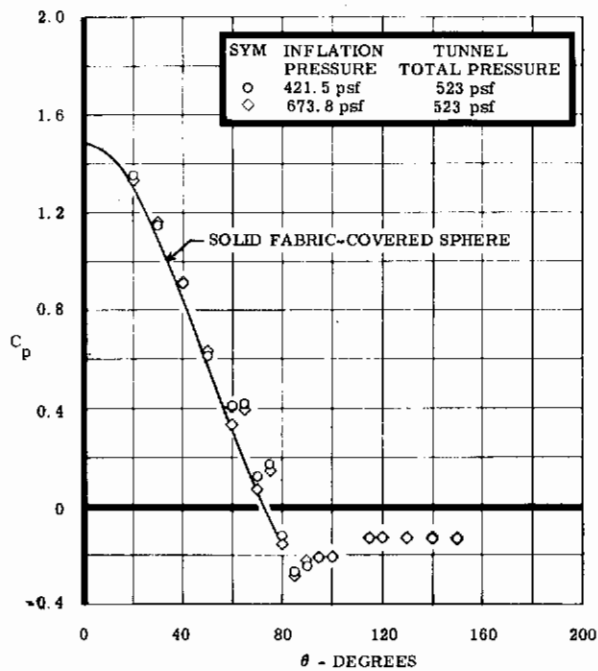
Figure 100. Pressure Coefficient Distribution on the Inflated Fabric Sphere, M = 1.50
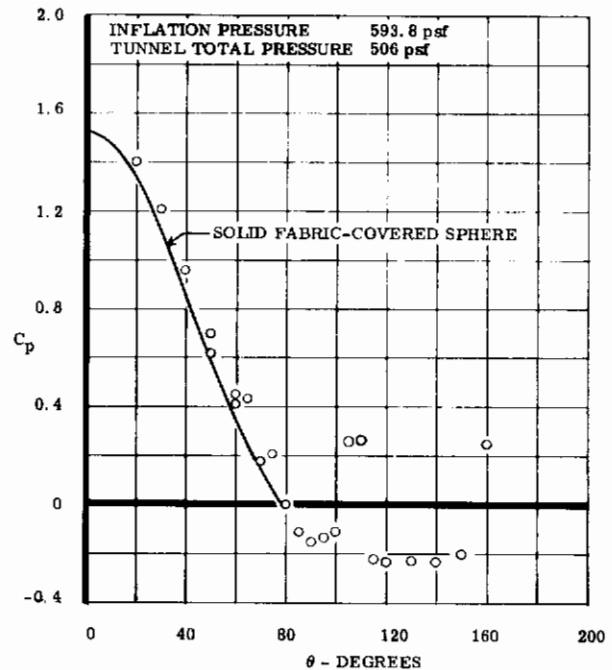
Figure 101. Pressure Coefficient Distribution on the Inflated Fabric Sphere, M = 2.00
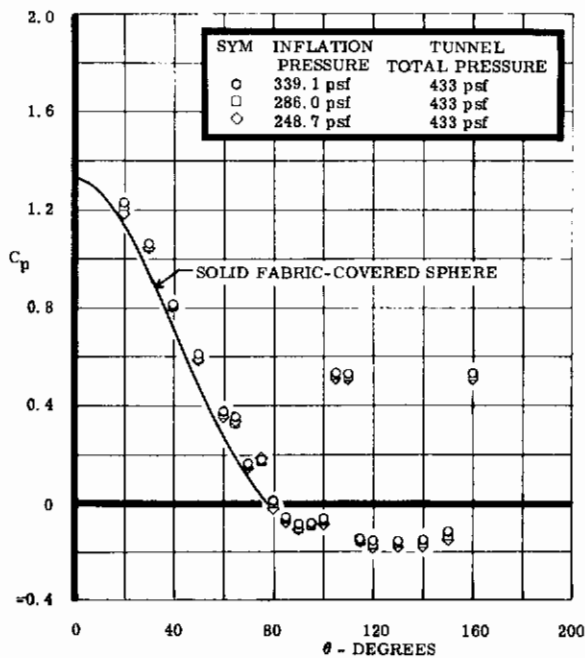
Figure 102. Pressure Coefficient Distribution on the Inflated Fabric Sphere, M = 2.50
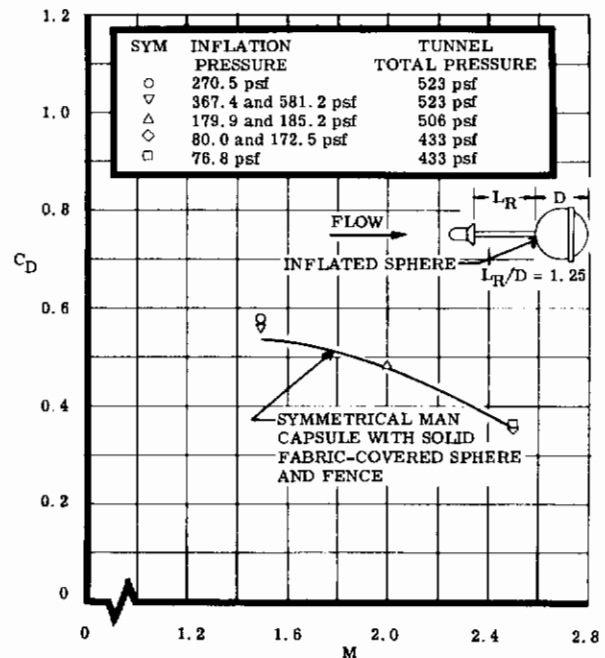
Figure 103. Total Drag Coefficient of the Primary Symmetrical Man Capsule and the Secondary Inflated Spherical Drag Body versus Mach Number

Figure 106. Pressure Coefficient Distribution on the Inflated Fabric Sphere in the Wake of the Symmetrical Man Capsule, $L_R/D = 1.25$, M = 2.50

Figure 105. Pressure Coefficient Distribution on the Inflated Fabric Sphere in the Wake of the Symmetrical Man Capsule, $L_R/D = 1.25$, M = 2.00
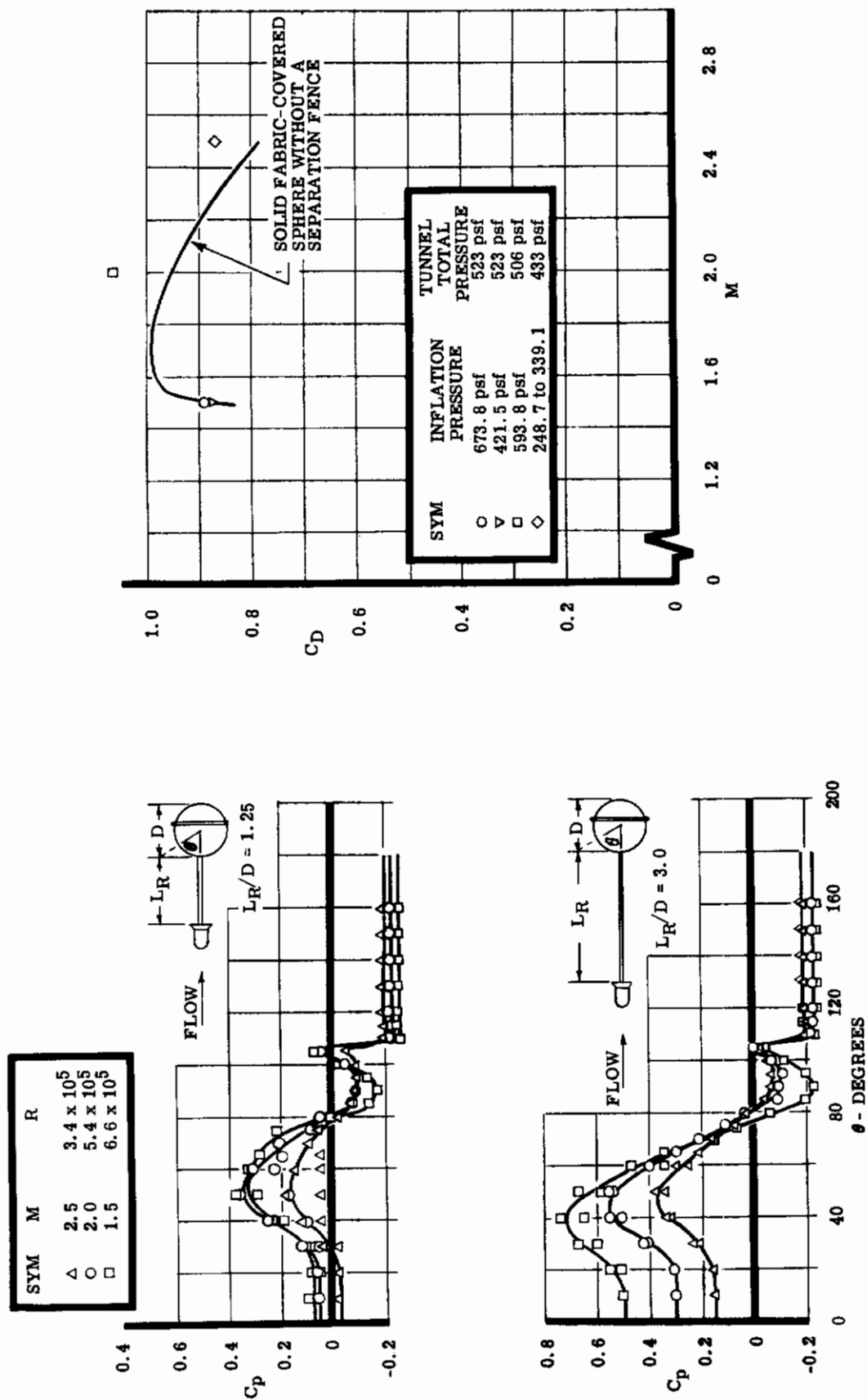
Figure 104. Pressure Coefficient Distribution on the Inflated Fabric Sphere in the Wake of the Symmetrical Man Capsule, $L_R/D = 1.25$, M = 1.50
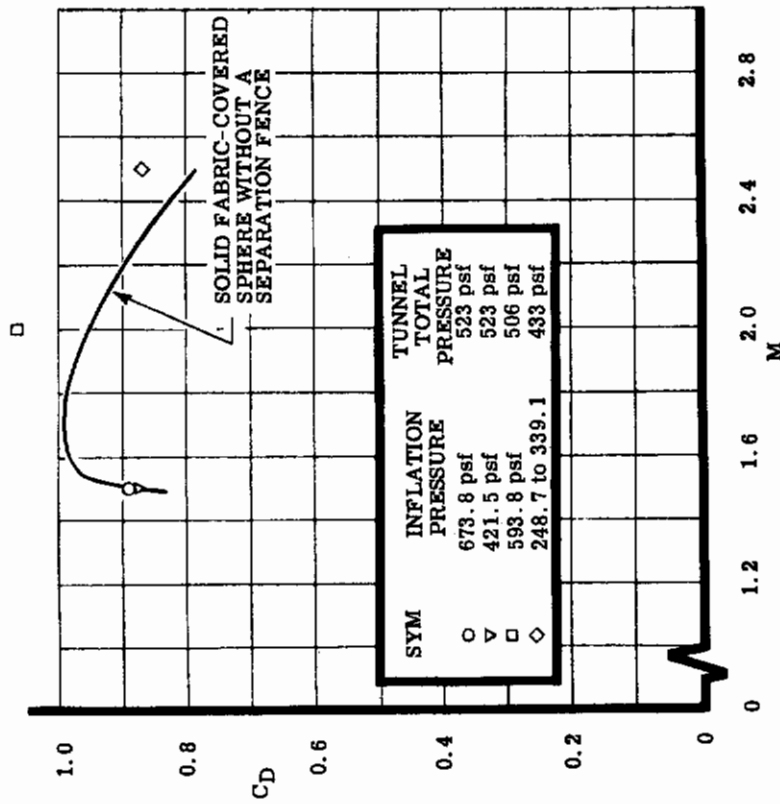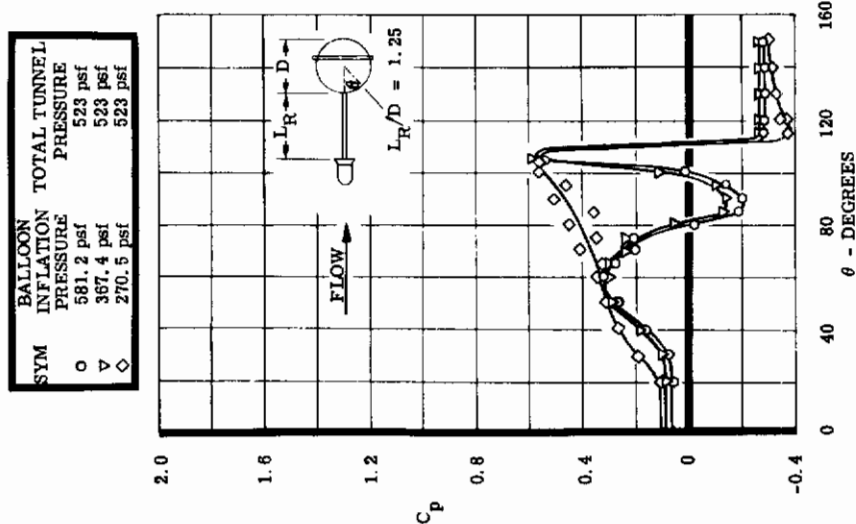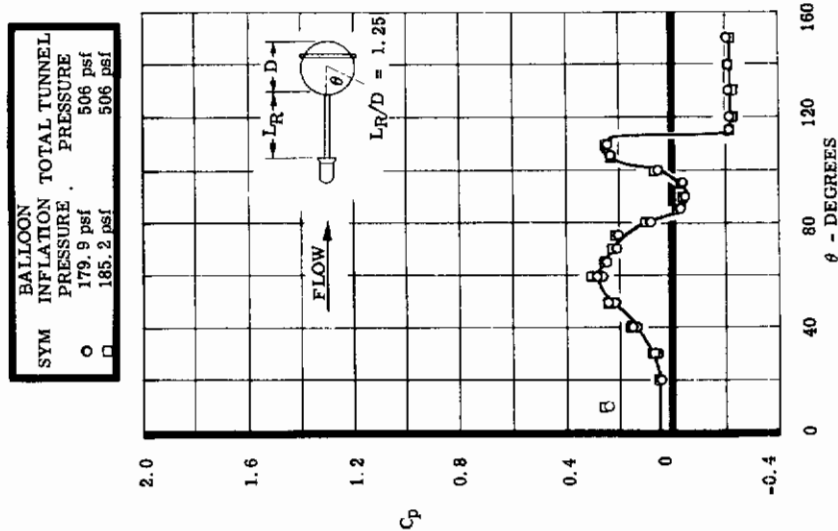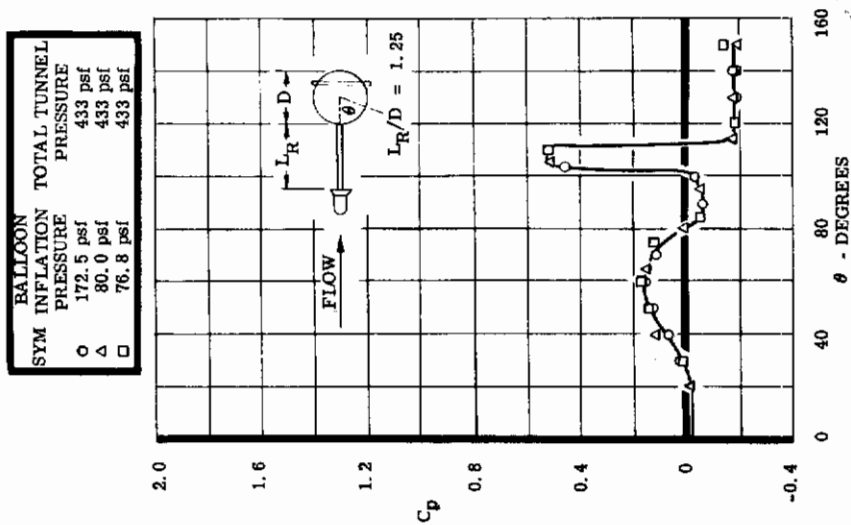
the solid, fabric-covered sphere did not have a separation fence. The drag coefficients of the inflated sphere, which in some cases was deformed to a pear shape, are higher than for the solid sphere. The inflation pressures for the inflated sphere are believed to be unreliable due to instrument error.

The pressure coefficient distributions for the inflated sphere at different inflation pressures are shown in Figures 100, 101, and 102. The distributions for the solid, fabric-covered sphere are also presented for comparison. The erratic test points at θ = 10, 105, 110, and 160 degrees are believed to be in error.

e. Inflated Sphere in the Wake of a Symmetrical Capsule. The total drag coefficients of the symmetrical man capsule and the inflated sphere, test model configuration 5, are shown in Figure 103. The inflation pressures for the inflated sphere are believed to be unreliable. A drag coefficient curve for the configuration that employed the solid, fabric-covered sphere is presented for comparison. As mentioned previously, the drag increment of the secondary, spherical body could not be determined because the drag coefficient of the primary body was not known.

The pressure distributions on the inflated spherical, secondary body are presented in Figures 104, 105, and 106.

f. Tethered Sphere Behind the Unsymmetrical Capsule. The inflated sphere which was attached to a variable length cable behind the unsymmetrical capsule, test model configuration 6, was tested at different distances behind the capsule for dynamic stability behavior. At a Mach number of 1.6 and a dynamic pressure of approximately 220 psf, the model behaved with a 5 degree oscillation in pitch of 3 to 6 cps and rolling greater than 360 degrees when the riser line between the capsule and the model was less than one model diameter (8 inches). With greater riser line lengths the model exhibited excellent stability characteristics with no oscillatory motion in pitch, and only an approximate ±10-degree roll. The variation of internal pressure allowed the model to deform from a spherical shape to a pear shape. The pear shaped model exhibited a slight but insignificant decrease in the degree of pitch stability. The internal model pressure was greater than the test section total pressure by 0.25, 0.15, and 0.10 psi. A 48 frames-per-second movie was used to record the degree of stability and deformation when the model was 19 to 21 inches behind the capsule.

As a further investigation into the stability of a tethered sphere beyond the formal scope of this program, a solid 6.75 inch diameter plastic sphere was suspended behind the escape capsule of the "Mercury Project." A separation fence was placed on the plastic sphere at θ = 105 degrees. The frontal area of capsule to sphere was approximately 1.2. The stability of the sphere at Mach 1.67 and 1.97 was excellent when tethered 7 to 24 inches behind the capsule. A slight instability in pitch occurred when the sphere was tethered less than 7 inches behind the capsule.

A six-sided airmat cone with a hollow base and a riser line attached to the conical apex was also tested at Mach 1.57. Although the pitch stability was excellent, the cone rolled rapidly at about 1 to 2 rps. Preliminary testing for a supplementary wind tunnel program at the NASA Lewis Research Center revealed that a solid tethered sphere at Mach 3.85 exhibited excellent stability characteristics.

g. Schlieren Photographs. The large vertical bars in the photographs are steel structural members used to support the glass panels of the test section.

Schlierens of the fabric-covered sphere without the separation fence are presented in Figures 107, 108, and 109. At Mach 1.5 the flow separation occurs between 85 and 90 degrees from the forward stagnation point, and the turbulent wake did not converge. At Mach 2.0 the flow separates at approximately 100 degrees from the forward stagnation point, and the turbulent wake converges with a visible trailing shock wave. At Mach 2.5 the flow separates at approximately 100 degrees from the forward stagnation point, and the turbulent wake converges, but interference of the support sting does not allow the formation of a trailing shock wave. Pressure coefficient distributions for this configuration are shown in Figure 73.

Schlierens of the spiked, fabric-covered sphere with separation fence are shown in Figures 110 through 115. The tip of the spike (L_R/D = 1.0) and the separation fence at θ = 105 degrees are not visible in Figures 110, 111, and 112 because of the vertical structural members which appear as large black vertical bars in the photographs. Flow separation occurs off the flat face of the spike
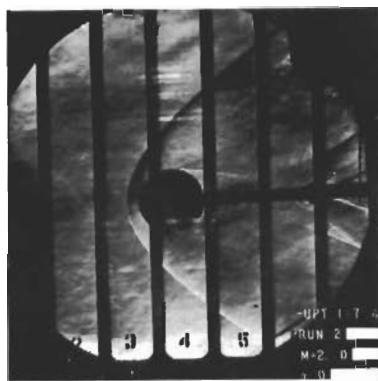
Figure 107. Fabric-Covered
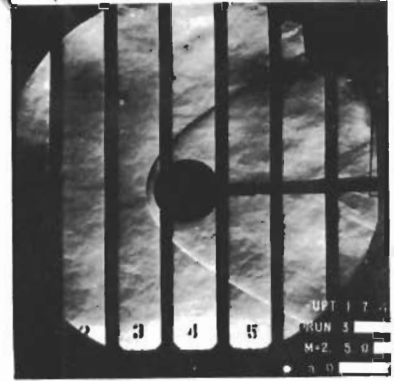Sphere, M = 1.50

Figure 108. Fabric-Covered
Sphere, M = 2.00

Figure 109. Fabric-Covered
Sphere, M = 2.50

resulting in a turbulent conical wake. The pressure coefficient distributions for this configuration
are shown at the bottom of Figure 77.

In Figures 113, 114, and 115 the tip of the spike (L_R/D = 3.0) is forward of the visible part
of the test section, and the separation fence is again obscured by the vertical structural members.
Flow separation occurs along the spike approximately one sphere diameter ahead of the sphere. The
flow separation off the spike is well defined at Mach 1.5 and 2.0, but at Mach 2.5, the undefined na-
ture of the separation shock wave leads to the possible conclusion that oscillatory separation occurred
along the spike where the point of flow separation oscillated back and forth along the spike. This phe-
nomena is reported in References 19 and 20. Reference 18 presents an excellent study at Mach 1.61
and 1.81 of the flow phenomena associated with spiked cylindrical bodies at various angles of attack.
The pressure coefficient distributions for this configuration are shown at the bottom of Figure 82.

The influence of the symmetrical primary bodies on the secondary, spherical body can be
generalized. Schlierens of the fabric-covered sphere in the wake of the four primary bodies are
shown at Mach 1.5 in Figures 116 through 119, at Mach 2.0 in Figures 120 through 123, and at Mach
2.5 in Figures 124 through 127. In all cases except the unsymmetrical man capsule, the wake of the
primary bodies, as influenced by the secondary, spherical body, is turbulent and divergent for
L_R/D = 1.25. This wake phenomena has also been reported in References 23 and 24 where cones
were used as the primary body.

The Schlierens for the primary bodies at three sphere diameters ahead of the secondary,
spherical body are not presented in this report. These Schlierens revealed that the secondary,
spherical body had no influence on the wake of the four primary bodies. Complete flow recovery with
a convergent wake occurred behind the four primary bodies at Mach 1.5, 2.0, and 2.5. Flow separa-
tion occurred off the variable length actuator rod approximately one sphere diameter ahead of the
sphere. This flow recovery phenomena is also evident in References 23 and 24. An analysis of Ref-
erence 23 is presented in Figure 128 where the cones were moved back and forth during the test for
Mach 1.5, 1.6, and 1.8. Although the flow analysis is for cones as the primary body and a flat faced
cylinder as the secondary body, the analysis proves to be consistent with the results reported herein
and in Reference 24 where a cylinder with a hemisphere-ogive nose was employed as a secondary body
in the wake of cones. From Figure 128, for a given frontal area ratio, the wake of the cones was tur-
bulent and divergent as the distance between the primary and secondary bodies increases from zero to
the top of the flow transition region as defined by the free stream Mach number. As the distance be-
tween the primary and secondary bodies was increased beyond the flow transition region, the wake of
the primary body converged and flow separation occurred along the support bar which simulates a
riser line. When a flow condition is established where the wake of the primary body is convergent,
the distance between the two bodies is decreased, and the wake of the primary body does not become
divergent until the bottom of the flow transition region is reached. The drag of the secondary, cy-
lindrical body was relatively greater when the distance between the two bodies allowed a primary
body wake convergence. The divergent primary body wake resulted in a relatively small secondary
body drag.

Contrails

Figure 112. Spiked, Fabric-Covered Sphere with Separation Fence, $L_R/D = 1.0$, M = 2.50

Figure 115. Spiked, Fabric-Covered Sphere with Separation Fence, $L_R/D = 3.0$, M = 2.50

Figure 111. Spiked, Fabric-Covered Sphere with Separation Fence, $L_R/D = 1.0$, M = 2.00

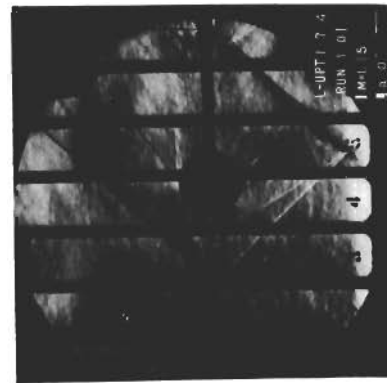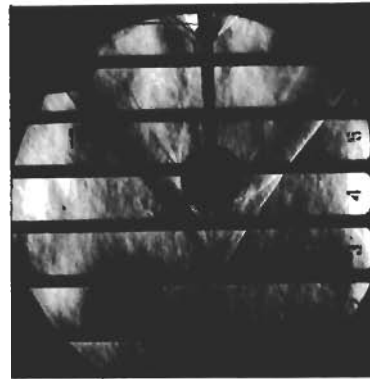Figure 114. Spiked, Fabric-Covered Sphere with Separation Fence, $L_R/D = 3.0$, M = 2.00

Figure 110. Spiked, Fabric-Covered Sphere with Separation Fence, $L_R/D = 1.0$, M = 1.50

Figure 113. Spiked, Fabric-Covered Sphere with Separation Fence, $L_R/D = 3.0$, M = 1.50

Figure 116. Fabric-Covered
Sphere with Separation
Fence in the Wake of
a Disc, L_R/D = 1.25,
M = 1.50

Figure 117. Fabric-Covered
Sphere with Separation
Fence in the Wake of
a Sphere,
L_R/D = 1.25, M = 1.50

Figure 118. Fabric-Covered
Sphere with Separation
Fence in the Wake of
a Symmetrical Man
Capsule,
L_R/D = 1.25, M = 1.50
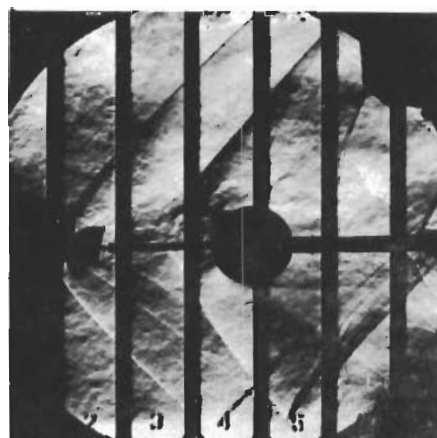
Figure 119. Fabric-Covered
Sphere with Separation
Fence in the Wake of
an Unsymmetrical
Man Capsule,
L_R/D = 1.25, M = 1.50

Figure 120. Fabric-Covered
Sphere with Separation
Fence in the Wake of
a Disc,
$L_R/D = 1.25$, M = 2.00
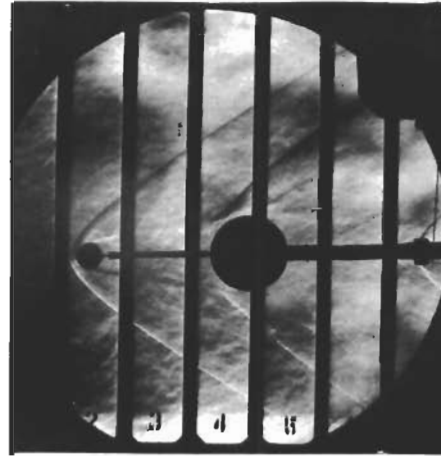
Figure 121. Fabric-Covered
Sphere with Separation
Fence in the Wake of
a Sphere,
$L_R/D = 1.25$, M = 2.00
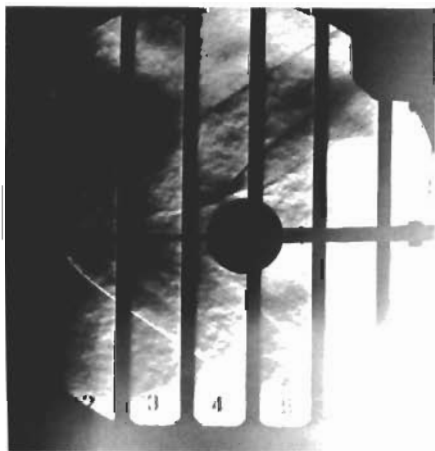
Figure 122. Fabric-Covered
Sphere with Separation
Fence in the Wake of
a Symmetrical Man
Capsule,
$L_R/D = 1.25$, M = 2.00
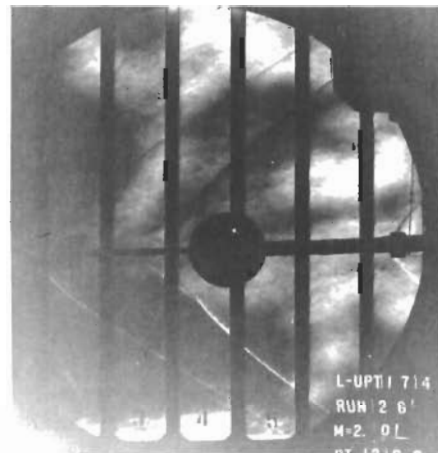
Figure 123. Fabric-Covered
Sphere with Separation
Fence in the Wake of
an Unsymmetrical
Man Capsule,
$L_R/D = 1.25$, M = 2.00

Figure 124. Fabric-Covered
Sphere with Separation
Fence in the Wake of
a Disc,
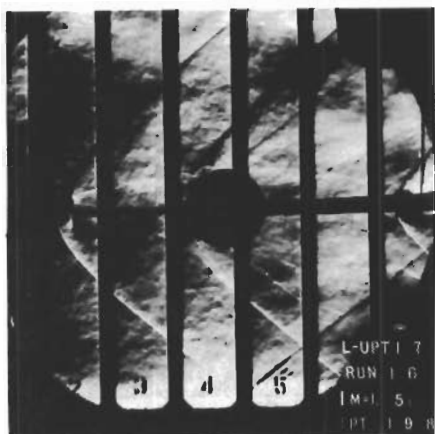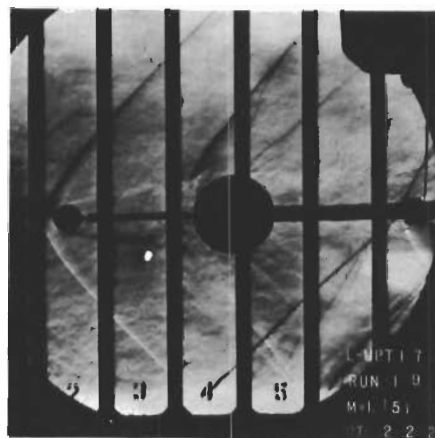$L_R/D = 1.25$, $M = 2.50$
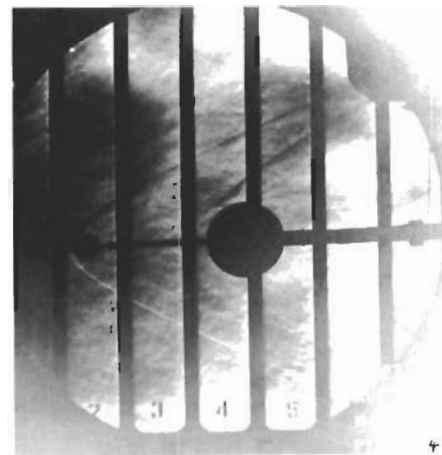
Figure 125. Fabric-Covered
Sphere with Separation
Fence in the Wake of
a Sphere,
$L_R/D = 1.25$, $M = 2.50$
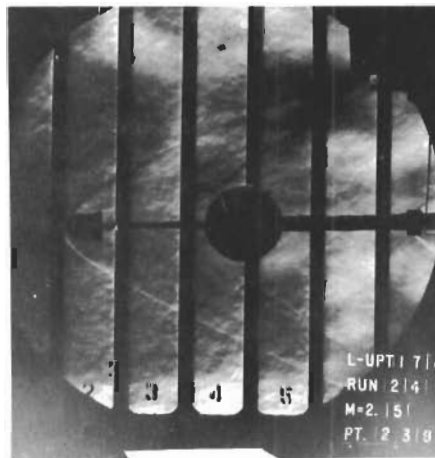
Figure 126. Fabric-Covered
Sphere with Separation
Fence in the Wake of
a Symmetrical Man
Capsule,
$L_R/D = 1.25$ $M = 2.50$
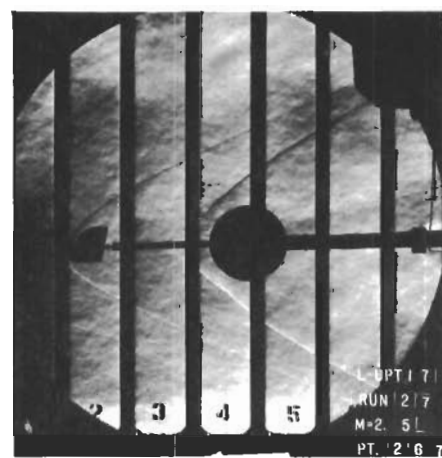
Figure 127. Fabric-Covered
Sphere with Separation
Fence in the Wake of
an Unsymmetrical
Man Capsule,
$L_R/D = 1.25$, $M = 2.50$

NOTES (REF 23 DATA)

1. FOR A GIVEN AREA RATIO - WITH INCREASING L_R/D FLOW, TRANSITION OCCURS AT TOP OF REGION - WITH DECREASING L_R/D FLOW, TRANSITION OCCURS AT BOTTOM OF REGION
2. CONE LENGTH NOT CHANGED
3. $R \approx 7.5 \times 10^5$/INCH

SYM	TOTAL CONE ANGLE	
$\circ$	30°	
$\triangle$	60°	REF 23
$\square$	80°	
$\diamond$	FROM DATA REPORTED HEREIN M = 1.5, 2.0, 2.5	

FLOW CHARACTER ABOVE TRANSITION REGION

SHOCKS
TURBULENT AIR
FLOW
D
L_R

FLOW CHARACTER BELOW TRANSITION REGION

SHOCK
TURBULENT AIR
FLOW
D
L_R

M=1.5
M=1.6
M=1.8

$\dfrac{L_R}{D}$

CONE FRONTAL AREA TO CYLINDER FRONTAL AREA RATIO

Figure 128. Regions of Flow Transition Between Cones and Flat-Faced Cylinders

As pointed out in Reference 24, the cone frontal area is more significant in the reduction of the secondary body drag than the cone apex angle. The drag and flow phenomena results of the investigation herein reported are consistent with the analysis of References 23 and 24 presented in Figure 128. The results of the data reported herein for Mach 1.5, 2.0, and 2.5 are also shown in Figure 128 for comparison. The frontal area ratios (A_p/A_B) for the various primary bodies were:

Primary Body	A_p/A_B
Disc	0.123
Sphere	0.123
Symmetrical Man Capsule	0.177
Unsymmetrical Man Capsule	0.135

A Schlieren of the inflated sphere in the wake of the symmetrical man capsule at Mach 2.5 is presented in Figure 129 along with a standard photograph in Figure 130 to show the deformation of the inflated sphere at Mach 2.5. High-speed Schlieren movies were taken of the tethered plastic sphere at Mach numbers up to approximately 2.0. At all Mach numbers the flow separated off the riser line approximately one sphere diameter ahead of the tethered sphere.

7. CONCLUSIONS

Excellent pitch and roll stability characteristics over a Mach number range of 1.5 to 3.85 have been exhibited by rigid spheres and/or inflatable spheres which were tethered at riser line lengths greater than one sphere diameter. Riser line lengths of less than one diameter resulted in moderate pitch and roll instability at Mach 1.6. Inflatable spheres which were deformed to a pear shape because of low inflation pressure exhibited a slight but insignificant pitch instability at Mach 1.6.

The drag coefficient of a sphere in the wake of various primary bodies is significantly reduced by an amount which is a function of the primary body to sphere frontal area ratio, the distance between the primary body and the sphere, and the Mach number. There exists an optimum riser line length where the greatest drag is realized from the sphere in the wake of various primary bodies. This optimum riser line length is a function of the Mach number and the primary body to sphere frontal area ratio. The drag coefficient of an inflated sphere was higher than that of a solid sphere. The drag and stability characteristics of inflatable and solid spheres are comparable even when the sphere is slightly deformed because of low inflation pressure.

The pressure distribution on a sphere in the wake of various primary bodies is similar to the pressure distribution which occurs on a spiked sphere. Negative and positive pressure coefficients were observed on the front of a sphere which was in the wake of various bodies. Pressure coefficients on spiked spheres at angles of attack were observed to be greater than on a sphere with no spike.

The separation fence had no effect on the degree of pitch or roll stability of a tethered sphere at Mach 1.5 to 2.0. The addition of a separation fence on a spiked sphere resulted in a drag decrease at Mach 1.5 and a drag increase at Mach 2.5.

The wake of the primary body, as influenced by the secondary body, is characterized by three types of wake flow. The wake flow phenomena is dependent upon the distance between the two bodies, the frontal area ratio, and the Mach number. For relatively short distances between the two bodies the wake of the primary body is turbulent and divergent. For relatively large distance between the two bodies the wake of the primary body is convergent and a laminar wake flow exists. At intermediate distances between the two bodies the wake of the primary body will either diverge or converge. When the primary body wake converges so that a laminar wake flow exists, flow separation occurred off the riser line of the tethered spheres leaving a conical wake similar to that which was observed for a spiked sphere.

B. NASA LANGLEY RESEARCH CENTER TESTS (THERMODYNAMIC)

1. General

The objective of this analysis was to determine the thermal effects upon a sphere in the wake of various bodies in supersonic flow; effects applicable to the aerodynamic feasibility study of

Figure 129. Spark Schlieren of the
Inflated Sphere in the Wake of the
Symmetrical Man Capsule,
L_R/D = 1.25, M = 2.5

Figure 130. Wide Angle Photograph of the
Inflated Sphere in the Wake of the
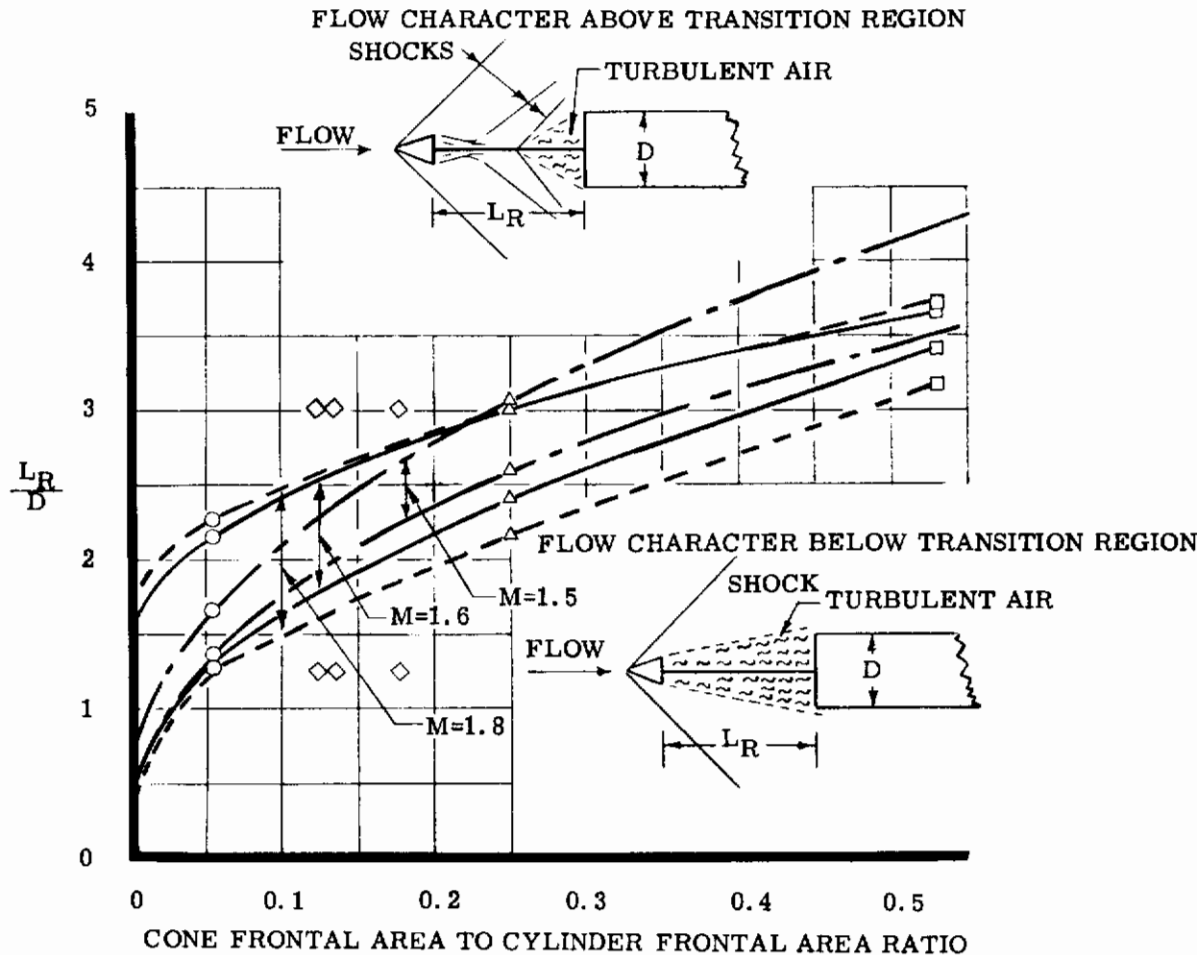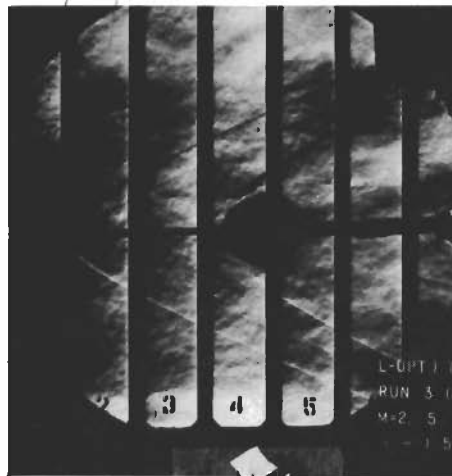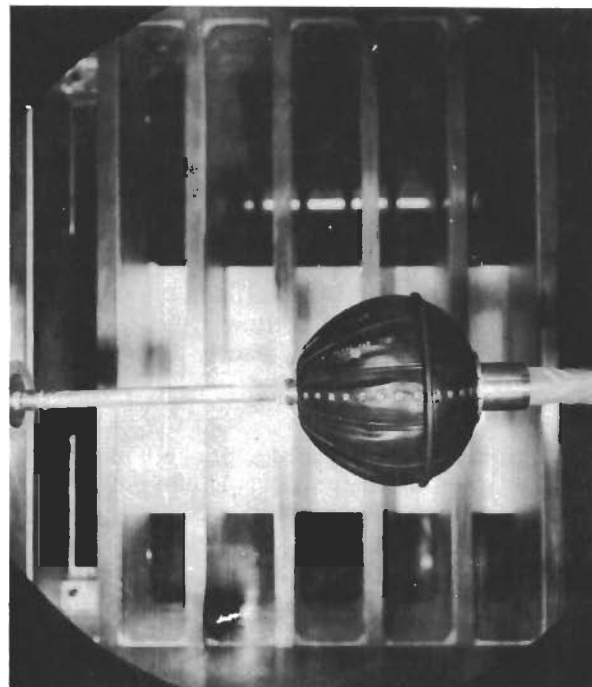Symmetrical Man Capsule,
L_R/D = 1.25, M = 2.5

using spheres as stabilizing and drag devices.

The solid sphere, instrumented for obtaining heat transfer data, simulates a thin-shell model wherein the local temperature measurements assume values that would be obtained when the local value of the heat flux $q_w = 0$. These are identified as "recovery temperatures." The aerodynamic heating rate, neglecting longitudinal heat conduction, is:

$$q_w = W_{c_m} \qquad \Delta T_w + \qquad \sigma \epsilon (T_w^4 - T^4_{ref})$$

The tests were conducted over relatively long periods of time at steady stagnation conditions, and, as a result, the storage term in the equation is negligible. Computation of the radiation term shows negligible values due to the relatively small values of T_w and T_{ref}. This analysis thus indicates $q_w \neq 0$ and the data as presented in Figures 131 through 153 represents a measure of the recovery temperature distributions on the test models.

Inasmuch as these models were instrumented for measurements of the recovery temperatures rather than the aerodynamic heat transfer rates, a discussion of the apparent trends is presented on the temperature recovery distribution, transition, and the effects on the thermal characteristics of a sphere in the wake of various bodies. For purposes of this report, this discussion will include only the symmetrical bodies.

The theoretical local non-dimensional heat transfer parameter, the Nusselt number, is presented as a function of local Reynolds number in Figure 154 for a sphere in the wake of a spherical body, and for a clean, rigid sphere at similar free stream conditions.

2. Discussion of Results

The ratio of the model recovery temperatures to tunnel total temperatures is presented as a function of angular distance from the theoretical stagnation point. Figure 131 shows that boundary layer separation appears to occur on the clean, rigid sphere from $\theta = 75$ to 100 degrees, occurring more forward at the higher Reynolds numbers. This is evidenced by the slightly increasing values of T_e/T_0 in the vicinity of these points. Reference 25 reports similar results in tests conducted at higher Reynolds numbers.

The point of maximum flux in the clean sphere is the stagnation point where the maximum temperature exists. As the flow accelerates around the body, the boundary layer may undergo transition from laminar to fully turbulent flow. The leading half of the sphere did not undergo boundary layer transition, shown by the steadily decreasing recovery temperature in Figure 131.

Attachment of spikes on blunt bodies has long been considered as a method of reducing body drag. The effects of spikes upon the thermal characteristics of these bodies are presented in References 26 and 27. Inasmuch as spiked bodies are of interest solely from a comparative aspect, they will not be the subject of lengthy discussion in this report.

In the study of spheres in the wake of various bodies, the spherical primary body configuration as shown in Figure 132 was considered for these studies as typical of all the symmetrical configurations. Examination of the pressure and temperature data does not reveal any significant differences in these data for the same L_R/D.

Figure 132 indicates separation of the boundary layer as occurring in a fashion directly opposite to the case for the clean, rigid sphere, that is, separation occurring more forward on the secondary body at the lower Reynolds numbers. The significance of this phenomena is not known. The maximum recovery temperature occurs at $\theta = 40$ degrees for the riser length ratio $L_R/D = 3$, and at $\theta = 50$ degrees for $L_R/D = 1.25$. The pressure coefficient distribution data generally peaks at these same points.

Figure 155 shows the average recovery temperature ratios T_e/T_0 at the leading half of the various configurations, plotted as a function of free stream Reynolds number. It is noted that the
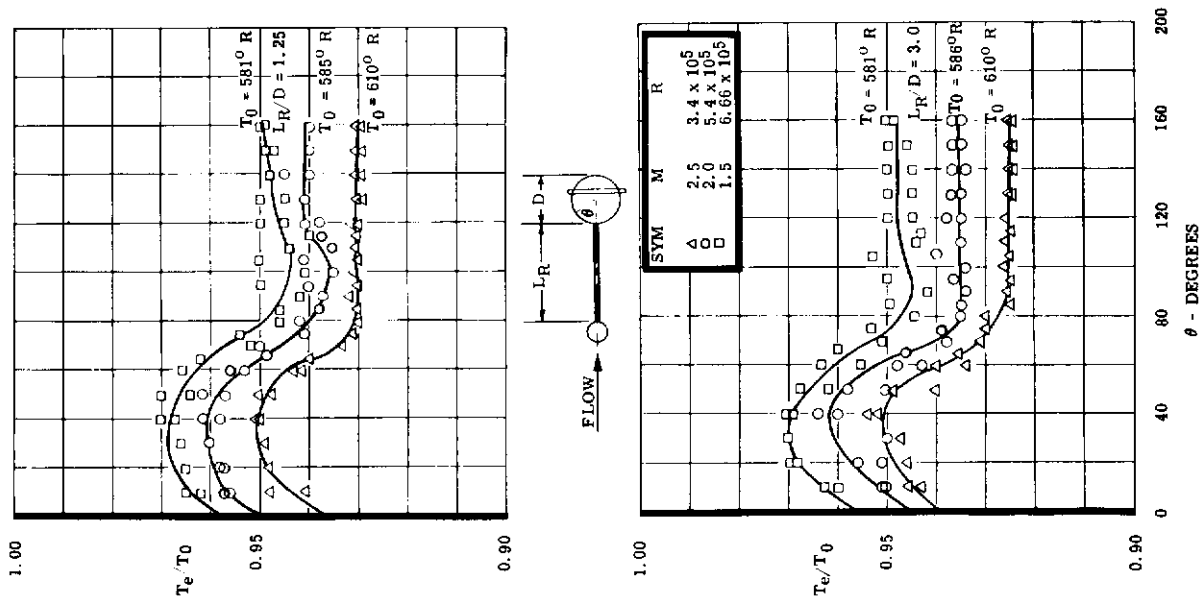
Figure 132. Temperature Recovery Distribution on a Sphere with a Fence and a Sphere
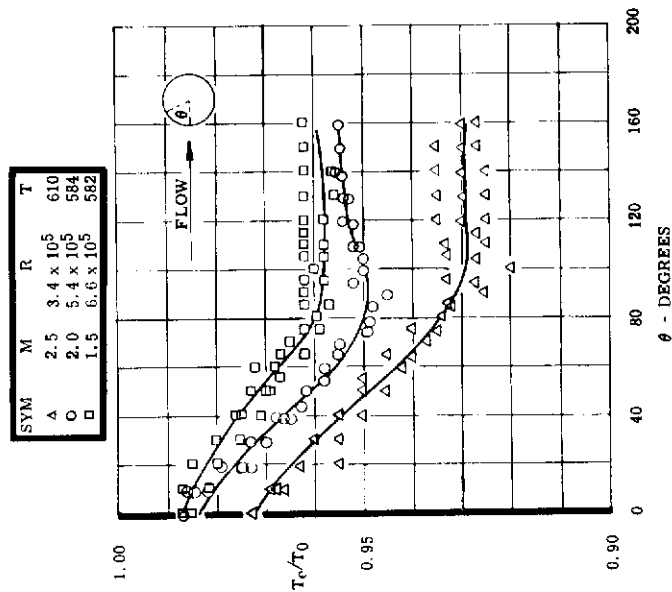
Figure 131. Temperature Recovery Distribution on a Clean, Rigid Sphere
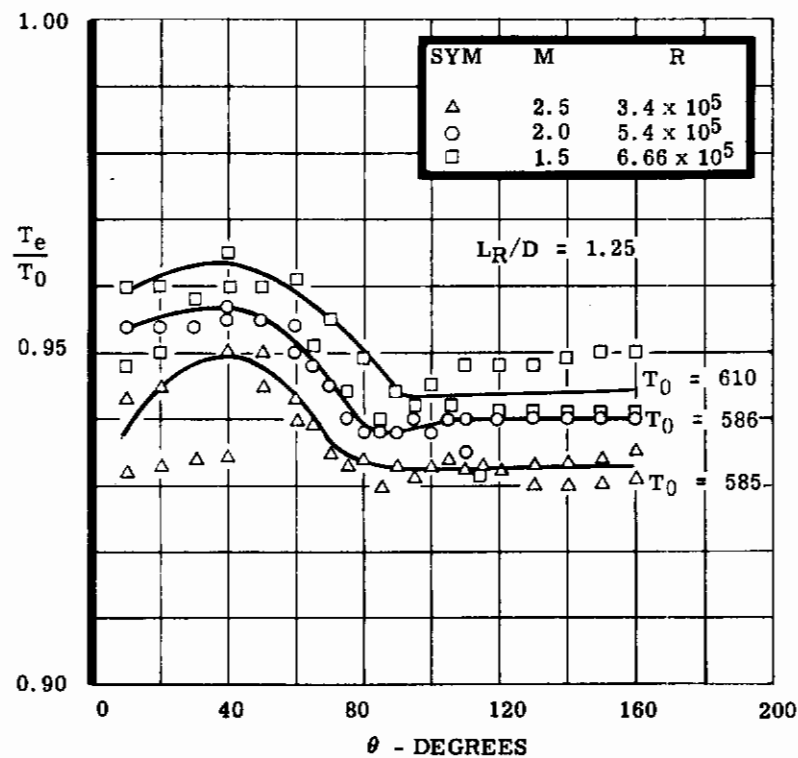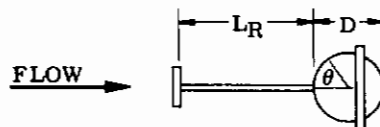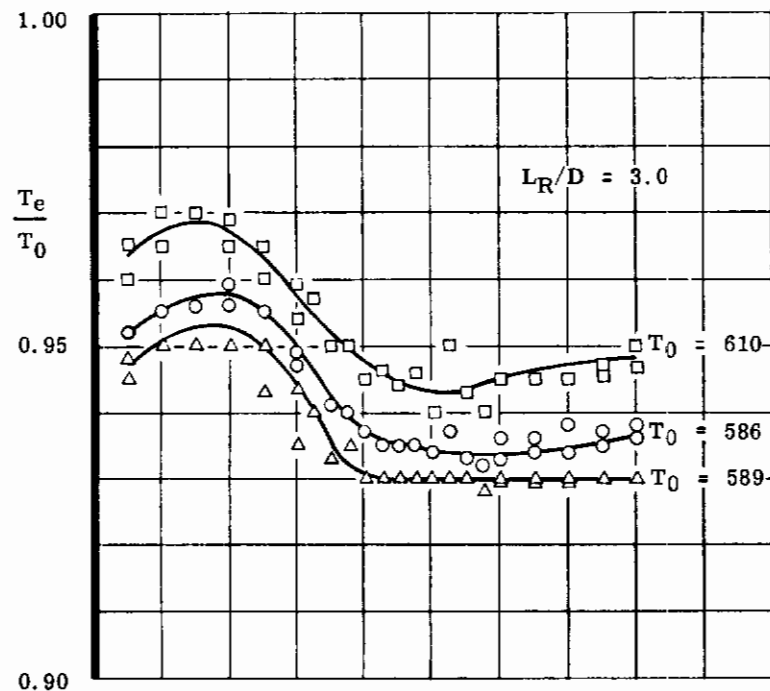
Figure 133. Temperature Recovery Distribution on a Sphere with a Fence and Disc
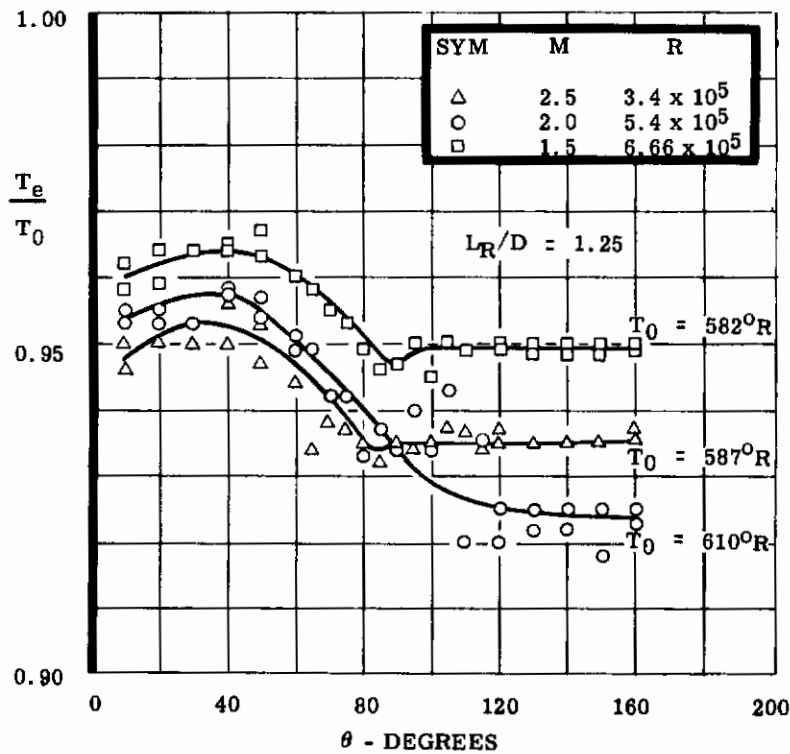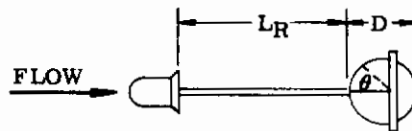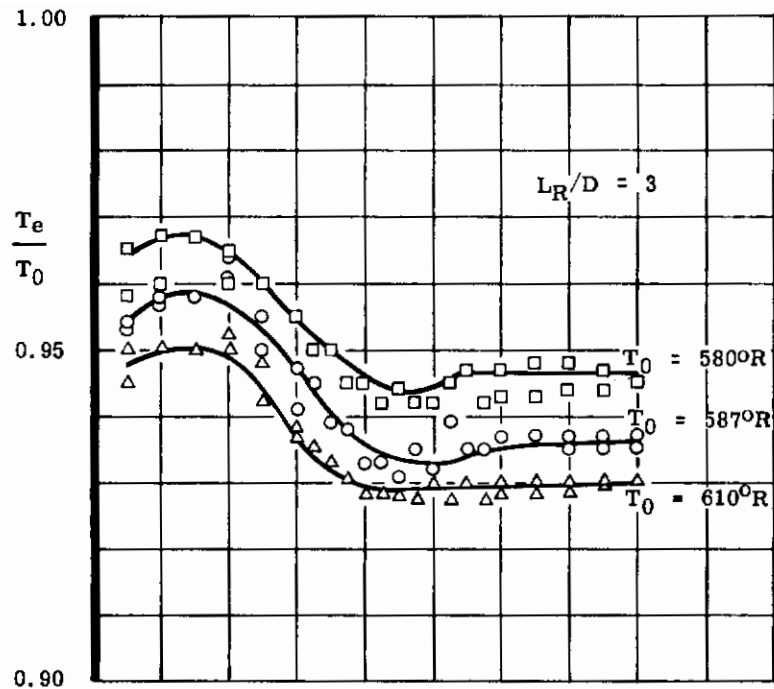
Figure 134. Temperature Recovery Distribution on a Sphere with Fence and Symmetrical Capsule
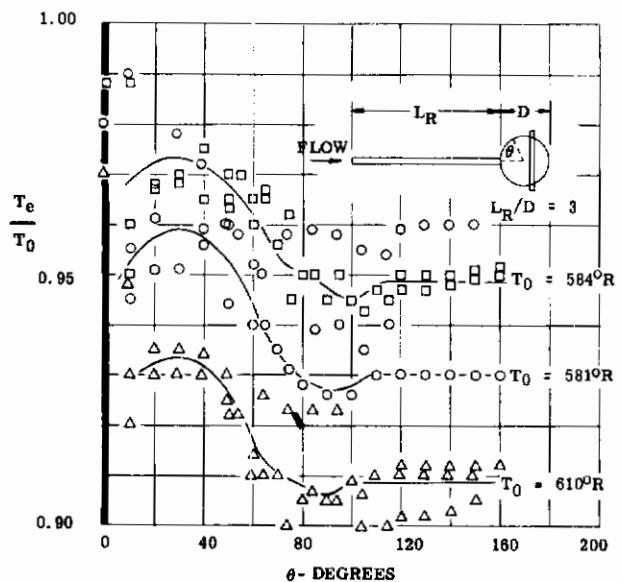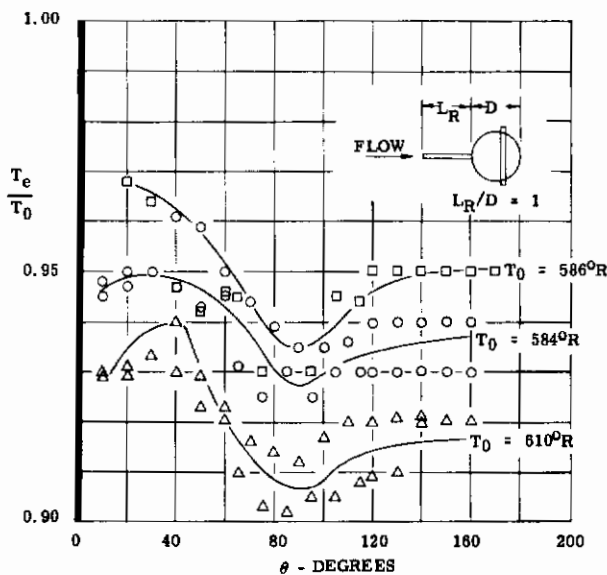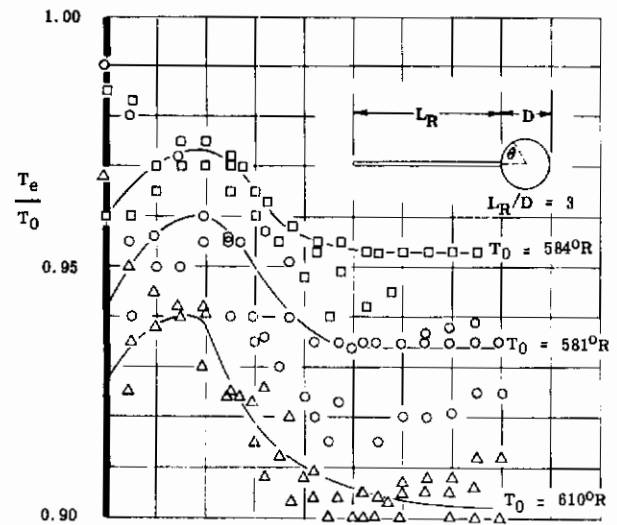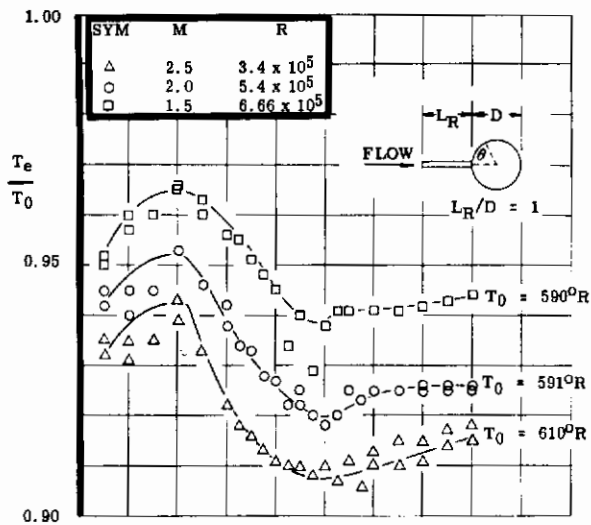
Figure 135. Temperature Recovery Distribution with a Spike, $L_R/D = 3$

Figure 136. Temperature Recovery Distribution with a Spike, $L_R/D = 1$
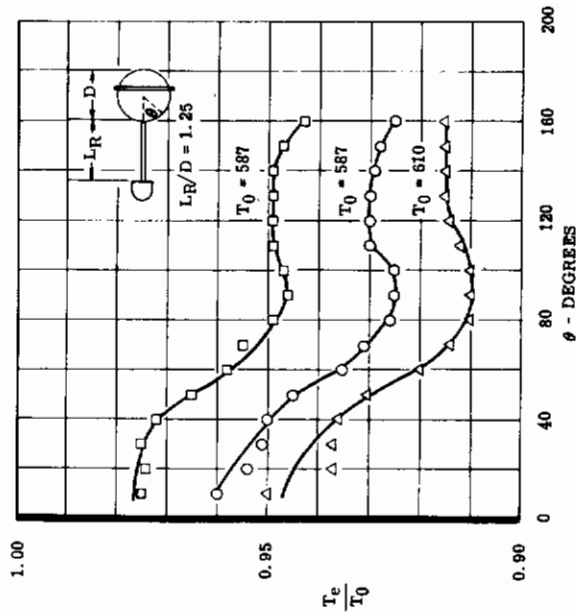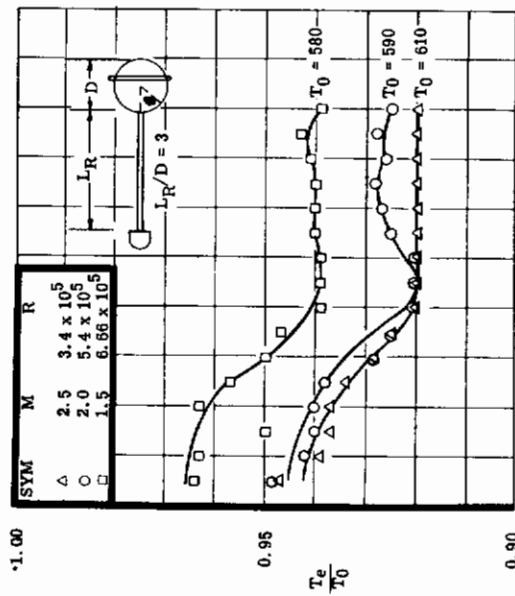
Figure 138. Temperature Recovery Distribution with Symmetrical Forebody, $L_R/D = 1$
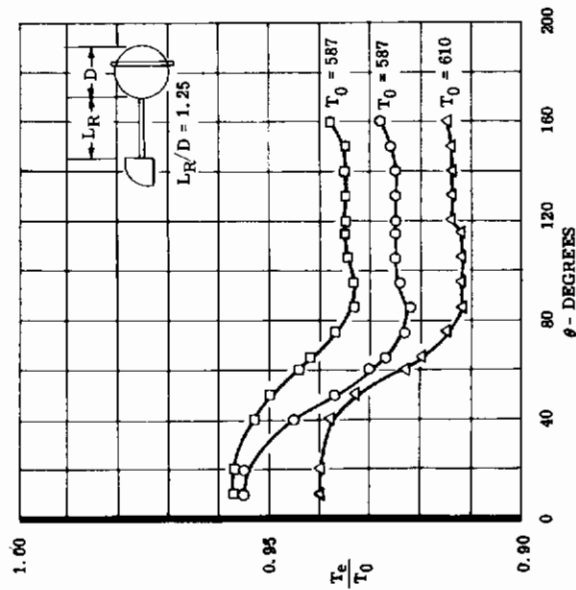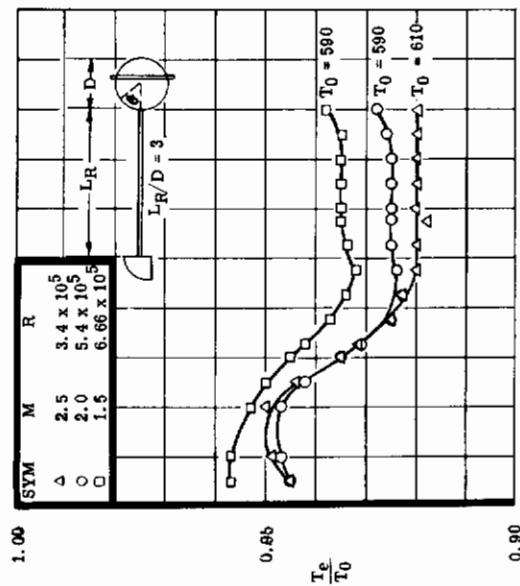
Figure 137. Temperature Recovery Distribution with Unsymmetrical Forebody, $L_R/D = 3$
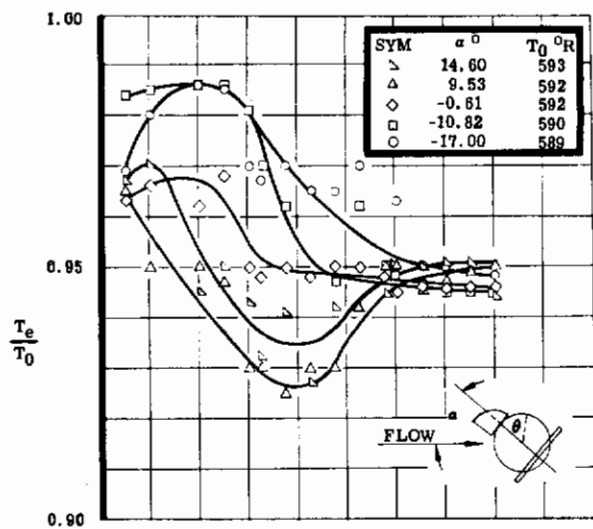
Figure 139. Temperature Recovery Distri-
bution, M = 1.5, R = 6.66 x 10^{5}
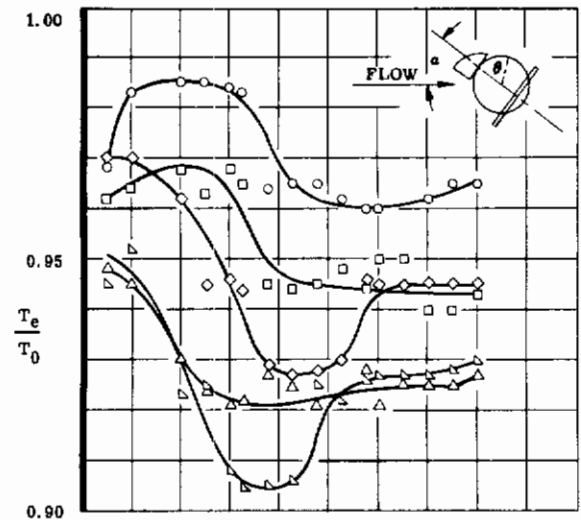
Figure 140. Temperature Recovery Distri-
bution, M = 2.0, R = 5.4 x 10^{5}
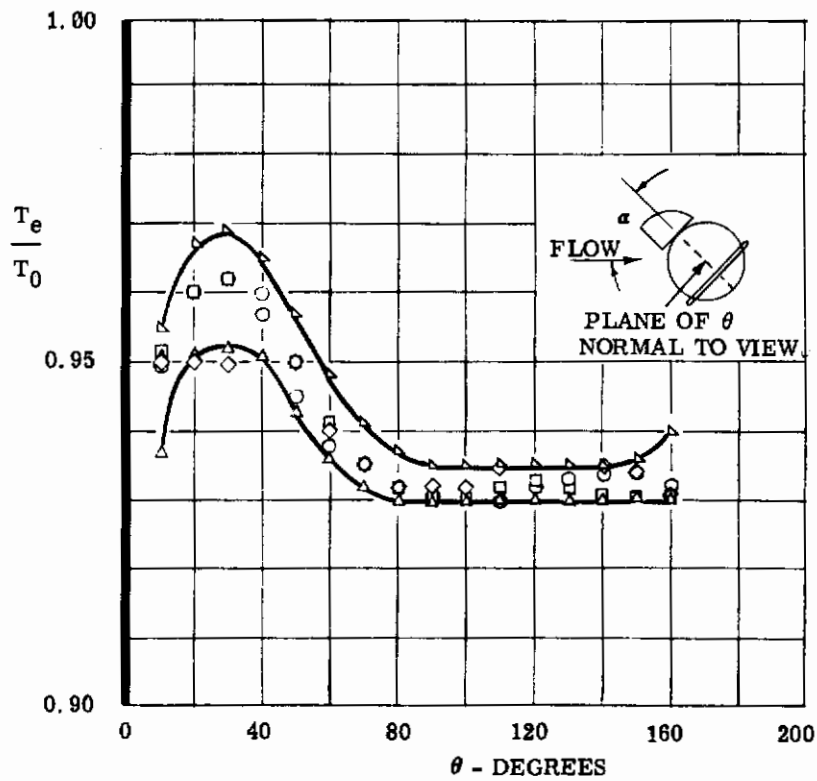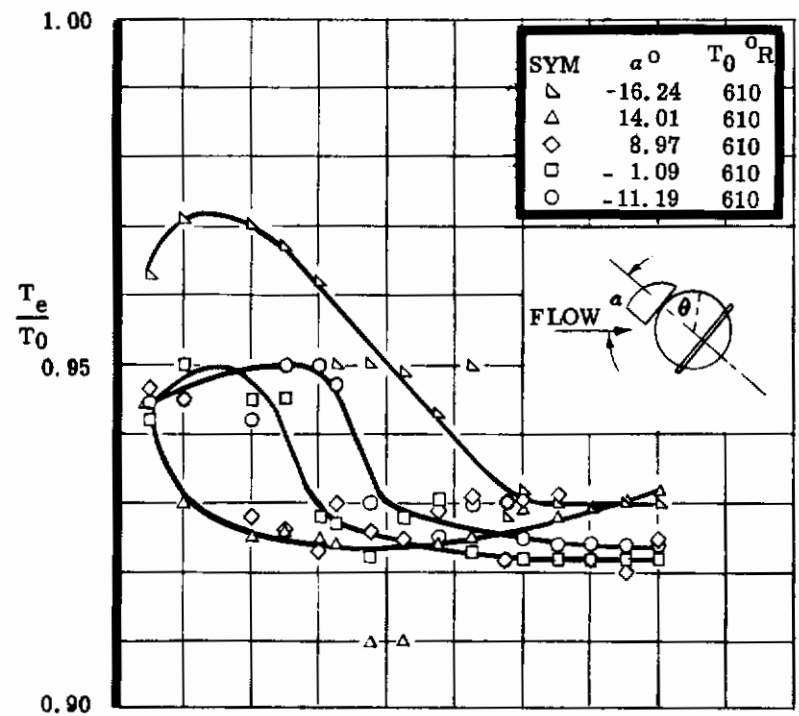
Figure 141. Temperature Recovery Distribution, M = 2.5, R = 3.4 x 10^5
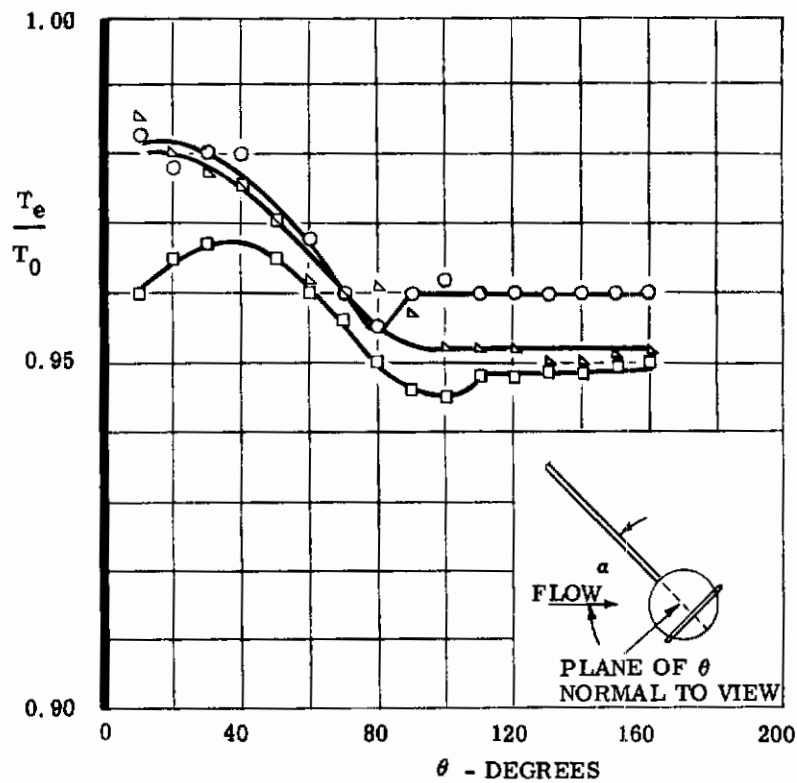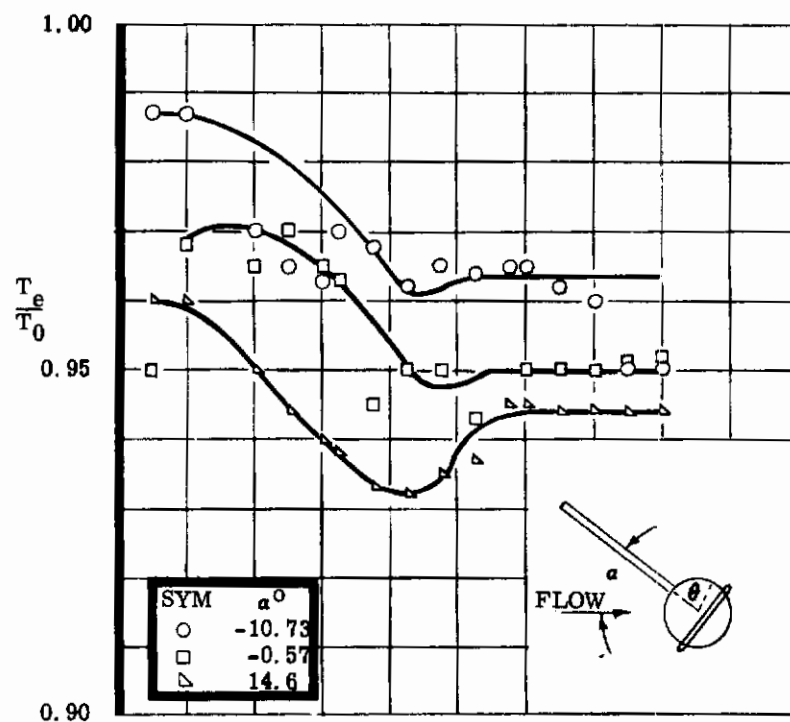
Figure 142. Temperature Recovery Distribution, $M = 1.5$, $T_0 = 584^O R$, $L_R/D = 3$
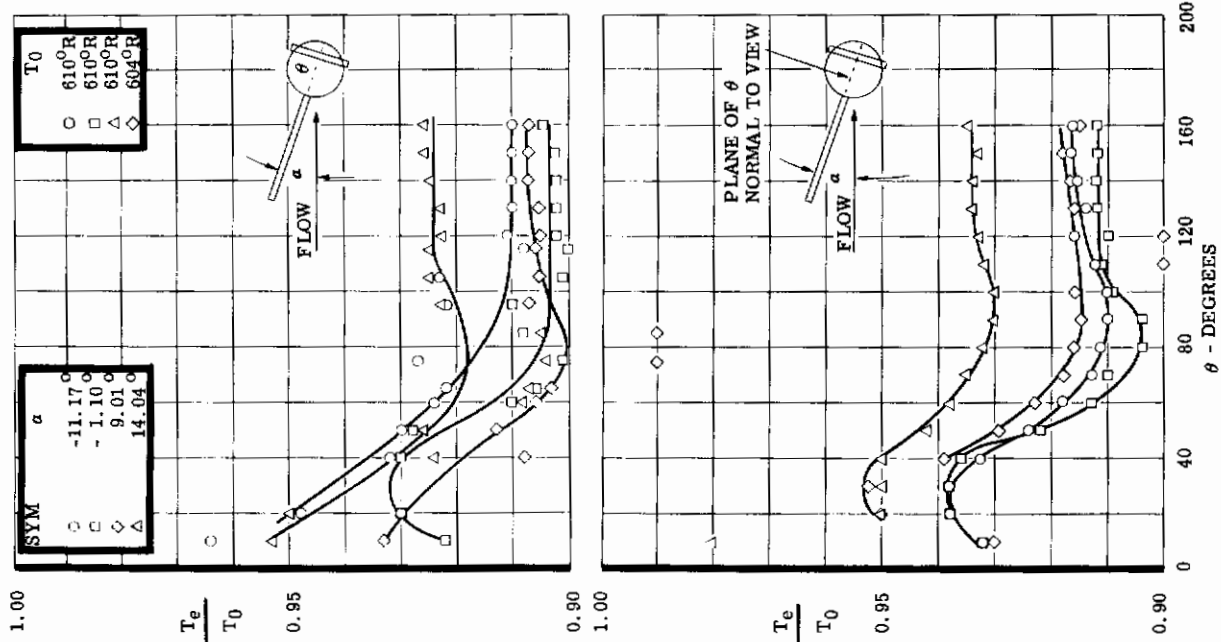
Figure 143. Temperature Recovery Distribution, M = 2.00, T₀ = 581°R, LR/D = 3
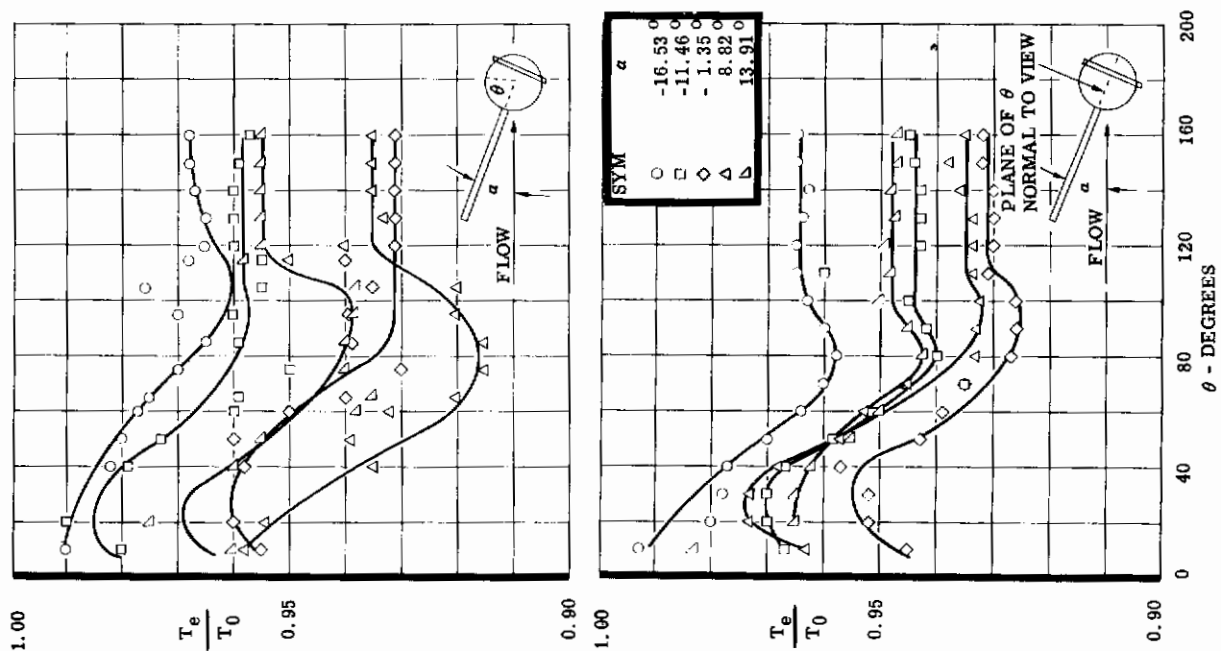
Figure 144. Temperature Recovery Distribution, M = 2.5, LR/D = 3
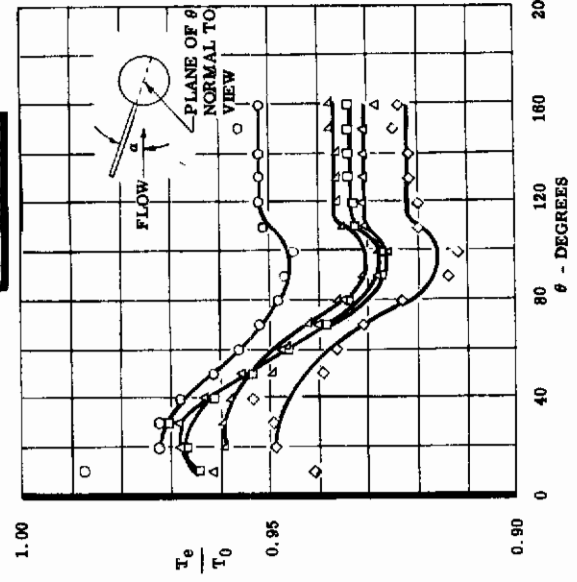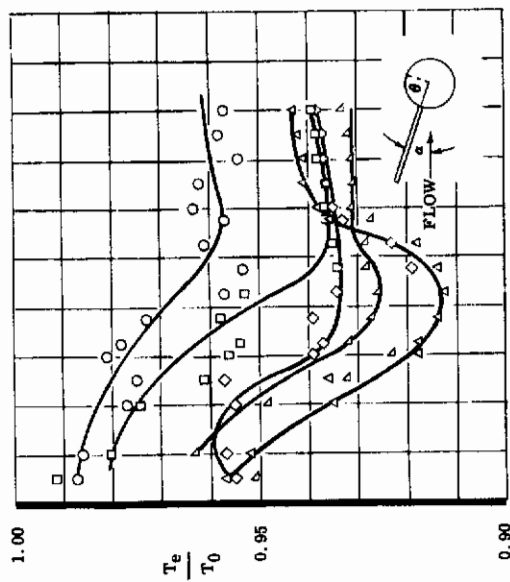
Figure 146. Temperature Recovery Distribution,
M = 2.0, L_R/D = 3
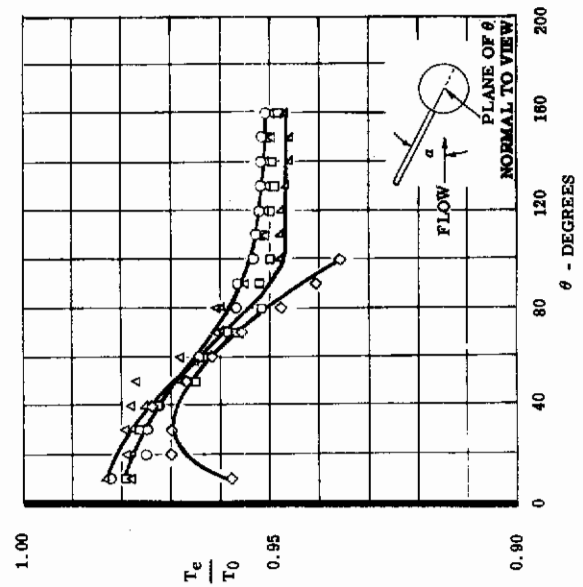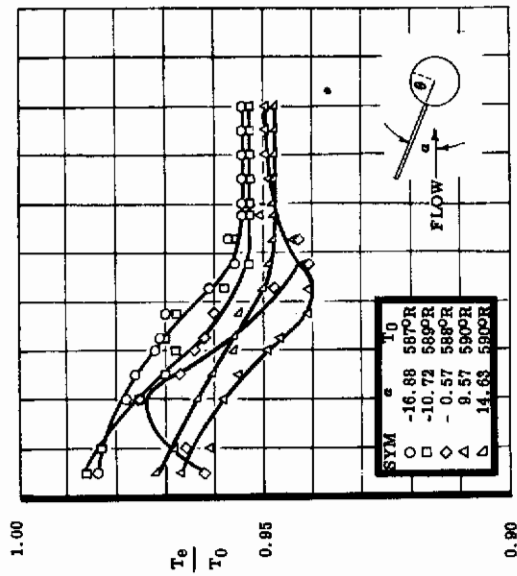
Figure 145. Temperature Recovery Distribution,
M = 1.5, L_R/D = 3
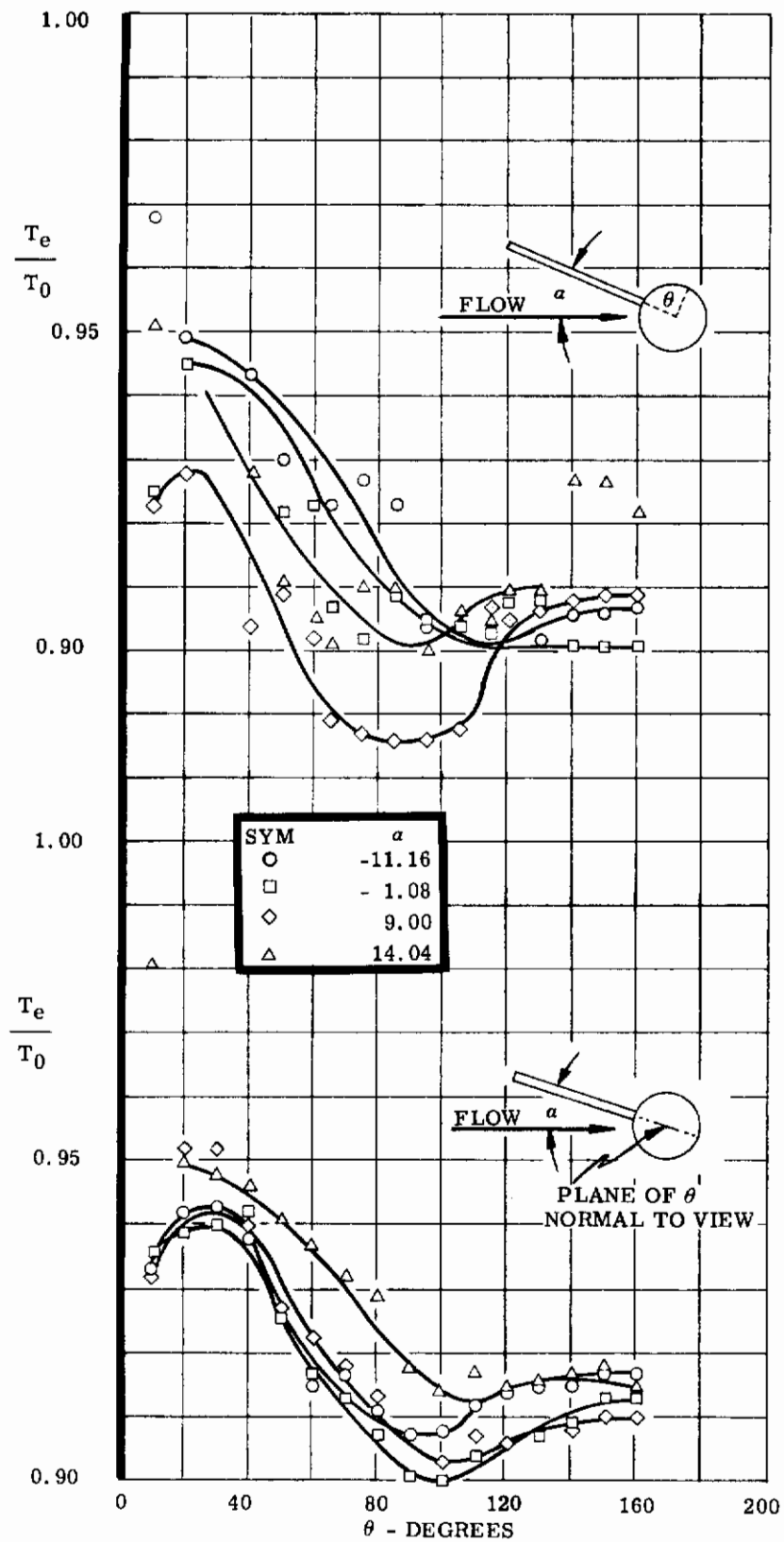
Figure 147. Temperature Recovery Distribution, M = 2.5, $T_0 = 610^O R$, $L_R/D = 3$
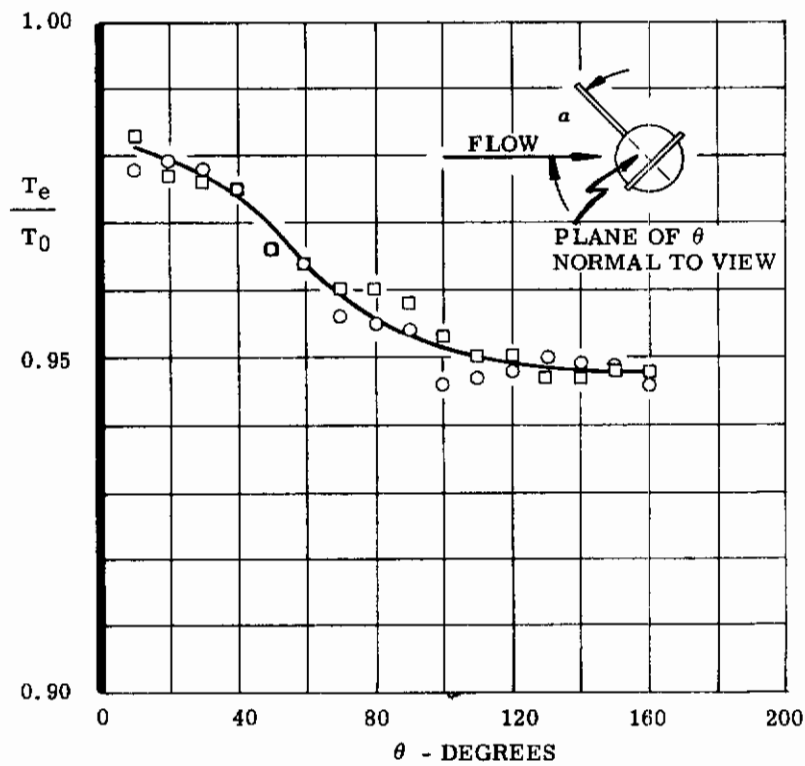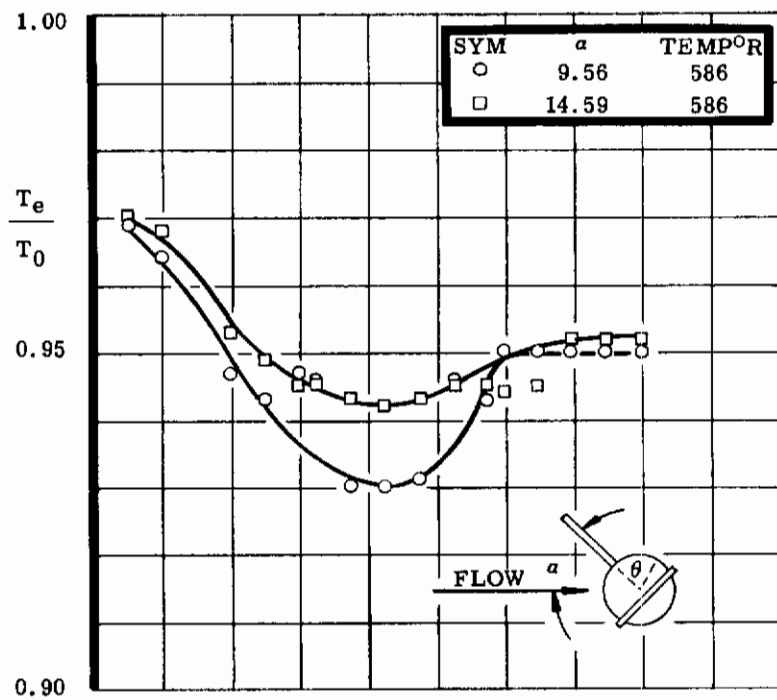
Figure 148. Temperature Recovery Distribution, $M = 1.5$, $R = 6.6 \times 10^5$, $L_R/D = 1$
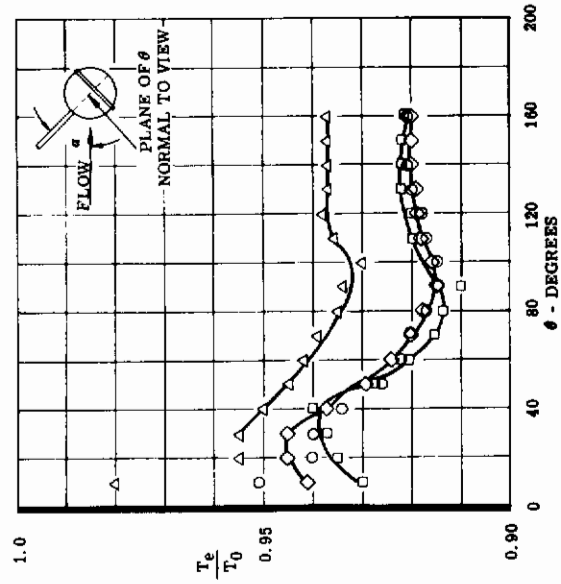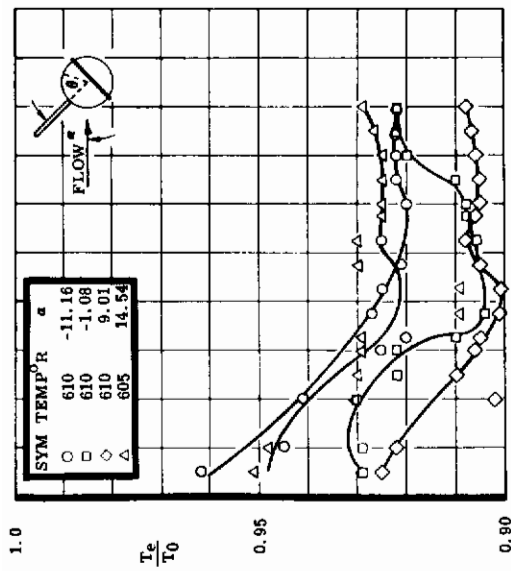
Figure 150. Temperature Recovery Distribution,
M = 2.5, R = 3.4 x 105, L_R/D = 1
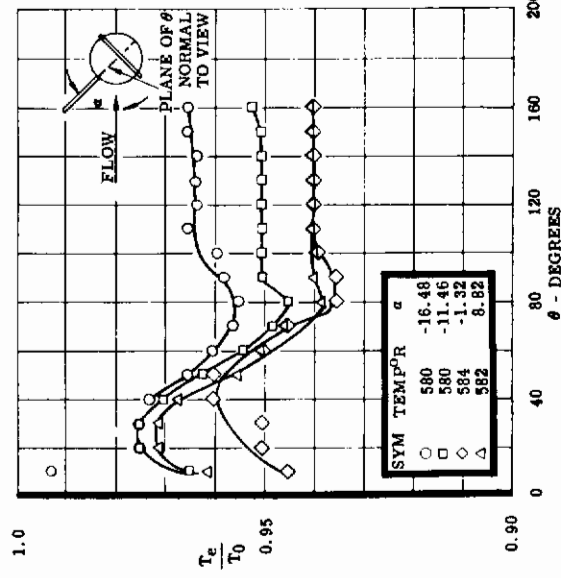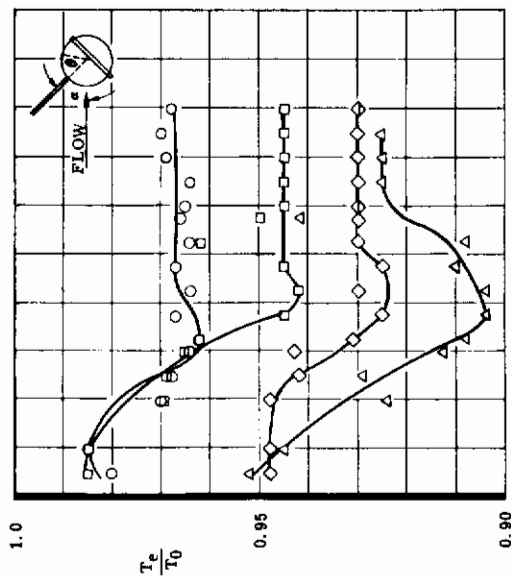
Figure 149. Temperature Recovery Distribution,
M = 2.0, R = 5.4 x 105, L_R/D = 1

Figure 152. Temperature Recovery Distribution, $M = 2$, $L_R/D = 1$

Figure 151. Temperature Recovery Distribution, $M = 1.5$, $L_R/D = 1$, $R_n = 10^6$
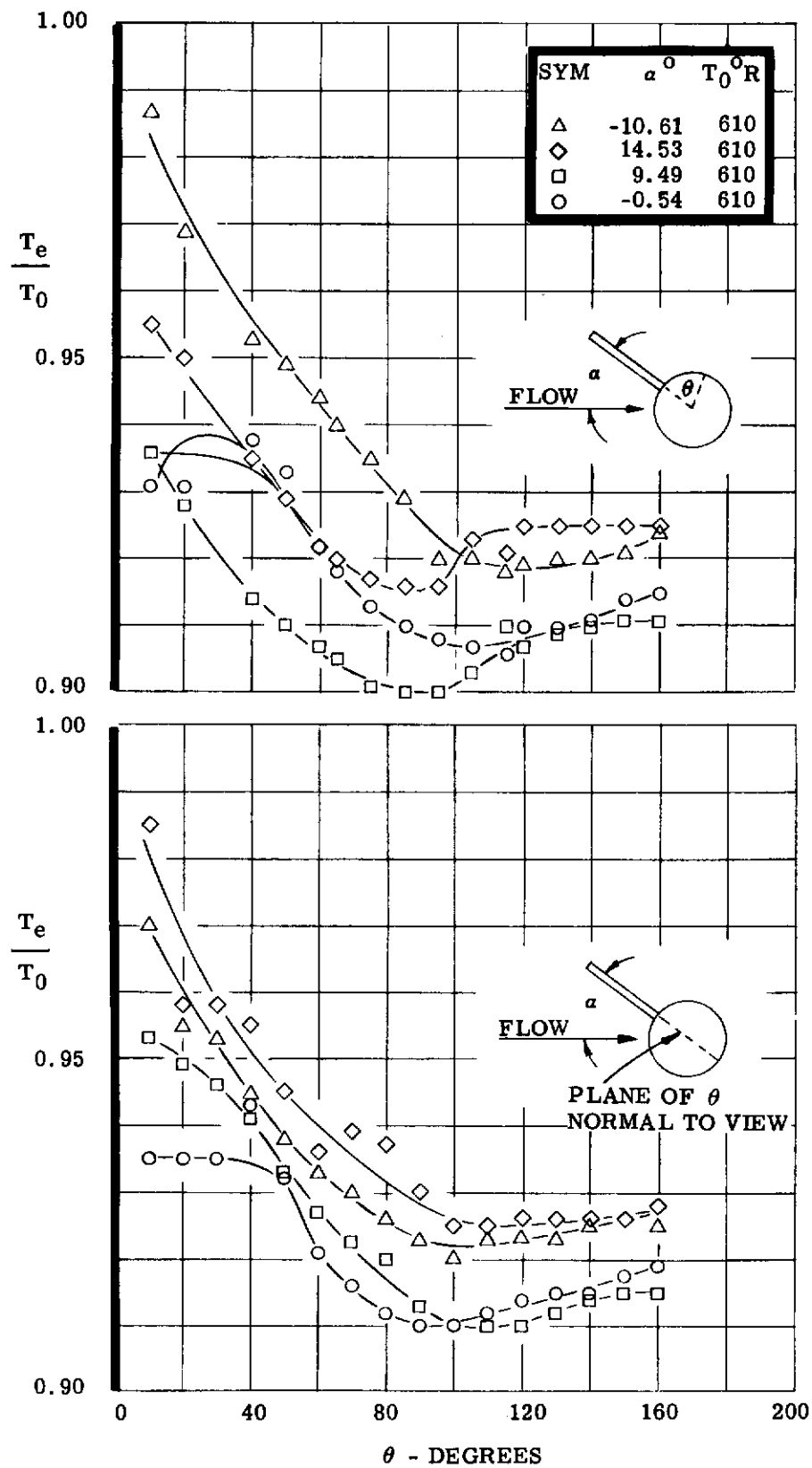
Figure 153. Temperature Recovery Distribution, M = 2.5; L_R/D = 1;
R = 3.4 x 10^5 and a = 10.61, 14.53, 9.49, -0.54

average T_e/T_0 is somewhat lower for the spheres in the wake of primary bodies than that for the clean sphere model.

The theoretical local heat transfer parameter, the Nusselt number, is presented as a function of local Reynolds number in Figure 154 for the sphere in the wake of a spherical body, at $L_R/D = 3$ and $L_R/D = 1.25$, and for a clean sphere in similar free stream conditions. The data presented represents calculated values based upon the local pressure data taken during the tests. The reference used in these calculations is $\theta = 90$ degrees where the pressure coefficients from Figures 80 and 99 show similar values for the two different configurations at similar free stream Reynolds number. Isentropic conditions were assumed to exist in the vicinity of the sphere, thereby permitting calculation of the local properties.

Laminar flow correlations were utilized in calculation of the Nusselt number for the clean sphere. An examination of the Schlieren photographs indicates turbulence in the flow existing on the leading half of the sphere in the wake of a spherical body. The results as presented in Figure 154 are based upon turbulent flow theory.

The theoretical local heat transfer coefficients were calculated and are plotted as a function of local Reynolds number in Figure 156. These data show a definite increase in the theoretical heat transfer coefficient for the sphere in the wake of a sphere configuration, over that for the clean sphere.

The conclusions herein have been verified in part in Reference 26. Reference 27, however, notes a decrease in the heat transfer coefficient under some conditions of laminar flow in the separated region.

Additional testing including heat transfer rate and time parameters would be desirable for definite determination of the flow conditions from a thermal standpoint. This experimental data is required for support of the theoretical results presented in this report.

C. NASA LEWIS RESEARCH CENTER TESTS

1. General

The purpose of the NASA Lewis wind tunnel tests was to study (at supersonic ranges) the inflation, deployment, and stability characteristics of a 25-percent (26.1 inch diameter) scale model and to study the stability characteristics of a 7.5 percent (7.9 inch diameter) scale model. Prior to these tests NASA wind tunnel personnel advised Goodyear Aircraft Corporation that the Mach number and pressure would be difficult to define due to the extremely low density test conditions. Subsequent to these tests it was determined that the method used to obtain drag data could not be established as a reliable method. Therefore, the aerodynamic data presented will be referred to as "indicated" data.

2. Discussion

In January 1960, two series of wind tunnel tests were conducted, using dynamic drag models depicted in Figures 157 through 160. The capsule model was supported in the tunnel by a yoke attached to a ceiling support strut. On command the yoke allowed the capsule to pitch freely about the capsule's center of gravity which was placed (by means of ballast) at 64 percent capsule length aft of the capsule nose. A ceiling-to-floor strut located approximately 30 feet down-stream of the capsule support strut was used to channel a model restraint chord to the outside of the tunnel. This restraint chord was pulled tight during tunnel shutdown in order to keep the model from being damaged.

There were basically three test configurations:

(1) Tethered 25-percent scale model partially inflated.

(2) Tethered 7.5-percent scale model fully inflated.

(3) Tethered 25-percent scale model fully inflated.
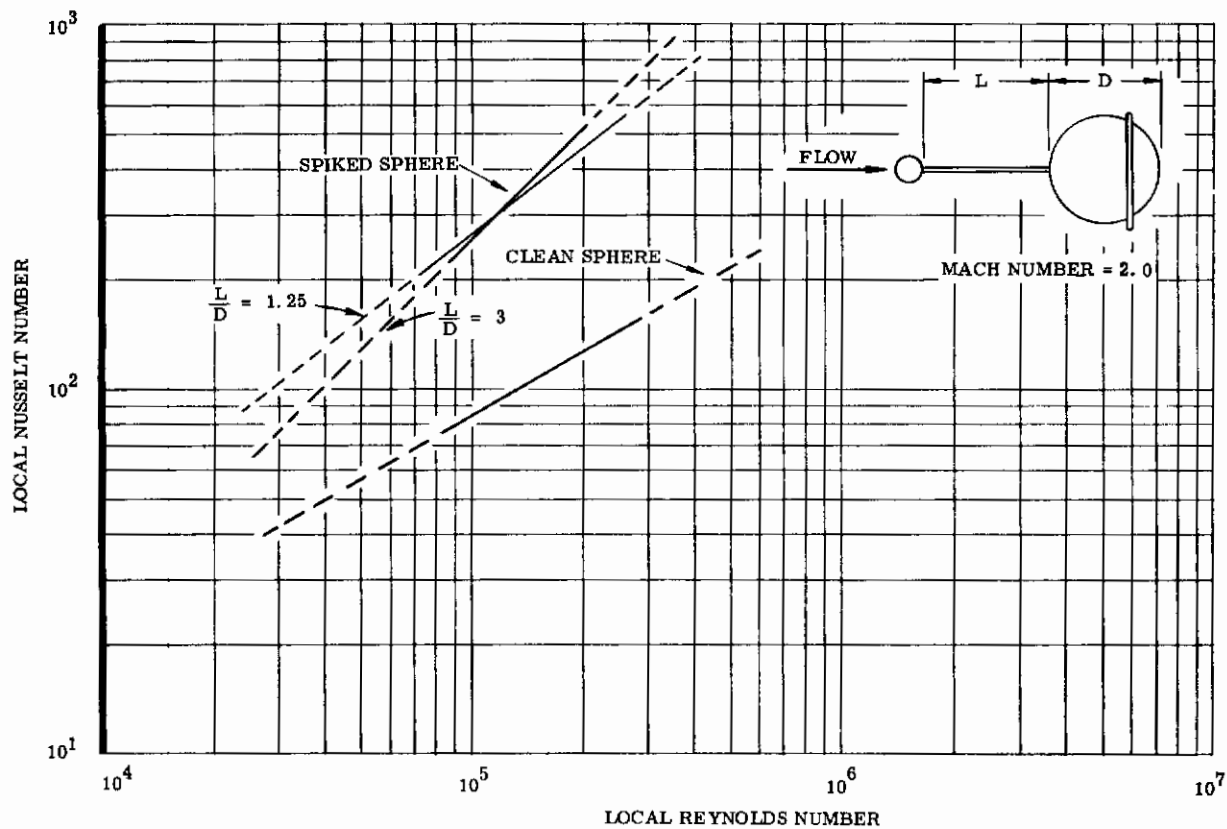
Figure 154. Nusselt Number versus Reynolds Number for Clean and Spiked Spheres
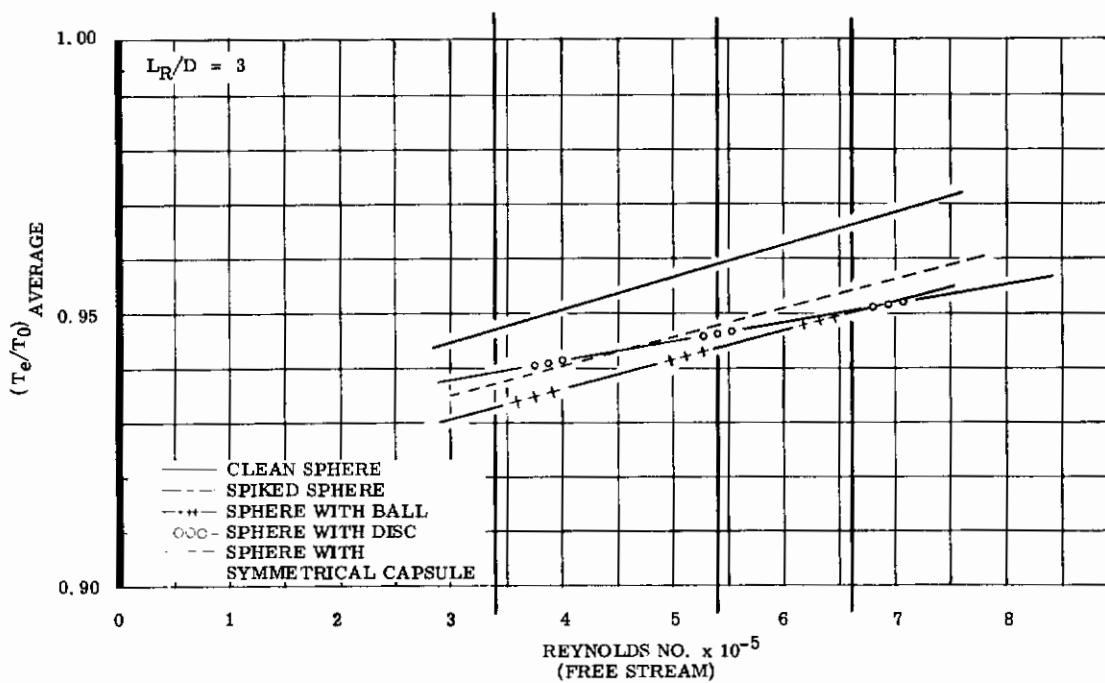
Figure 155. Average Recovery Temperature Ratio versus Free-Stream Reynolds Number
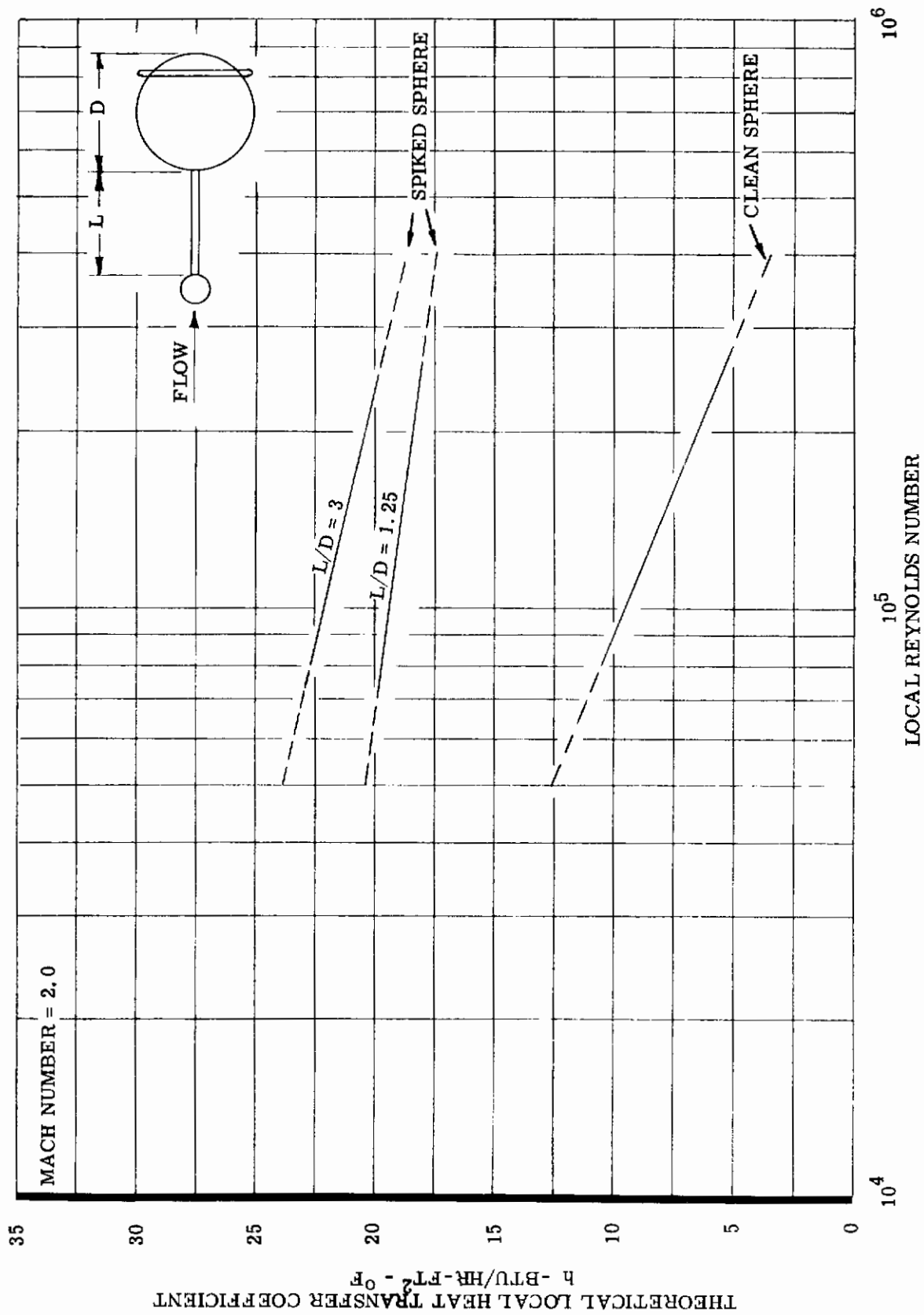
Figure 156. Theoretical Local Heat Transfer Coefficient versus Local Reynolds Number for Clean and Spiked Spheres

Figure 157. Wind Tunnel Test Setup of 25-Percent Capsule and Stowed Model
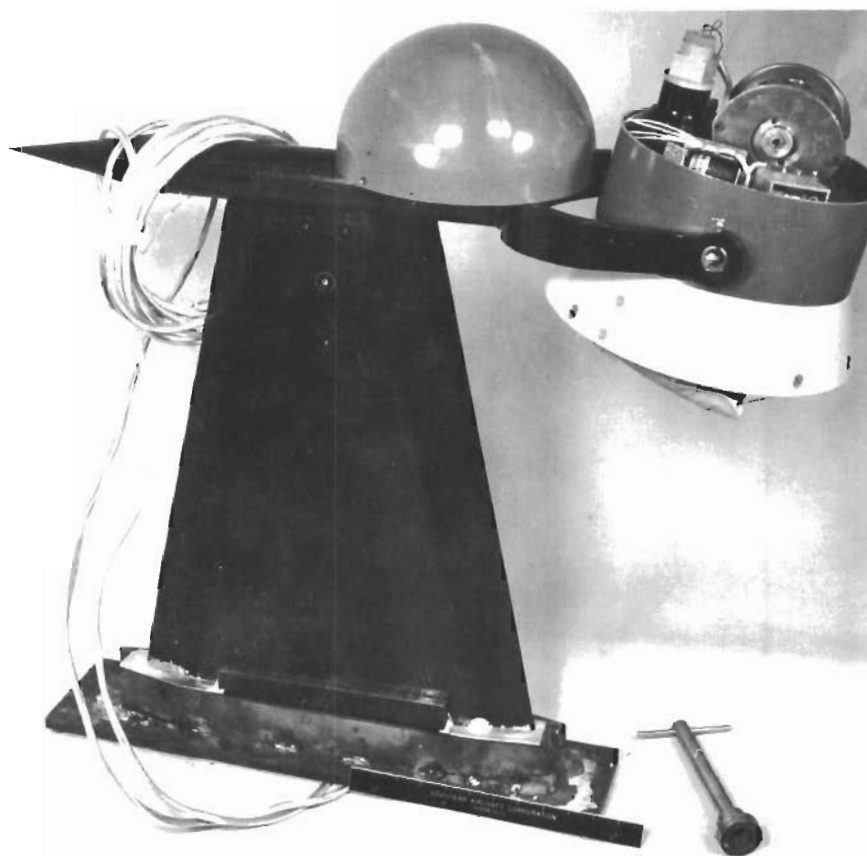
Figure 158. Deployment Reel and Pressure Bottle in 25-Percent Capsule
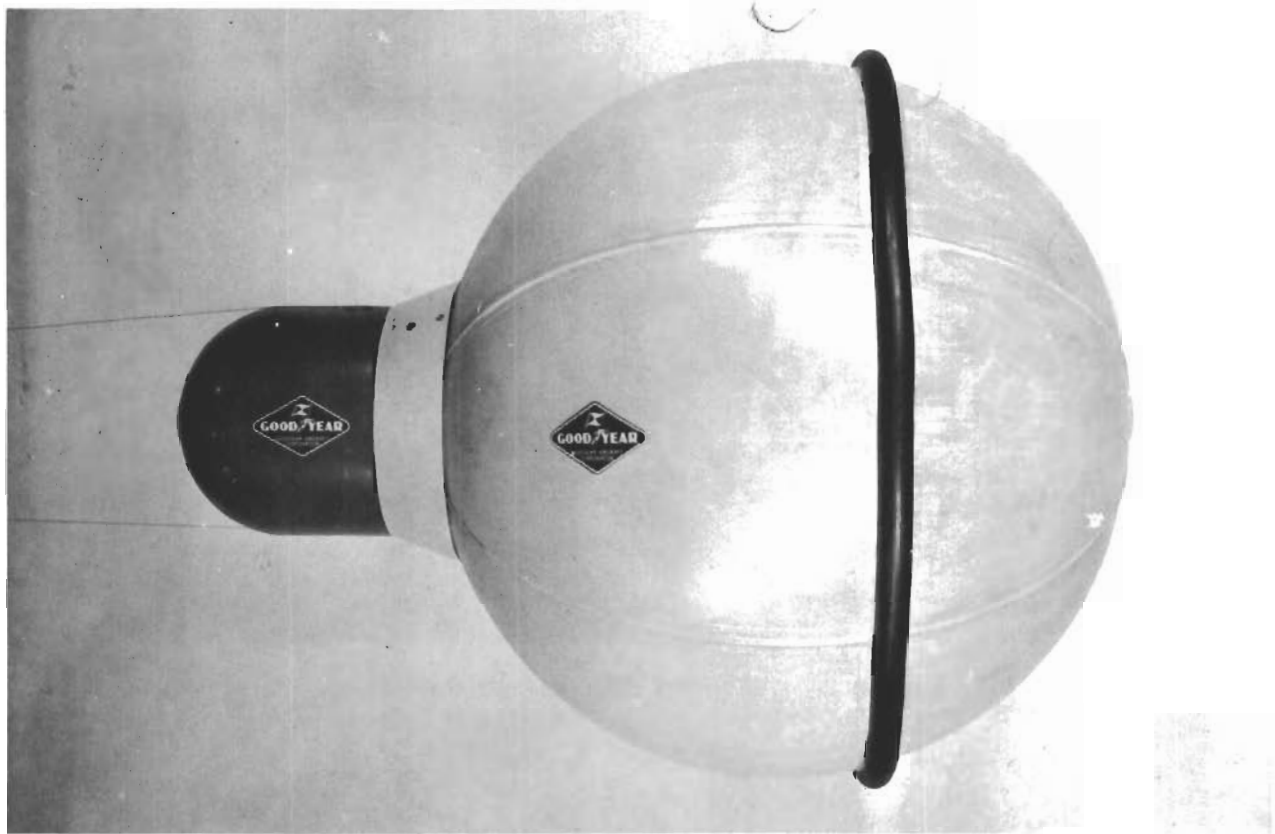
Figure 159. Inflated Sphere in First Stage of Deployment Behind 25-Percent Capsule
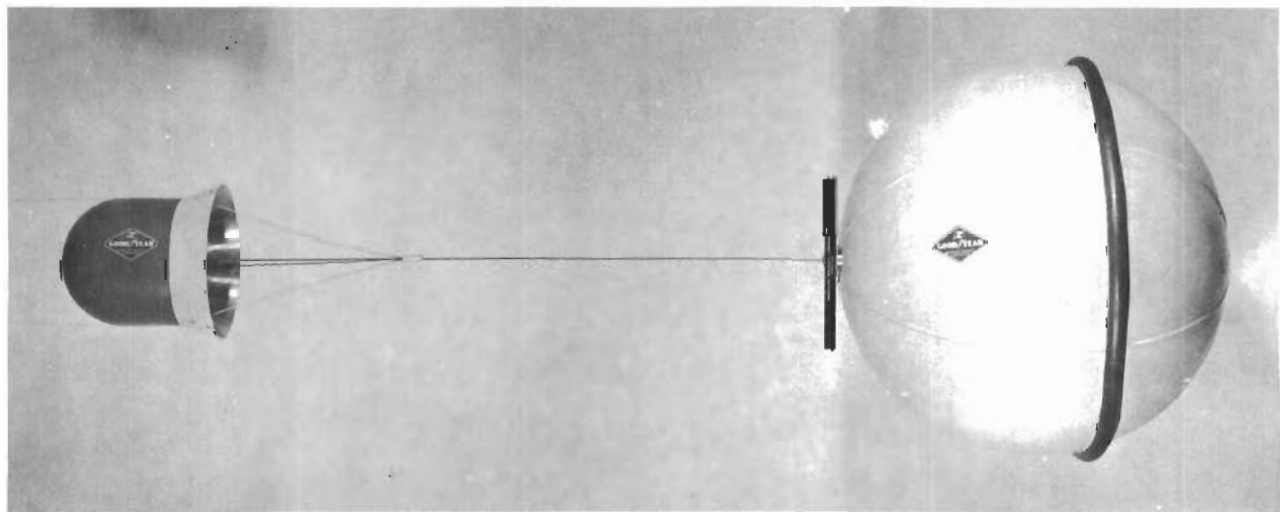
Figure 160. Inflated Sphere Fully Deployed Behind 25-Percent Capsule

A 30 cubic inch, 480 psi inflation bottle, housed in the capsule, was used to inflate the 26.1 inch diameter model. The stress analysis of the 25-percent scale model is presented in Reference 28.

3. Test Program

a. Test I - Inflation and Deployment of the 26.1-Inch Diameter Model. The 25-percent scale model was spiral-folded into the rear opening of the capsule after a vacuum pump was used to pump the ambient air out of the model. The deflated model was held in place by a lace of threads across the rear of the capsule.

The capsule was locked into a 30-degree angle of attack position by means of a solenoid actuated pin. The restraint chord remained slack to prevent pulling the model out of the capsule.

The tunnel was started at a Mach number of 2.0 and a dynamic pressure of 54 psf. The model restraint chord whipped up and down and pulled the model out of the capsule. The model inflation squib was fired on command but the model was pulled off the inflation valve as it was being inflated. Because the model was under-inflated it was deformed to a pear shape. The separation fence which was 15 degrees aft of the equator was not inflated. The angle of attack, lock pin solenoid was energized but did not release the capsule from the 30-degree angle of attack position due to the unscheduled high drag load. The model, approximately 3 inches from the base of the capsule, exhibited excellent pitch stability, but appeared to have a high spin rate. The riser line reel lock was released and the model reeled out to a riser line length of 65 inches. As the model was reeled out, the resulting drag released the set angle of attack of the capsule and stabilized the capsule to a zero angle of attack altitude. At this 65-inch riser line position the model exhibited excellent pitch and yaw stability with no rolling. A high-speed movie was taken to record the degree of aerodynamic stability. The drag coefficient of the partially-inflated model was measured at a riser line length of 65 inches and varied from 0.743 to 0.695 due to inaccuracies in the strain gage balance read-out equipment. The Mach number was not varied from 2.0 because determination of the aerodynamic characteristics of a partially-inflated model was not necessary.

During tunnel shutdown the restraint chord became tangled at the rear ceiling-to-floor strut and could not be pulled taut. Consequently, the model was violently pitched against the tunnel floor and ceiling during tunnel shutdown. Post-run inspection revealed that the model had completely deflated. The meridian cable cover strips were torn back 1/4 to 1/2 inch by the meridian cables. It was later concluded that the drag strain gage link was damaged during tunnel shutdown of this test.

b. Test II - Stability Study of the 7.5-Percent Scale Model. The 7.5-percent model was not packed into the capsule. With an internal pressure of approximately 5 to 10 psi, the model was attached to the capsule with the riser line length at 65 inches. The capsule was at zero angle of attack for this test. The restraint chord was attached to the rear of the model and pulled taut from outside the tunnel so the model was held suspended 65 inches aft of the capsule base. The tunnel was again started at Mach 2.0 with a dynamic pressure of 54 psf. The Mach number was increased to 3.5 where the tension in the restraint chord was released. A slight $\pm$ 3 degree pitch and yaw activity was caused by the whipping action of the restraint chord. No rolling was observed. The slight $\pm$ 3 degree pitch and yaw activity was observed and recorded on standard and high-speed movie film. However, due to the inadequate photographic lighting facilities, a satisfactory film record was not obtained.

The following indicated test parameters were achieved for this test:

Mach Number	Pressure Altitude	Dynamic Pressure
3.5	162,000 ft	16.8 psf
3.2	151,000 ft	21.8 psf
3.0	143,000 ft	25.8 psf
2.5	123,000 ft	38.4 psf
2.0	104,000 ft	53.7 psf

Drag data could not be obtained since the strain gage link was damaged during Test I tunnel shutdown.

c. Test III - Inflation and Deployment of the 25-Percent Scale Model. The capsule was locked into a zero angle of attack position and the unfilled model was spiral-folded into the capsule. The model was held in place by a lace of thread and tape over the base of the capsule. The restraint chord was taped to the capsule yoke support providing a loop in the chord to the model attachment point. When the restraint chord was pulled taut from outside the tunnel the model could not be deployed. The same procedure as for Tests I and II was followed in starting the tunnel and increasing the flow to Mach 3.5. A 50-pound weight which was attached to the end of the restraint chord outside the tunnel was dropped to a predetermined distance to rip the chord free from the yoke support. The chord was pulled taut to take up the slack, and the angle of attack lock pin was released. The inflation squib was fired and the model began to inflate (approximately 0.1 second for inflation). As the model was inflated, the string and tape lacing broke, causing full deployment. The model was fully inflated and symmetrical. The riser line reel lock was released and the riser line increased at about one foot per second from the initial 3-inch length to a 65-inch length. The stability behavior in roll, pitch, and yaw was excellent over the range of riser line lengths. The absence of roll, pitch, and yaw activity was observed and recorded on standard and high-speed movie film at the following indicated test parameters:

MACH NUMBER	PRESSURE ALTITUDE	DYNAMIC PRESSURE (PSF)	RISER LINE LENGTH (INCHES)
3.5	162,000	16.8	3 to 65
3.2	151,000	21.8	65
3.0	143,000	25.8	65
2.5	123,000	38.4	65

The second series of tests conducted on January 14-15, 1961 consisted of two runs. The setup was the same as that used in Test III of the first series. The capsule was locked in a zero angle of attack position. The restraint chord was taped to the capsule yoke support to prevent the chord's whipping action from prematurely pulling the model from the capsule. During the first run after inflation and deployment the model exhibited excellent yaw, pitch, and roll stability characteristics. However, the model deflated due to a faulty inflation valve. Drag link data was somewhat erratic and was not considered valid.

After minor adaptations the final run was conducted. The model was inflated and deployed just aft of the capsule in approximately 0.1 second. The reel release was then actuated and the model was deployed at a rate of approximately 2 feet per second. The model remained fully inflated throughout the entire run and exhibited excellent yaw, pitch, and roll stability over the entire Mach number range. The degree of stability was recorded on standard and high-speed movie film. The drag of the 25-percent scale model tethered 65 inches aft of the symmetrical capsule (maximum diameter of 11.125 inches) is presented as indicated data in coefficient form at the following nominal tunnel parameters:

MACH NUMBER	PRESSURE ALTITUDE (FEET)	DYNAMIC PRESSURE (PSF)	REYNOLDS NUMBER PER FOOT	C_D
3.5	162,000	17.1	0.99×10^5	0.745
3.0	142,000	25.8	1.30×10^5	0.720
2.5	123,000	38.4	1.70×10^5	0.712
2.5	121,000	41.5	2.20×10^5	0.720
2.3	114,000	47.4	2.20×10^5	0.784
2.0	107,000	47.3	2.30×10^5	0.805

4. Summary

(1) The 25-percent scale model (26.1 inch diameter) was successfully inflated and deployed from a symmetrical escape capsule at a pressure altitude of 162,000 feet and a Mach number of 3.5.

(2) Excellent pitch, yaw, and roll stability were exhibited by a spherical drag body at Mach 3.5 as the riser line length was increased from 3 to 65 inches.

(3) The 25-percent scale model, when under-inflated, deformed to a pear shape at Mach 2.0 and exhibited excellent pitch and yaw stability characteristics at riser line lengths of approximately 3 to 65 inches. At a 3-inch riser line length the under-inflated model had an apparent rapid spin rate about the riser line axis. At a riser line length of 65 inches, however, the under-inflated pear-shaped model exhibited no spinning. The measured drag coefficient at Mach 2.0 for the deformed, pear-shaped model at a 65-inch riser line length varied from 0.743 to 0.695. This resulted from a temperature influence on the drag strain gage link.

(4) At a riser line length of 65 inches, excellent pitch, yaw, and roll stability characteristics were exhibited by both 7.5- and 25- percent scale models at the following nominal tunnel test parameters:

MACH NUMBER	PRESSURE ALTITUDE	DYNAMIC PRESSURE
3.5	162,000 ft	16.8 psf
3.2	151,000 ft	21.8 psf
3.0	143,000 ft	25.7 psf
2.5	123,000 ft	38.4 psf

SECTION VII

FLIGHT TESTS

A. GENERAL

Flight testing utilizing a Cree test missile, the final phase of the study and test program, was accomplished at the Air Proving Ground Center, Elgin Air Force Base, Florida. The Cree test missile, launch hardware, and test methods and procedures were products or developments of the Cook Research Laboratories Division of the Cook Electric Company.

B. TEST EQUIPMENT

Equipment used on both test missions was the standard Cree missile and related hardware shown in Figures 161, 162, and 163.

1. Test Vehicle

A standard Model 60 Cree test vehicle was used to accomplish the test missions. This vehicle contains a five-channel telemetry system, a high-speed motion picture camera, a programming system, a parachute recovery system, and a flotation system.

a. Telemetry System. The following data was gathered by the five-channel telemetry system:

(1) Shock Force
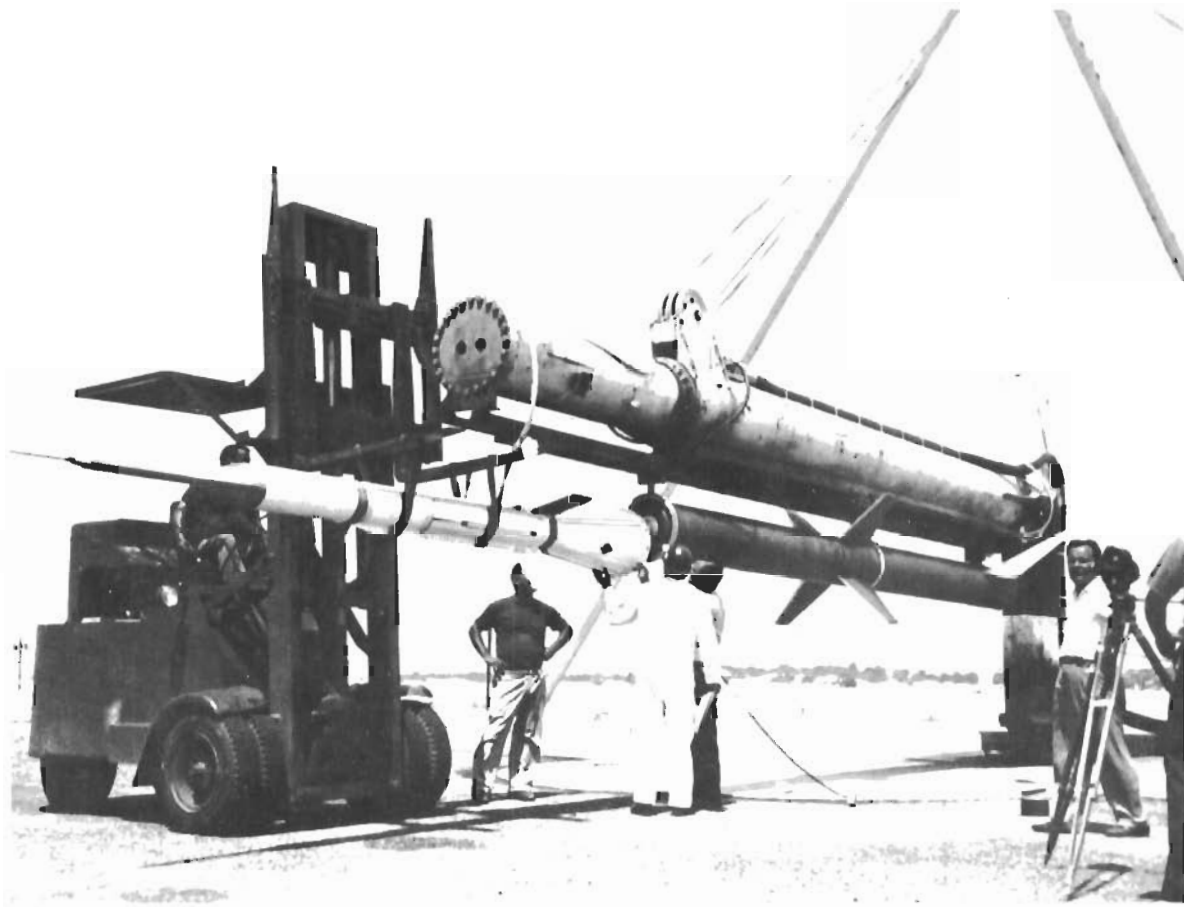
Figure 161. Missile Loading Operation

TEST PACKAGE
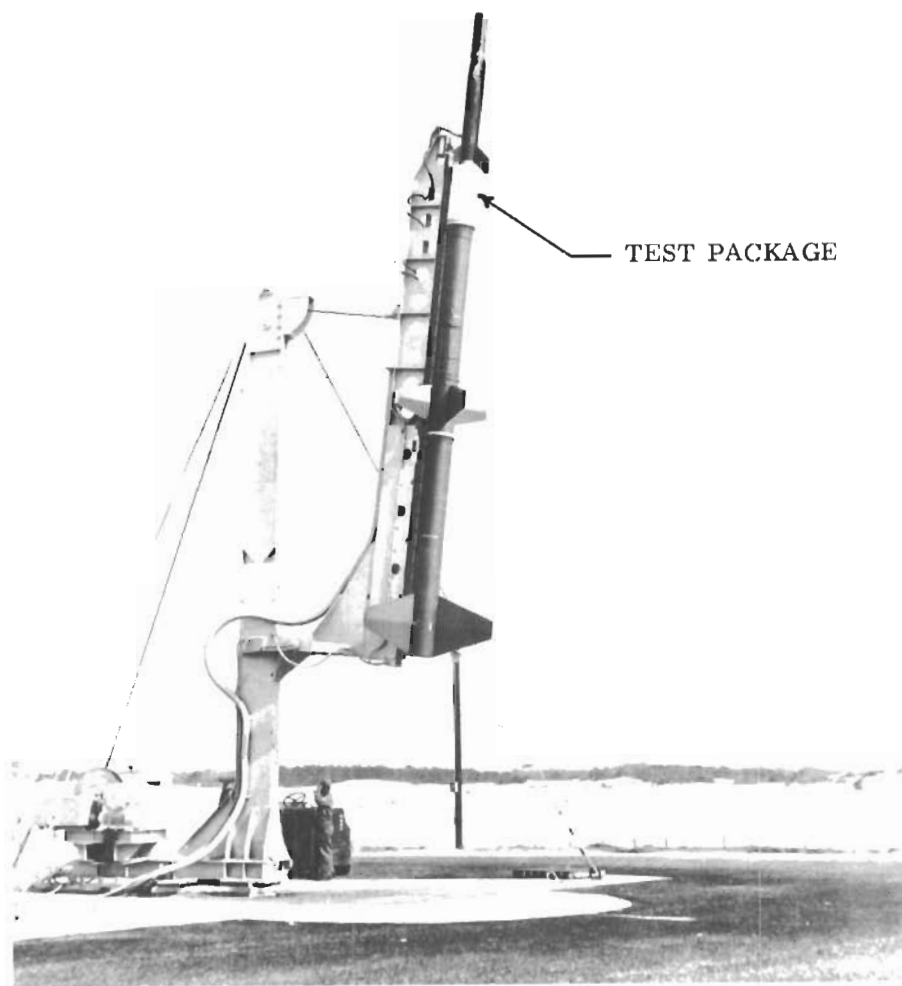
Figure 162. Nike-Nike-Type II Cree
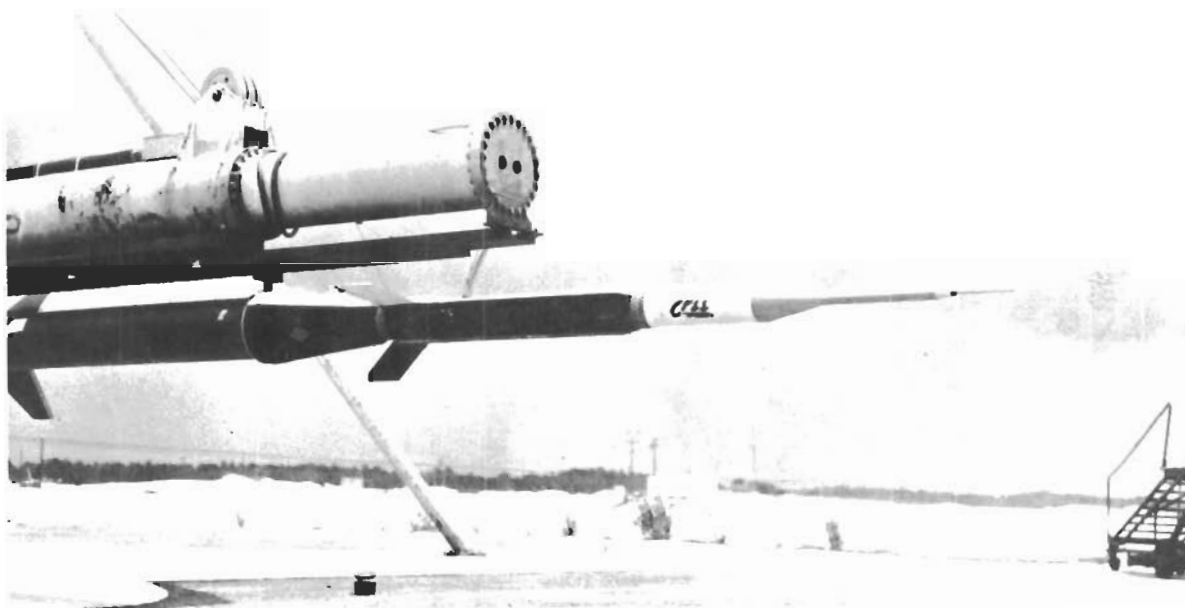
Figure 163. Inflatable Drag Device Package and Type II Cree

(2) Drag Force

(3) Acceleration

(4) Differential Pressure

(5) Inflatable Decelerator Internal Pressure

The two force inputs are obtained from strain gage bridges located on a ring-type tension measuring link located between the missile and the drag device. An accelerometer is located on the missile longitudinal axis in the forward or main instrumentation compartment. Differential pressure is measured by a pressure transducer which receives input from a probe on the tip of the vehicle nose spike. Internal pressure is measured by an absolute-type pressure transducer mounted within the inflatable drag device.

b. Photography. A motion picture camera of the rotating prism type is mounted in the aft compartment of the test vehicle. The camera is oriented to view the drag device being tested. A frame speed of approximately 200 frames/second was employed.

c. Programming System. The Cree missile programming system consists of two electro-mechanical timers. These timers operate independently and are capable of controlling a number of functions. The timers have a 120-second capacity. The functions which are normally controlled are:

(1) Pre-test calibration

(2) Second-stage separation

(3) Test item deployment

(4) Post-test calibration

(5) Recovery system initiation

(6) Flotation balloon inflation

d. Recovery System. After a suitable test period the programming system initiates the recovery phase. The recovery door is broken open by a pair of blasting caps and a strip of shaped charge. Approximately 1/10 second later the recovery parachute is deployed and the nose ballast separated.

e. Flotation System. When the payload, descending on its recovery parachute, reaches a pre-set altitude of 10,000 feet, the programming system, triggered by aneroid switches, initiates the flotation system. An explosive valve opens and air stored at about 2250 psi inflates a 24-inch-diameter flotation balloon. A short time later the balloon is separated from the missile by a device which cuts the filling hose and the tethering lines. The balloon then moves behind the recovery parachute on the end of its 25-foot riser.

2. Test Package

The test package or canister is a conically-shaped unit enclosing the supersonic inflatable decelerator and stabilization test device. The canister measures 43 inches in length tapering down from a diameter of 18-1/4 inches at its aft end, to 9.4 inches at its forward end (see Figure 164). The skin is made in three 120-degree sections joined together at the ends by two cast rings. The aft ring mounts to a mating ring on the last-stage Nike booster. The forward ring fits over an extension on the Cree missile rear bulkhead. The stress analysis of the full scale decelerator is presented in Reference 29.

Each ring has a groove running around its entire circumference. The groove is filled with an explosive (flexible linear-shaped charge). Setting off the explosive will in one case separate the booster from the test package and in the other separate the package from the Cree missile. When the aft ring is separated the three skin sections are held together at the aft end by three small clips. The package remains intact until the forward ring is broken. Once this is accomplished the skin sections are free to swing outward. Springs in the forward section force the skin panels outward.
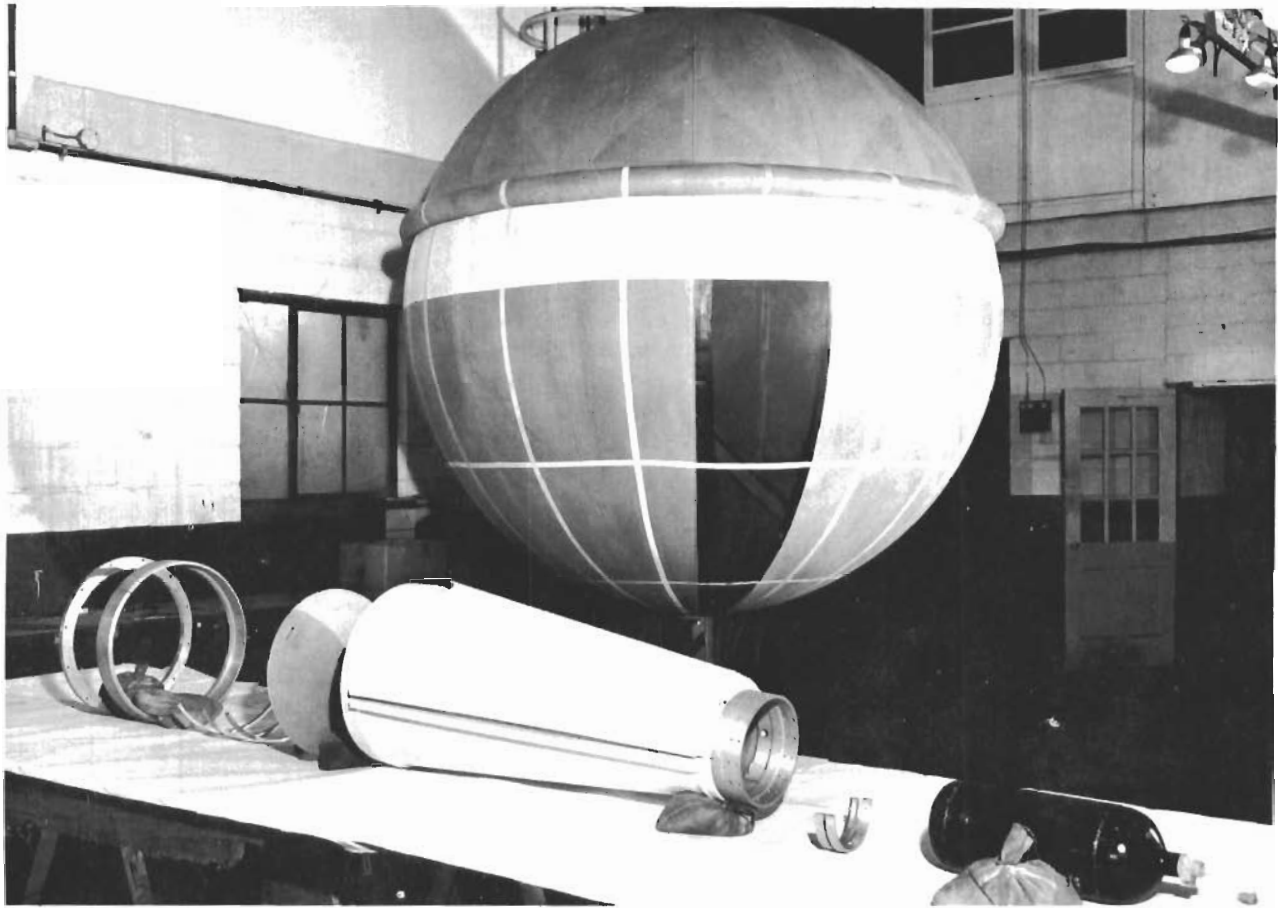
Figure 164. Nine-Foot-Diameter Inflated Deceleration Balloon, Packaging Canister, Deployment Reel, and Associated Ejection Hardware

The decelerator and stabilizator test device is an inflatable sphere of 16-gore construction, 107 inches in diameter. The material of the sphere is a high-tenacity, temperature-resistant, Dacron-neoprene fabric consisting of single-ply, square-woven cloth arranged with warp and fill directions parallel.

Inflation is delayed for 0.35 second to permit complete separation of the skin panels. Inflation is initiated by the actuation of an explosive valve located on the air reservoir within the inflatable drag device. As the drag device inflates, a constant velocity deployment reel permits the decelerator to move away from the Cree missile to a predetermined position.

C. TEST RESULTS

1. GAC Test No. 1

Description

> Date: 22 August 1960

> Time: 1206

> Test Vehicle: Type II Cree (500 pounds)

> Method: Ground launch - zero length

> Equipment: Cree launcher (Pad No. 1)

WADD TR 60-182   130

Launch Angle: 83 degrees

Azimuth: 128 degrees

Boosters: Nike first-stage, Nike second-stage

Second-Stage Ignition Time: t + 20 seconds

Second-Stage Separation Time: t + 58 seconds

Test Item Deployment: t + 68 seconds

Initiation of Recovery Phase: t + 100 seconds

Initiation of Flotation System: 10,000 foot altitude

Test Item: Goodyear 9-foot diameter inflatable drag device

Expected Test Velocity: Mach 1.44

Expected Test Altitude: 123,000 feet

Expected Dynamic Pressure at Test Altitude: 13.0 lb/sq feet

Location Aids: (1) Dye marker
            (2) Auxiliary marker buoy
            (3) Sonar beacon
            (4) Radar beacon

Tracking Aid: Radar Beacon

Data Gathering: (1) Five-channel telemetry system
              (2) Contrave Phototheodolites
              (3) DOETS telemetry system
              (4) Radar beacon and skin track

Results

The missile launch appeared normal. First stage burnout and separation occurred on schedule. Second stage ignited at the scheduled time of t + 20 seconds, and burning appeared normal. It was not possible to determine the time of second stage separation. The recovery phase apparently functioned on schedule and in a normal manner. Telemetry records and rate of descent indicate that the nose weight separated and the recovery parachute deployed. Telemetry records show time of flight was about 8 minutes and 40 seconds.

There is no evidence to indicate that the flotation system functioned. In the impact area three definite dye marker patches were signted. No flotation balloon or auxiliary marker block was visible. A search in the impact area by recovery boats proved negative. The sonar detector received no signal, and the search operation was complicated by very rough seas. After a short period the sonar detector became inoperative and the search had to be temporarily abandoned.

The search was resumed the following day after the sonar detector had been repaired. The search activity was continued for several days with negative results. It was considered impractical to call in divers until a more accurate impact point could be determined. The splash point was assumed to be within the 3/4-mile circle flown by the helicopter which was orbiting about the three dye marker patches on the water surface.

The search was never resumed since the available data did not produce an accurate impact point.

The radar beacon was tracked from launch to t + 47.8 seconds, and a skin track was established at approximately 34,000 feet during missile descent and was lost at approximately 25,000

feet. A plot of the reduced radar data, altitude versus range, is presented in Figure 165. The predicted trajectory is also presented for comparison purposes. At t + 45 seconds the radar trajectory shows a marked deviation from the predicted no-wind trajectory.

Figure 166 is a plot of MSQ-1A radar data. Altitude, velocity, Mach number, and dynamic pressure are shown as a function of time from t = 0 to t + 47.8 seconds. Although data was obtained by the contrave phototheodolites for the initial 18 seconds of flight, the results were of questionable accuracy and were abandoned in favor of the radar data.

Figure 167 shows the response of various instrumentation to loading immediately following deployment of the inflatable drag device. This figure is not presented to show load magnitudes but rather to indicate the various events occurring during the deployment sequence. Figure 167 shows that a very erratic drag device internal pressure trace was recorded. The missing segments of the curve represent times at which the frequency of data oscillation exceeded the response level of the playback instrumentation. A partial profile of the internal pressure data trace deflections (measured in millimeters) is presented. No further data were available after deployment + 0.97 seconds.

The apparent drag forces shown in Figure 167 represent only the steady state response of a damaged tensiometer. Investigation of telemetry records at times subsequent to deployment + 1.4 seconds showed no change in apparent force level to the end of the record. Tensiometer response to shock forces (70 KC channel), though not presented here, exhibit similar characteristics with an apparent force level of 560 pounds attained at deployment + 0.5 second and maintained throughout the remainder of the data record. Peak drag and shock forces, though not measurable, show indications of exceeding the operational limit (1000 pounds) of the tensiometer.

A study of Figure 167 to determine only a sequence of events will show:

(1) Deployment, separation of the Goodyear package from the Cree missile, was initiated at t + 69.44 seconds (from accelerometer data, see (1)). It is not known if separation had been accomplished at this time.

(2) Acceleration began to decrease at deployment + 0.11 second (see (2)) and became negative at deployment + 0.14 second. However, investigation of the drag data shows that no load measurement was recorded at this time. It must be concluded that drag forces causing missile negative acceleration were transferred from the deployed stabilizator-decelerator to the missile by

    (a) The riser line momentarily hanging on a protrusion such as a bolt-end.
    (b) Momentary kinking of the riser line around the tensiometer.
    (c) Incomplete cutting action of the shaped charge preventing separation or causing binding between the ring and mounting plate that was sufficient to prevent separation.
    (d) The second stage booster still attached or in close proximity to the payload.

(3) Internal pressure at time of deployment was probably higher than ambient at test altitude but somewhat less than sea level ambient, and most likely exceeded the range (0-2 psia) of the Statham transducer. Thus, the zero pressure reading of Figure 166 would represent a 100 percent deflection. After deployment and release of one or more of the canister panels, the drag device would expand due to residual pressure in the balloon resulting in a decreasing measured pressure and increasing volume. Accompanying the increase in drag area is a corresponding increase in negative acceleration from deployment + 0.14 second to deployment + 0.32 second.

(4) At approximately deployment +0.32 second negative acceleration began to decline towards zero indicating the possibility that separation of the inflatable drag device and the missile had occurred and that a portion of the drag force generated by the inflatable drag device was being expended in unreeling cable while the remaining force was expended by imparting a negative acceleration to the missile. At the corresponding deployment time the tensiometer channel indicated presence of a negatively applied load. It was impossible to ascertain the reason for the negative load. The fact that a data deflection did occur at this time must lead to the conclusion that physical load of some sort was subjected to the tensiometer.

NOTES
1. MSQ 1-A RADAR LOST TRACK
   AT LAUNCH + 47.7999 SECONDS
2. MISSILE RELOCATED DURING
   DESCENT AT AN ALTITUDE OF
   APPROX 34,000 FEET, AND
   LOST AGAIN AT APPROX
   25,000 FEET
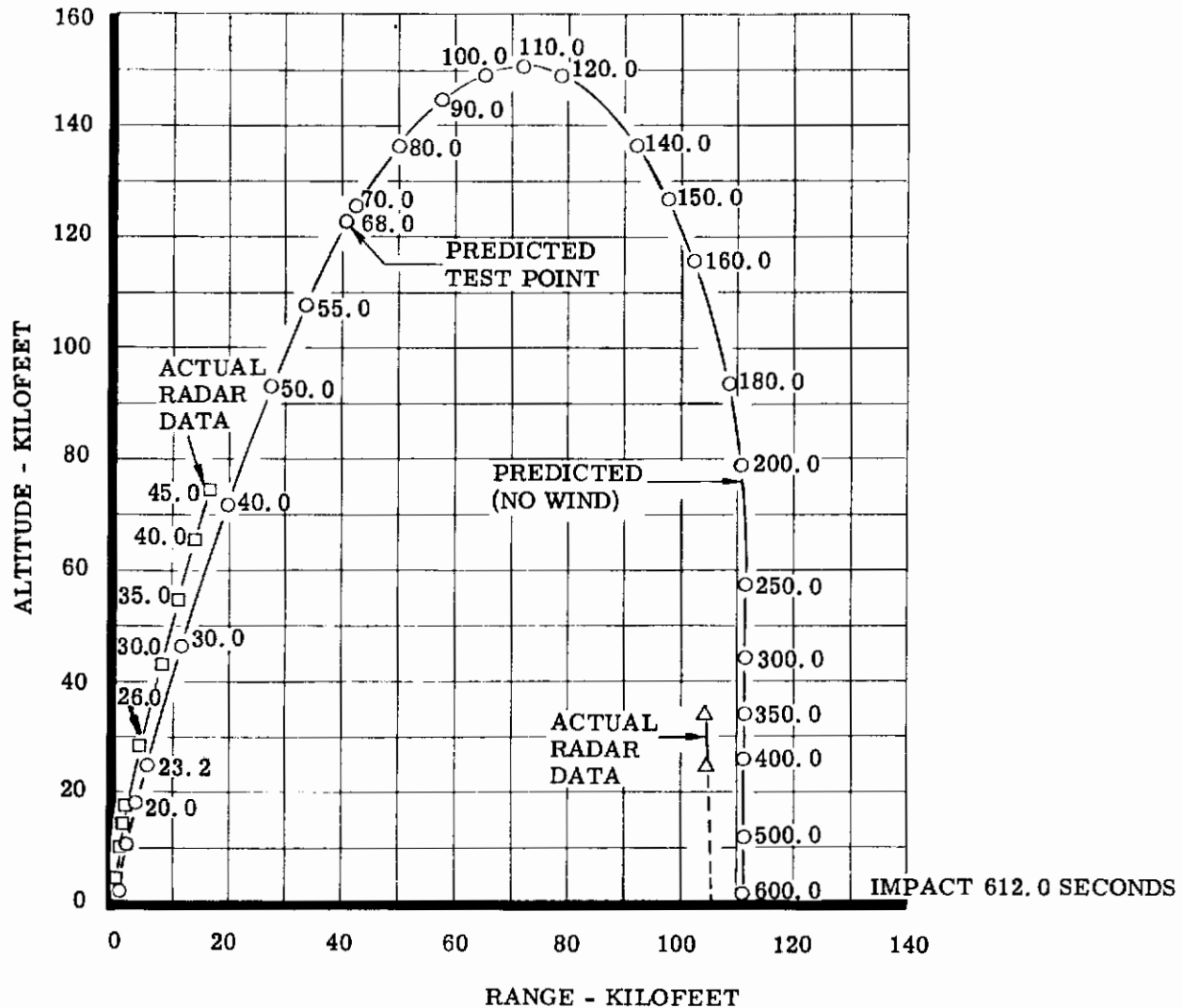
Figure 165. Predicted and Actual Trajectories for Cree Mission GAC No. 1
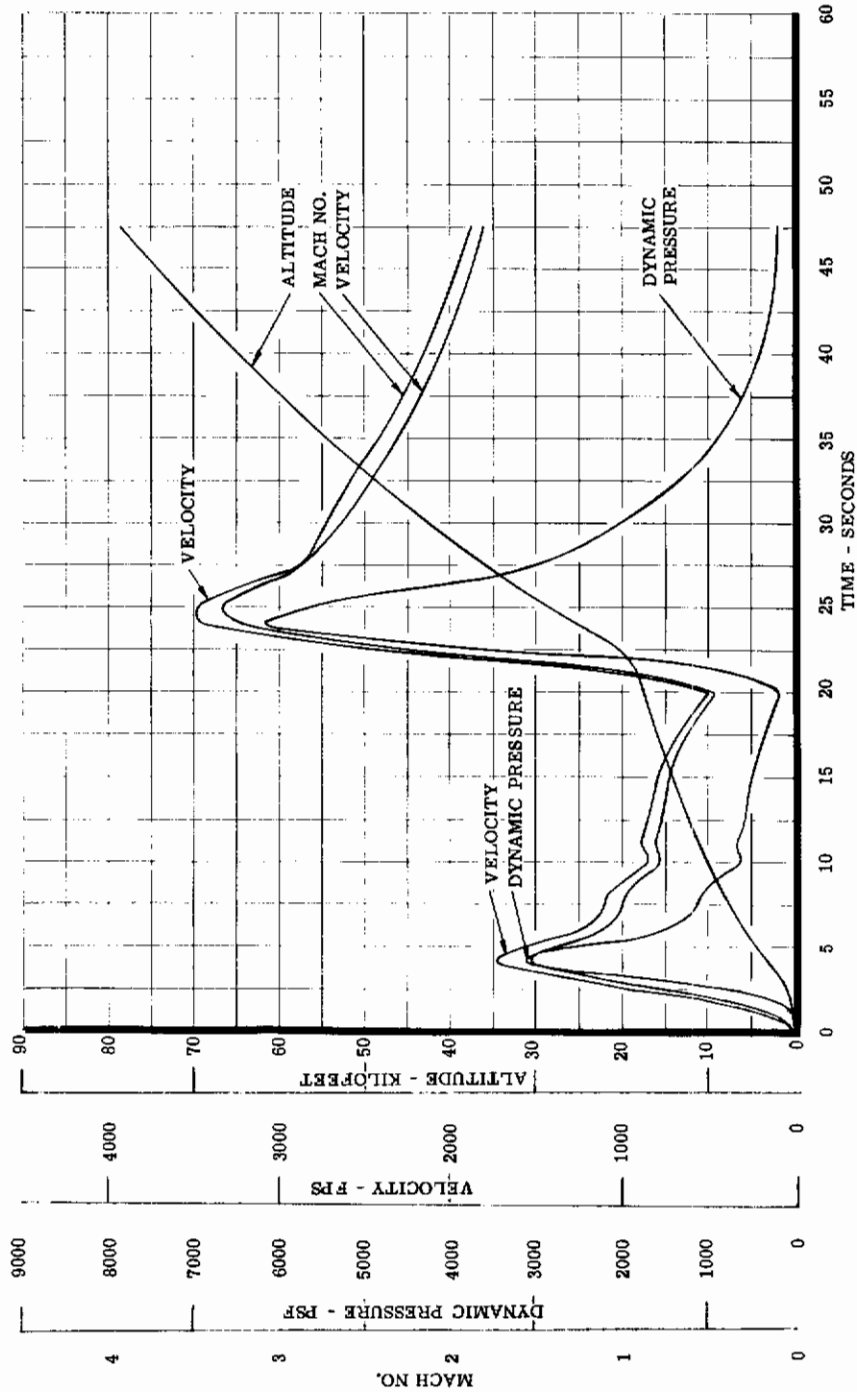
Figure 166. Radar Data versus Time on Cree Mission GAC No. 1

134
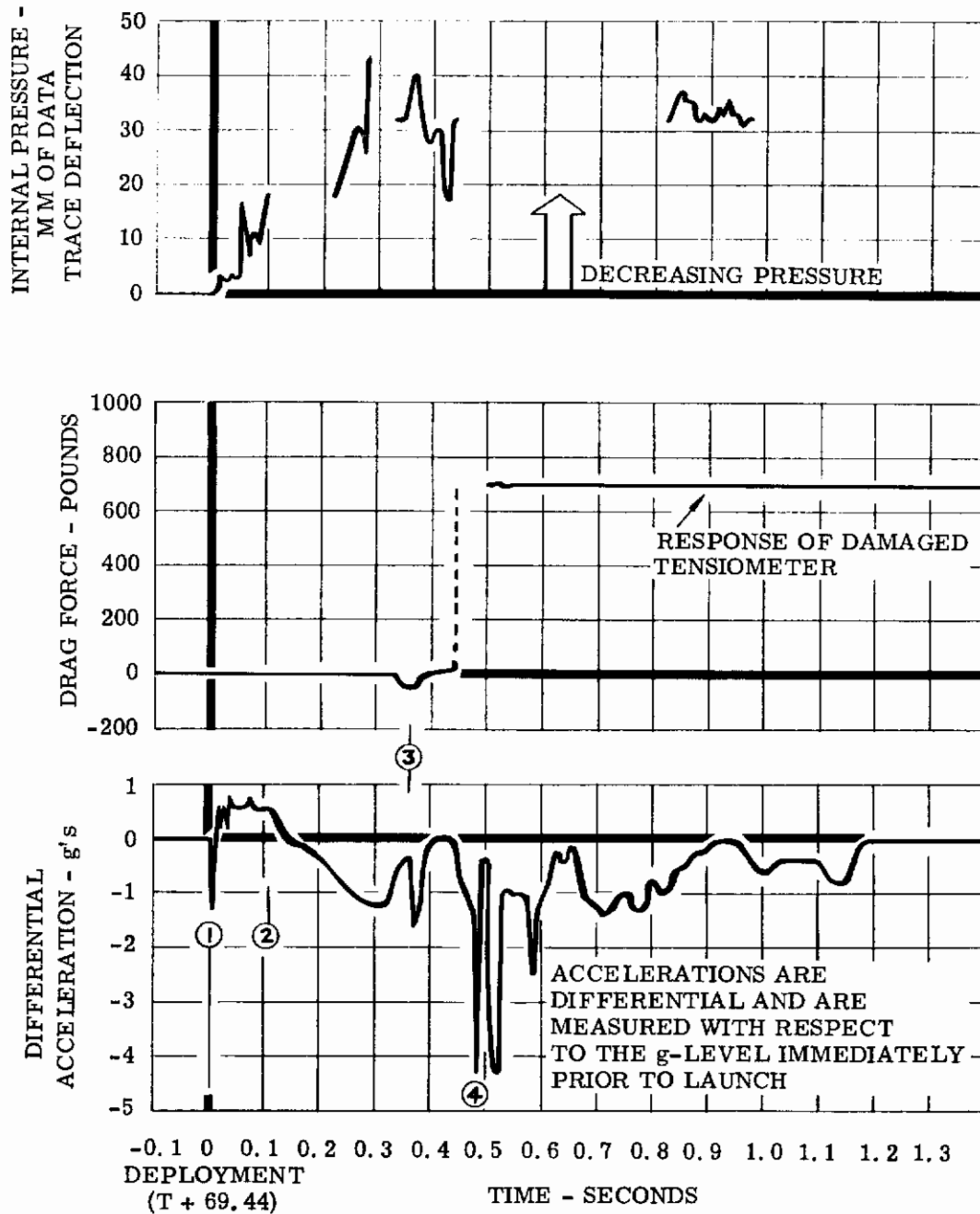
Figure 167. Telemetry Data versus Time Test Mission GAC No. 1

(5) Initiation of inflation (programmed to occur at deployment + 0.35 second) may be evidenced by event (3).

(6) Maximum drag forces (not shown on force channel) and corresponding peak negative acceleration occurred at deployment + 0.48 second, approximately 0.12 second subsequent to initiation of inflation (see (4)). If the peak negative acceleration is assumed to be correct an approximate drag force of 2100 pounds is generated at a full inflated condition.

2. GAC Test No. 2

Description

Date: 21 November 1960

Time: 1200

Test Vehicle: Type II Cree (500 pounds)

Method: Ground launch from rails

Equipment: Jason launcher (Pad No. 2)

Launch Angle: 83 degrees

Azimuth: 150 degrees

Boosters: First-stage Nike, second-stage Nike

Second-Stage Ignition Time: t + 20 seconds

Second-Stage Separation Time: t + 40 seconds

Test Time: t + 65 seconds

Initiation of Recovery Phase: t + 100 seconds

Flotation System Inflation: 10,000-foot altitude

Test Item: Goodyear 9-foot diameter inflatable drag device

Expected Test Velocity: Mach 1.52

Expected Test Altitude: 122,000 feet

Expected Dynamic Pressure at Test Altitude: 13.5 lb/sq feet

Location Aids: (1) Radar beacon
(2) Sonar beacon
(3) Dye marker

Tracking Aids: (1) Radar beacon
(2) Flares

Data Gathering Capability: (1) Five-channel telemetry system
(2) Contrave Phototheodolite
(3) DOETS telemetry system
(4) Radar skin and beacon track

Results

Launch and trajectory through second stage burning appeared normal. Radar tracked the missile by beacon to t + 65 seconds and an altitude of 99,000 feet. At this point the beacon was lost and a skin track was maintained to the splash point. Splash was at t + 11.56 minutes at an azimuth of 117 degrees and a range of 74,810 yards. The flotation system functioned perfectly, the balloon and dye marker was sighted by the search aircraft and the missile was on board the crash boat within 45 minutes of the splash time. Examination of the recovered test vehicle revealed that the flotation and recovery systems had functioned satisfactorily. The Goodyear inflatable drag device was not attached to the test vehicle. The 3/16-inch diameter attachment cable was broken at the tensiometer connector (see Figure 168). The 3000 pound range tensiometer suffered an overload during the test. The missile camera was operating during the entire test. Water leaked into the camera compartment causing the exposed film to become wet. However, the film was not damaged appreciably.
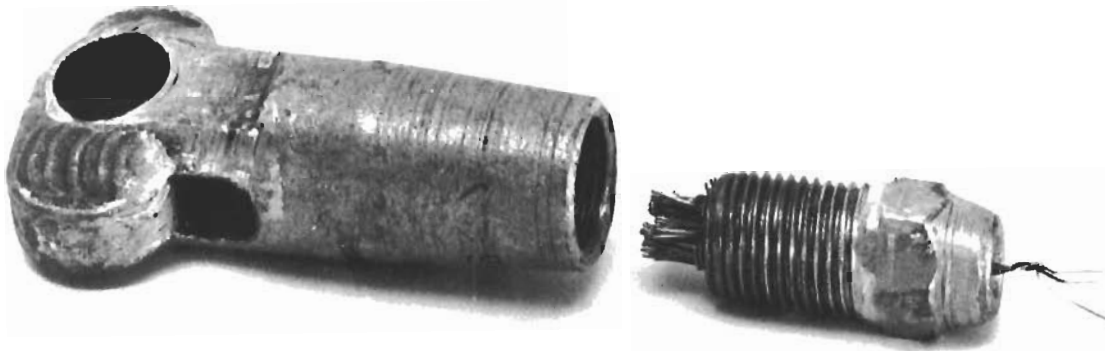
Figure 168. Ballute-to-Tensiometer Connector

Data Reduction

The radar beacon was tracked from launch to t + 65 seconds and altitude of approximately 99,000 feet. Contrave phototheodolite tracked from launch to t + 23.0 seconds. A successful skin track was obtained by the FPS-16 radar for the entire mission. A plot of the reduced radar data, altitude versus range, is presented in Figure 169. The predicted trajectory is also presented for comparison purposes. There was a rather large difference between predicted (no wind) trajectories and actual trajectories. This deviation from the predicted becomes more apparent at times subsequent to t + 20.0 seconds.

Figure 170 shows radar and contrave data as a function of time. Inflection points in the velocity and Mach number profiles at t + 40 seconds indicate an event occurred at this time.

A telemetry check prior to launch showed the system to be in satisfactory working order, and good signal strength was received throughout the test period.

Figure 171 presents time history profiles of pertinent data accumulated during test mission No. 2. Shown are differential acceleration, measured with reference to the missile's acceleration immediately prior to decelerator deployment, drag force, and internal pressure. Reduction of telemetry recordings revealed that deployment occurred prematurely at t + 40.23 seconds. At this time the acceleration channel experienced a high frequency disturbance with deflections exceeding the limits + 1 g and - 7 g (see Figure 171) and inflation was initiated. Pressures are measured from full scale deflection. Pressure before deployment exceeds or equals the range of the pressure transducer (5 psia in this case) and will decline to an equilibrium pressure after deployment. During preflight testing of the missile it was noted that one arm of the transducer strain gage bridge was open. The arm was replaced with a precision resistor and its response was presented as data trace
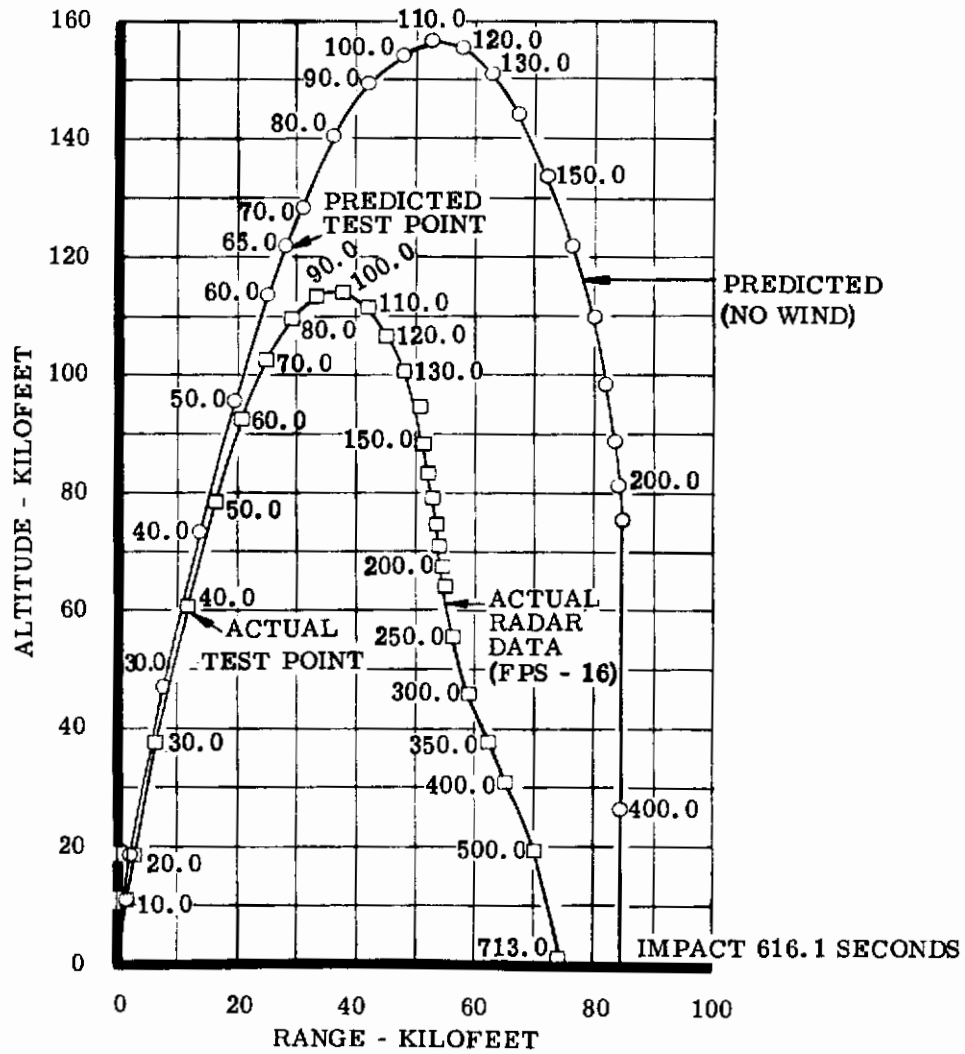
Figure 169. Predicted and Actual Trajectories for Cree Mission GAC No. 2
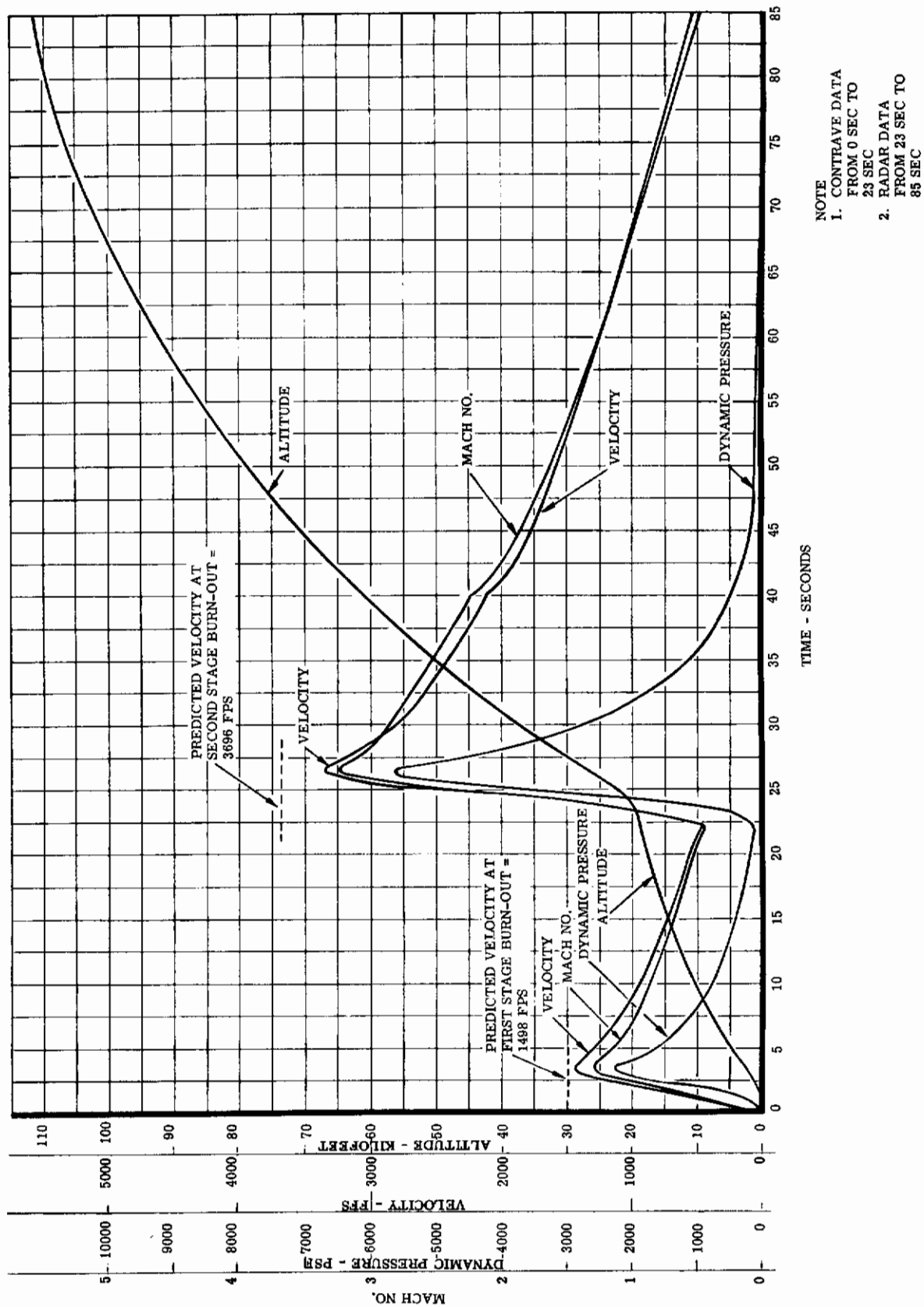
Figure 170. Radar and Contrave Data versus Time on Cree Mission GAC No. 2
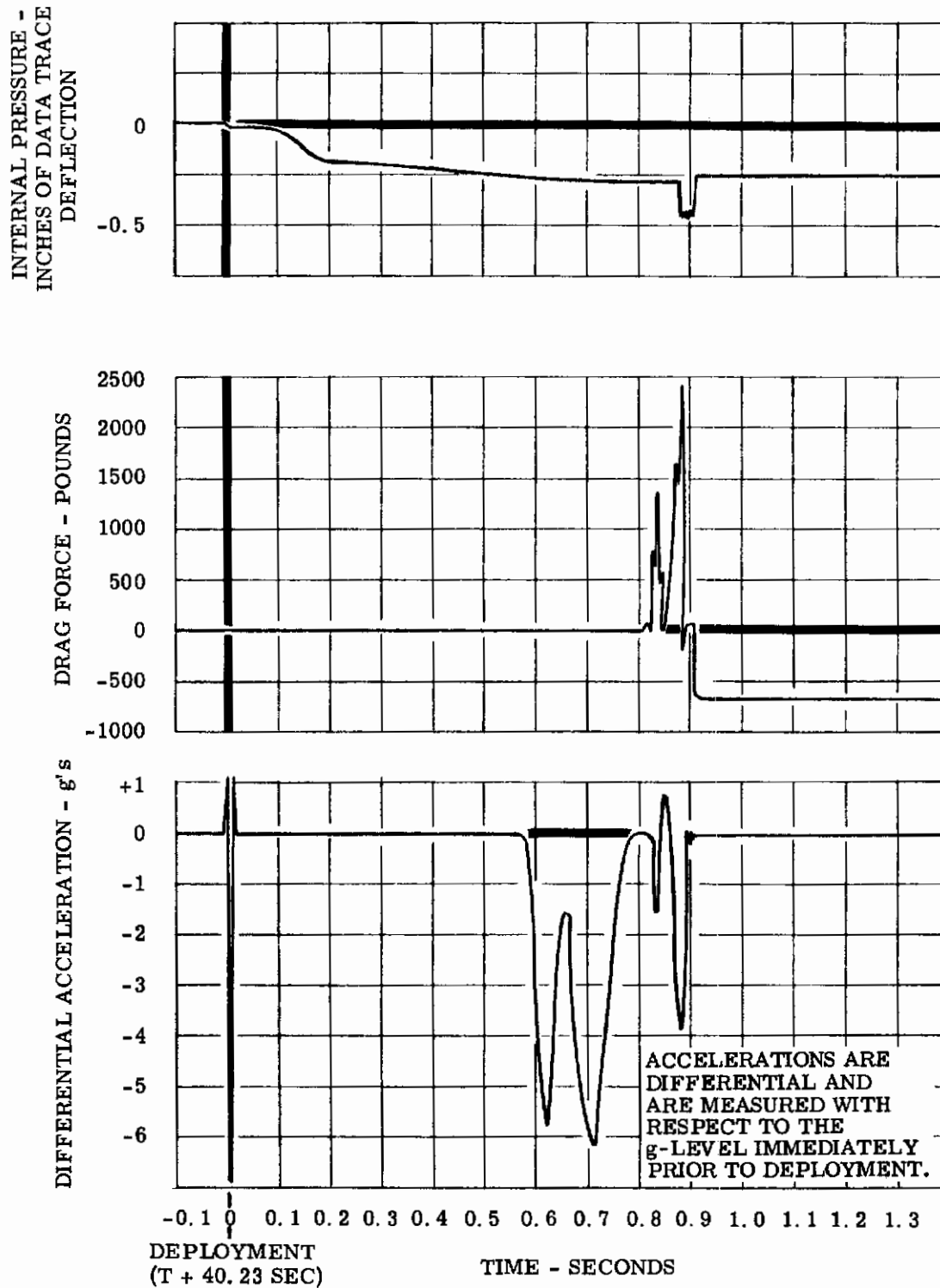
Figure 171. Telemetry Data versus Time on Cree Test Mission GAC No. 2

The chart labels:

INTERNAL PRESSURE - INCHES OF DATA TRACE DEFLECTION

DRAG FORCE - POUNDS

DIFFERENTIAL ACCELERATION - g's

ACCELERATIONS ARE DIFFERENTIAL AND ARE MEASURED WITH RESPECT TO THE g-LEVEL IMMEDIATELY PRIOR TO DEPLOYMENT.

DEPLOYMENT (T + 40.23 SEC)

TIME - SECONDS

deflection measured in inches. However, it was found by estimating a calibration that one inch of pressure data deflection was approximately equal to 5.45 psia. Thus, the internal pressure attained at deployment + 0.80 second was on the order of 1.5 psia.

Negative acceleration reaches peak values of 5.8 g's and 6.2 g's at deployment + 0.62 and 0.71 seconds. At corresponding deployment times it should be noted that no load measurement was recorded. As in the previous test, it is believed that drag loads were transferred from the Goodyear package to the missile before actual physical separation had occurred. Departure of the two packages apparently results at deployment + 0.81 second as evidenced by the trace of drag force shown in Figure 171. The peak recorded drag load was 2400 pounds occurring at deployment + 0.82 second. Both force channels were in good agreement with a peak shock force of 2360 pounds occurring at deployment +0.82 second. The data further indicates that at this time malfunction of the tensiometer occurred and that the actual maximum load was not recorded. Very shortly thereafter, both force channels and the internal pressure channel apparently became inoperative. The data traces shift to a new level where they remain to the end of the record. Inspection of telemetry records at the time of the programmed deployment (t + 65 seconds) shows no indication of an event.

Post-test examination of the tensiometer revealed that the strain gages had separated and neither channel was functioning. Recalibration of the tensiometer to maximum load revealed a break in one of the arms. Therefore, it can be concluded that the tensiometer suffered an overload during the test. The magnitude of this force can be estimated as being more than 3000 pounds, which is the peak force the tensiometer could measure, and less than 6000 pounds which is the ultimate strength of the tensiometer.

A further indication of the magnitude of the force can be deduced from the fact that the 3/16-inch diameter steel cable used to fasten the inflatable aerodynamic decelerator to the tensiometer had parted at the tensiometer fitting. This cable had a rated breaking strength of 4200 pounds.

Cause of premature initiation of the test item deployment could not be ascertained.

During the pre-flight checkout, the various program functions were led to their associated, clearly marked connectors. When the test package was installed all connections were made and inspected by experienced personnel from both Goodyear and Cook. A post-flight inspection of the timing system revealed that the missile programming functions were correct as marked and that the programming system was still functioning properly.

Camera coverage was initiated, as programmed, at t + 63 seconds. Viewing of the film showed that the drag device had deployed prematurely and had broken free of the missile before t + 63 seconds. At the preliminary viewing of the test film many speculations as to the nature of various objects within the camera's field of view were advanced for consideration. Among these were:

(1) A fragment of the drag device

(2) The flotation balloon

(3) The recovery parachute

(4) Drag device suspension cable

(5) Electrical cables for various functions

After close investigation of the film it was ascertained that the tensiometer cable and front and rear Goodyear explosive cables were all visible at various intervals throughout the film. The object that was tentatively identified as a fragment of the drag device or recovery parachute was positively identified to be taped-up De Jur Amsco connectors viewed at very close range rather than a relatively large object viewed at a distance. The method by which these connectors were taped is shown in Figure 172.

It becomes obvious that the resulting shape is identical to that appearing in the test film (see Figure 173).
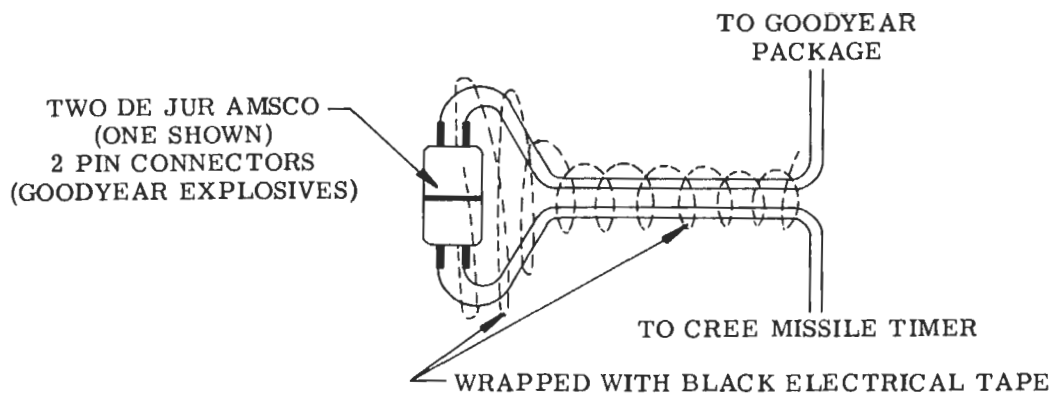
Figure 172. Missile Camera View at t + 63.35 Seconds
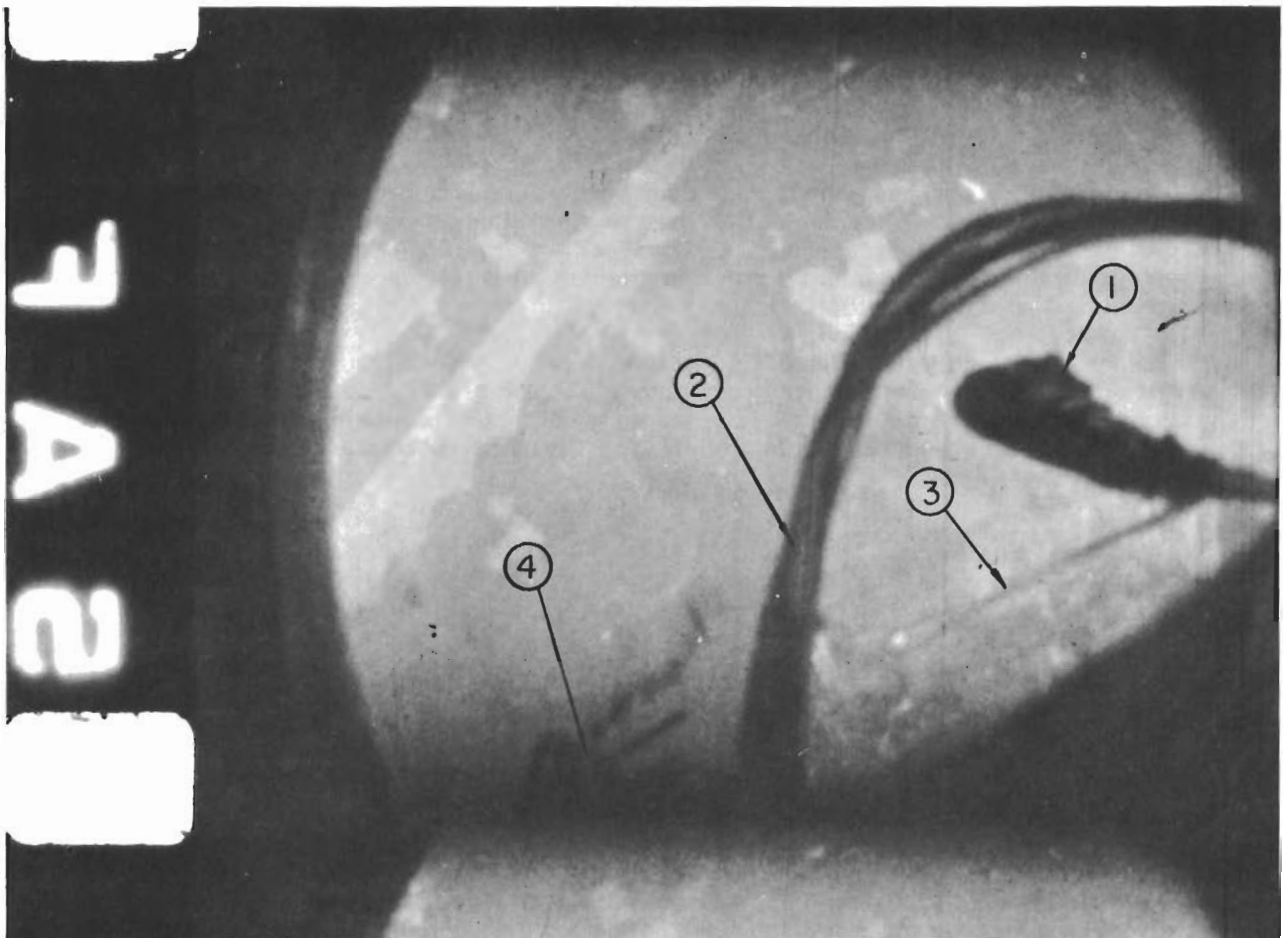
Figure 173. Missile Camera View at t + 64.00 Seconds

Shown in Figure 173 are the positions of:

(1) Wrapped connector

(2) Tensiometer cable

(3) Front explosive cable

A metallic object that remains unidentified is shown as item (4).

D. CONCLUSIONS

Since dynamic pressure, altitude, and Mach number as a function of time for test No. 1 (see Figure 166) do not include the deployment period (t + 69.44), comments will be presented on test No. 2 results only.

In Test No. 2, comparison of the expected dynamic pressure (13.5 psf) with the actual dynamic pressure (500 psf) (see Figure 169) results in a flight condition that exceeded the design criteria by a magnitude of approximately 37 to 1. This extreme flight condition resulted in overloading the inflatable decelerator to the extent that the decelerator was operable for a short period of time (see Figure 170). The differential drag oscillation shown in Figure 170 could be attributed to the dampening action of the riser line and the deploying period of the reel.

Test results indicate that an inflatable stabilizator-decelerator can be of lightweight design, packaged in a relatively small volume, and deployed and inflated with a high degree of reliability due to the simplicity of design and operation.

SECTION VIII

CONCLUSIONS AND RECOMMENDATIONS

A. CONCLUSIONS

It can be concluded from the theoretical analysis and its substantiation by wind tunnel test data that an inflatable stabilization and deceleration system for high-speed, high-altitude flight regimes is feasible and practical.

The stability and drag data obtained during the theoretical analysis is confirmed by the wind tunnel tests conducted by deployment in a high-altitude and high-speed regime. The flight test data verifies the feasibility of an inflatable drag-producing system which can be packaged and stored in a light-weight container, and inflated and deployed with a minimum of initial aerodynamic loading.

The theoretical thermodynamic data indicates that the inflatable system can be designed to withstand aerodynamic heating.

Wind tunnel tests indicate that three distinct types of wake flow exist between two bodies when a secondary body is in the wake of a primary body. The three types of flow are turbulent, transitional, and laminar. The three types of flow are governed by the Mach number, the distance between the two bodies, and the relative size of the bodies. The wind tunnel tests provide the following information:

(1) The drag from the secondary body is greater when laminar wake flow exists between the primary and secondary bodies.

(2) The optimum distance for greatest drag is governed by Mach number and relative size of the primary body to the secondary body.

(3) Excellent stability characteristics have been exhibited by tethered, inflatable, rigid spheres in the wake of various-shaped primary bodies.

Flight tests of an inflatable drag device with a ballistic coefficient of 10 in a high-speed, high-altitude flight regime indicate the following:

(1) Light-weight, temperature-resistant fabrics can be used in fabrication.

(2) A small, light-weight container can be used for packaging and storing.

(3) The device can be positively ejected.

(4) Inflation can be accomplished by a self-contained, light-weight pressurization system.

(5) Deployment from the primary body can occur at a constant velocity. This would minimize the initial aerodynamic loading.

Generally, it can be concluded that an inflatable sphere utilizing readily available material and present-day manufacturing methods is feasible and a practicable method of decelerating and stabilizing a recoverable payload from high-altitude and high-speed flight regimes.

B. RECOMMENDATIONS

To establish more complete data, consideration should be given to performing additional full-scale, free-flight tests at conditions commensurate with the design parameters of the present configuration. The free flight could be accomplished by utilizing a stratospheric ascension balloon or a Cree-Nike booster, programmed to more accurately achieve the flight test deployment condition.

Various payload and drag-producing configurations should be investigated to ascertain capabilities and limitations for operation at hypersonic speeds and high altitudes. The flight conditions could encompass a regime of Mach 4.0 at 70,000 to 120,000 feet altitude over a weight-to-drag ratio range of 1, 10, 50, and 100.

A parametric performance study should be conducted to establish the aerodynamic, thermo-dynamic, and material requirements for the flight regime described in the preceding paragraph. Various configurations should be investigated to determine the optimum drag device. These configurations should include sperical, hemispherical toroids, various-shaped cones, and their combinations. Variation of the drag area in these configurations should also be investigated. Various techniques for inflating the optimum shape should be investigated and should include a determination for maintaining inflation pressure throughout the descent trajectory down to sea level. This could eliminate the requirement for deployment of a final-stage parachute. A material investigation should be conducted to evaluate gas-tightness, flexibility, and strength of metallic and non-metallic fabric at elevated temperatures up to $1500^\circ F$ which would extend the initial recovery capability into the hypersonic flight regime. Material determination should include consideration of fabrication and field maintenance techniques.

LIST OF REFERENCES

1. Minzer and Ripley, U. S. Standard Atmosphere, 1957.

2. Kuathe and Schetzer, Foundations of Aerodynamics.

3. Modern Development in Fluid Mechanics. Vol. II.

4. Hilton, W. J., High Speed Aerodynamics.

5. Van Driest's, "The Problem of Aerodynamic Heating," Aeronautical Engineering Review, October 1956.

6. Timoshenko, Theory of Plates and Shells, N. Y., 1940.

7. Manual for Users of the Unitary Plan Wind Tunnel Facilities of the National Advisory Committee for Aeronautics, NACA, Washington, 1956.

8. May, Albert, and W. R. Witt, Jr., Free Flight Determinations of the Drag Coefficient of Spheres. NAVORD Report 2352, August 1952.

9. Hoerner, S. F., Fluid Dynamic Drag, (Published by the Author), Midland Park, N. J., 1958.

10. Stine, H. A., and K. Wanlass, Theoretical and Experimental Investigation of Aerodynamic-Heating and Isothermal Heat-Transfer Parameters on a Hemispherical Nose with Laminar Boundary Layer at Supersonic Mach Numbers. NACA TN3344, December 1954.

11. Chauvin, L. T., Pressure Distribution and Pressure Drag for a Hemispherical Nose at Mach Numbers 2.05, 2.54 and 3.04. NACA RM L 52K06, December 1952.

12. Cooper, M., and E. E. Mayo, Measurements of Local Heat Transfer and Pressure on Six 2-Inch-Diameter Blunt Bodies at a Mach No. of 4.95 and at Reynolds Numbers Per Foot Up to 81×10^6. NASA Memo 1-3-59L, March 1959.

13. Kendall, J. M. Jr., Experiments on Supersonic Blunt-Body Flows. JPL-CIT Progress Report No. 20-372, February 27, 1959.

14. Katz, J. R., Pressure and Wave Drag Coefficients for Hemispheres, Hemisphere-Cones and Hemisphere-Ogives. NAVORD Report 5849, March 1958.

15. Van Dyke, M. D., "The Supersonic Blunt Body Problem - Review and Extension", Journal of the Aero/Space Sciences, Vol. 25, No. 8, August 1958.

16. Trout, O. F., Jr., Experimental Investigation of Several Copper and Beryllium Hemispherical Models in Air at Stagnation Temperatures of $2000^\circ F$ to $3600^\circ F$. NASA TM X-55, September 1959, Classified Confidential.

17. Kaplan, C., Flow of a Compressible Fluid Past of a Sphere. NACA TN 762.

18. Hunt, G. K., Supersonic Wind-Tunnel Study of Reducing the Drag of a Bluff Body at Incidence by Means of a Spike, British Report Aerodynamics 2606, May 1958, ASTIA AD 206515.

19. Daniels, Lloyd E. Capt. USAF, Effects of the Upstream Influence of a Shock Wave at Supersonic Speeds in the Presence of Separated Boundary Layers. WADC TR 54-31, January 1954.

20. Mair, W. A., "Experiments on Separation of Boundary Layers on Probes in Front of Blunt - Nosed Bodies in a Supersonic Air Stream," Philosophical Magazine, Vol. 43, No. 342.

21. Bonney, E. A., M. J. Zucrow, and C. W. Besserer, Aerodynamics-Propulsions-Structures. D. Van Nostrand Co., Inc., Princeton, N. J., 1956.

22. Jackson, P. H., Effect of a Probe on the Drag and Pressure Distribution of a Hemispherical Nose, Consolidated Vultee Aircraft Report CF-2140, 3 June 1954.

23. Beastall, D. and J. Turner, The Effect of a Spike Protruding in Front of a Bluff Body at Supersonic Speeds, British ARC RM-3007, January 1952.

24. Jones, J. J., Experimental Drag Coefficients of Round Noses with Conical Windshields at Mach Number 2.72. NACA RM L55E10, June 1955.

25. Bechwith, I. E., and Gallagher, J. J., Heat Transfer and Recovery Temperatures on a Sphere with Laminar, Transitional, and Turbulent Boundary Layers at Mach Numbers of 2.00 and 4.15. NACA TN-4125, December 1957.

26. Stalder, J. R., and Nielsen, H. V., Heat Transfer from a Hemisphere - Cylinder Equipped with Flow Separation Spikes. NACA TN-3287, September 1954.

27. Crawford, D. H., Investigation of the Flow Over a Spiked-Nose Hemisphere - Cylinder at a Mach Number of 6.8. NACA TN-D-118, December 1959.

28. Stress Analysis of the 25 Percent Scale Dynamic Deceleration and Stabilization Balloon Test Model. Goodyear Aircraft Engineering Report 10383, 26 August 1959.

29. Stress Analysis of the Balloon Stabilization Equipment for the Cree Missile Test, Phase III. Goodyear Aircraft Engineering Report 10384, 24 February 1960.

30. Love, E. S., Base Pressure at Supersonic Speeds on Two-Dimensional Airfoils and on Bodies of Revolution with and without Fins Having Turbulent Boundary Layers. NACA TN 3819, January 1957.

TRAJECTORY ANALYSIS
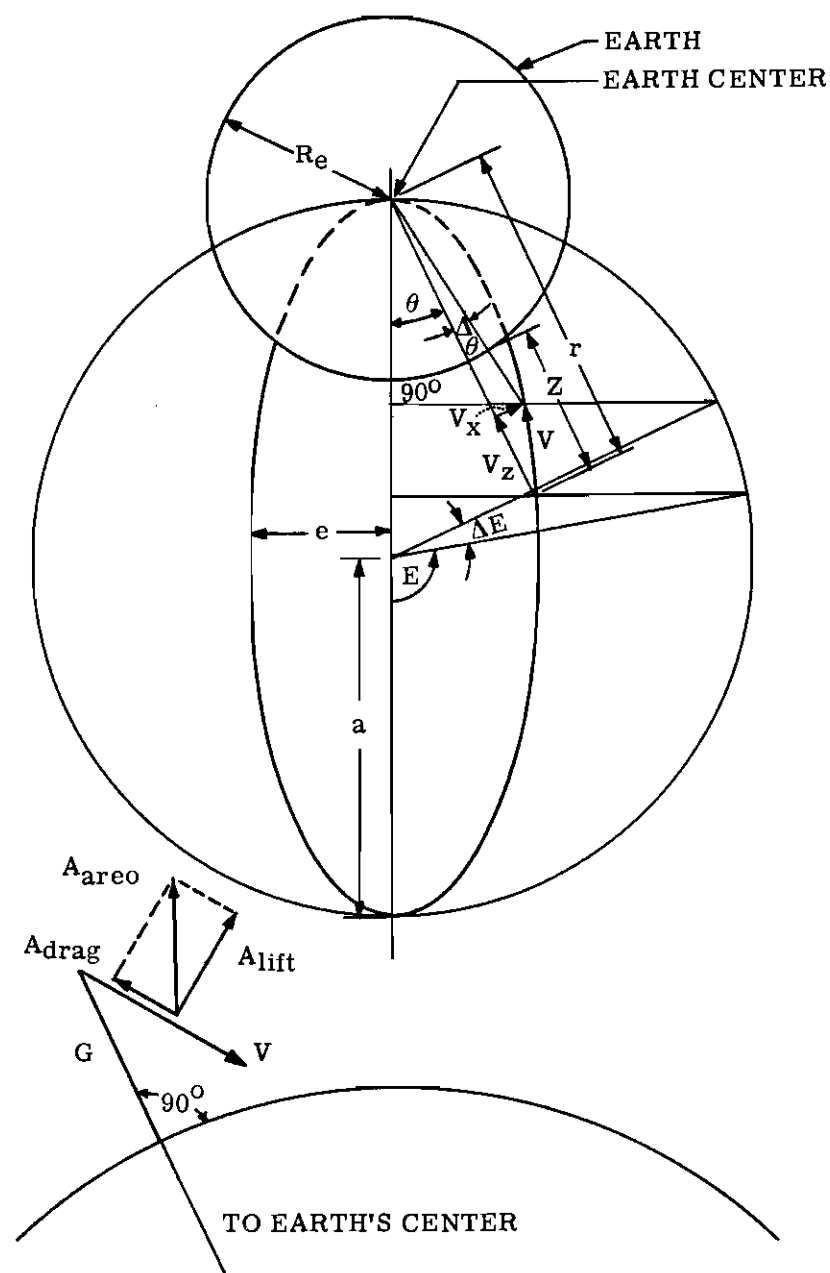
A_{aero}	=	acceleration due to vector sum of $A_{drag} + A_{lift}$
A_{drag}	=	acceleration due to drag
A_{lift}	=	acceleration due to lift
a	=	semi-major axis (applies for eccentricity ≤ 1)
C_d	=	coefficient of drag
d	=	diameter of equivalent frontal area (ft)
E	=	geometric variable (useful for simplifying equations)
e	=	eccentricity of orbit
G	=	universal gravity constant
H	=	geopotential altitude (ft)
L_M	=	rate of change of temperature with altitude ^{O}R
M_e	=	mass of the earth = M/G
P	=	pressure (subscript B = at base of layer) psi
Q	=	$0.0341647942 \, ^{O}K/meter$
q	=	dynamic pressure $(1/2 \rho V^2)$
R_e	=	radius of the earth (3960 miles)
r	=	distance from center of earth from point considered (ft)
T_M	=	molecular scale temperature ^{O}R
t	=	time (seconds)
V	=	total velocity (vector sum) (ft/sec)
V_s	=	velocity of sound (ft/sec)
V_x	=	local horizontal velocity
V_z	=	local vertical velocity in feet per second
Z	=	geometric altitude in feet
μ	=	1.4065107×10^6
Δ	=	increment of a variable
ρ	=	atmosphere density (slugs/ft^2)
θ	=	angular displacement from apogee

THERMODYNAMICS

C_H	=	Stanton Number - free stream
C_{p_a}	=	specific heat - air (BTU/lb/°F)
C_{p_m}	=	specific heat - material (BTU/lb/°F)
c_m	=	specific heat of sink
h	=	convective heat transfer coefficient
K	=	Thermal conductivity (BTU/hr sq ft °F/ft)
M_∞	=	free stream Mach number
q_w	=	heat flux to body wall
T_∞	=	ambient temperature (°F)
$T_{1\ to\ 8}$	=	temperature of increment 1 to 8 (°F)
T_{aw}	=	adiabatic wall temperature (°F)
T_n	=	temperature of nth thickness increment (°F)
T_r	=	recovery temperature (°F)
T_{ref}	=	free stream temperature
T_s	=	wall temperature (°F)
T_w	=	body wall temperature
V_∞	=	velocity-free stream (fps)
w	=	weight of platinum heat sink
ΔX	=	material thickness increment
ρ_∞	=	density air free stream (slugs/sq ft)
ϵ	=	emissivity of sink
σ	=	Stefan-Boltzmann constant of radiation
θ	=	time increment (sec)
ρ_m	=	density material (lb/sq ft)

STRESS ANALYSIS

a	=	sphere radius (in.)
A, B	=	constant coefficients
C_1, C_2	=	constants of integration
D	=	total drag (lb)

STRESS ANALYSIS (Continued)

D_ψ	=	drag on area $\psi = 0$ to ψ (lb)
D_B	=	drag on back half of sphere (lb)
D_F	=	drag on front half of sphere (lb)
E	=	modulus of fabric in tension (lb/in.)
H	=	radial loads on hoop cable (lb)
N_ψ, N_θ	=	fabric stresses (lb)
P_i	=	internal pressure (psig)
P_0, psig	=	pressure buildup on sphere surface = absolute pressure - P_∞
P_∞	=	local ambient pressure (psia)
R	=	tension in main cable (lb)
r_1, r_2	=	principle radii of curvature at any point (in.)
r_0	=	radius of attaching circle (in.)
R_0	=	sum of external loads, pounds, in vertical direction on segment subtended by angle ψ
Subscript 1 =		region inside hoop cable ($0 < \psi < \psi_0$)
Subscript 2 =		region outside hoop cable ($\psi_0 < \psi < {}^\pi/2$)
T	=	tension in attaching cables (lb)
T_h	=	tension in hoop cable (lb)
T_p	=	tangential load applied to sphere (lb/cable)
v	=	tangential deflection of a point (lb)
w	=	radial deflection of a point (in.)
W	=	weight of payload and spherical decelerator system (lb)
W_p	=	weight of payload (lb)
β	=	angle of attaching cables with parallel circle (degrees)
ϵ	=	fabric strain in direction of parallel circles
μ	=	Poisson's ratio

AERODYNAMICS

A_B	=	sphere frontal area (ft²)
A_p	=	primary body (payload) frontal area (ft²)
a	=	speed of sound at free stream condition (ft/sec)

C_D	=	drag coefficient (X/qA_B)
$(C_D)_p$	=	pressure drag, $\int_0^\pi C_p \sin 2\theta \, d\theta$
$(C_D)_f$	=	skin friction drag
C_p	=	pressure coefficient $(P_\theta - P_1)/q$
D	=	sphere diameter (8 inches)
L_R	=	spike length or riser line length (in.)
M	=	Mach number (V/a)
P_1	=	free stream static pressure (psi)
P_θ	=	local pressure on sphere (psi)
q	=	$\rho V^2/2$ (lb/ft^2)
R	=	Reynolds number $(VD\rho/\mu)$
V	=	free stream velocity (ft/sec)
W	=	weight (lb)
X	=	drag (lb)
α	=	angle of attack (deg)
θ	=	angular measurement on sphere (deg)
μ	=	dynamic viscosity (slugs/ft sec)
ρ	=	free stream air density (slugs/ft^3)